Control of Hybrid Renewable Energy Power Plant for Autonomous Systems

Phatiphat Thounthong

Université de Lorraine

ECOLE DOCTORALE "Informatique, Automatique, Electronique-Electrotechnique, Mathématiques"

N° attribué par la bibliothèque

|_|_|_|_|_|_|_|_|_|_|

Mémoire

en vue d'obtenir

L'Habilitation à diriger des recherches

Spécialité : Génie Electrique

par

Phatiphat THOUNTHONG

Docteur, Génie Électrique de l'Institut National Polytechnique de Lorraine

Soutenue publiquement le 1 décembre 2020

Control of Hybrid Renewable Energy Power Plant for Autonomous Systems

Membres du Jury :

Président :

Christophe TURPIN	Directeur de Recherche CNRS, LAPLACE, Toulouse

Rapporteurs :

Éric MONMASSON	Professeur – Université de Cergy Pontoise
Daniel HISSEL	Professeur – Université de Franche-Comté
Manuela SECHILARIU	Professeur – Université de Technologie de Compiègne

Examinateurs :

Betty LEMAIRE-SEMAIL	Professeur – Université de Sciences et Technologies de Lille
Bernard DAVAT	Professeur – Université de Lorraine
Serge PIERFEDERICI	Professeur – Université de Lorraine
Babak NAHIDMOBARAKEH	Professeur – Université de Lorraine

Invité :

Noureddine TAKORABET	Professeur – Université de Lorraine

Abstract (English)

This application to Habilitation to Advise Researches is prepared with the GREEN laboratory of the University of Lorraine. It is a synthesis of my research work and a vision of my future projects, mainly in the spirit of scientific collaboration of the RERC (Renewable Energy Research Center) of the King Mongkut's University of Technology North Bangkok and the GREEN Laboratory of the University of Lorraine.

This document composes of three main parts. Part I is a long curriculum vitae. In Part II, it is the synthesis research works that I have done after my PhD thesis. It composed of two main topics: 1) a study of DC/DC converter (interleaved converter, three-level converter) for FC, PV, Battery, and supercapacitor applications; 2) energy management for hybrid system (FC/SC, FC/Battery, etc…). For the control approach, a classic linear control and a nonlinear control based on differential flatness estimation have been studied and compared in hybrid energy source. Finally, in Part III, it is a research perspective, developed for the next years, and a short conclusion.

Abstract (Français)

Ce dossier d'Habilitation à Diriger des Recherches est préparé en collaboration avec le laboratoire GREEN de l'Université de Lorraine. Il constitue une synthèse de mes travaux de recherche et une vision sur mes projets à venir principalement dans un esprit de collaboration scientifique du RERC (Renewable Energy Research Center) du King Mongkut's University of Technology North Bangkok et le Laboratoire GREEN de l'Université de Lorraine.

Ce document est composé de trois grandes parties. La première partie correspond à mon curriculum vitae détaillé. La seconde est la synthèse des travaux de recherche réalisés après mon doctorat ou je présente deux principaux axes à savoir un axe sur les convertisseurs DC/DC (interleaved converter, three-level converter) pour les applications Pile à Combustible, Panneaux Photovoltaïques, batteries et super-condensateurs et un axe sur la gestion d'énergie des systèmes hybrides (association Pile à combustible-supercondensateur, Pile à combustible-batteries, etc…). Quant aux stratégies de commande, des régulateurs linéaires conventionnels et non linéaires basés sur le concept de platitude des systèmes différentiels ont été étudiés et comparés pour des applications liées à la gestion d'énergie des sources hybrides d'énergie électrique. Finalement la troisième partie est consacrée aux perspectives pour les prochaines années et à une brève conclusion.

Table of Content

@@@ END @@@

II.1 Introduction

Energy is important to everyone's life. Among different types of energy, electric energy is one of the most essential that people need every day. Electricity can be generated in many ways from various energy sources. Electric power can be generated by conventional thermal power plants (using fossil fuels, or nuclear energy), hydropower stations, and other alternative power generating units (such as wind turbine generators, photovoltaic arrays, fuel cells, biomass power plants, geothermal power stations, etc.). Fossil fuels (including coal, oil and natural gas) and nuclear energy are not renewable, and their resources are limited. Currently, most of the energy demand in the world is met by fossil and nuclear power plants. A small part is drawn from renewable energy technologies such as wind, solar, fuel cell, biomass and geothermal energy [Raj08], [Too09]. Wind energy, solar energy and fuel cells have experienced a remarkably rapid growth in the past ten years [Agl09], [Ber09a], [Mil09] because they are pollution-free sources of power.

The cost of wind turbine, solar photovoltaic, and fuel cell electricity is still high [Moc09], [Pat09], [Sal09]. Nevertheless, with ongoing research, development and utilization of these technologies around the world, the costs of solar cells and fuel cell energy are expected to fall in the next few years. As for solar cell and fuel cell electricity producers, they now sell power freely to end-users through truly open access to the transmission lines. For this reason, they are likely to benefit as much as other producers of electricity. Another benefit in their favour is that the cost of renewable energy falls as technology advances, whereas the cost of electricity from conventional power plants rises with inflation. The difference in their trends indicates that wind, hydrogen, and solar power will be more advantageous in future. In the near future, the utility power system at a large scale will be supplied by renewable energy sources, i.e., hybrid energy systems, in order to increase their reliability and make them more effective for grid connected applications, as shown in Fig. II.1.1.

Additionally, they generate power near the load centres (called "autonomous system" or "grid independence", which eliminates the need to run high-voltage transmission lines through rural and urban landscapes. However, there are still some severe concerns about several sources of renewable energy and their implementation, e.g.,

1) capital costs and

2) their intermittent power production, called the "intermittency problem."

The intermittency problem, for example, of solar energy is that solar panels cannot produce power steadily because their power production rates change with seasons, months, days, hours, etc. If there is no sunlight, no electricity will be produced from the photovoltaic (PV) cell [Kol09], [Sen09]. For fuel cell, when a large load is applied to the cells, the sudden increase in the current can cause the system to stall if the depleted oxygen or hydrogen cannot be replenished immediately and sufficiently. Cell starvation can lead to a system stall, permanent cell damage or reduced cell lifetime [Tan04], [Cor06], [Cor08]. To protect the fuel cells from overloading and starvation, especially during transient conditions, excessive oxygen and hydrogen can be supplied to the cells during the steady-state operation, which increases the reserve of available power in anticipation of a load increase. This strategy, however, is conservative and leads to increased parasitic losses, decreased air utilization and thereby compromised system performance. Therefore, the fuel cell power or current slope must be limited to prevent a fuel cell stack from experiencing the fuel starvation phenomenon and to optimize the system.

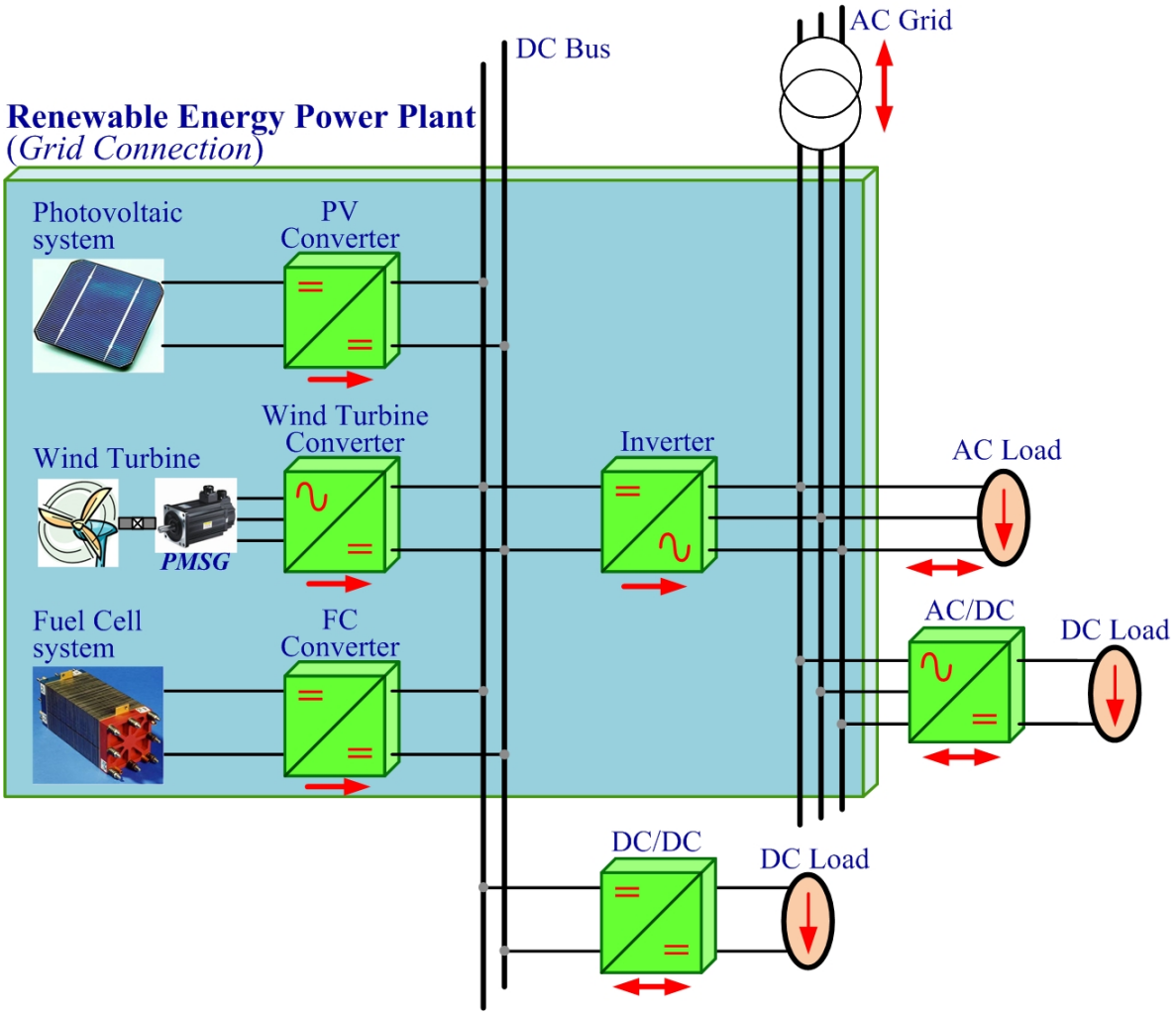

Fig. II.1.1. Grid connection: renewable energy hybrid power plant.

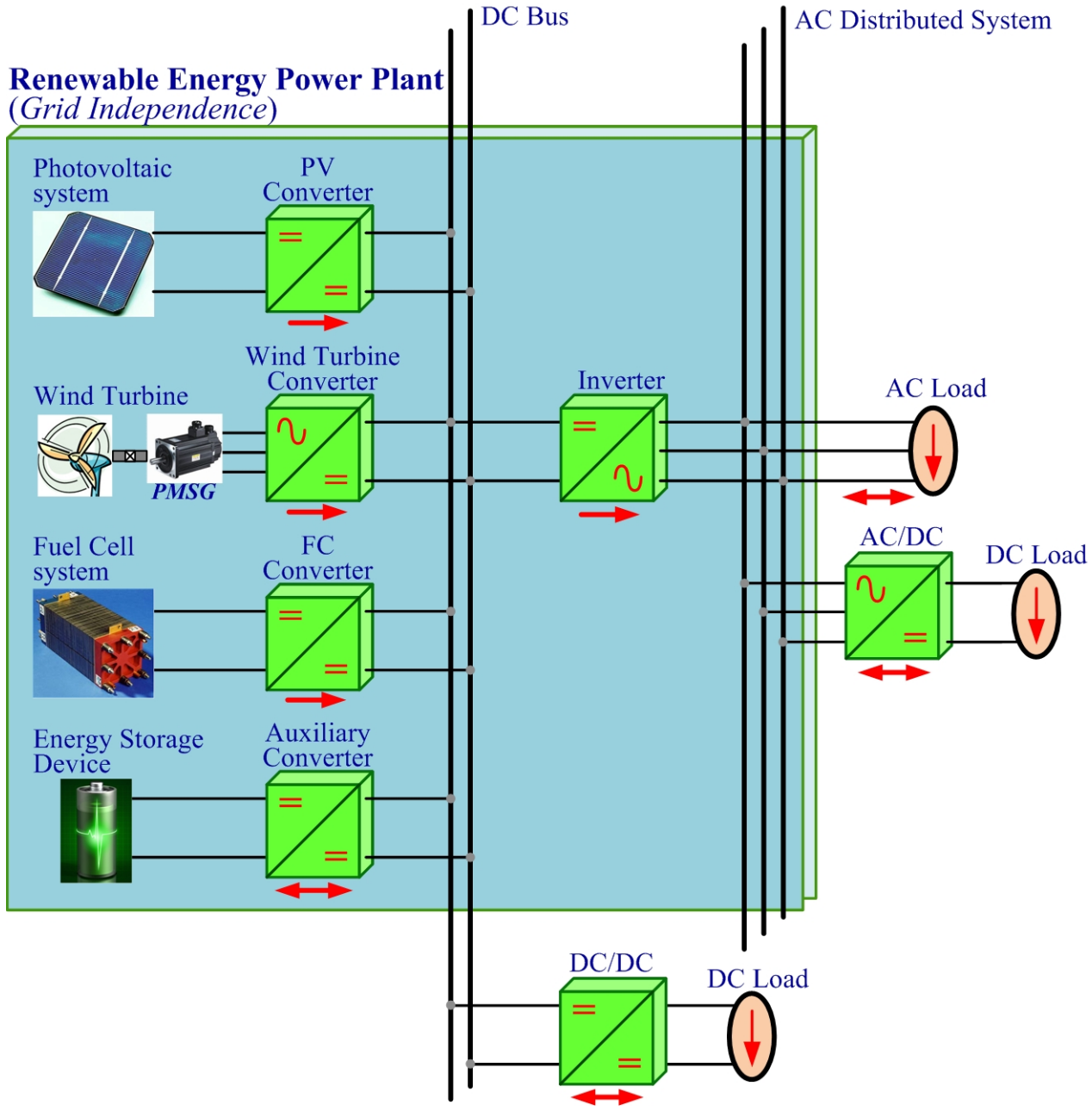

Fig. II.1.2. Grid Independence: renewable energy hybrid power plant.

Therefore, in order to supply electric power to fluctuating loads with a renewable hybrid power system in autonomous system, an electric energy-storage system [a battery or/and a supercapacitor (SC)] is needed to compensate for the gap between the output from the renewable energy sources and the load, in addition to the collaborative load sharing among those energies [Kak09], [Rea09], [Tho08b], see Fig. II.1.2.

Moreover, hydrogen as an energy storage media has the potential to address both daily and seasonal buffering requirements. Systems that employ an electrolyzer to convert excess electricity to hydrogen coupled with hydrogen storage and regeneration using a fuel cell can, in principle, provide power with zero (or near zero) emissions. Hydrogen production by solar energy or wind energy is a 'renewable–regenerative system' [Ber09a], and this process is known as the electrolysis process. The basic principle is the following: when the photovoltaic input power exceeds the load power demand, the system controller determines that the energy should be directed to hydrogen production. In this kind of operation, i.e., a solar based renewable–regenerative system, almost half of the solar input energy is directed to hydrogen production and converted with 60% energy efficiency.

Based on present storage device technology, battery design has to supply the trade-off between specific energy, specific power, and cycle life. The difficulty in obtaining high values of these three parameters has led to some suggestions that the energy-storage system of distributed generation systems should be a hybridization of an energy source and a power source [Coo09], [Tho09g]. The energy source, mainly fuel cells or/and solar cells in this document, has high specific energy, whereas the power source has high specific power. The power sources can be recharged from the main energy source(s) when there is less demand. The power source that has received wide attention is the supercapacitor (or 'ultracapacitor', or 'electrochemical double-layer capacitor') [Bau09], [Ber09b], [Sch09].

The enhancements in the performance of renewable energy source power systems that are gained by adding energy storage are all derived from the ability to shift the system output. Firming up the renewable system is accomplished by ensuring that energy is available when there is a demand for it rather than being limited by the availability of the renewable resource. As a result, the system output may need to be shifted to periods when the hydrogen and/or the sun, for example, are not available [Tho07]. Depending on the size and type of the energy-storage system and the load, it may be possible to provide all of the power needed to support the load. A much more common scenario is for the energy storage to simply provide enough power for applications, like peak shaving, without having full load support capability. The energy-storage system may also provide sufficient energy to ride out electric service interruptions that range from a few seconds to a few hours. This is especially important for service disruptions that occur when the renewable resource is not available.

For FC vehicle applications, General Motors (GM; USA) became the first automaker to demonstrate a drivable FC vehicle named the Electrovan in 1966. There are many types of FCs characterized by their electrolytes. One of the most promising to be used in electric vehicle applications is the polymer electrolyte membrane FC (PEMFC) because of its relatively small size, light weight, and ease to build [Na07], [Per07]. Today, many automobile companies (such as GM, Renault, Opel, Suzuki, Toyota, Daihatsu, DaimlerChrysler, Ford, Mazda) have demonstrated the possibilities of using the PEMFC as a main source in electric vehicles called FC vehicles (FCVs). The concept of an FCV is depicted in Fig. II.1.3. For example, after a long history of FC research and development from 1964, GM unveiled an FCV powered by PEMFC (75 kW, 125–200 V, 200 cells) to drive a wheel motor (a permanent magnet synchronous: 60 kW, 305 Nm) with a driving range of 400 km in 2000. In the United States, in 2002, the Honda FCX was the first FC car to be certified for use by the general public, and so theoretically become publicly available. This four-seater city car has a top speed of 150 km/h and a range of 270 km. The hydrogen fuel is stored in a high pressure tank [Hoo03].

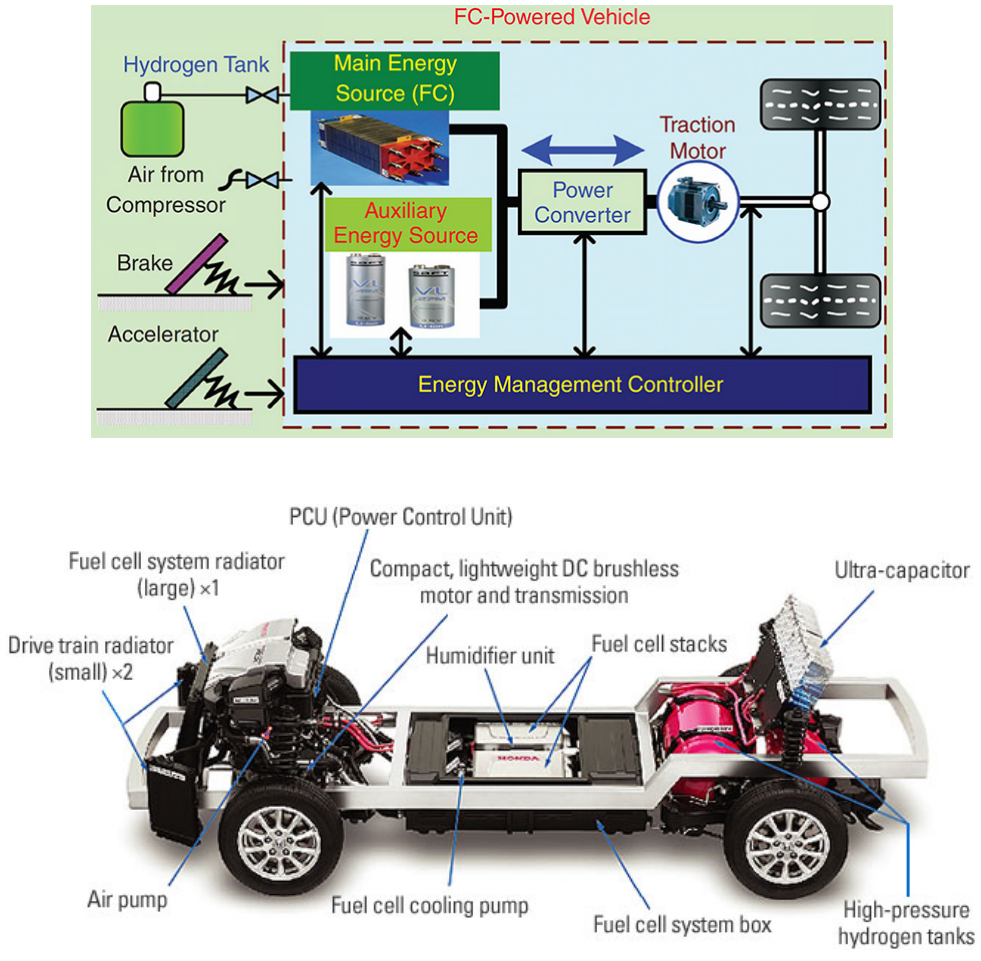

Fig. II.1.3. Concept of an FC vehicle.

In industry, United Technologies Corporation (UTC) FC (USA) is involved in the development of the FC systems for space and defense applications. UTC FC activity began in 1958 and led to the development of the first practical FC application used to generate electrical power and potable water for the Apollo space missions. In 1998, UTC FC delivered a 100-kW FC power plant, with 40% efficiency, to Nova Bus for installation in a 40-ft, hybrid drive electric bus under a DOE/Georgetown University contract [Var06].

GM is involved in the development of PEMFCs for stationary power and the more obvious automotive markets [Hel07]. In February 2004, they began the first phase of installation operations in Texas at Dow's chemical manufacturing, the largest facility in the world. These FC systems are used to generate 35MWof electricity.

Axane (France) was created in 2001 and is working on PEM FC technology [Lec04]. It is positioning itself to the objective three markets that are likely to provide large commercial outlets in the short term: 1) portable multiapplication generators (500 W–10 kW), 2) stationary applications (more than 10 kW), 3) mobile applications for small hybrid vehicles (5 kW–20 kW).

In this HDR document in Part II, many structures of renewable hybrid power source are proposed for both grid independence and vehicle applications. The basic principles, characteristics, and working constraints of the FC, PV, battery, and supercapacitor are presented in Section 2. The power circuit structures, the power electronics topologies, energy management and innovative energy control law (based on linear system and nonlinear differential flatness approach) are presented in Section 3.

II.2 Renewable Energy Sources and Storage Devices

II.2.1 Renewable Energy Source

II.2.1.1 Fuel Cell

A. Fuel Cell Principle

Sir William Robert Grove (11 July 1811 – 1 August 1896) was a Welsh judge and physical scientist. He was a pioneer of fuel cell technology.

An FC is a device that converts the chemical energy of a fuel directly to electrical energy. Its concept was proposed approximately 170 years ago when William Robert Grove conceived the first FC in 1839, which produced water and electricity by supplying hydrogen (H_2) and oxygen (O_2) into a sulfuric acid bath in the presence of porous platinum electrodes [Tho08a], see Fig. II.2.1. The process by which this is done is very similar to the electrochemical process by which a battery generates power; at one electrode, a fuel such as hydrogen is oxidized, and at the other electrode an oxidant such as oxygen is reduced. The reactions exchange ions through a solid or liquid electrolyte and electrons through an external circuit, as shown in Fig. II.2.2.

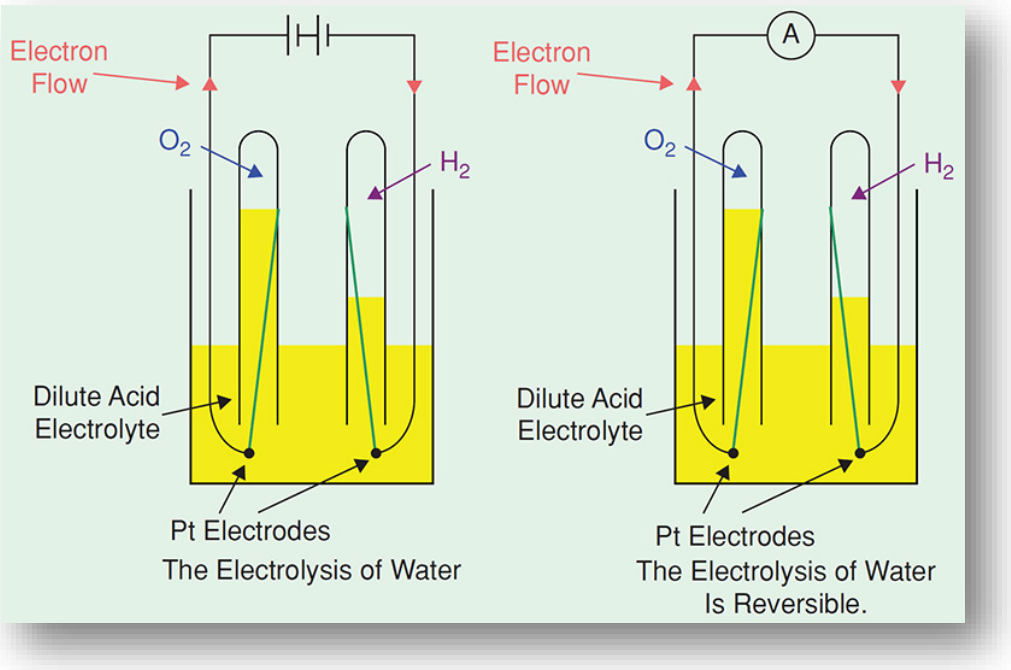

Fig. II.2.1. Fuel cell principle discovered by Sir William Grove.

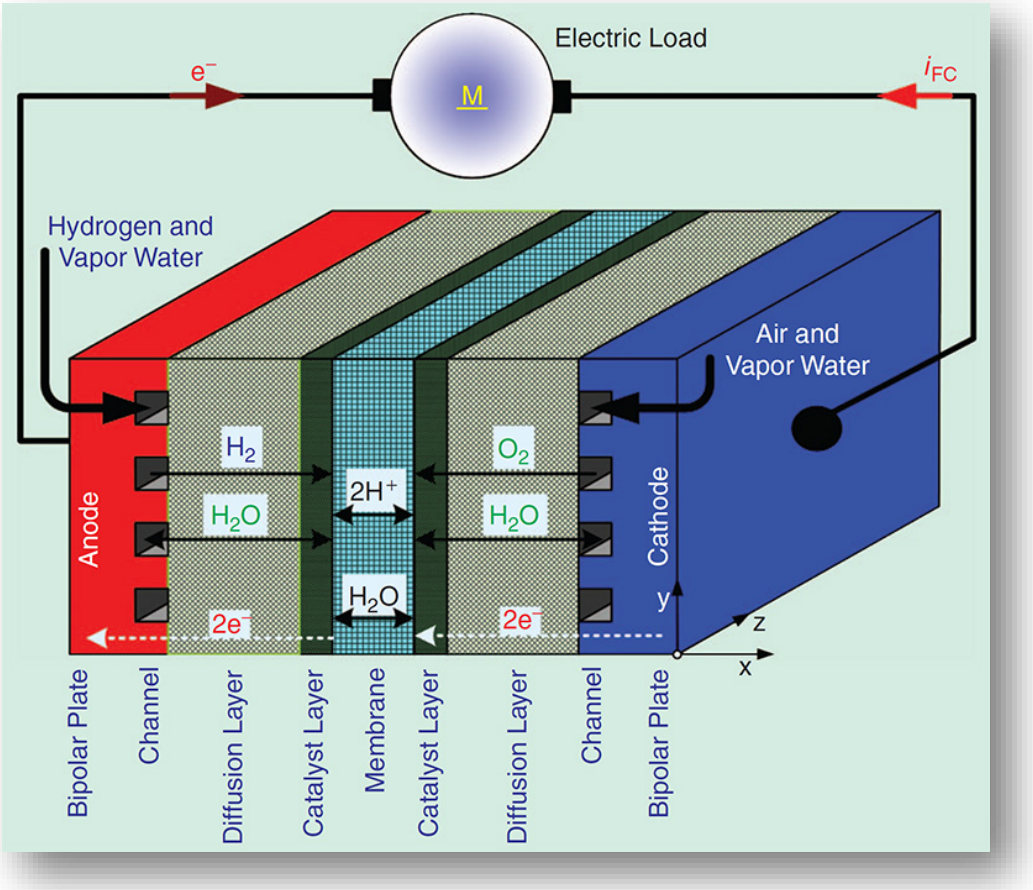

Fig. II.2.2. Different layers of an elementary cell of PEMFC.

There are many different types of FCs, with the principal differences between them being the type of electrolyte and/or the type of fuel that they use. For instance, both the phosphoric acid FC (PAFC) and the molten carbonate FC (MCFC) have a liquid electrolyte, whereas a solid oxide FC (SOFC) has a solid, ceramic electrolyte [Cho06a], [Suz08], [Wan07a]. A proton exchange FC or polymer electrolyte membrane FC (PEMFC) and a direct methanol FC (DMFC) may have the same solid polymer electrolyte, but the DMFC uses liquid methanol for fuel whereas the PEMFC uses gaseous hydrogen [Ko08], [Paq08].

The PEMFC has many of the qualities required of an automotive power system including relatively low operating temperature, high power density, and rapid startup [Cor08], [Ema08], [Mit06]. In addition, PEMFC may also be used in residential and commercial power systems [Neh06].

The FC model here is for a type of PEM, which uses the following electrochemical reaction:

$$H_2 + \frac{1}{2}O_2 \rightarrow H_2O + Heat + Electrical\ Energy. \quad (2.1)$$

The theoretical value of a single cell voltage of FC is 1.23 V. It is never reached even at no load. At the rated current, the voltage of an elementary cell is about 0.6–0.7 V [Sad06], [Pag07], [Pas07]. Therefore, an FC is always an assembly of elementary cells that constitute a stack, as Fig. II.2.3 depicts. The examples of a FC stack are shown in Fig. II.2.3 to Fig. II.2.5 that have been used for studying in the following works both in the GREEN lab and the RERC lab.

In a single FC, the two plates [Fig. II.2.3(b)] are the last of the components making up the cell. The plates are made of a light weight, strong, gas-impermeable, electron-conducting material; graphite or metals are commonly used. The first task performed by each plate is to provide a gas flow field. The channels are used to carry the reactant gas from the point at which it enters the FC to the point at which the gas exits. Flow-field design also affects water supply to the membrane and water removal from the cathode. The second task served by each plate is that of current collector. With the addition of the flow fields and current collectors, the PEMFC is completed.

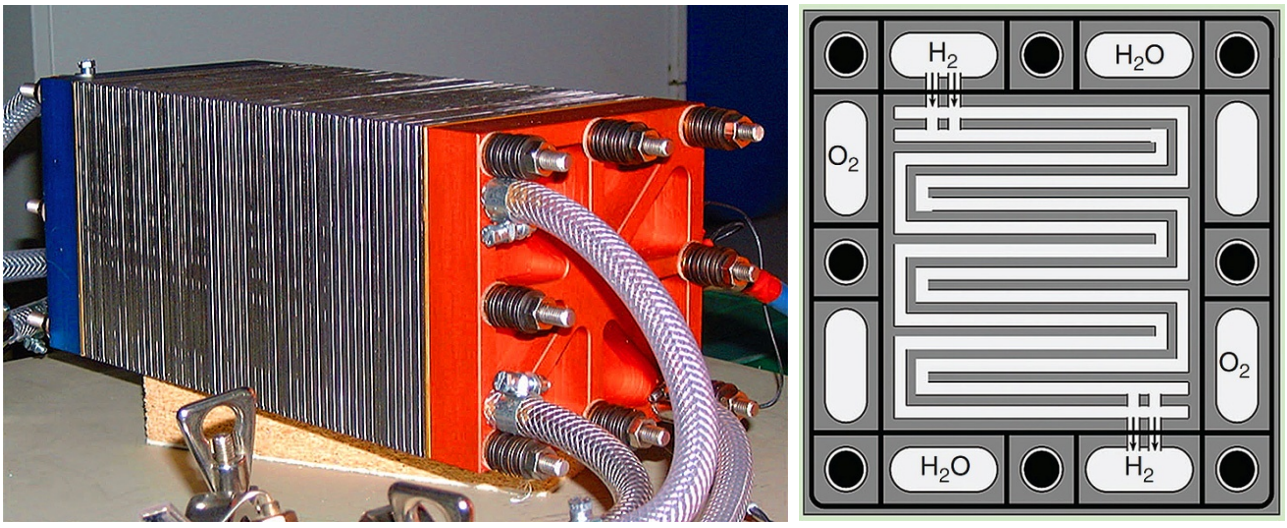

(a) (b)

Fig. II.2.3. PEMFC (23 cells, 500 W, 40 A, around 13 V), manufactured by the Centre for Solar Energy and Hydrogen Research Baden-Württemberg (ZSW) Company (Germany): (a) stack and (b) a serpentine flow field plate of 100 cm2. Pressed against the outer surface of each backing layer is a piece of hardware, called a plate, which often serves the dual role of flow field and current collector. It was functioned at the GREEN laboratory during 2002-2005.

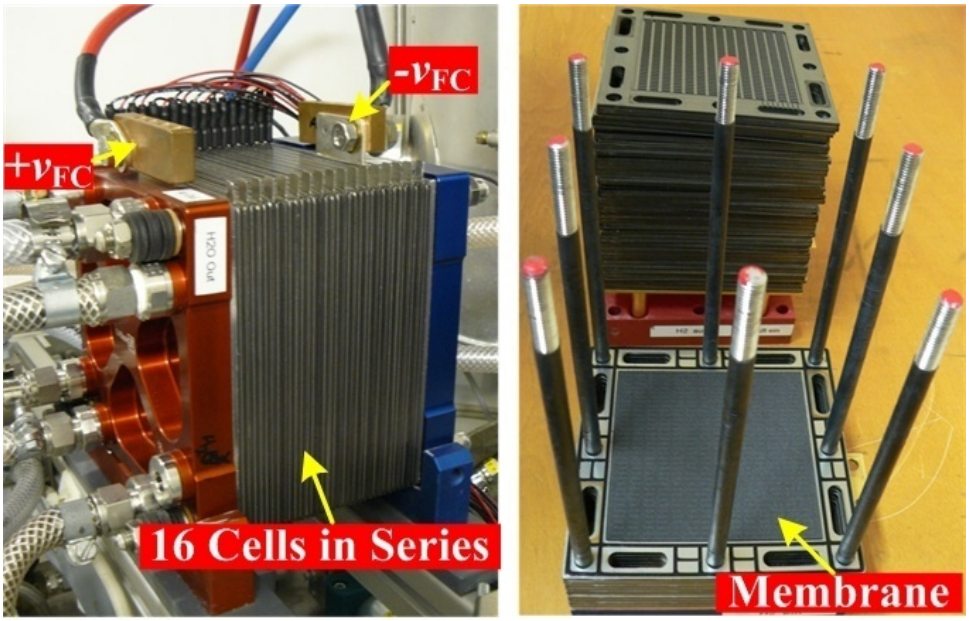

Fig. II.2.4. PEMFC (16 cells, 500 W, 50 A, and around 11 V), manufactured by the Centre for Solar Energy and Hydrogen Research Baden-Württemberg (ZSW) Company (Germany). It is being functioned at the GREEN laboratory.

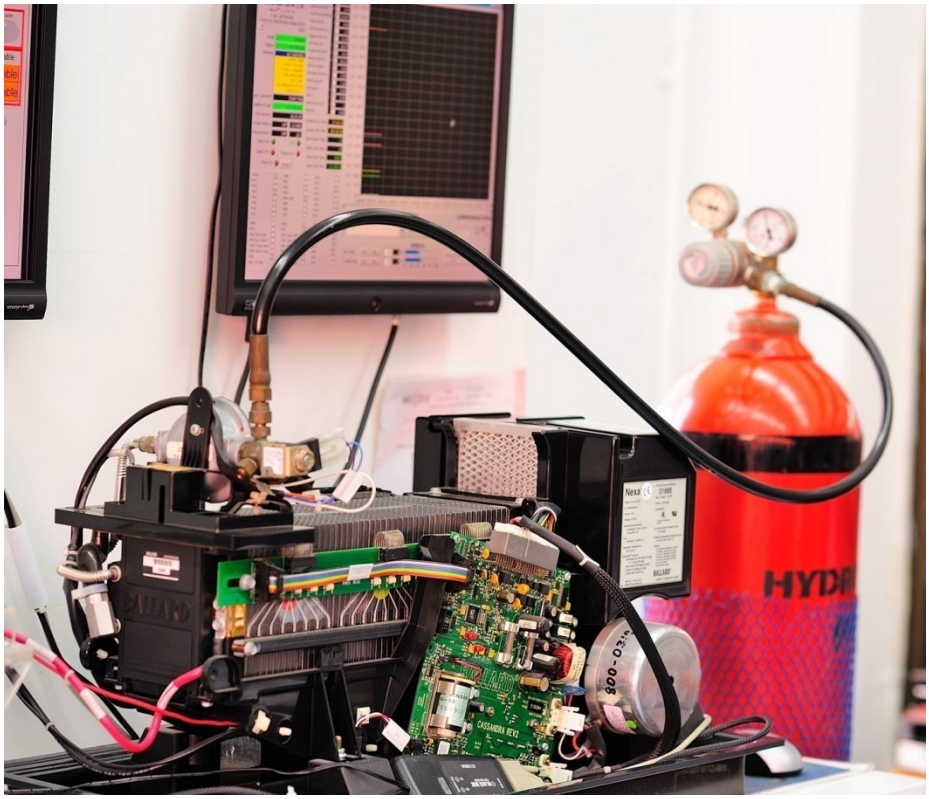

Fig. II.2.5. The Nexa PEMFC (1.2 kW, 46 A, around 26 V), developed and commercialized by the Ballard Power Systems Inc. It is being functioned at the RERC laboratory.

As developed earlier [Adz08], [Pas07], the Nernst equation for the hydrogen/oxygen FC, using literature values for the standard-state entropy change, can be written as

$$E = \left\{1.229 - 0.85\times10^{-3}\cdot(T - 298.15) + 4.3085\times10^{-5}T\cdot\left[\ln\left(p_{H_2}\right) + \frac{1}{2}\ln\left(p_{O_2}\right)\right]\right\}\cdot n_{Cell}\,. \tag{2.2}$$

where E is the reversible no-loss voltage of the FC (the thermodynamic potential), T is the cell temperature (K), p_{H2} and p_{O2} are the partial pressure of hydrogen and oxygen (bar), respectively, and n_{Cell} is the number of cells in series.

The FC voltage V_{FC} is modeled as [Adz08], [Pas07], [Sad06]

$$V_{FC} = E - \overbrace{A\cdot\log\left(\frac{I_{FC}+i_n}{i_O}\right)}^{Activation\ loss} - \overbrace{R_m\cdot(I_{FC}+i_n)}^{Ohmic\ loss} + \overbrace{B\cdot\log\left(1-\frac{I_{FC}+i_n}{i_L}\right)}^{Concentration\ loss} \tag{2.3}$$

where I_{FC} is the delivered FC current, i_O is the exchange current, A is the slope of the Tafel line, i_L is the limiting current, B is the constant in the mass transfer term, i_n is the internal current, and R_m is the membrane and contact resistances. These parameters can be determined from experiments. So, a typical fuel cell polarization characteristic with electrical voltage against current is shown in Fig. II.2.6.

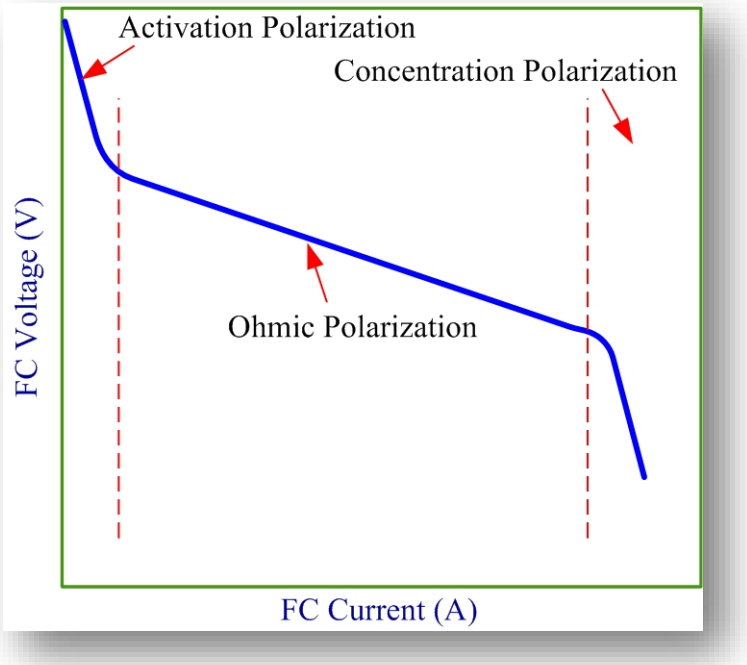

Fig. II.2.6. Typical fuel cell polarization curve.

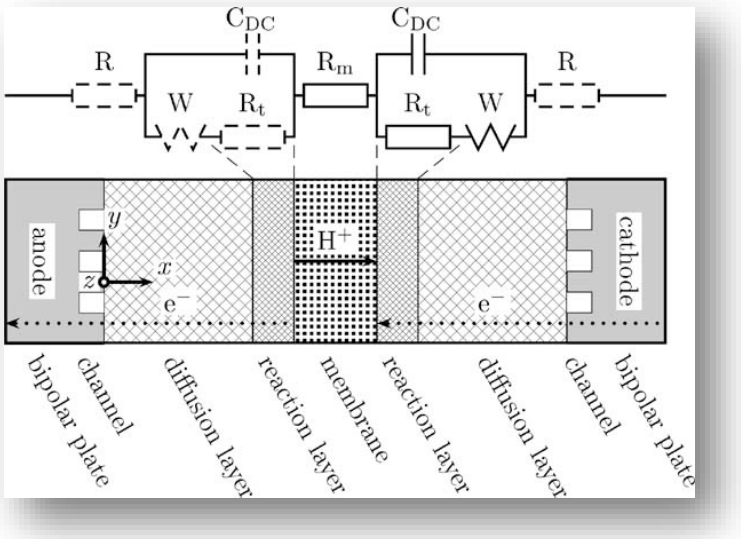

Fig. II.2.7. Small signal equivalent electric circuit of the fuel cell.

Finally, Fig. II.2.7 shows an equivalent circuit valid for small signals [Fri04]. The electrodes are represented by a capacitor C_{DC} which takes into account the double layer capacity appearing because of an accumulation of electrons and protons on both sides of the reactive layer. The chemical reaction is represented by resistors R_t, diffusion effects by a Warburg impedance W, and finally the membrane by an ohmic resistance R_m. The dashed parts of the circuit—electric resistance of the bipolar plates and voltage drop of the anode—are neglected. By choosing a high frequency, the influence of the electrodes can be separated from the one of the membrane.

B. Fuel Cell System

Figure II.2.3 shows some of the tubes that deliver gases. There are usually 2 × 4 connections: two wires for the current, 2 × 2 tubes for the gases, and 1 × 2 tubes for the cooling system. As the gases are supplied in excess to ensure a good operation of the cell, the non consumed gases have to leave the FC carrying with them the produced water (Fig. II.2.8). Generally, a water circuit is used to impose the operating temperature of the FC (approximately 60–70 °C). At start up, the FC stack is warmed and later cooled at the rated current. Nearly, the same amount of energy generated is heat and electricity.

An FC stack requires fuel, oxidant, and coolant to operate. The pressure and flow rate of each of these streams must be regulated. The gases must be humidified, and the coolant temperature must be controlled. To achieve this, the FC stack must be surrounded by a fuel system, fuel delivery system, air system, stack cooling system, and humidification system.

Once operating, the output power must be conditioned. Suitable alarms must shut down the process if unsafe operating conditions occur, and a cell-voltage monitoring system must monitor FC stack performance. These functions are performed by the electrical control systems.

Figure II.2.9 shows the simplified diagram of the PEMFC system of the stack presented in Fig. II.2.3. When an FC system is operated, its fuel flows are controlled by an FC controller that receives an FC current demand (reference), i_{FCREF}, from the user (manual operation) or from the energy-management controller (in case of automatic operation). The fuel flows must be adjusted to match the reactant delivery rate to the usage rate by the FC controller. For the FC system considered here, the FC current demand signal i_{FCREF} is in a linear scale of 50 A/10 V.

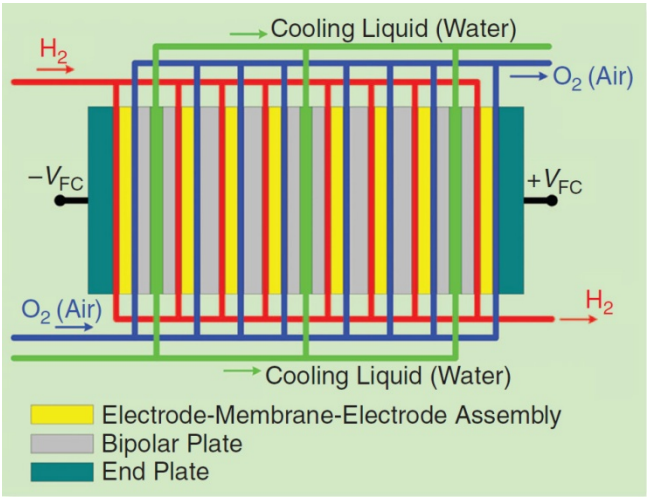

Fig. II.2.8. External and internal connections of a PEMFC stack.

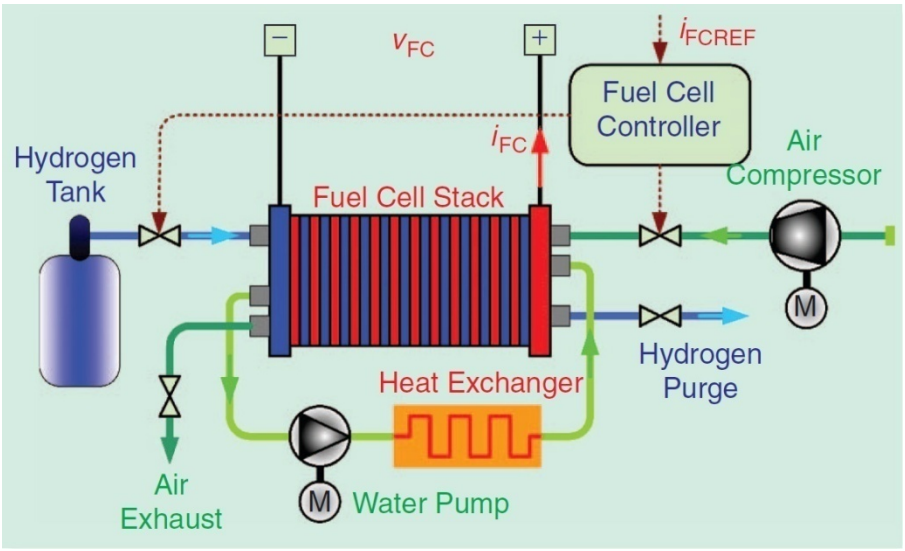

Fig. II.2.9. Simplified diagram of the PEMFC system. v_{FC}, i_{FC}, and i_{FCREF} are the FC voltage, current, and current demand, respectively.

C. Fuel Cell Characteristics

Refer to (2.3) and Fig. II.2.6, the polarization curves of a selection of commercially available fuel cells (Fig. II.2.3) are shown in Fig. II.2.10, at pressures close to atmospheric. An FC power source is always connected to the dc bus by a DC/DC converter. Switching characteristics of the PEMFC (500 W, 40 A, refer to Fig. II.2.3) at steady-state when connecting with a boost converter are presented in Fig. II.2.11. It can be seen that the PEMFC contains a complex impedance component, which it is not purely resistive at a high switching frequency of 25 kHz [Tho06a], [Hin09]. One can observe that its output impedance depends on operating point. One can also see the nonlinearity of the FC voltage curve during the change of current slope from positive to negative or vice versa. It can be concluded that an FC model is composed of complicated impedances [Jun07], [Pag07].

Thounthong *et al*. [Tho07] (who worked with a 500-W PEMFC system by ZSW Company, Fig. II.2.3), Corrêa *et al*. [Cor04], [Cor05a] (who worked with a 500-W Ballard and 500- W Avista PEMFC system), and Zhu *et al*. [Zhu06] (who worked with a 500-W PEMFC system) have demonstrated that the electrical response time of an FC is generally fast, being mainly associated with the speed at which the chemical reaction is capable of restoring the charge that has been drained by the load. On the other hand, because an FC system is composed of many mechanical devices, the whole FC system has slow transient response and slow output power ramping [Jur05], [Wan07b].

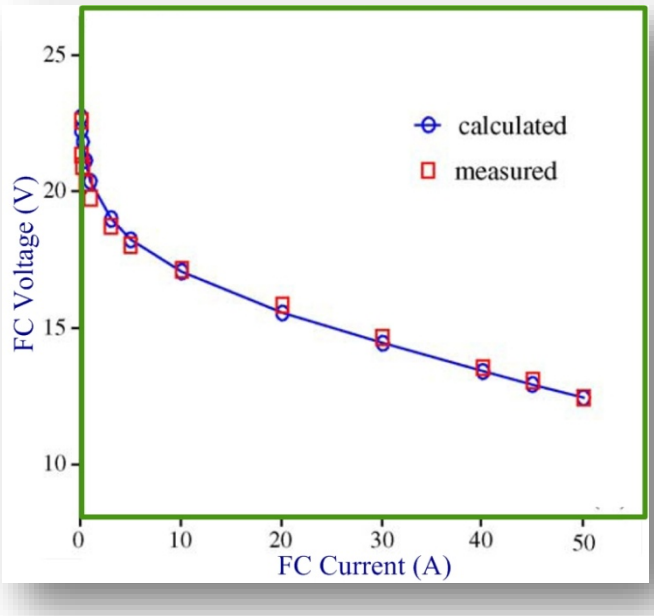

Fig. II.2.10. An FC polarization curve of the ZSW PEMFC (500 W), refer to Fig. II.2.3.

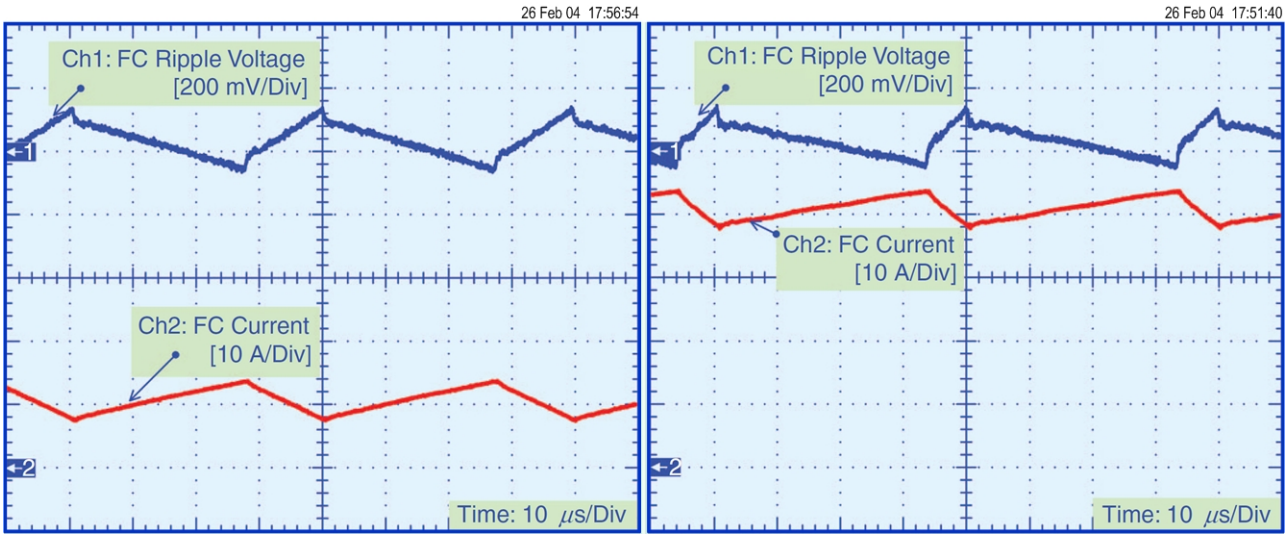

(a) (b)

Fig. II.2.11. Experimental Result: Switching characteristics of a 500 W PEMFC of 25 kHz at the FC current supply of (a) 10 A and (b) 40 A (rated current).

For clarity about the FC dynamics, Figure II.2.12 illustrates a ZSW PEMFC system (Fig. II.2.3), and it depicts the FC voltage response to a current demand of the PEMFC stack. The tests operate in two different ways: current step and controlled current slope of 4 $A \cdot s^{-1}$. One can scrutinize the voltage drop in Fig. II.2.12(a), compared to Fig. II.2.12(b), because fuel flows (particularly the delay of air flow) have difficulties following the current step. This characteristic is called fuel starvation phenomenon [Gay08], [Mei08], [Puk04], [Tho08a]. For the second test, Figure II.2.13 illustrates a Nexa PEMFC system (Fig. II.2.5), and it depicts the FC voltage response to a current demand of the PEMFC stack. One may see again the fuel starvation phenomenon. As illustrated in Fig. II.2.14, it also presents the worse case in which the FC system (Fig. II.2.3) shuts down because of a high FC-voltage drop from the fuel starvation problem. As already explained earlier, after the FC system is operated in many times of fuel starvation, its performance is reduced.

Reliability and lifetime are the most essential considerations in such power sources. Previous research, by Taniguchi *et al*. [Tan04], has clearly demonstrated that hydrogen and oxygen starvation caused severe and permanent damage to the electrocatalyst of the FC, as well as reducing its performance of voltage–current curve. They have recommended that fuel starvation must absolutely be avoided, even if the operation under fuel starvation is momentary, in just 1 s. As a result, to utilize the FC in dynamic applications, its current or power slope must be limited, for example, 4 $A \cdot s^{-1}$ for a PEMFC (0.5 kW, 12.5 V) [Tho06b]; a 2.5 $kW \cdot s^{-1}$ for a PEMFC (40 kW, 70 V) [Rod05]; and 500 $W \cdot s^{-1}$ for a PEMFC (2.5 kW, 22 V) [Cor05b].

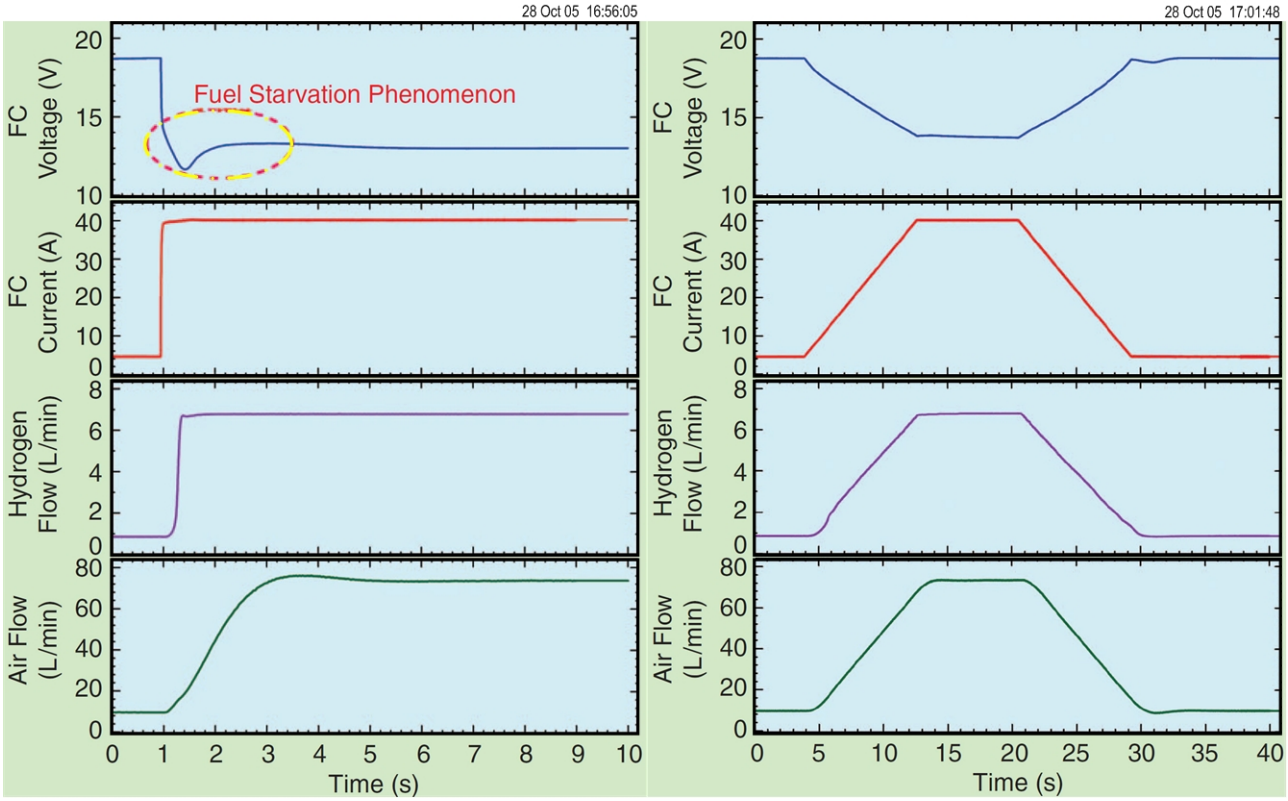

(a) (b)

Fig. II.2.12. Experimental Result: Dynamics characteristics of a 500 W ZSW PEMFC to (a) a high current step from 5 A to 40 A (rate current), (b) controlled current slope of 4 $A \cdot s^{-1}$.

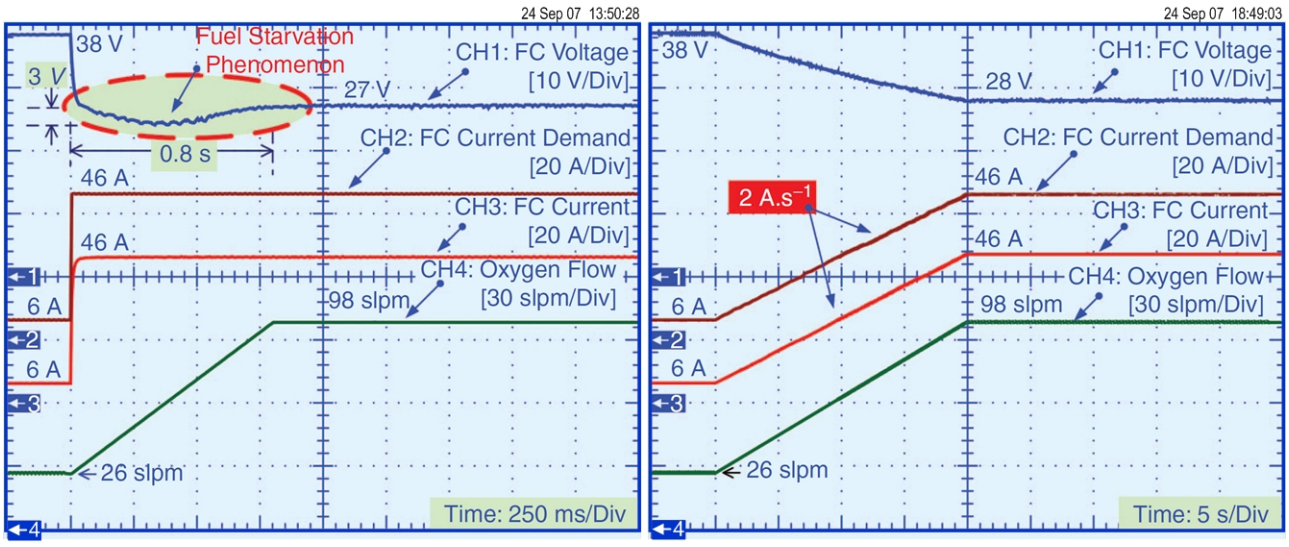

(a) (b)

Fig. II.2.13. Experimental Result: Dynamics characteristics of a 1.2 W Nexa PEMFC to (a) current step and (b) controlled current slope of 2 $A \cdot s^{-1}$.

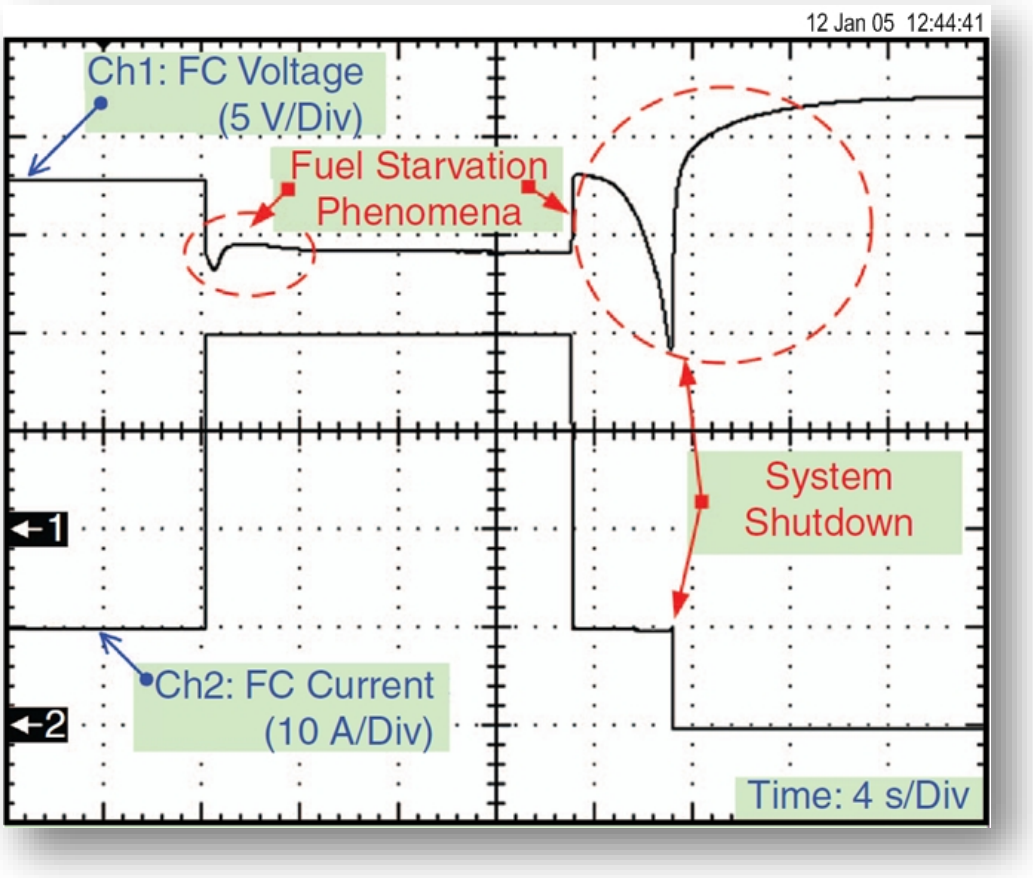

Fig. II.2.14. FC starvation problem.

Remark 1: one may summarize the constraints to operate an FC as follows:

1) The FC power or current must be kept within an interval (rated value, minimum value or zero).
2) The FC current must be controlled as a unidirectional current.
3) The FC current slope must be limited to a maximum absolute value (for example, 4 $A \cdot s^{-1}$), to prevent an FC stack from the fuel starvation phenomenon.
4) Switching frequency of the FC current must be greater than 1.25 kHz, and the FC ripple current must be lower than around 5% of rated value, to ensure minor impact to the FC conditions [Cho04], [Gem03].

II.2.1.2 Photovoltaic

A. Photovoltaic Principle

Alexandre-Edmond Becquerel (24 March 1820 – 11 May 1891) was a French physicist who studied the solar spectrum, magnetism, electricity and optics. He is credited with the discovery of the photovoltaic effect, the operating principle of the solar cell, in 1839.

Photovoltaic effect is a basic physical process through which solar energy is converted into electrical energy directly. The physics of a PV cell, or solar cell, is similar to the classical p-n junction diode, shown in Fig. II.2.15 [Wan06a]. A PV cell can basically be considered as a diode. When the cell is illuminated, the energy of photons is transferred to the semiconductor material, resulting in the creation of electron-hole pairs. The electric field created by the p-n junction causes the photon-generated electron-hole pairs to separate. The electrons are accelerated to n-region (N-type material), and the holes are dragged into p-region (P-type material), shown in Fig. II.2.15. The electrons from n-region flow through the external circuit and provide the electrical power to the load at the same time. The PV cell shown in Fig. II.2.15 is the basic component of a PV energy system. Since a typical PV cell produces less than 2 W at approximately 0.5 V DC, it is necessary to connect PV cells in series-parallel configurations to produce desired power and voltage ratings. Figure II.2.16 shows how single PV cells are grouped to form modules and how modules are connected to build arrays. There is no fixed definition on the size of a module and neither for an array. A module may have a power output from a few watts to hundreds of watts. And the power rating of an array can vary from hundreds of watts to megawatts.

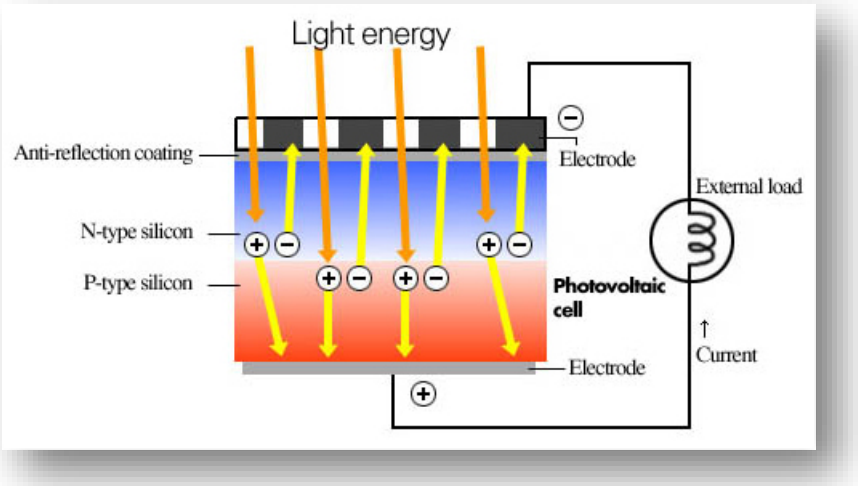

Fig. II.2.15. Schematic block diagram of a PV cell.

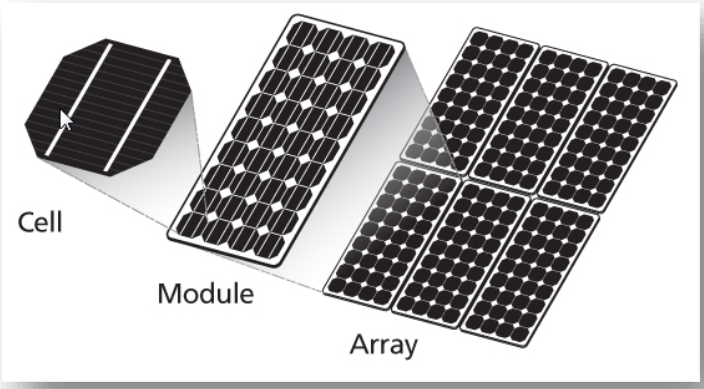

Fig. II.2.16. PV Cell, module, and array.

The most commonly used model for a PV cell is the one-diode equivalent circuit as shown in Fig. II.2.17. Since the shunt resistance R_{sh} is large, it normally can be neglected. The five parameters model shown in Fig. II.2.17(a) can therefore be simplified into that shown in Fig. II.2.17(b). This simplified equivalent circuit model is commonly used in many studies [Wan04], [Amo00].

The relationship between the PV voltage V_{PV} and the PV current I_{PV} can be expressed as [Xia06]:

$$I_{PV} = I_L - I_D = I_L - I_O\left[e^{\left(\frac{V_{PV}+I_{PV}\cdot R_S}{\kappa}\right)} - 1\right] \tag{2.4}$$

where I_L = light current (A); I_O = saturation current (A); I_{PV} = PV current (A); V_{PV} = PV output voltage (V); R_s = series resistance (Ω); κ = thermal voltage timing completion factor (V). There are four parameters (I_L, I_O, R_s and κ) that need to be determined before the *I*-*V* relationship can be obtained. That is why the model is called a four-parameter model. Both the equivalent circuit shown in Fig. II.2.17 and (2.4) look simple. However, the actual model is more complicated than it looks because the above four parameters are functions of temperature, load current and/or solar irradiance.

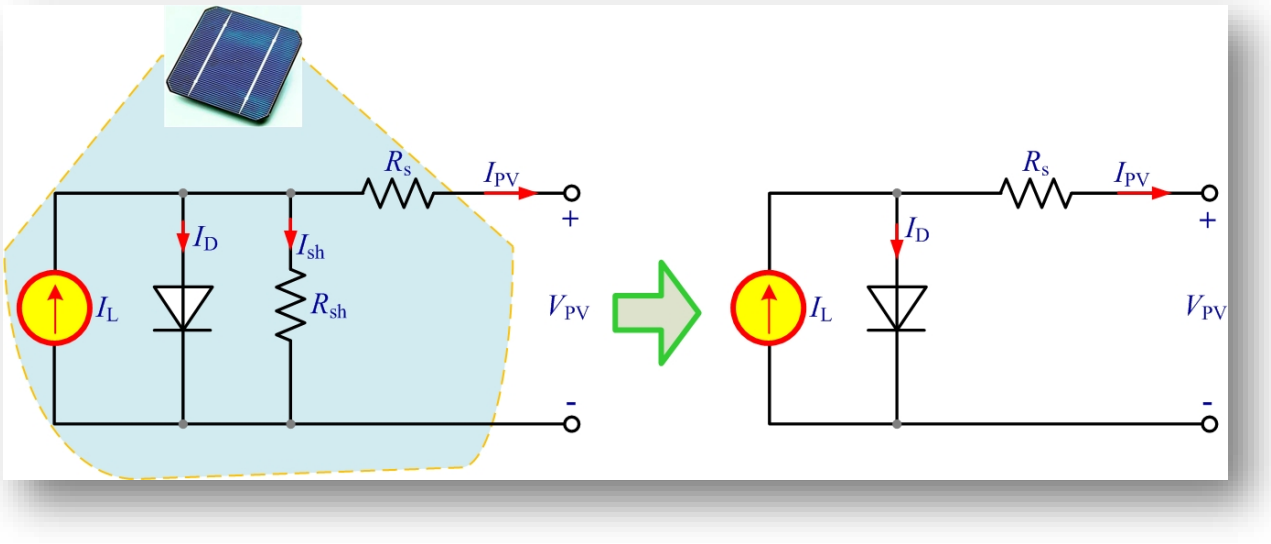

(a) (b)

Fig. II.2.17. One-diode equivalent circuit model for a PV cell. (a) Five parameters model; (b) Simplified four parameters model.

B. Photovoltaic Characteristics

The model *I-V* and *P-V* characteristic curves under different irradiances are given in Fig. II.2.18 at 25 °C. It is noted from the figure that the higher is the irradiance, the larger are the short-circuit current (I_{SC}) and the open-circuit voltage (V_{OC}). And, obviously, the larger will be the maximum power. The maximum power point (MPP), short-circuit current and open-circuit voltage are also illustrated in the figure.

The effect of the temperature on the PV model performance is illustrated in Fig. II.2.19. It is noted that the lower the temperature, the higher is the maximum power and the larger the open circuit voltage. On the other hand, a lower temperature gives a slightly lower short circuit current.

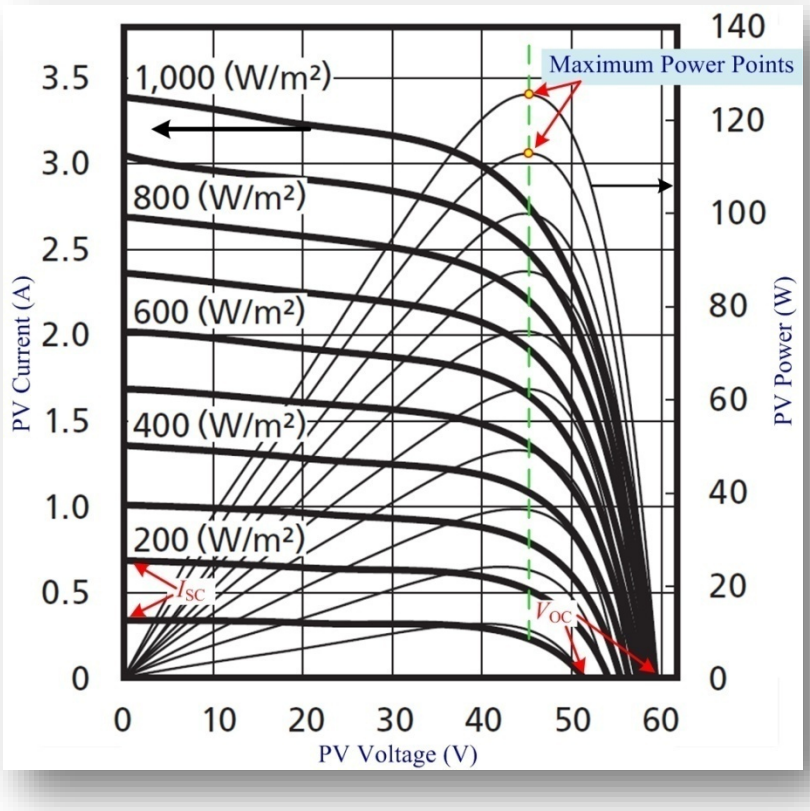

Fig. II.2.18. Characteristic curves: current/power vs. voltage (cell temperature: 25 °C) of Sharp solar modules (Na-E125G5, 94.8 W) model under different irradiances.

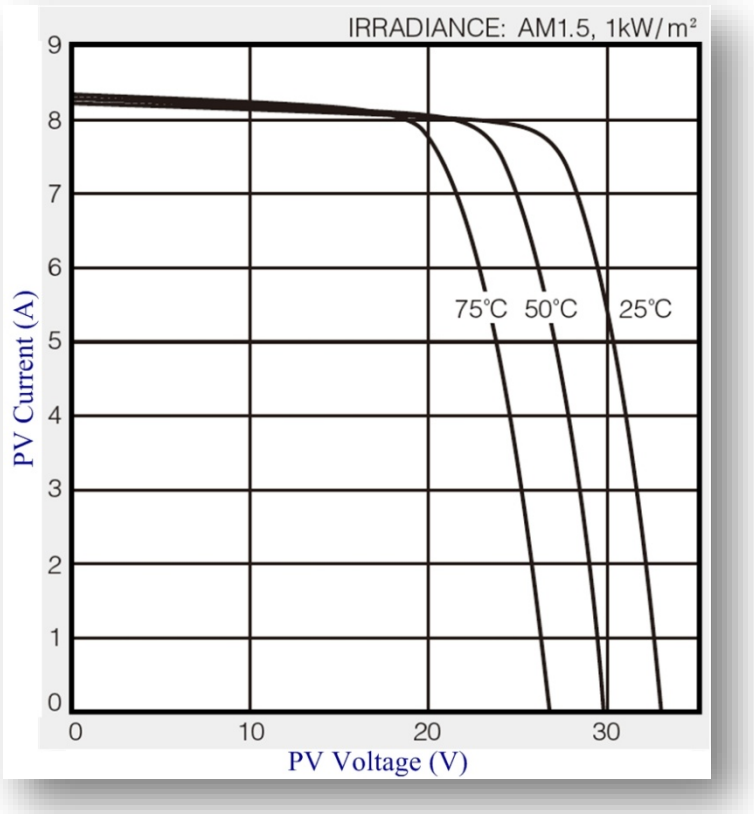

Fig. II.2.19. *I-V* characteristic curves of the PV model [Kyocera PV Module (KC200GT, 142 W)] under different temperatures.

Solar power source requires so much larger initial cost compared to conventional electricity generation techniques. Therefore, it is very natural to desire to draw as much power as possible from a PV array which has already been installed. Otherwise, the system would lose valuable solar energy. Maximum power output of the PV array changes when solar insolation, temperature, and (or) load levels vary. Control is, therefore, needed for the PV generator to always keep track of the maximum power points [Che10], [Gib10]. Trajectory of those maximum power points has been drawn in Fig. II.2.18. Maximum power point tracking (MPPT) is one of the techniques to obtain maximum power from a PV system.

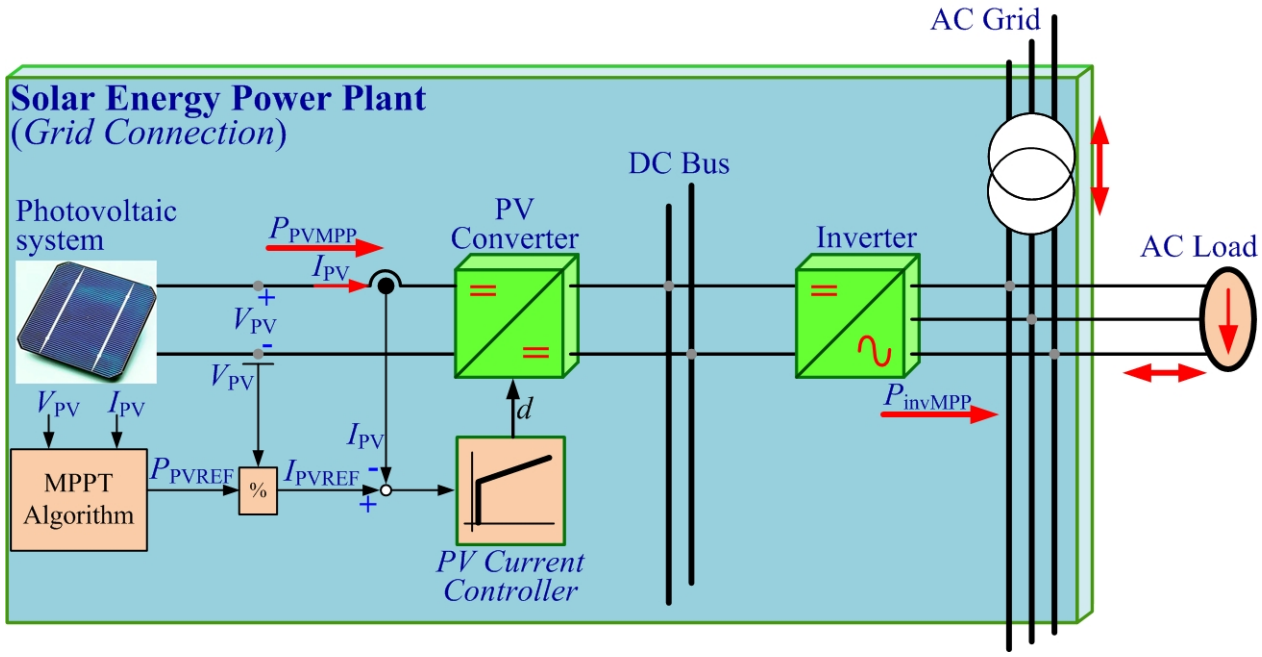

Fig. II.2.20. Concept of MPP for PV system.

The problem considered by MPPT techniques is to automatically find the voltage V_{PVMPP} or current I_{PVMPP} at which a PV array should operate to obtain the maximum power output P_{MPP} under a given temperature and irradiance. It is noted that under partial shading conditions, in some cases it is possible to have multiple local maxima, but overall there is still only one true MPP. Most techniques respond to changes in both irradiance and temperature, but some are specifically more useful if temperature is approximately constant. Most techniques would automatically respond to changes in the array due to aging, though some are open-loop and would require periodic fine-tuning. By controlling the switching scheme of the converter(s) connected to the PVs the maximum power points of the PV array can always be tracked, as shown in Fig. II.2.20.

Several different MPPT techniques have been proposed in the literature. Two popular tracking methods based on power measurement are widely adopted in PV power systems: the perturbation and observation method (P&O, or "Hill climbing") and the incremental conductance method (IncCond) [Xia06], [Esr07]. Actually, both P&O and IncCond are based on the same technique. Here, only a classic P&O technique is studied as following.

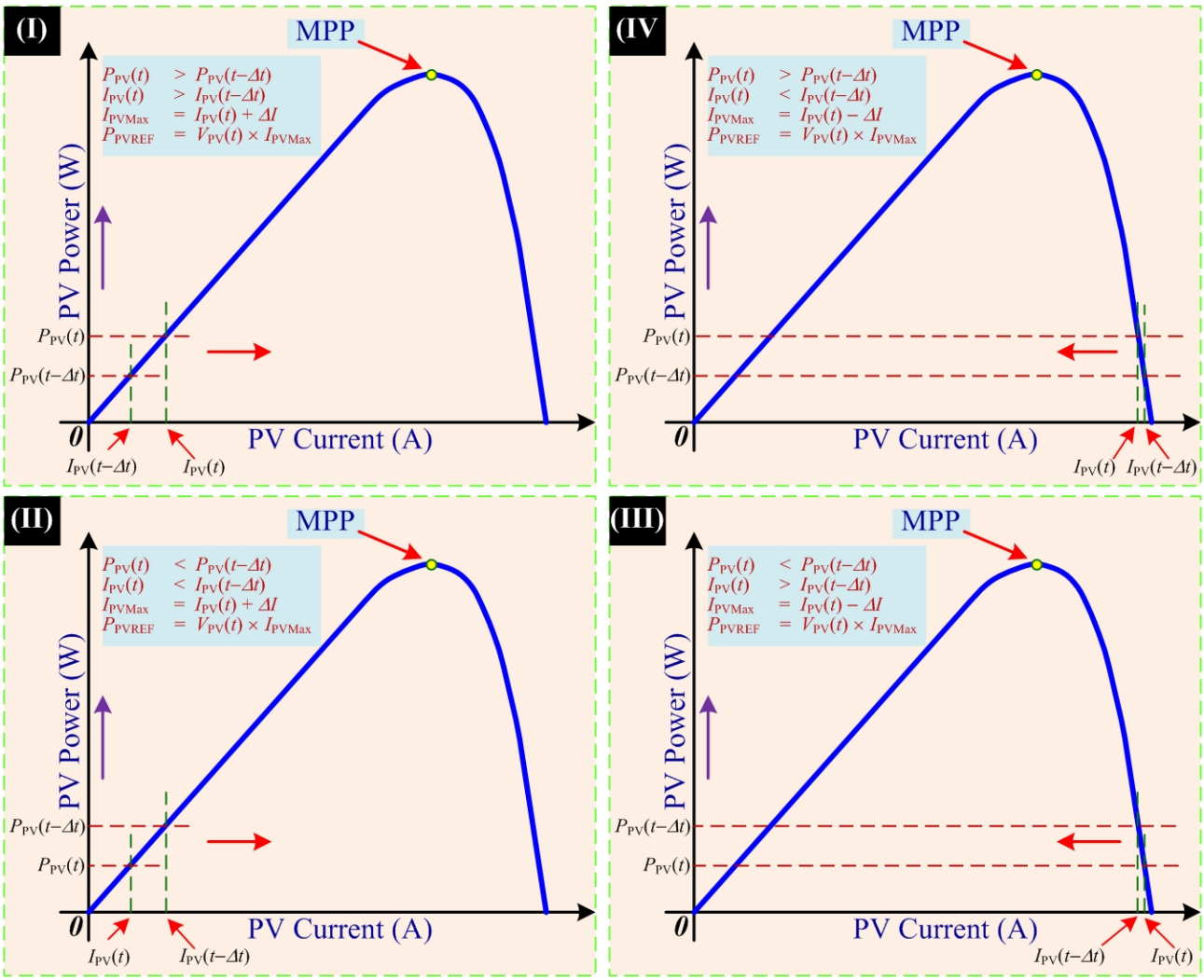

Fig. II.2.21. Divergence of hill climbing/P&O from MPP.

P&O involves a perturbation in the duty ratio of the power converter or a perturbation in the operating current of the PV array. In the case of a PV array connected to a power converter, perturbing the duty ratio or the PV array current and consequently perturbs the PV array voltage. From Fig. II.2.21, it can be seen in 4 cases:

I. Incrementing the current increases the power when operating on the left of the MPP,

II. Decrementing the current decreases the power when operating on the left of the MPP,

III. Incrementing the current decreases the power when operating on the right of the MPP,

IV. Decrementing the current increases the power when operating on the right of the MPP,

Based on P&O MPPT, the algorithm for the P_{PVMPP} is described in Fig. II.2.22, where the ΔI defined PV current step size and Δt the sampling time. *Note that this sampling time must be higher than a main program sampling time*. Two sensors are usually required to measure the PV array voltage and current from which power is computed. The process is repeated periodically until the MPP is reached. The system then oscillates about the MPP. The oscillation can be minimized by reducing the perturbation step size (ΔI). However, a smaller perturbation size slows down the MPPT. A solution to this conflicting situation is to have a variable perturbation size that gets smaller towards the MPP [Esr07].

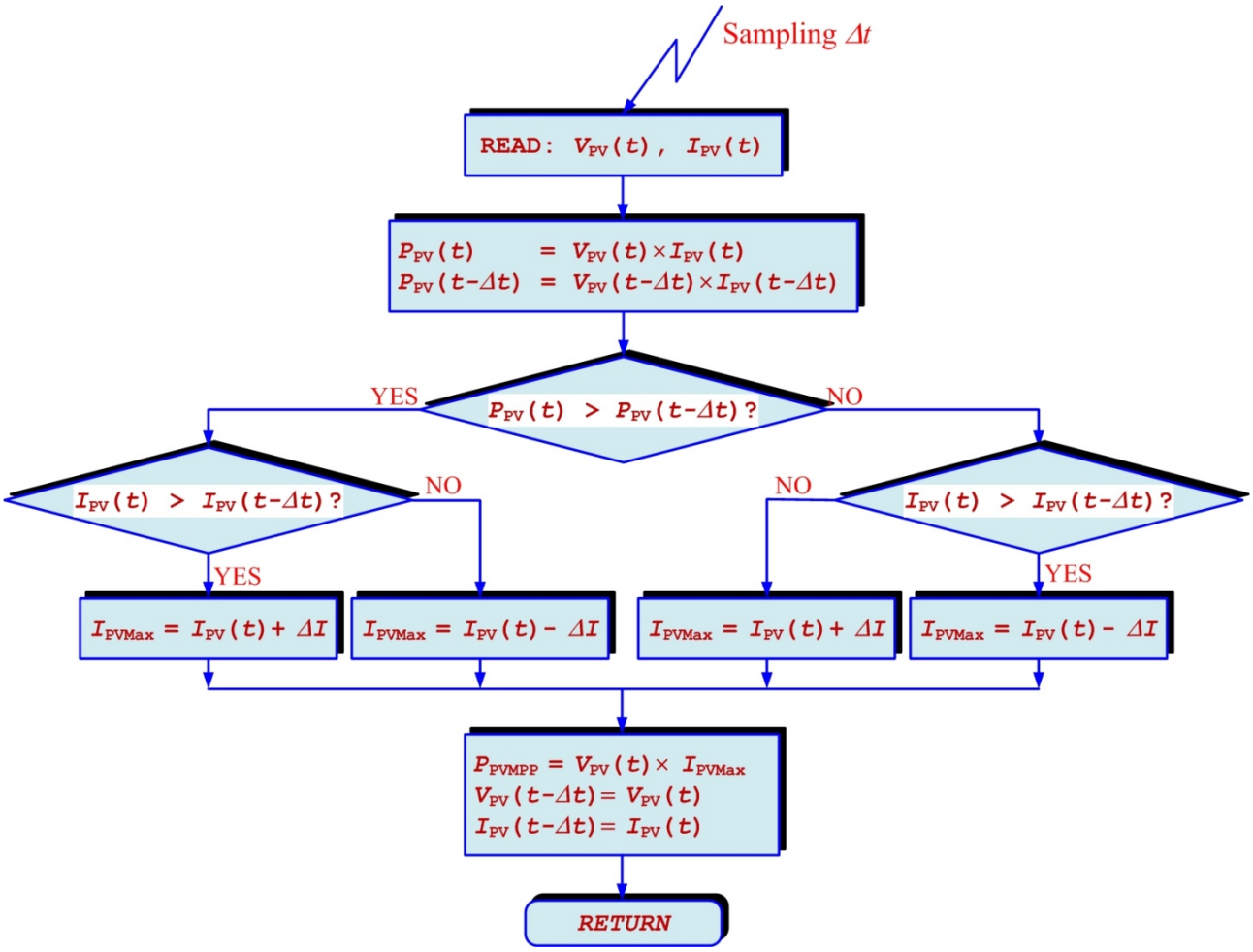

Fig. II.2.22. Algorithm P&O.

Finally, to prove the implemented P&O for a PV panel, the PV (Ekarat Solar 800 W, 25 V) has been in installed on the roof of the laboratory building (KMUTNB, Thailand) and also used in the following work, see Fig. II.2.23. The P&O has been implemented in MATLAB/Simulink with a dSPACE controller. The ΔI is set at 0.1 A and Δt is set at 6 ms. Fig.II.2.24 shows the experimental results of MPPT at t = 15:01:29 (estimate P_{PVMPP} = 260 W) and at t = 09:30:17 (estimate P_{PVMPP} = 300 W). One can see the excellent performance of the P&O algorithm.

Fig. II.2.23. PV panel (Ekarat Solar, 800 W) is installed on the roof of the laboratory building (KMUTNB, Thailand).

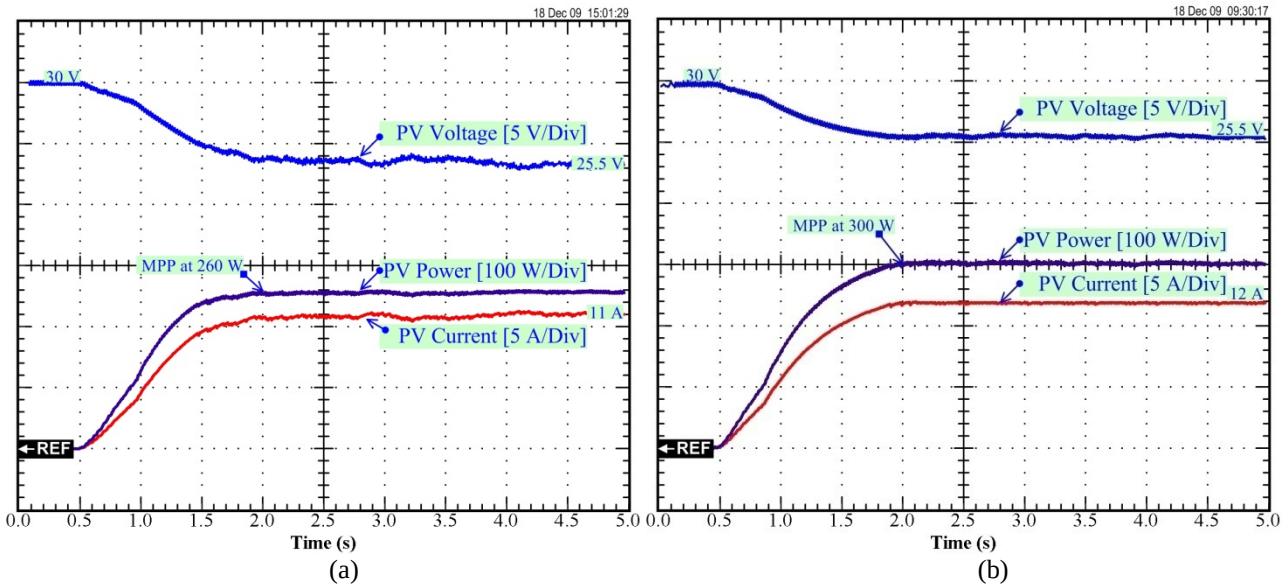

(a) (b)

Fig. II.2.24. Experimental result: P&O algorithm of PV Ekarat Solar 500 W, (a) at t = 15:01:29, (b) at t = 09:30:17.

Remark 2: one may summarize the constraints to operate a PV system as follows:

> PV power systems require some specific estimation algorithms to deliver the MPP. Because of the typical low-efficiency characteristics of PV panels, it is very important to deliver the maximum instantaneous power from these energy sources to the load. It is obligatory to use DC/DC or DC/AC converters with effective MPPT techniques.

II.2.2 Energy Storage Devices

II.2.2.1 Battery

A. Battery Principle (lead-acid battery)

Electrochemical batteries (or "batteries,") are electrochemical devices that convert electrical energy into potential chemical energy during charging, and convert chemical energy into electric energy during discharging. A cell is an independent and complete unit that possesses all the electrochemical properties. Basically, a battery cell consists of three primary elements: two electrodes (positive and negative) immersed into an electrolyte as shown in Fig. II.2.25.

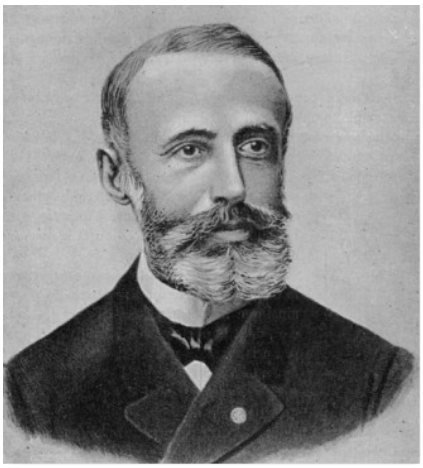

Gaston Planté (1834–1889) was the French physicist who invented the lead-acid battery in 1859.

Because it is the most widespread battery technology in today's automotive and power system applications, the lead-acid battery case is used as an example to explain the operating principle theory of electrochemical batteries. A lead-acid battery uses an aqueous solution of sulfuric acid ($2H^+ + SO_4^{2-}$) as the electrolyte. The electrodes are made of porous lead (Pb, anode, electrically negative) and porous lead oxide (PbO_2, cathode, electrically positive). The processes taking place during discharging are shown in Fig. II.2.26(a), where lead is consumed and lead sulfate is formed [Ro97], [Ehn09]. The chemical reaction on the anode can be written as

$$Pb + SO_4^{2-} \rightarrow PbSO_4 + 2e^- \tag{2.5}$$

This reaction releases two electrons and, thereby, gives rise to an excess negative charge on the electrode that is relieved by a flow of electrons through the external circuit to the positive (cathode) electrode. At the positive electrode, the lead of PbO_2 is also converted to $PbSO_4$ and, at the same time, water is formed. The reaction can be expressed as

$$PbO_2 + 4H^+ + SO_4^{2-} + 2e^- \rightarrow PbSO_4 + 2H_2O \quad (2.6)$$

During charging, the reactions on the anode and cathode are reversed as shown in Fig. II.2.26(b) that can be expressed by:

Anode: $$PbSO_4 + 2e^- \rightarrow Pb + SO_4^{2-} \quad (2.7)$$

And

cathode: $$PbSO_4 + 2H_2O \rightarrow PbO_2 + 4H^+ + SO_4^{2-} + 2e^- \quad (2.8)$$

The overall reaction in a lead-acid battery cell can be expressed as

overall: $$Pb + PbO_2 + 2H_2SO_4 \Leftrightarrow 2PbSO_4 + 2H_2O \quad (2.9)$$

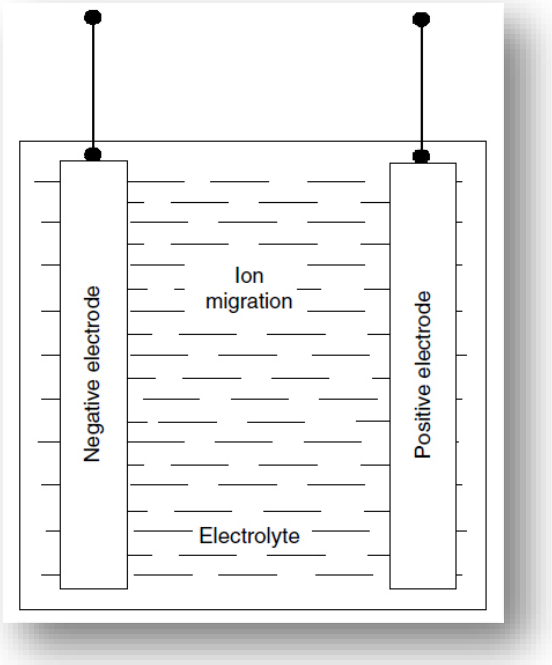

Fig. II.2.25. A typical electrochemical battery cell.

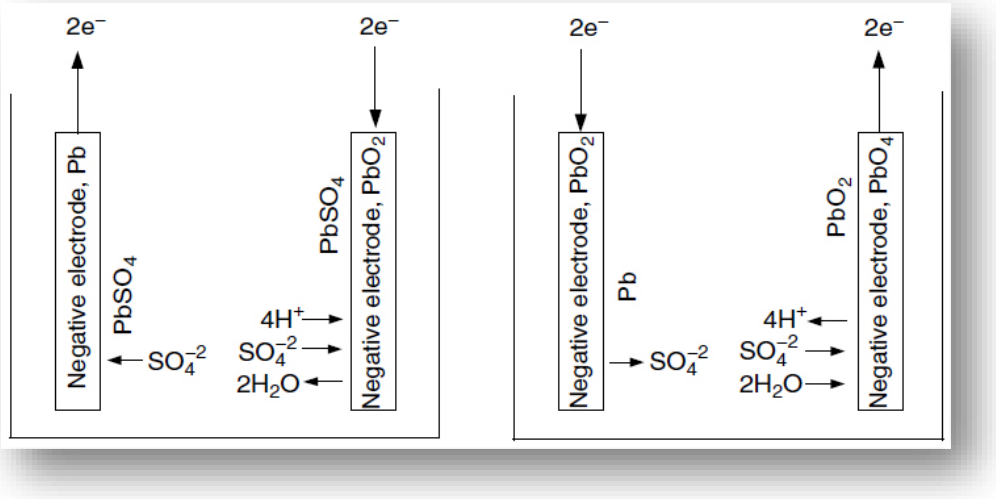

(a) Discharging (b) Charging

Fig. II.2.26. Electrochemical processes during the discharge and charge of a lead-acid battery cell.

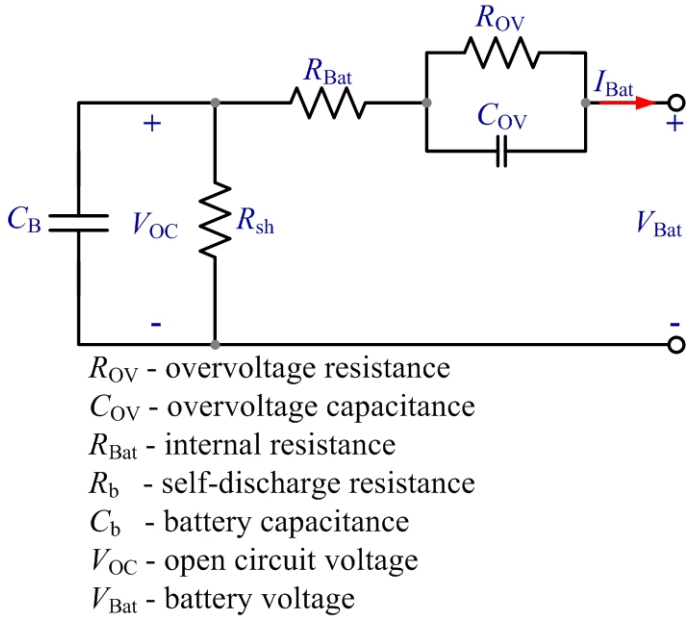

Fig. II.2.27. Lead-acid battery model.

The lead-acid battery has a cell voltage of about 2.03 V at standard condition, which is affected by the concentration of the electrolyte and the nominal discharge voltage level is 1.75V/cell, or approximately 87.5% of the nominal cell voltage rating. Then, the number of cells connected in series determines the nominal voltage of the battery system, and the capacity of the battery system is the basic factor in determining the discharge rate. The voltage is the force enforcing each of the electrons coming out of the battery and the capacity is the number of electrons that can be obtained from the battery. While the voltage is fixed by cell chemistry, the capacity is variable depending on the quantity of active materials.

The equivalent circuit for a battery is shown in Fig. II.2.27. The internal resistance is due to the resistance of electrolyte and electrode. Self-discharge resistance is a result of electrolysis of water at high voltages and slow leakage across the battery terminals at low voltages. The overvoltage is modeled as an *RC* circuit with a time constant in the order of minutes [Cas92], [Sal92].

B. Battery Characteristics

Battery manufacturers usually specify the battery with coulometric capacity (C, amp-hours), which is defined as the number of amp-hours gained when discharging the battery from a fully charged state until the terminal voltage drops to its cut-off voltage, as shown in Fig.II.2.28. It should be noted that the same battery usually has a different number of amp-hours at different discharging current rates. Generally, the capacity will become smaller with a large discharge current rate, as shown in Fig.II.2.29. Battery manufacturers usually specify a battery with a number of amp-hours along with a current rate. For example, a battery labeled 100 Ah at C5 rate has a 100 amp-hour capacity at 5 hours discharge rate (discharging current 100/5 = 20 A).

Another important parameter of a battery is the state-of-charge (*SOC*). *SOC* is defined as the ratio of the remaining capacity to the fully charged capacity. With this definition, a fully charged battery has an *SOC* of 100% and a fully discharged battery has an *SOC* of 0%. However, the term "fully discharged" sometimes causes confusion because of the different capacity at different discharge rates and different cut-off voltage (refer to Fig.II.2.28). The change in *SOC* in a time interval, *dt*, with discharging or charging current i_{Bat} may be expressed as

$$\Delta SOC = \frac{i_{\text{Bat}} dt}{Q_{\text{Bat}}} \tag{2.10}$$

where Q_{Bat} is the rated capacity (Ah). For discharging, i_{Bat} is positive, and for charging, i_{Bat} is negative. Thus, the SOC of the battery can be expressed as

$$SOC(t) = -\frac{1}{Q_{\text{Bat}}} \int_{t_o}^{t_n} i_{\text{Bat}}(\tau) d\tau + SOC_0 \tag{2.11}$$

where SOC_0 is the initial value of the *SOC*.

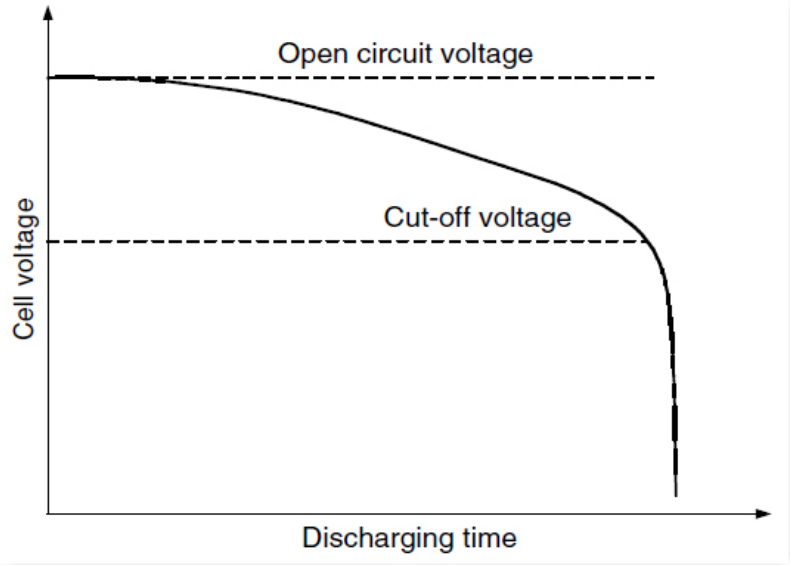

Fig. II.2.28. Cut-off voltage of a typical battery.

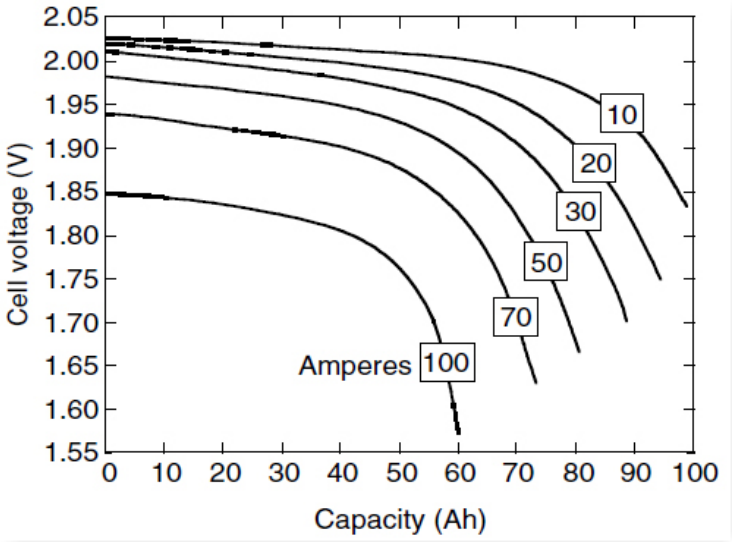

Fig. II.2.29. Discharge characteristics of a lead-acid battery.

Another important parameter of a battery is the state-of-health (*SOH*) of a battery is the percentage of its capacity available when fully charged relative to its rated capacity. For example, a battery rated at 30 Ah, but only capable of delivering 24 Ah when fully charged, will have a state-of-health of 24/30 × 100 = 80%. Thus, the state-of-health takes into account the loss of capacity as the battery ages.

Remark 3: one may summarize the constraints to operate a battery as follows:

1) A lower current charges the battery more uniformly. Also, excessive charging rates increase the chance of overheating, which can mean battery damage. Battery charging current may set at $Q_{Bat}/5 - Q_{Bat}/10$, in normal operation.

2) Avoid over-discharge which leads to “sulfation” and the battery is ruined. The reaction becomes irreversible when the size of the lead-sulfate formations become too large.
3) Avoid overcharging causes other undesirable reactions to occur: Electrolysis of water and generation of hydrogen gas; electrolysis of other compounds in electrodes and electrolyte, which can generate poisonous gasses; bulging and deformation of cases of sealed batteries

II.2.2.2 Supercapacitor

A. Supercapacitor Principle

Recent progress in supercapacitor technology has principally been applied in computer memory backup systems, but with the latest increases in capacitor energy storage levels, higher power applications [especially uninterruptible power supply (UPS) and hybrid vehicle] have become practicable. Electrochemical capacitors are presently called by a number of names: supercapacitor, ultracapacitor, or electrochemical double-layer capacitor. These terms are used interchangeably, and they refer to a capacitor that stores electrical energy in the interface that lies between solid electrodes and an electrolyte, as delineated in Fig. II.2.30 and Fig. II.2.31.

Hermann von Helmholtz (August 31, 1821 – September 8, 1894) was a German physician and physicist who made significant contributions to several widely varied areas of modern science.

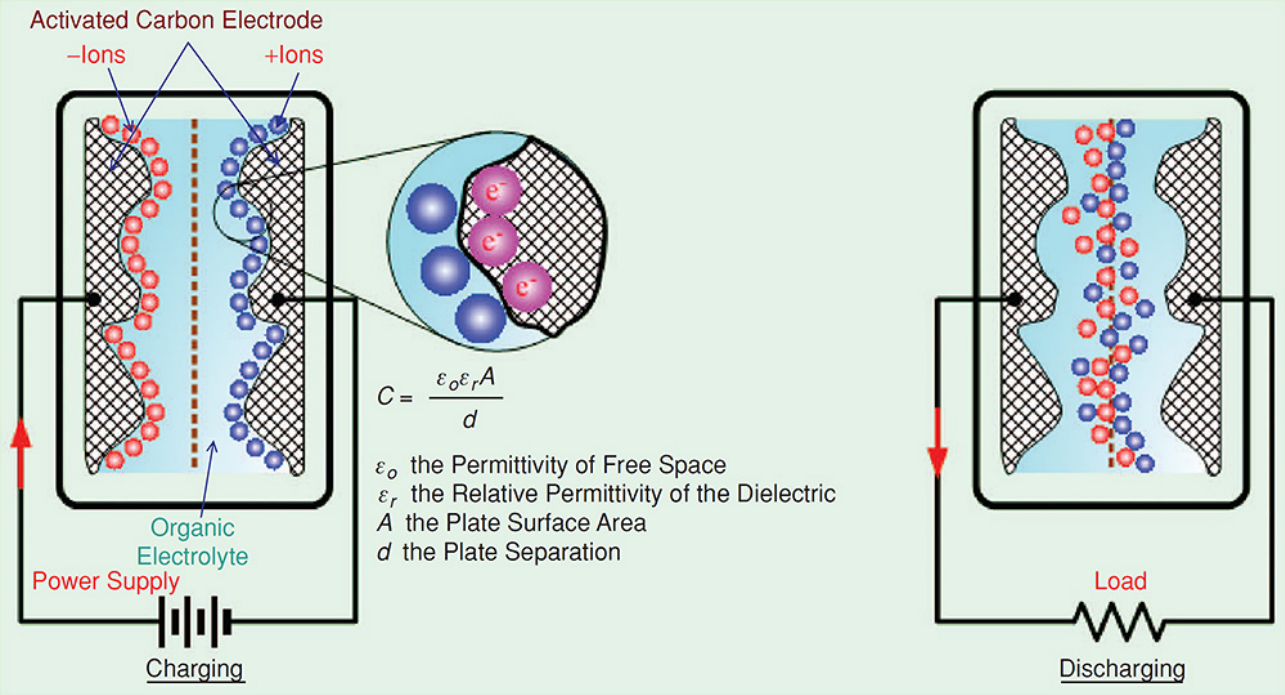

Fig. II.2.30. Principle of operation of a supercapacitor.

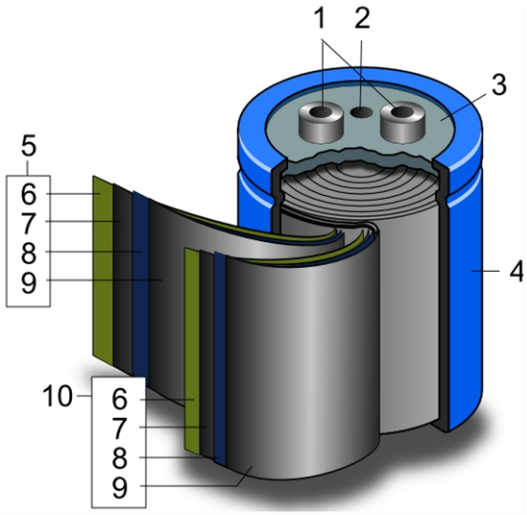

Schematic construction of a wound supercapacitors:
1. Terminals,
2. Safety vent,
3. Sealing disc,
4. Aluminum can,
5. Positive pole,
6. Separator,
7. Carbon electrode,
8. Collector,
9. Carbon electrode,
10. Negative pole

Fig. II.2.31. Construction details of supercapacitors with activated carbon electrodes.

The double-layer capacitor phenomenon was discovered by Helmholtz, one of the greatest natural scientists, who mathematically formulated the first main theorem of thermodynamics, in the 1800s. To maximize the capacitance *C*, the area *A* must be maximized and *d* minimized. Nowadays, the equivalent plate separation distance at the double layer consists of a few electrolyte molecule diameters of about 10^{-10} m. This plate separation distance is impossible in a conventional capacitor due to traditional dielectric breakdown, consisting of ionization followed by spark discharge. Terminal voltage of the supercapacitor is limited though, due to dissociation of the electrolyte. This

limits the maximum voltage (2.5–3 V) of a supercapacitor cell used in this experiment to 2.5 V. Electrode area in the supercapacitor is maximized by use of activated carbon with an effective surface area up to 3,000 m^2/g of material. The large surface area combined with the high capacitance per unit area yields the very large capacitance seen in the supercapacitor [Nel03].

Since the early 1990s, supercapacitors dedicated to high power industrial applications (capacitance up to some thousands farads, specific energy and specific power of several Wh/kg and kW/kg, respectively) have been available. The first high-power supercapacitors were developed by the Pinnacle Research Institute (PRI) for U.S. military applications such as laser weaponry and missile guidance systems. However, only in the 20th century did supercapacitors become well known in the context of hybrid electric vehicles promoted by the Department of Energy (DOE) under a supercapacitor development program. DOE supercapacitor development programs of long-term goals are specific energy >15 Wh/kg, specific power >2.0 kW/kg after 2003. Some example of recent supercapacitor technology can be seen in Fig.II.2.32-34.

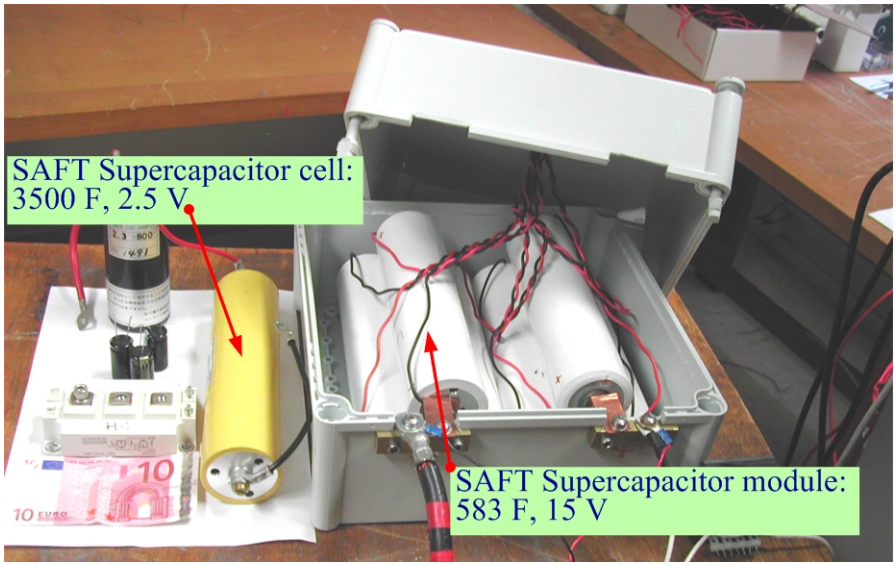

Fig. II.2.32. SAFT supercapacitor cell and module studied in the GREEN lab since 2001.

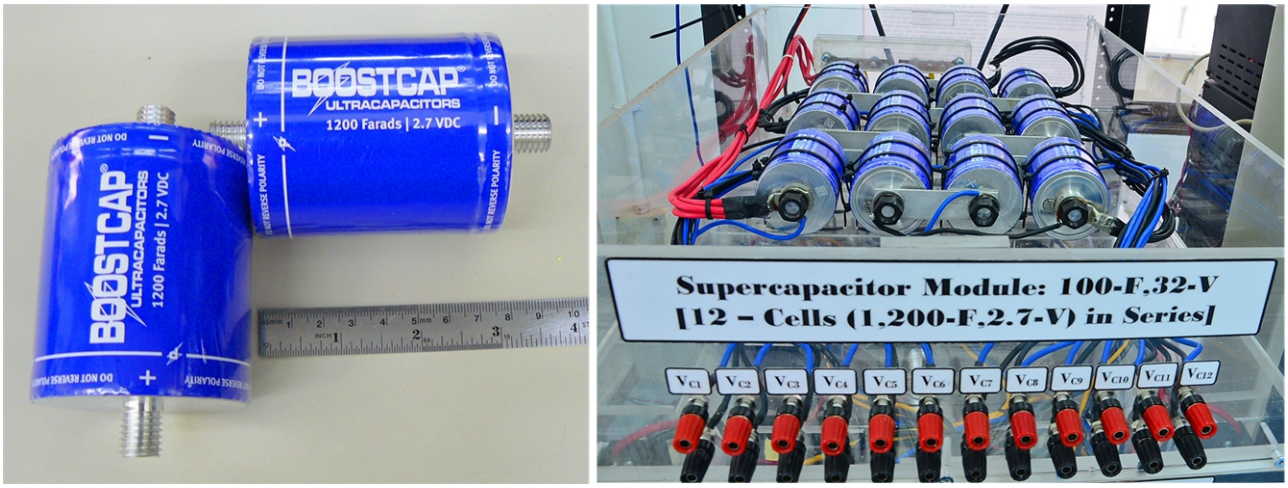

Fig. II.2.33. Maxwell supercapacitor cell and module studied in the RERC laboratory since 2007.

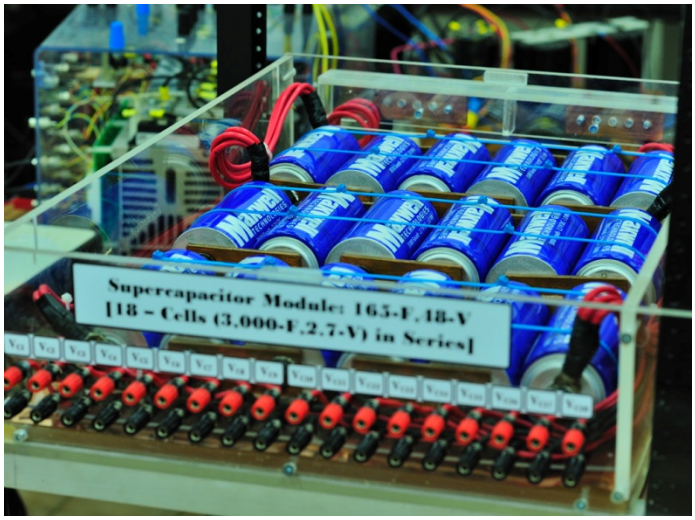

Fig. II.2.34. Maxwell supercapacitor bank (165 F, 48 V) studied in the RERC laboratory since August 2013.

B. Supercapacitor Characteristics

The supercapacitor model is very complex because of the distributed-parameter model. Many different models have been proposed for the double-layer effect [Nel03]. Recent works [Uzu08], [Nel03] have proposed that the reduced order model (as portrayed in Fig. II.2.35) for a supercapacitor cell is presented because of its simplicity and its operating times on the order of a few seconds. It is comprised of three ideal circuit elements: a capacitor C_{Cell}, a series resistor R_{S} called the equivalent series resistance (*ESR*), and a parallel resistor R_{p}. The parallel resistor R_{p} models the leakage current found in all capacitors. This leakage current is equal to a few milliamps in a big supercapacitor.

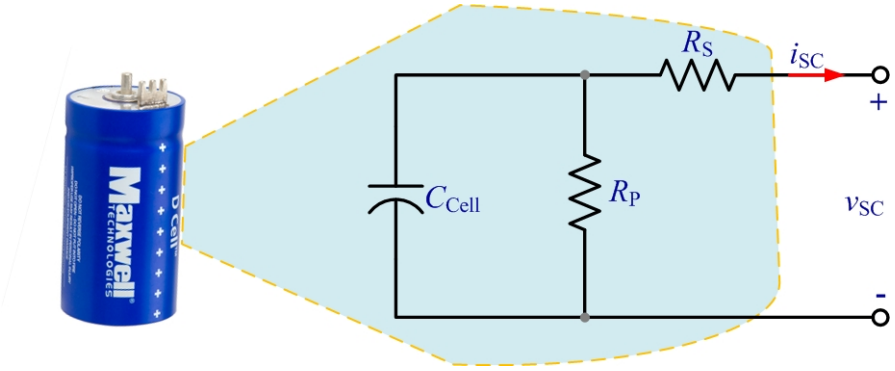

Fig. II.2.35. Simplified equivalent circuit of a supercapacitor cell including R_P.

Many applications require the capacitors to be connected together, in series and/or parallel combinations, to form a "bank" with a specific voltage and capacitance rating. Normally, they are always connected in series. Capacitance variations affect the voltage distribution during cycling, and voltage distribution during sustained operation at a fixed voltage is influenced by leakage current variations. For this reason, an active voltage balancing circuit is employed to regulate the cell voltage.

It is common to choose a specific voltage, and thus, calculating the required capacitance. In analyzing any application, one first needs to determine the following system variables affecting the choice of supercapacitor:

1) maximum voltage, V_{SCMax};
2) working (nominal) voltage, V_{SCNom};
3) minimum allowable voltage, V_{SCMin};
4) current requirement, I_{SC} , or the power requirement, P_{SC};
5) time of discharge, t_d;
6) capacitance per cell, C_{Cell};
7) cell voltage, V_{Cell}.

Connecting many cells in series to form a bank, this does lead to an increase in total *ESR* and to a decrease in total capacitance. Defining n_S as the number of capacitors connected in series, the maximum capacitor voltage V_{SCMax}, total *ESR*, and capacitance C_{SC} of the capacitor bank can be estimated as:

$$V_{SCMax} = n_S \cdot V_{Cell} \tag{2.12.1}$$

$$ESR = n_S \cdot R_S \tag{2.12.2}$$

$$C_{SC} = \frac{C_{Cell}}{n_S} \tag{2.12.3}$$

The discharge profile for a supercapacitor bank under a constant current is shown in Fig. II.2.36. A constant discharging current I_{SC} is particularly useful when determining the parameters of the supercapacitor. Nevertheless, Fig. II.2.36 should not be used to consider sizing supercapacitors for constant power applications such as a general power profile (drive cycle) used in electric vehicle. Worst case scenarios from drive cycle determine size of the storage devices. For example, Mitchell *et al.* [Mit06] presented that the Renault fuel cell automobile (SCENIC II, rated power of 70 kW of a PEMFC) needs a supplementary constant power (from battery) of around 30 kW for a 3 s for transient power (vehicle acceleration). Then, the discharge profile for a supercapacitor under a constant power P_{SC} is shown in Fig. II.2.37.

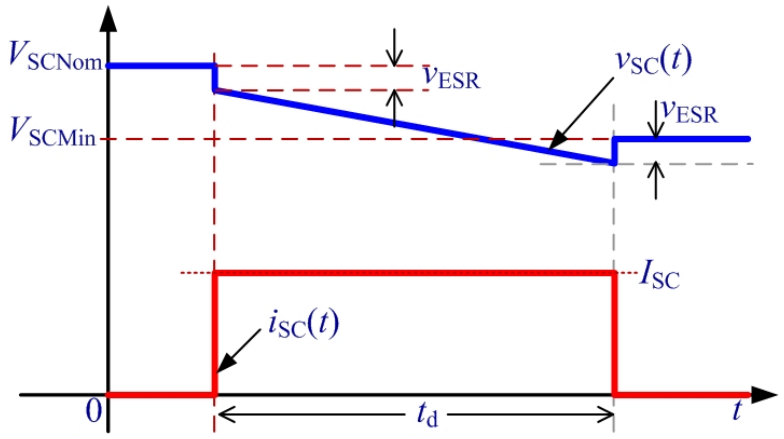

Fig. II.2.36. Discharge profile for a supercapacitor under constant current.

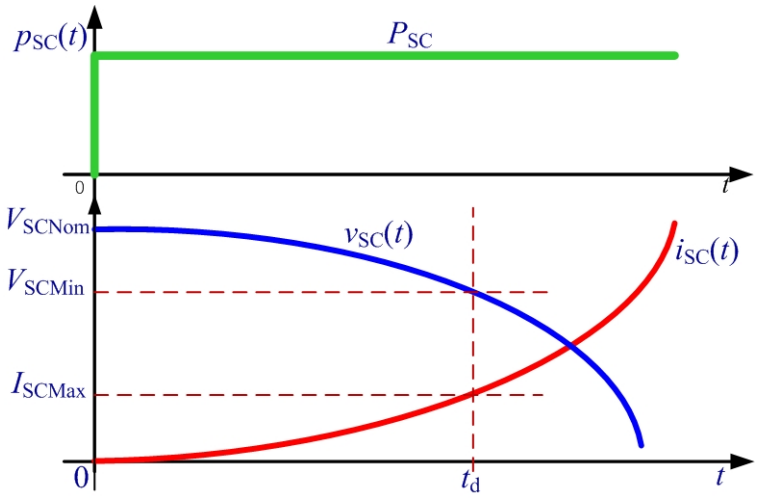

Fig. II.2.37. Discharge profile for a supercapacitor under constant power.

To estimate the minimum capacitance requirement C_{SCMin}, one can write an energy equation without losses (*ESR* neglected) under a discharging constant power P_{SC} as:

$$\frac{1}{2}C_{SCMin}\left(V_{SCNom}^2 - v_{SC}^2(t)\right) = P_{SC}t \tag{2.13}$$

Where $v_{SC}(t)$ is the supercapacitor terminal voltage. Then,

$$C_{SCMin} = \frac{2 \cdot P_{SC}t_d}{V_{SCNom}^2 - v_{SC}^2(t)} \tag{2.14}$$

Since the power being delivered is constant, the minimum voltage V_{SCMin} and maximum current I_{SCMax} can be determined based on the current conducting capabilities of the supercapacitor. Equations (2.13) and (2.14) can then be rewritten as:

$$V_{SCMin} = \sqrt{V_{SCNom}^2 - \frac{2 \cdot P_{SC}t_d}{C_{SCMin}}} \tag{2.15}$$

$$I_{SCMax} = \frac{P_{SC}}{\sqrt{V_{SCNom}^2 - \frac{2 \cdot P_{SC}t_d}{C_{SCMin}}}} \tag{2.16}$$

The variables V_{SCMax} and C_{SC} are related by the number of cells in series. Voltage rating is important, but the capacitor will also fail if the current is too high. The assumption is that the capacitors will never be charged above the combined maximum voltage rating of all the cells. Generally, V_{SCMin} is chosen as $V_{SCMax}/2$, from (2.13), resulting in the remaining energy of 25%.

In applications where high currents are drawn, the effect of the *ESR* has to be taken into account. The energy dissipated E_{loss} in the *ES*R, as well as in the cabling, connectors, and converter, could result in an undersizing of the number of capacitors required. For this reason, one can theoretically calculate the losses in the *ESR* as:

$$E_{loss} = \int_0^{t_d} i_{SC}^2(\tau) \cdot ESR \, d\tau \tag{2.17.1}$$

$$E_{loss} = P_{SC} \cdot ESR \cdot C_{SCMin} \cdot \mathbf{ln}\left(\frac{V_{SCNom}}{V_{SCMin}}\right) \tag{2.17.2}$$

To calculate the required capacitance C_{SC}, one can rewrite (2.13) as:

$$\frac{1}{2}C_{SCMin}\left(V_{SCNom}^2 - v_{SCMin}^2\right) = P_{SC}t_d + E_{loss} \tag{2.18}$$

From (2.13) and (2.18), one obtains:

$$C_{SC} = (1+\chi)\cdot C_{Min} \tag{2.19.1}$$

$$\chi = \frac{E_{loss}}{P_C \cdot t_d} \tag{2.19.2}$$

where χ is the defined energy ratio [Tho09b].

The SC bank is always connected to the dc bus by means of a two-quadrant dc/dc converter (bidirectional converter), as illustrated in Fig. II.2.38. Firstly, to demonstrate the high dynamics of supercapacitor source, Fig. II.2.40 presents the transient response of an SC converter interfacing between the dc bus and the SC bank (SAFT SC module: 292 F, 30 V, see Fig. II.2.39) [Tho09b]. The initial voltage of the SC bank is 30 V. It shows the SC current set-point (reference) i_{SCREF} and the measured SC current i_{SC}. One can observe the high dynamic response of the supercapacitor source from 0 to 50 A (discharging) in 0.4 ms. Unquestionably, the fast response of supercapacitor power source can function with the high inertia main source to improve the slow dynamics of the whole system. For the discharging characteristics of the SAFT SC module (292 F, 30 V), Fig. II.2.41 presents the transient response at a discharging constant current of 50 A. It shows the SC voltage v_{SC} and the SC current i_{SC}. Because of an aged supercapacitor bank, one can observe the high voltage drop in *ESR*. One may verify the total capacitance C_{SC} as:

$$C_{SC} = \frac{I_{SC}\cdot\Delta t}{\Delta v_{SC}} = 300\ F.$$

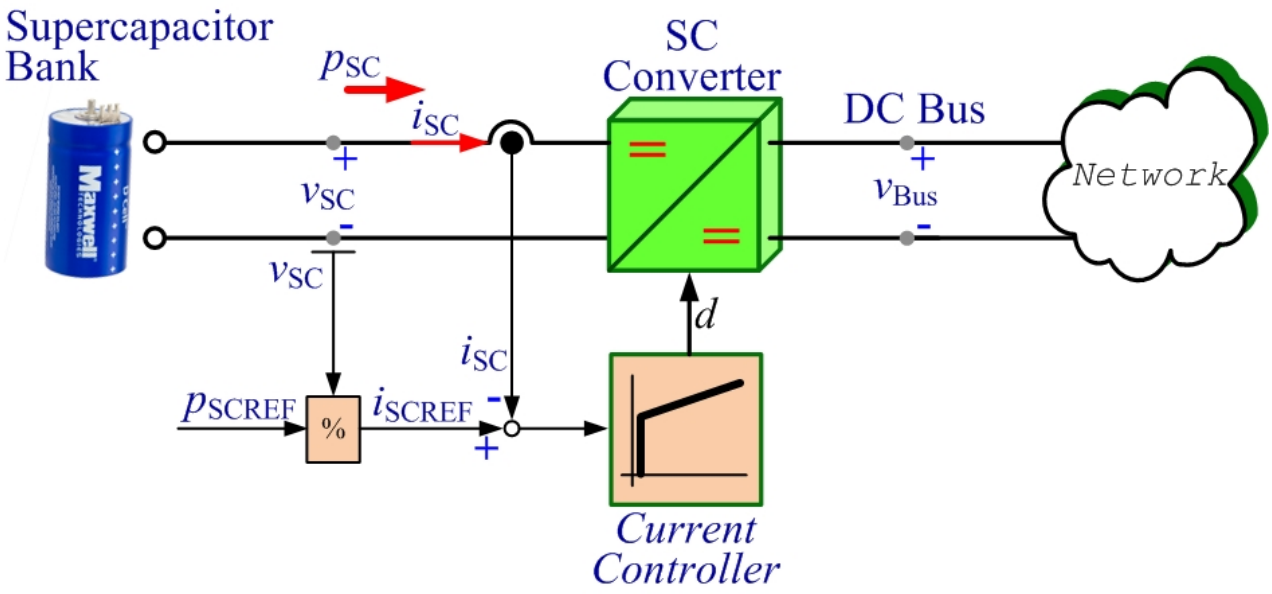

Fig. II.2.38. Supercapacitor converter testing concept.

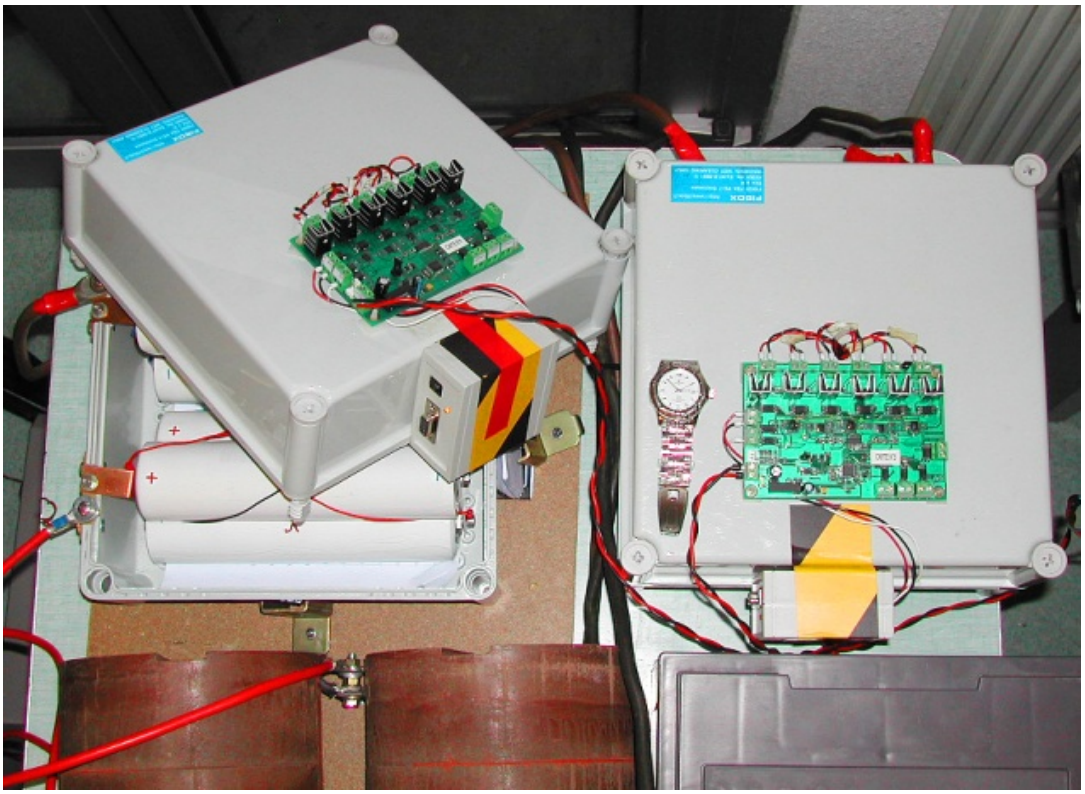

Fig. II.2.39. SAFT supercapacitor bank (292 F, 30 V) studied in the GREEN lab since 2001.

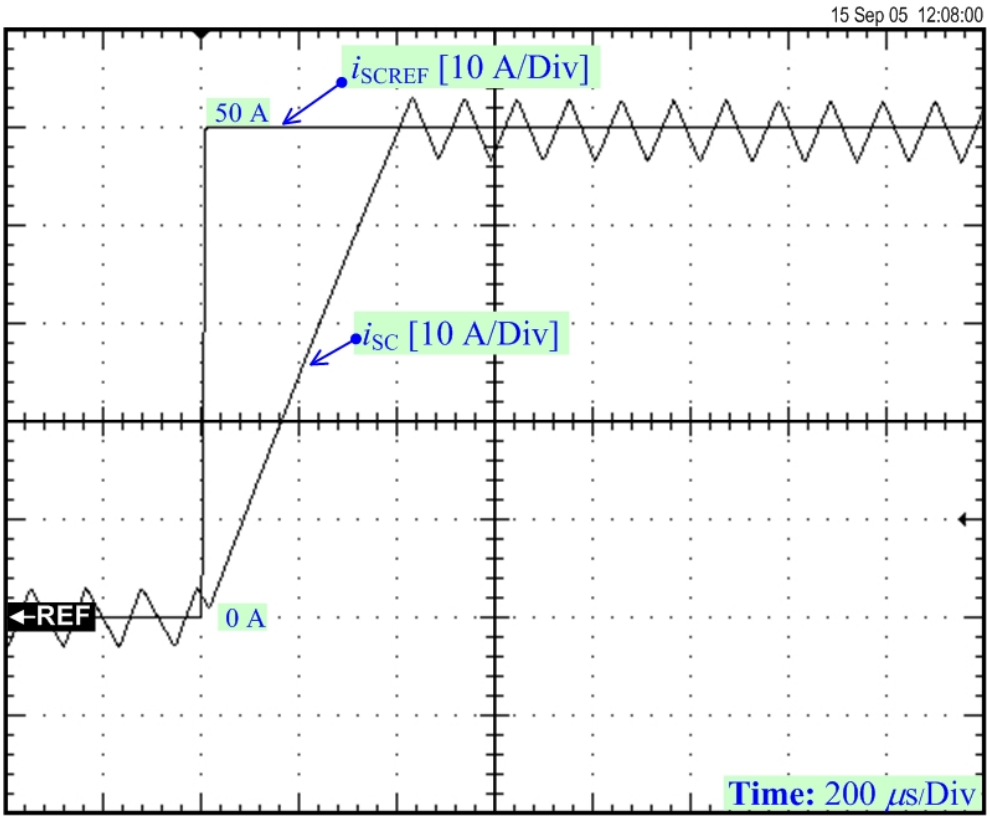

Fig. II.2.40. Experimental Result: Supercapacitor dynamics response to a current step 0 A to 50 A of SAFT supercapacitor bank (292 F, 30 V).

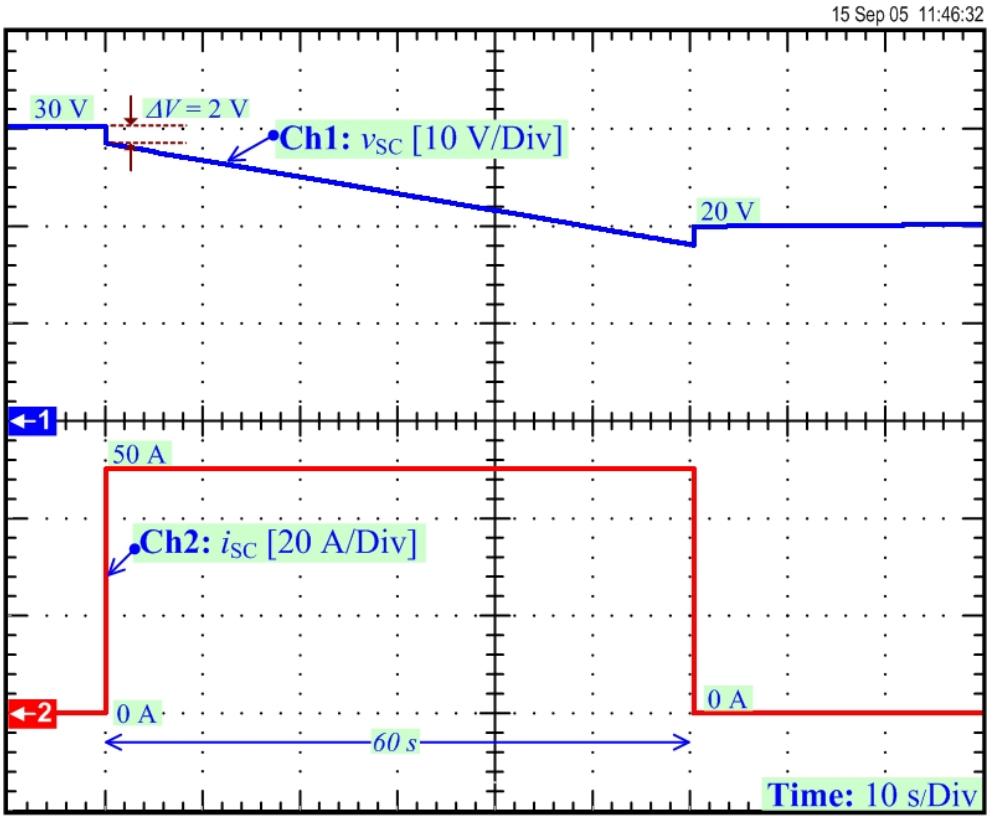

Fig. II.2.41. Experimental Result: Discharge profile for a supercapacitor under a constant current of 50 A of SAFT supercapacitor bank (292 F, 30 V).

For the next testing, Fig. II.2.42 presents the discharging characteristics of the Maxwell SC module (100 F, 32 V, see Fig. II.2.33) under a constant current of 50 A. It shows the SC voltage v_{SC} and the SC current i_{SC}. One again may verify the total capacitance C_{SC} as:

$$C_{SC} = \frac{I_{SC} \cdot \Delta t}{\Delta v_{SC}} = 105\,F.$$

Finally, Fig. II.2.43 presents the discharging characteristics of the Maxwell SC module (100 F, 32 V, see Fig. II.2.33) under a constant power of 400 W. It shows the SC power reference, the measured SC power, the SC voltage, and the SC current. One again may verify the total capacitance C_{SC} as:

$$C_{SCMin} = \frac{2 \cdot P_{SC} t_d}{V_{SCNom}^2 - v_{SC}^2(t)} = 100\,F.$$

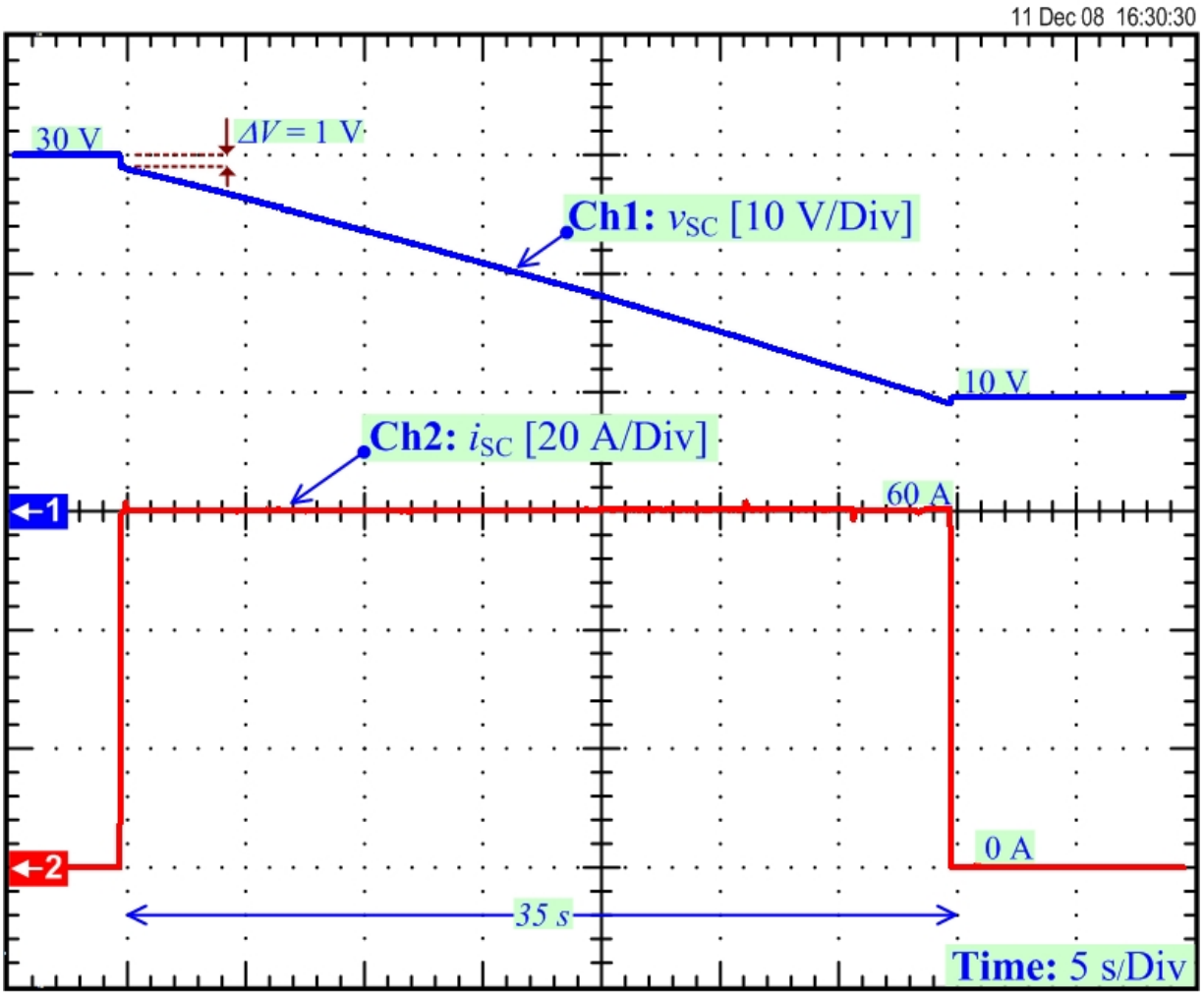

Fig. II.2.42. Experimental Result: Discharge profile for a supercapacitor under a constant current of 50 A of Maxwell supercapacitor bank (100 F, 32 V).

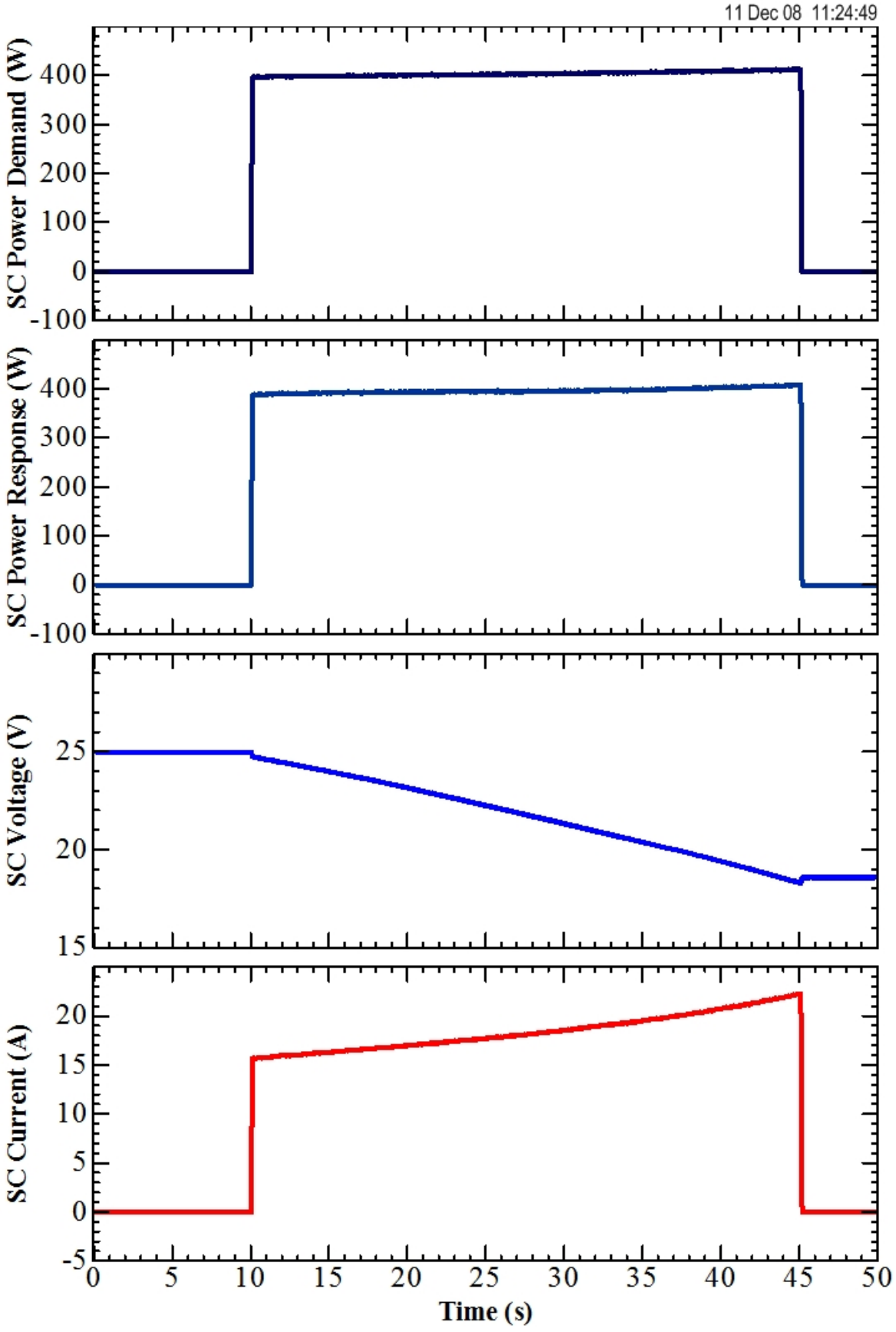

Fig. II.2.43. Experimental Result: Discharge profile for a supercapacitor under a constant power of 400 W of Maxwell supercapacitor bank (100 F, 32 V).

C. Supercapacitor Versus Battery as an Energy Storage Device

The battery is still the most extensive energy storage device to provide and deliver electricity. Today, there are many kinds of battery technologies used, such as lead-acid, NiCd, NiMH, or Li ion. Using analytical expressions to model a battery behavior has always been limited by the complex nature of battery electrochemistry [Col07], [Lee08], [Szu08]. For lead-acid cell, the terminal voltage of battery V_{Bat} (see Fig. II.2.27) and internal resistance R_{Bat} are strong functions of the SOC. The actual voltage curve is linear over most of its operating range; nevertheless, at the end of discharge, the voltage decreases very rapidly toward zero. This is because the internal resistance of a lead-acid battery is almost linear during discharge, but the losses are substantial below 25% SOC because of the increase in internal resistance of the battery. This is a reasonable work for the case of batteries used in electric vehicles, because the battery is typically operated only down to 60% SOC [or 40% depth of discharge (DOD), the amount of energy capacity that has been removed from a battery]. Usually, DOD is expressed as a percentage of the total battery capacity, and DOD = 100% – SOC.

For the supercapacitor, an innovative prototype supercapacitor SC3500 model developed and manufactured by SAFT is 3,500 F, 2.5 V, 500 A, and 0.65 kg with a maximum energy storage capacity of 10,938 J (2 $kW \cdot kg^{-1}$ and 4:67 $Wh \cdot kg^{-1}$) in an equivalent series resistance (ESR) of only 0.8 mΩ (representing small losses). Terminal voltage of the supercapacitor is limited, though, because of dissociation of the electrolyte. This limits the maximum voltage of 2.5–3 V.

When comparing the power characteristics of supercapacitors and batteries, the comparisons should be made for the same charge/discharge efficiency. Only one half of the energy at the peak power from the battery is in the form of electrical energy to the load, and the other one half is dissipated within the battery as heat in the ESR. This is to say that the efficiency of batteries is around 50%. For supercapacitors, the peak power is usually for a 95% efficient discharge, in which only 5% of the energy from the device is dissipated as heat in the ESR. For a corresponding high-efficiency discharge, batteries would have a much lower power capability.

Furthermore, the main drawback of the batteries is a slow-charging time, limited by a charging current [Yan07]; in contrast, the supercapacitors may be charged/discharge in a short time depending on a high-charging current (power) available from the main source (see Fig. II.2.40 – Fig. II.2.43). The capacitor voltage v_{SC} can then be found using the following classical equation:

$$v_{SC}(t) = \frac{1}{C_{SC}} \int_{t_o}^{t} i_{SC}(\tau)\, d\tau + v_{SC}(t_o) \tag{2.20}$$

where i_{SC} is the capacitor charging current.

Moreover, Fig. II.2.44 compares the advanced technologies of batteries and supercapacitors in terms of specific power and energy. Even though it is true that a battery has the largest energy density (meaning more energy is stored per weight than other technologies), it is important to consider the availability of that energy. This is the traditional advantage of capacitors. With a time constant of less than 0.1 s, energy can be taken from a capacitor at a very high rate [Oru07], [Uzu08], [Wan07c]. On the contrary, the same-size battery will not be able to supply the necessary energy in the same time. More advantageous, unlike batteries, supercapacitors can withstand a very large number of charge/discharge cycles without degradation (or visually infinite cycles) [Tho08a].

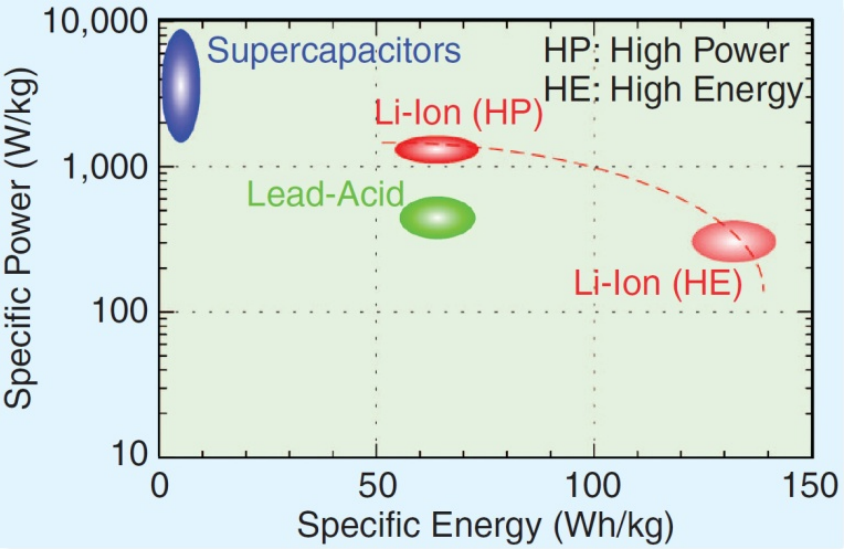

Fig. II.2.44. Specific power versus specific energy of modern storage devices: supercapacitor, lead-acid, and Li-ion battery technology. The supercapacitors and Li-ion batteries are based on the SAFT company.

Remark 4: one may summarize the constraints to operate a supercapacitor bank as follows:

To operate the SC module, its module voltage is limited to an interval [V_{SCMin}, V_{SCMax}]. The higher V_{SCMax} value of this interval corresponds to the rated voltage of the storage device. In general, the lower V_{SCMin} value is chosen as $V_{SCMax}/2$, where the remaining energy in the SC bank is only 25% and the SC discharge becomes ineffective.

II.3 Hybrid Power Source

II.3.1 Power Converter Structure

Solar and wind power generation are two of the most promising renewable power generation technologies. Fuel cells also demonstrate large prospective to be clean power sources of the near future because of many merits they have and the fast development in FC technologies. However, none of these technologies is perfect now. Solar and wind power are highly dependent on climate while fuel cells need hydrogen-rich fuel and the cost for fuel cells is still very high at current stage. Nevertheless, because different renewable energy sources can complement each other, multi-source hybrid alternative energy systems (with proper control) have great potential to provide higher quality and more reliable power to customers than a system based on a single resource.

There are many combinations of different alternative energy sources (photovoltaic and/or wind and/or fuel cell) and storage devices (battery and/or supercapacitor) to form a hybrid system. The solutions can be generally classified into two categories: AC coupling and DC coupling.

In an AC coupling scheme, shown in Fig. II.3.1, different energy sources are integrated through proper power electronic interfacing circuits to a power frequency AC bus. Coupling inductors may also be needed to achieve desired power flow management. The advantages of this coupling are as follows:

1) High reliability. If one of the energy sources is out of service, it can be isolated from the system easily.
2) Ready for grid connection.
3) Standard interfacing and modular structure.
4) Easy multi-voltage and multi-terminal matching.

However, this structure has some disadvantages:

1) Synchronism required.
2) The need for power factor and harmonic distortion correction.

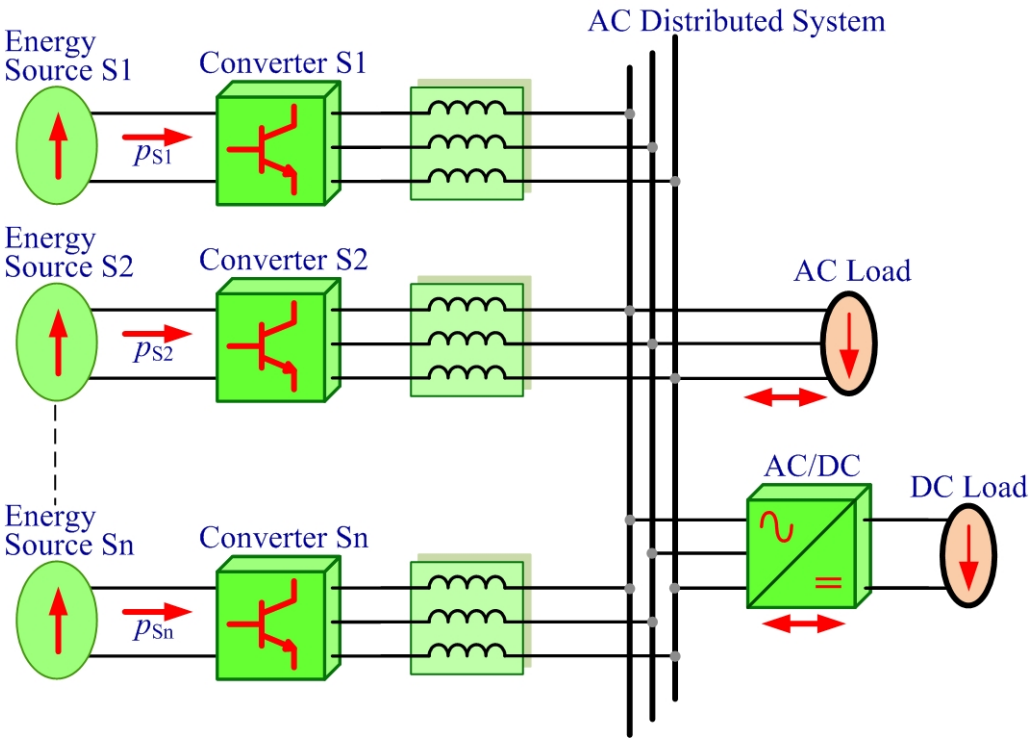

Fig. II.3.1. Hybrid energy system integration: AC coupling.

In a DC coupling configuration, shown in Fig. II.3.2, different alternative energy sources are connected to a DC bus through appropriate power electronic interfacing circuits. Then the DC energy is converted into 50 Hz (France, Thailand, for example) or 60 Hz (USA) AC through a DC/AC converter (inverter) which can be bi-directional. For the DC link voltage level, it is depending on its applications:

■ 270 V or 350 V for the standard on the all-electric aircraft [Dol06]

■ 48 V [Agb04], 120 V [Wai05], or 400–480 V [Lee06], [Wan06b], [Cho06b] for stand-alone or parallel grid connections

■ 42 V (PowerNet) a new standard voltage for automobile systems [Ema08], [Fah04], [Kei04]

■ 270–540 V for electric vehicles [Luk08], [Gok02], [Bit04]

■ 350 V (transit bus systems) to 750 V (tramway and locomotive systems) [Var06], [Fur06], [Mon03], [Kim08], [Mil06], [Mil07], [Yon07], [Oga07], [Nic03].

The advantages of the DC coupling are as follows:

1) Synchronism not needed for DC connection.

2) Suitable for long distance transmission; it has less transmission losses.

3) Single-wired connection

However, this structure has some disadvantages:

1) Concerns on the DC voltage compatibility

2) If the DC/AC inverter is out of service, the whole system fails to supply AC power.

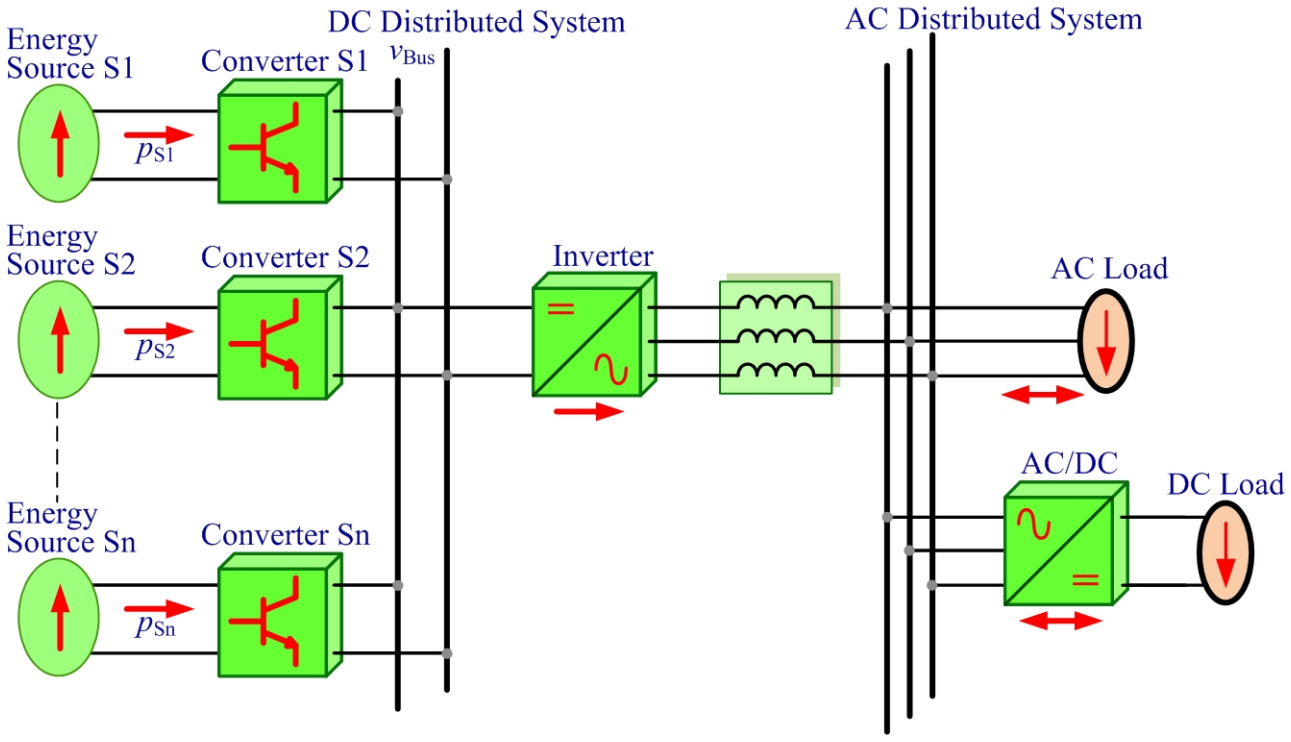

Fig. II.3.2. Hybrid energy system integration: DC coupling.

A hybrid energy system can either be stand-alone (autonomous) or grid-connected if utility grid is available. For an autonomous application, the system needs to have sufficient storage capacity to handle the power variations from the alternative energy sources involved. A system of this type can be considered as a micro-grid, which has its own generation sources and loads. For a grid-connected application, the alternative energy sources in the micro-grid can supply power both to the local loads and the utility grid. In addition to real power, these sources can also be used to give reactive power support to the utility grid. The capacity of the storage device for these systems

can be smaller if they are grid-connected since the grid can be used as system backup. However, when connected to a utility grid, important operation and performance requirements, such as voltage, frequency and harmonic regulations, are imposed on the system.

However, here the stand-alone (autonomous) applications both FC vehicles and the renewable energy power plant with the DC coupling will be presented as following. Firstly, to control the power or current from the main energy source(s), a nonreversible DC/DC converter is always chosen to interface a main source to a DC bus. Then, we propose 7-configurations for the power converter connections.

- For the first one as detailed in Fig. II.3.3, it is very simple one that a main energy source *S1* is connected to a DC bus by a DC/DC converter and an energy storage device *E1* is directly connected to a DC bus [Tho08b]. An energy storage device should be a battery bank because battery voltage, for example, in a lead-acid battery, is nearly constant and virtually independent from discharge current and drops sharply when almost fully discharged. The main advantage is that it is no need a reversible DC/DC converter for an energy storage device *E1*. However, a battery bank should be composed of many cells connected in series in order to increase the utilized DC bus voltage.

- For the second one as presented in Fig. II.3.4, it is common configuration that a main energy source *S1* is connected to a DC bus by a nonreversible DC/DC converter and an energy storage device *E1* is connected to a DC bus by a reversible DC/DC converter [Tho07], [Tho11b]. An energy storage device can be either a battery bank or supercapacitor module. The main advantage of this configuration is that one can fully control a power from a main source and an energy storage device.

- For the third configuration as presented in Fig. II.3.5, a main energy source *S1* is connected to a DC bus by a reversible DC/DC converter and an energy storage device *E1* is connected to a terminal of a main source by a reversible DC/DC converter [Pay11]. An energy storage device can be either a battery bank or supercapacitor module. The main advantage of this configuration again is that one can fully control a power from a main source and an energy storage device. An

FC voltage is high enough and an energy storage device is lower voltage operation. Therefore, the power switches in converter *E1* sustain a low-voltage stress, which leads to a lower-switching losses. The MOSFET switches can be used in this converter, while in the converter *S1* the insulated-gate bipolar transistor (IGBT) switches should be employed since the output capacitor has a high voltage.

- Supercapacitor and Battery may be connected together to form a high-power high energy storage device. So, a configuration 4 is presented in Fig. III.3.6 as published by Thounthong *et al.* [Tho09e]. A main source, an energy storage device *S1*, and an energy storage device *S2* are connected to a common DC link by the converters *S1*, *E1*, and *E2*, respectively.

- It is similar to a configuration 4 in order to form a high-power high energy storage device. One proposes a configuration 5 as detailed in Fig. III.3.7 as published by Zandi *et al.* [Zan11]. The main advantage is the energy storage device *E1* can be a supercapacitor bank and work at a low voltage.

- In a near future, a power plant may compose of many renewable energy sources *S1*, *S2*, …*Sn* and an energy storage device *E1*, as proposed in Fig. III.3.8. For example, the solar/hydrogen power plant with a supercapacitor storage device has been published by Thounthong *et al* [Tho11a] and [Tho13].

- Finally, one expects that a power plant may compose of many renewable energy sources *S1*, *S2*, …*Sn* and many energy storage devices *E1*, *E2*,...*En*, as proposed in Fig. III.3.9. Each source is connected to a DC link by a DC/DC converter.

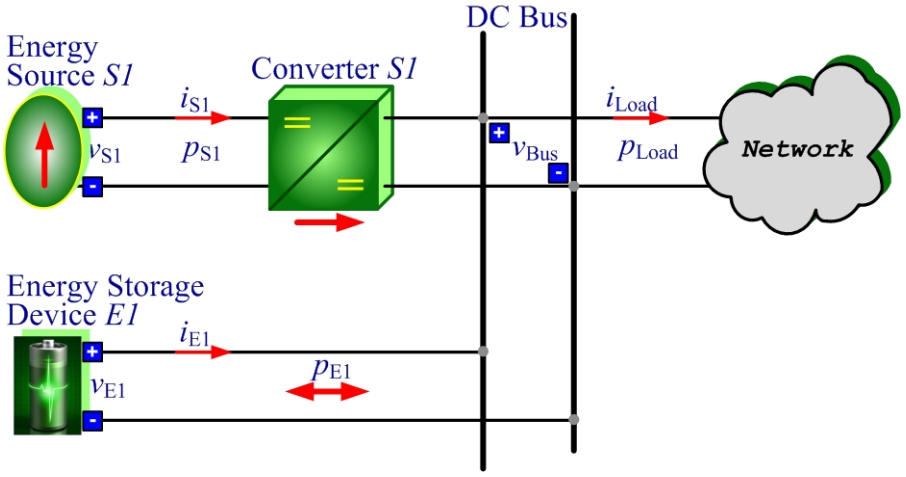

Fig. II.3.3. Configuration 1: Single Source/Single Energy Storage Device.

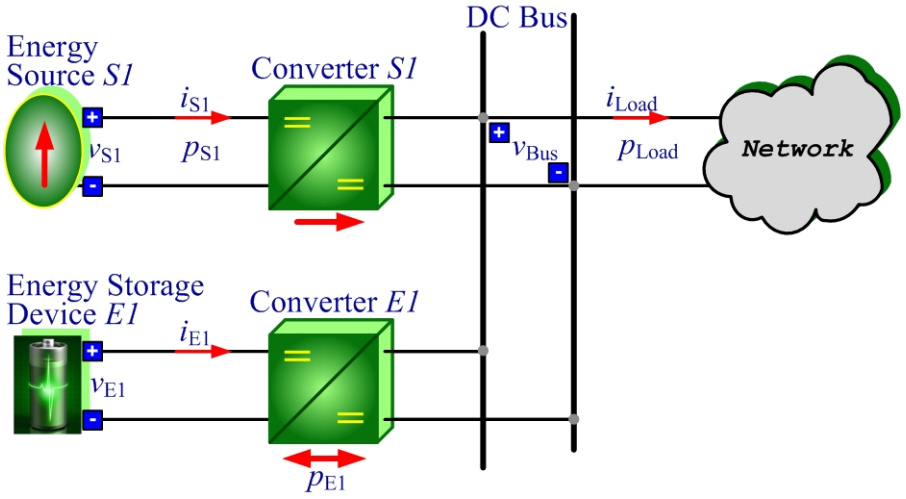

Fig. II.3.4. Configuration 2: Single Source/Single Energy Storage Device.

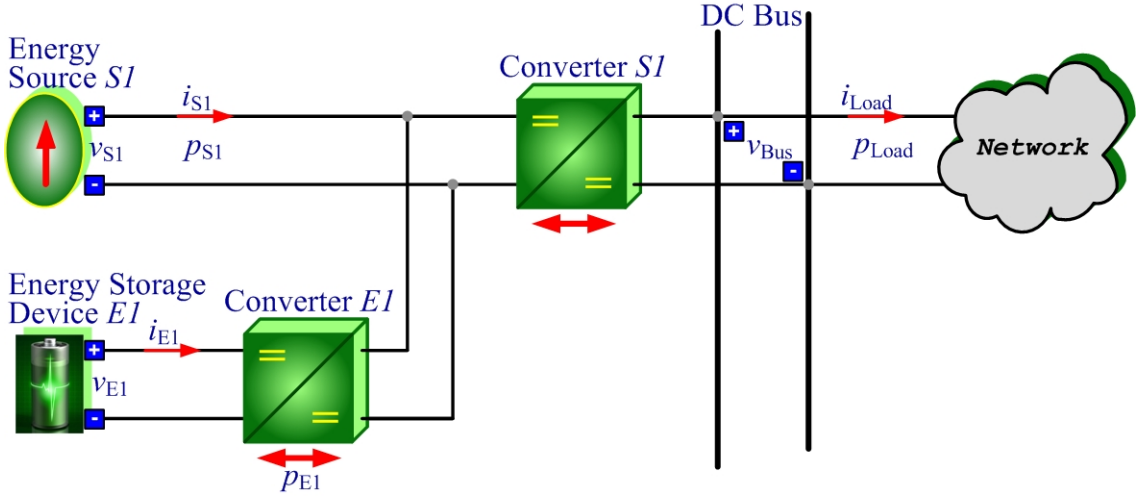

Fig. II.3.5. Configuration 3: Single Source/Single Energy Storage Device.

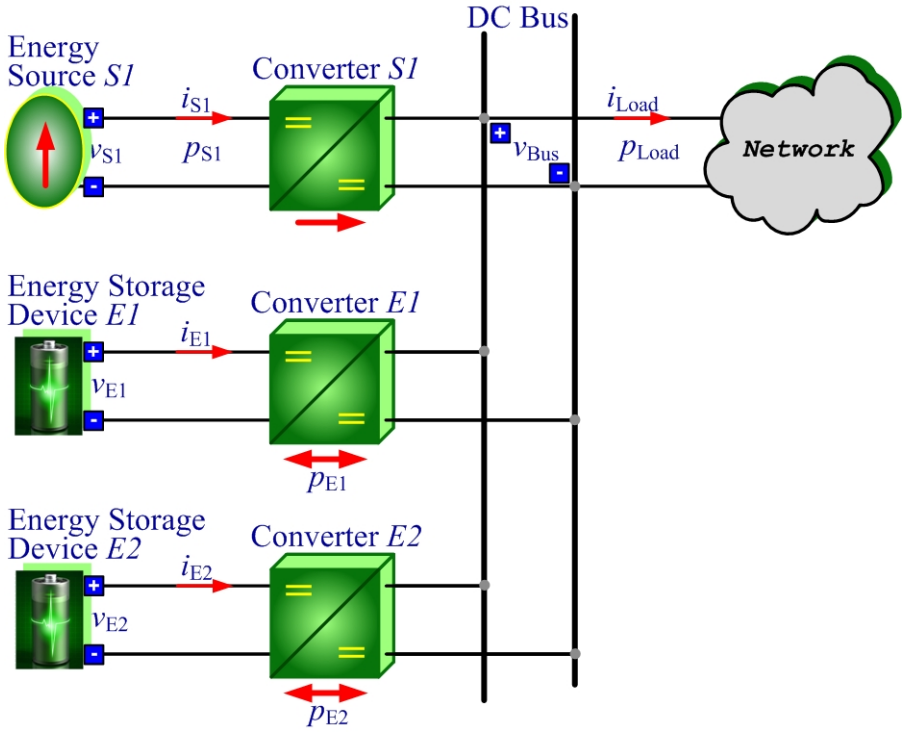

Fig. II.3.6. Configuration 4: Single Source/Two Energy Storage Devices.

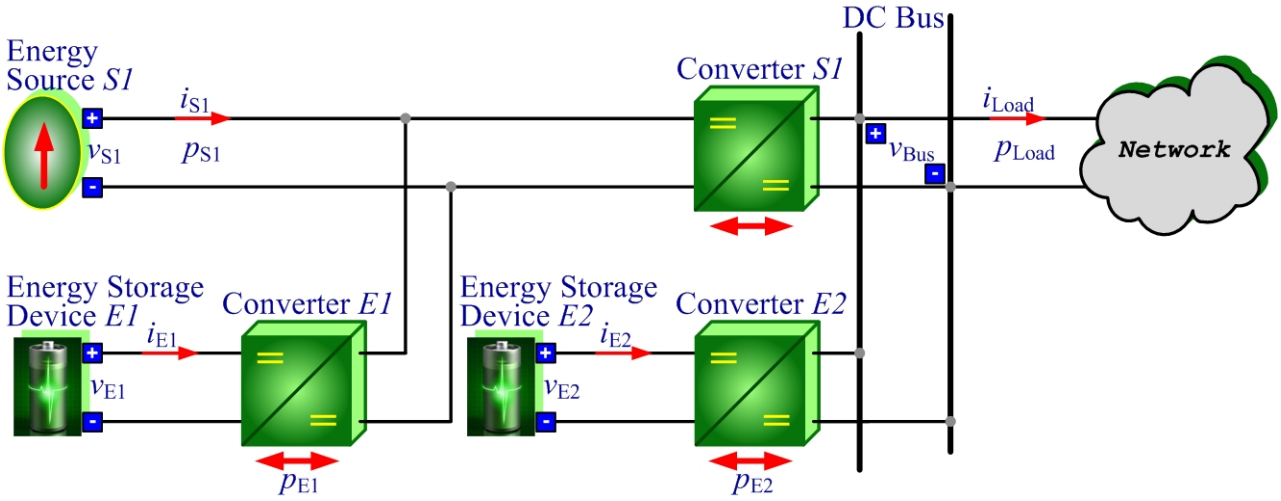

Fig. II.3.7. Configuration 5: Single Source/Two Energy Storage Devices.

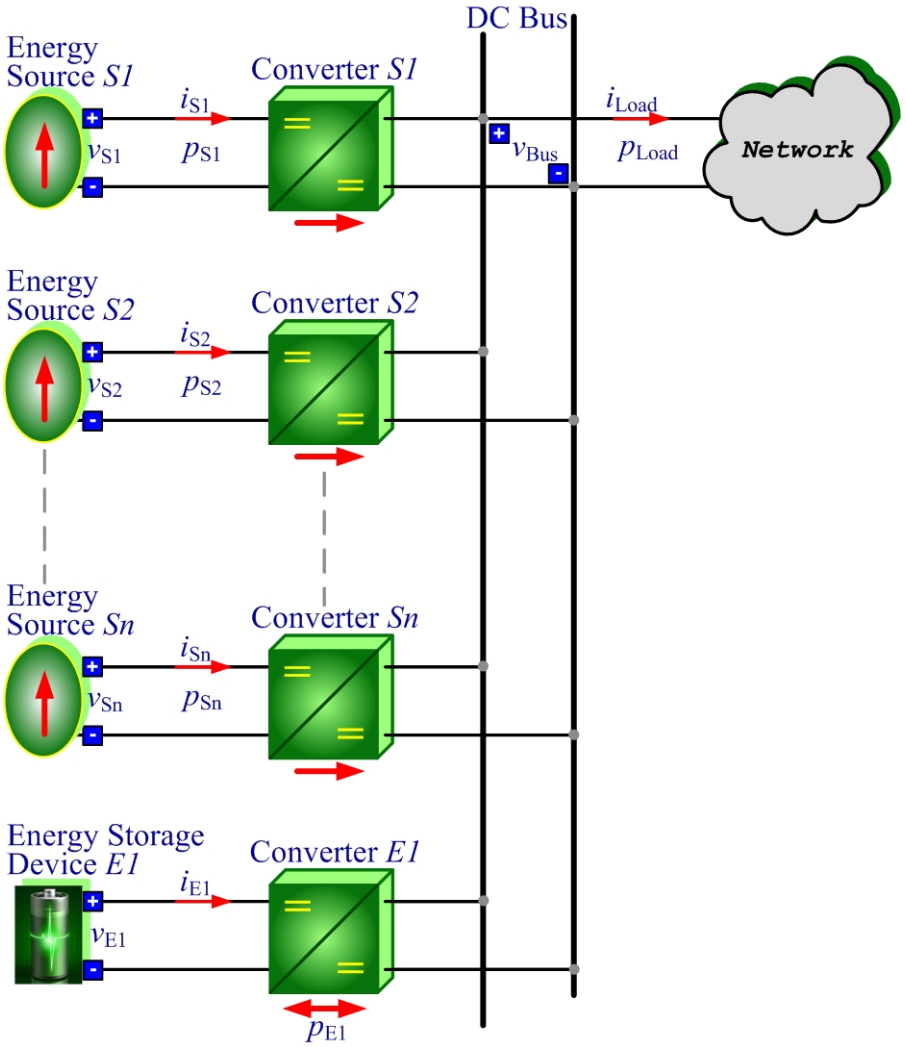

Fig. II.3.8. Configuration 6: Multisources/Single Energy Storage Device.

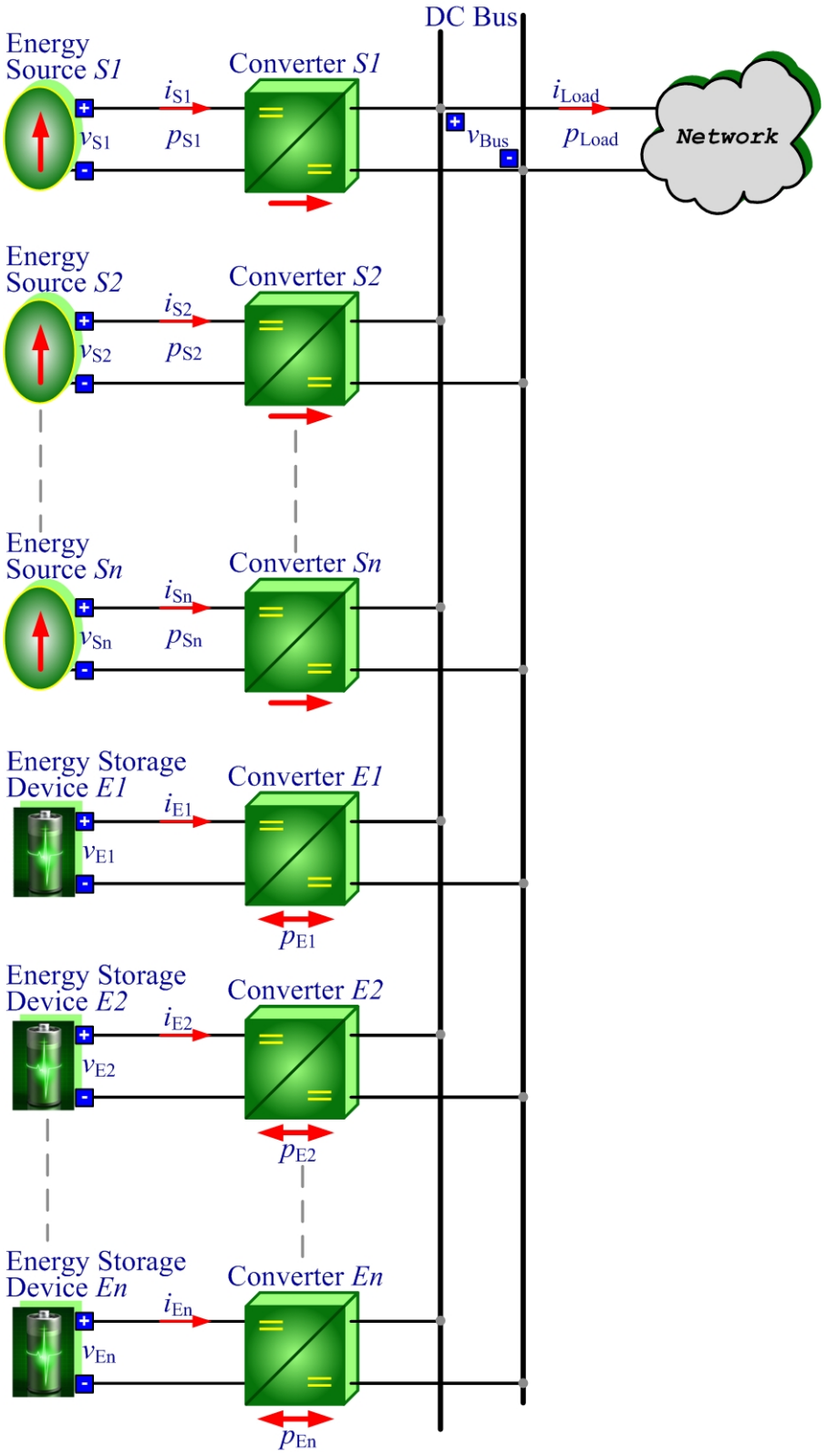

Fig. II.3.9. Configuration 7: Multisources/Multienergy Storage Devices.

II.3.2 DC/DC Converter

II.3.2.1 Classic Converter

A. Non-reversible Converter

The voltages of the fuel cell and photovoltaic panel vary with the current drawn by the load and decrease significantly at high current supplies. Therefore, a power-electronics system is needed to process the raw output power from the stack or panel and provide power to the load at a constant DC utility level (42 V or 400 V, for example). Basically, low-voltage, high-current structures are needed because of the FC or PV electrical characteristics. A classical boost converter (non-reversible) is often selected as an FC converter [Tho09a], [Wan06b], [Agb04], [Wai05], [Cho06b], [And08], [Moh05], [Bre07], because it can be operated in the current control mode in a continuous condition mode, as portrayed in Fig. II.3.10. Then, one does not need a blocking diode and passive filter between a main source and a converter. Based on the load conditions, the boost converter can be commanded to draw a specific amount of current from the main source with a ripple well defined by the frequency, size of the inductor, and duty ratio. The FC boost converter sizes of 0.5 kW [Tho06a] (1 kW [Wai05], [Cho06b], [And08]; 5 kW [Agb04]; 27 kW [Moh05]; and 50 kW [Wan06b] have been studied.

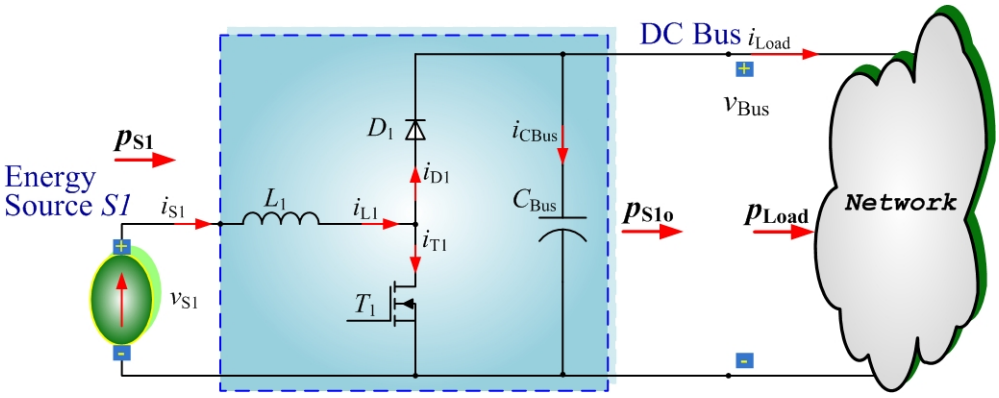

Fig. II.3.10. Classic Boost Converter.

B. Reversible Converter

Energy storage device(s) is connected to the dc bus by means of a two-quadrant dc/dc converter, as shown in Fig. II.3.11. Its current, which flows across the storage device, can be positive (discharging) or negative (charging), allowing energy to be transferred in both directions. L_1 represents the inductor used for energy transfer and filtering. The inductor size is classically defined by switching frequency and current ripple. The converter is driven by means of complementary pulses, generated by a hysteresis comparator or PWM, and applied on the gates of the two power switches T_1 and T_2.

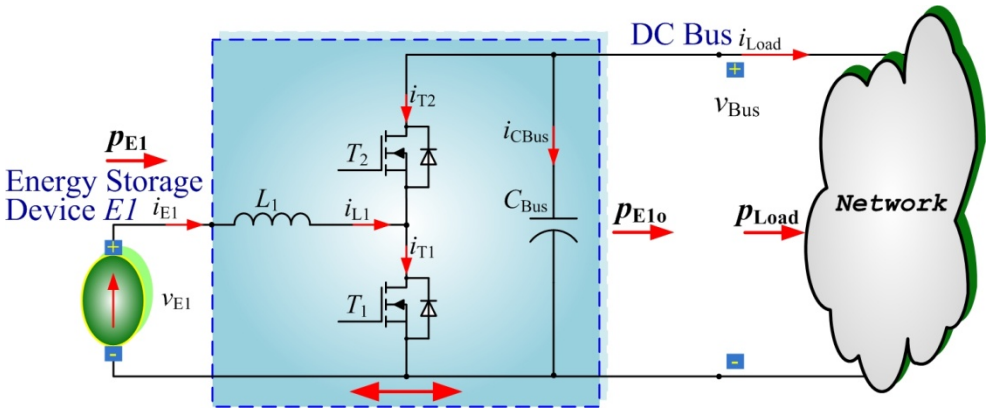

Fig. II.3.11. Classic bidirectional converter (2-quadrant converter).

II.3.2.2 Parallel Interleaved Converter

The classical non-reversible converter and reversible converter will be limited when the power increases or at higher step-up ratios. As such, the use of parallel power converters (multiphase converters in parallel) with interleaving may offer better performance [Tho09a]. Multiphase converters (Fig. II.3.12 and Fig. II.3.13) are proposed for high power applications. The number of parallel converter modules N would depend upon the rated power of the sources. For the interleaving method, the converter modules all operate at the same switching frequency. Their switching waveforms are displaced in phase with respect to one another by $2\pi/N$ radians over the switching period, with N being the number of converters working in parallel [Oze07].

For clarity, Fig. II.3.14 shows the functional diagram of a two phase interleaved boost converter (N = 2). It is simply two boost converters in parallel operating 180° out of phase. The switching functions are generated by pulsewidth modulators PWM1 and PWM2, where T_S is the

switching period. The modulation signals v_{C1} and v_{C2} are generated by a control circuit (the current control or power control loop). The carrier signals are triangular or saw tooth signals shifted by 180° (called the interleaving technique) and running at the same switching frequency f_S (= $1/T_S$). The input current i_{S1} is the sum of the two inductor currents i_{LS1} and i_{LS2}. Because the inductor's ripple currents are out of phase, they tend to cancel each other and reduce the input ripple current caused by the boost inductors. The best input inductor ripple current cancellation occurs at 50 percent duty cycle for N = 2. The benefits of this technique are associated with harmonic cancellation among the cells and include a low ripple amplitude and a high ripple frequency in the aggregate input and output waveforms [Tho09a].

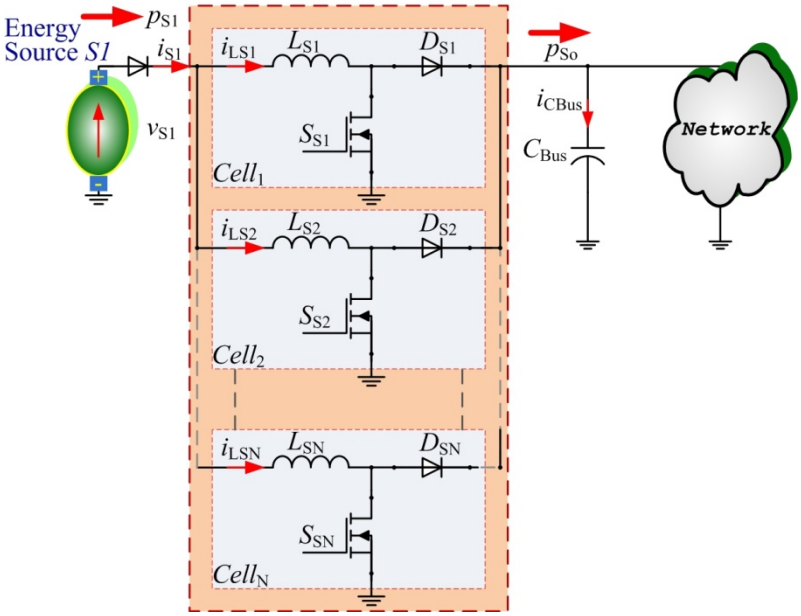

Fig. II.3.12. Proposed multiphase interleaved boost converter.

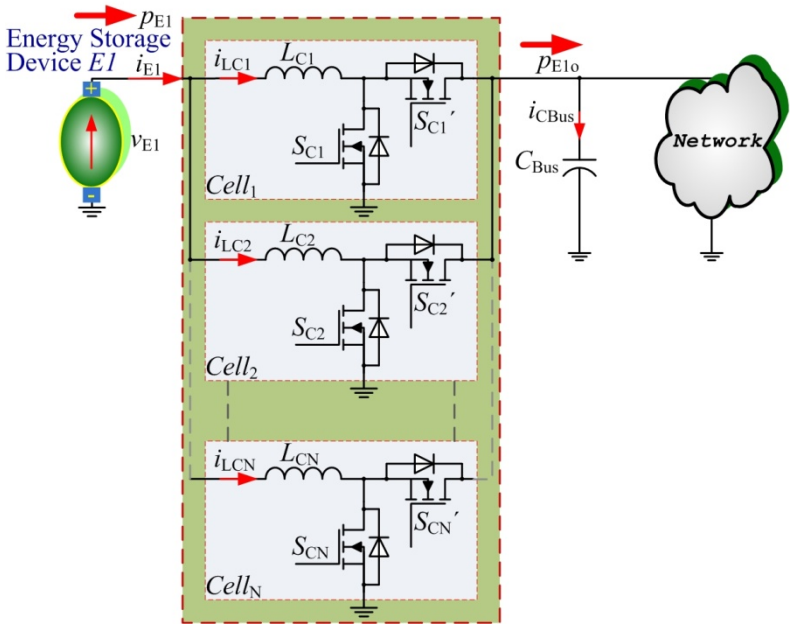

Fig. II.3.13. Proposed multiphase interleaved bidirectional converter.

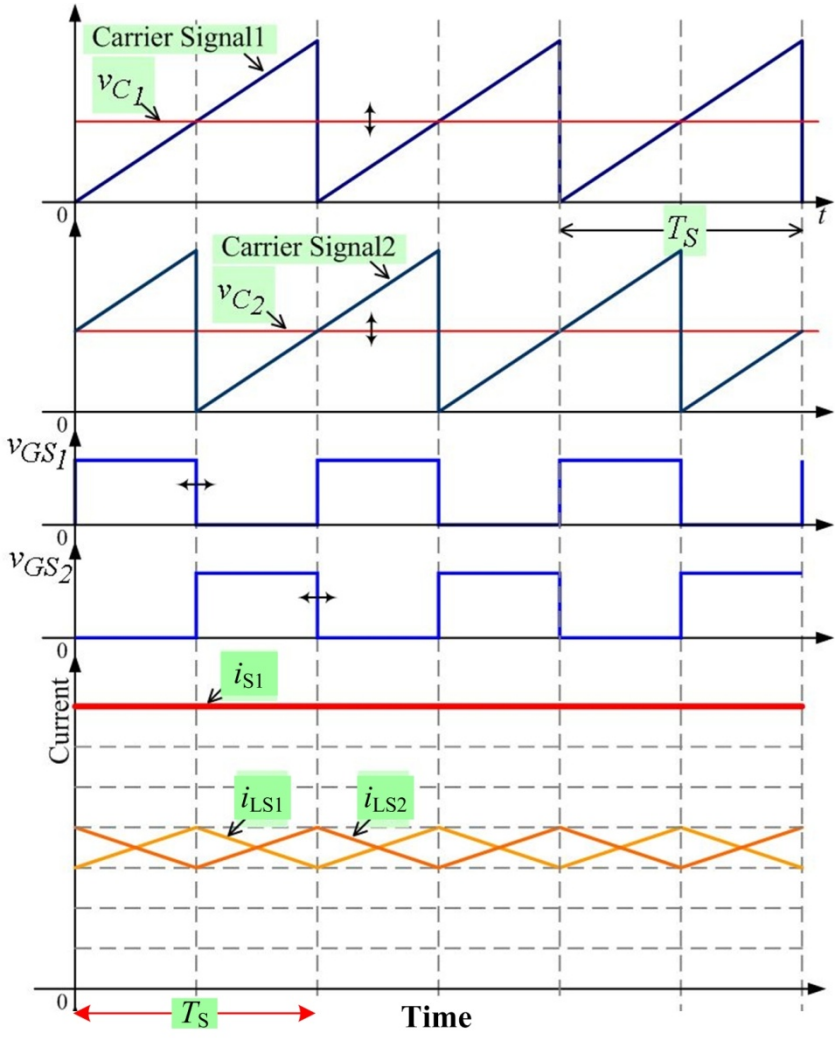

Fig. II.3.14. Key waveforms of a two-phase interleaved boost converter (N = 2).

To obtain the transfer function of the current input control loop, the linearized differential equations (which are developed from the switched state-space model through the state-space averaged model of a boost converter, refer to Fig. II.3.12) are defined as follows [Tho10a], [Tho10d]:

$$\begin{cases} L_1 \dfrac{d\tilde{i}_{L_1}(t)}{dt} = \tilde{v}_S(t) - R_{L_1}\tilde{i}_{L_1}(t) - (1-D_1)\tilde{v}_{Bus}(t) + V_{Bus}\tilde{d}_1(t) \\ L_2 \dfrac{d\tilde{i}_{L_2}(t)}{dt} = \tilde{v}_S(t) - R_{L_2}\tilde{i}_{L_2}(t) - (1-D_2)\tilde{v}_{Bus}(t) + V_{Bus}\tilde{d}_2(t) \\ \cdot \quad \cdot \quad \cdot \\ L_N \dfrac{d\tilde{i}_{L_N}(t)}{dt} = \tilde{v}_S(t) - R_{L_N}\tilde{i}_{L_N}(t) - (1-D_N)\tilde{v}_{Bus}(t) + V_{Bus}\tilde{d}_N(t) \\ C_{Bus} \dfrac{d\tilde{v}_{Bus}(t)}{dt} = (1-D_1)\tilde{i}_{L_1}(t) - I_{L_1}\tilde{d}_1(t) + (1-D_2)\tilde{i}_{L_2}(t) - I_{L_2}\tilde{d}_2(t) + (1-D_N)\tilde{i}_{L_N}(t) - I_{L_N}\tilde{d}_N(t) - \tilde{i}_{Load}(t) \end{cases} \quad (2.21)$$

where the subscript numbers (1, 2, … N) represent parameters of each converter module, and

D : the nominal duty cycle of the PWM converter;

$\tilde{d}$: the duty cycle variation;

V_{Bus} : the nominal dc bus voltage;

$\tilde{v}_{Bus}$: the dc bus voltage variation;

I_L : the nominal inductor current;

$\tilde{i}_L$: the inductor current variation;

$\tilde{i}_{Load}$: the load current variation;

$\tilde{v}_S$: the source voltage variation;

R_L : the series resistance of inductor L.

Note that series resistance of C_{Bus} is ignored.

As portrayed in Fig. II.3.15, for current measurements of each inductor current, a first order filter $H_{iN}(s)$ is used to reduce harmonics due to high switching frequency. A classical proportional–integral (PI) controller $C_{iN}(s)$ associated to a pulse width modulation (PWM) generator $G_{PN}(s)$ is selected for inductor current control. If we consider that the parameters in each converter are ideally the same values, the inductor current control loops can be modeled from (2.21), taking into account V_P, the amplitude of the PWM saw tooth carrier signals, by the following closed-loop transfer function:

$$\frac{\tilde{i}_{\mathrm{L}}(s)}{\tilde{i}_{\mathrm{LREF}}(s)} = \frac{C_i(s)G_P(s)G_{id}(s)}{1+C_i(s)G_P(s)G_{id}(s)H_i(s)} \tag{2.22}$$

with:

$$C_i(s) = \frac{K_i(T_{Ci}s+1)}{T_{Ci}s}, \tag{2.23}$$

$$G_P(s) = \frac{1}{V_P}, \tag{2.24}$$

$$H_i(s) = \frac{K_f}{T_f s+1}, \tag{2.25}$$

$$G_{id}(s) = \frac{\tilde{i}_L(s)}{\tilde{d}} = \frac{K_{id}(T_z s+1)}{\left(\frac{s}{\omega_n}\right)^2 + \frac{2\zeta}{\omega_n}s+1}, \tag{2.26}$$

and:

$$\begin{cases} K_{id} = \dfrac{I_L}{(1-D)} \\ T_z = \dfrac{V_{Bus}C_{Bus}}{(1-D)I_L} \end{cases} \text{ and } \begin{cases} \omega_n = \sqrt{\dfrac{(1-D)^2}{L\cdot C_{Bus}}} \\ \zeta = \dfrac{R_L\cdot C_{Bus}}{(1-D)^2}\dfrac{\omega_n}{2} \end{cases} \tag{2.27}$$

The gain K_i and the integral time constant T_{Ci} of the PI controller are set to obtain the desired phase margin. For the equations above, we consider that the FC power source is an ideal source (no FC complex impedances [Noi12] taken into account).

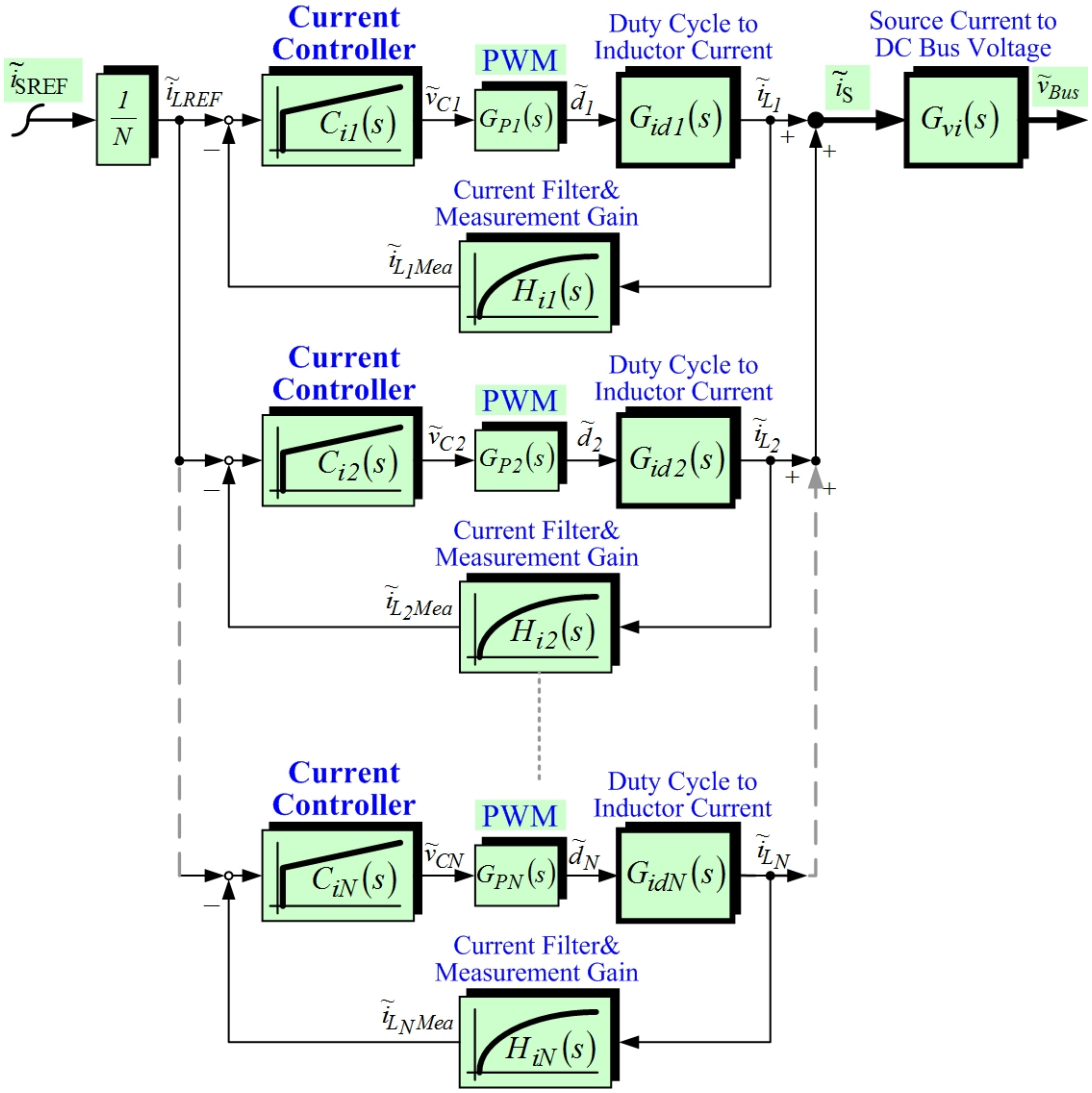

Fig. II.3.15. Proposed current control loop (linear control) of *N*-phase interleaved converter.

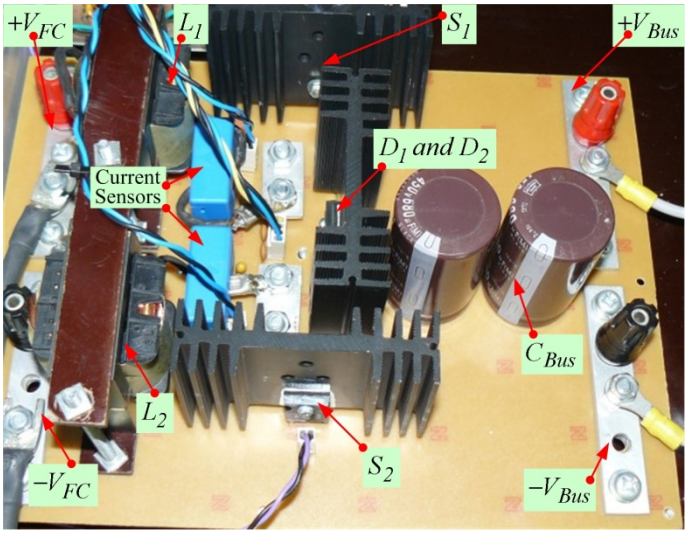

Fig. II.3.16. Photograph of an implement 2-phase step-up power converter in parallel for an FC converter.

The 2- phase power converters tested hereafter are illustrated in Fig. II.3.16. Some guidelines of a boost power converter design can be seen in [Tho06a]. The inductors L_1 and L_2 are 216 μH (2 x Double Ferrite Core E55 [33 turns, 1.1 mm of air-gap]) and the Output Capacitor C_{Bus} is 2 x 3900 μF + 2 x 680 μF Electrolytic (Connected in Parallel). The oscilloscope waveforms in Fig. II.3.17 and Fig. II.3.18 portray the steady state characteristics of the 2- phase interleaved converters connected with the 1.2 kW FC power source (refer to Fig. II.2.5) at different operating points, the load at dc bus being adjusted in order to obtain a constant dc bus voltage of 60 V (rated dc bus voltage or operating point of the specification). They illustrate the FC current, and the first and second inductor currents of the 2-phase parallel converter at the average FC current of 4 A and 46 A (rated current), respectively. One can observe again that the FC current is the sum of the inductor currents, and that the FC ripple current is 1/N the individual inductor ripple currents. In addition, it can be seen the FC ripple frequency is N-times the switching frequency of 25-kHz.

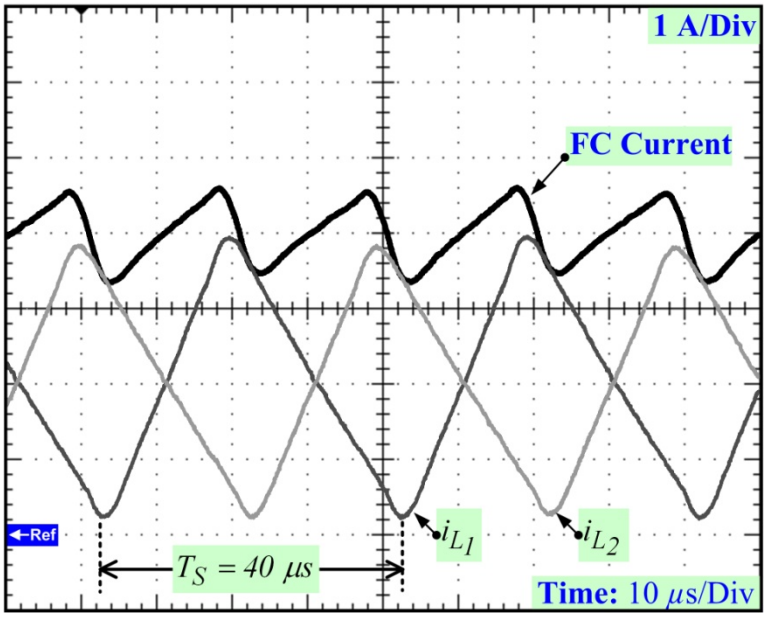

Fig. II.3.17. Experimental Result: steady-state waveforms of the 2-cell interleaved converter system at a FC current of 4 A (v_{FC} = 35.8 V).

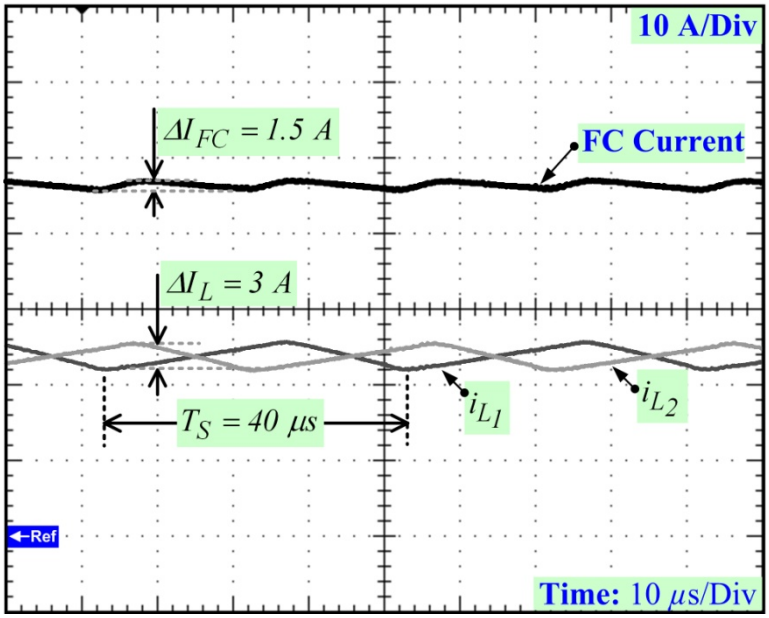

Fig. II.3.18. Experimental Result: steady-state waveforms of the 2-cell interleaved converter system at a FC current of 46 A (v_{FC} = 26.3 V).

For dynamics testing, the implemented 2-phased FC converter was operated by using an ideal 26-V power supply, which has the same rated voltage as the considered FC system, in order to confirm that the converters can operate correctly, and also to observe the dynamic performances of the inductor current control loops. The oscilloscope waveforms in Figs. II.3.19 and II.3.20 depict the large-signal responses of the converters to an input current set-point step. They present the input current demand, the input current response, and the first and second inductor current responses of the 2-phase parallel converters. One can observe that current responses of the converter have high dynamics with optimum response by the current compensator (PI controller). Absolutely, the input current is the sum of the inductor currents.

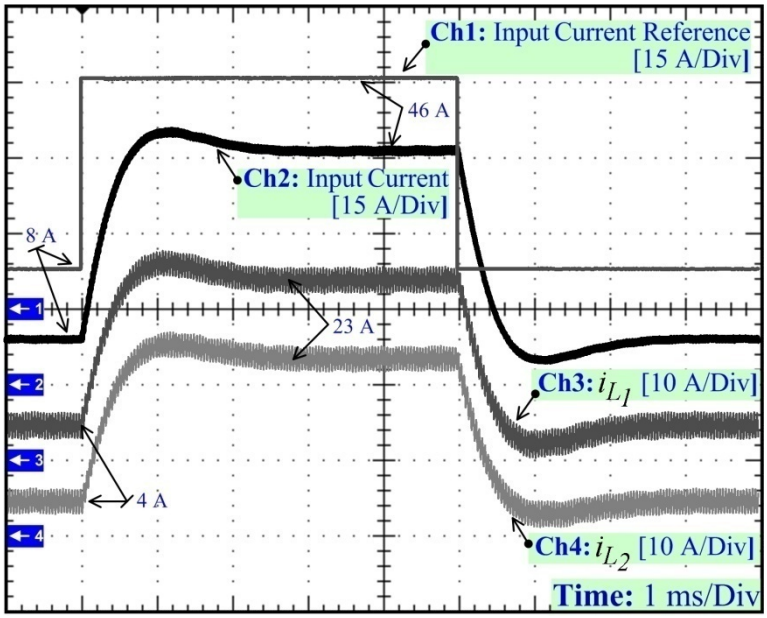

Fig. II.3.19. Experimental Result: Transient response of the 2-cell converter current loops to an input current reference step varying from 8 A to 46 A (rated current) and vice versa.

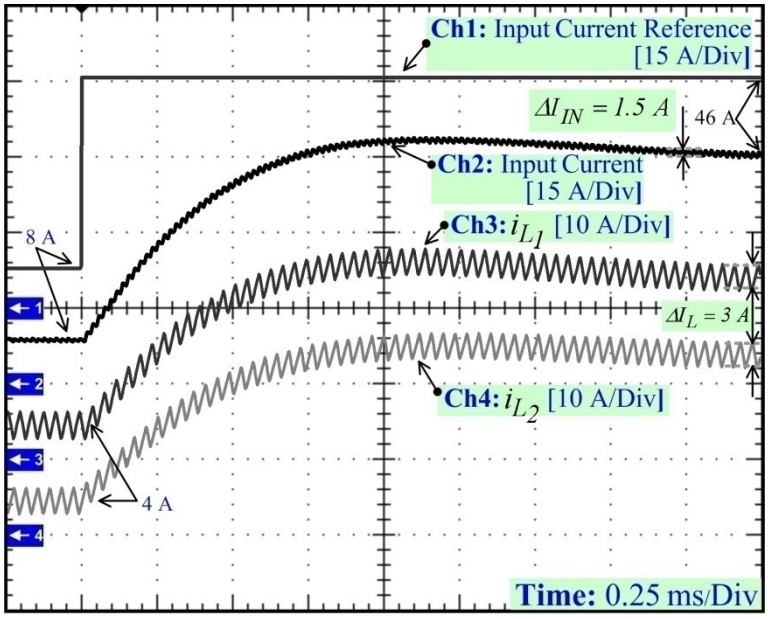

Fig. II.3.20. Experimental Result: Transient response of the 2-cell converter current loops to an input current reference step varying from 8 A to 46 A (rated current).

Moreover, the prototype 4-phase interleaved converters for an FC source and a PV source are shown in Fig. II.3.21. The oscilloscope waveforms in Fig. II.3.22 portray the steady state characteristics of the 4-phase interleaved converter connected with the 1.2 kW Nexa^{TM} PEMFC (refer to Fig. II.2.5) at different FC current operations. It demonstrates the dc bus voltage, the FC voltage, the FC current, the first, second, third and forth inductor currents. Fig. II.3.22(a) and (b)

presents the characteristics at the average FC current of 8 A and 44 A (rated), respectively. The oscilloscope waveforms in Fig. II.3.23 also show the steady state characteristics of the 4-phase interleaved converter connected with the photovoltaic panels (refer to Fig. II.2.23) at different PV current operations. It demonstrates the dc bus voltage, the PV voltage, the PV current, the first, second, third and forth inductor currents. Fig. II.3.23(a) and (b) presents the characteristics at the average PV current of 6 A and 10 A, respectively. One can observe that the FC and PV currents are the sum of the inductor currents and that the source ripple current is 1/N the individual inductor ripple currents. So, the source ripple current of the four-cell interleaved converter is nearly zero. It means that the source mean current is close to the source rms current.

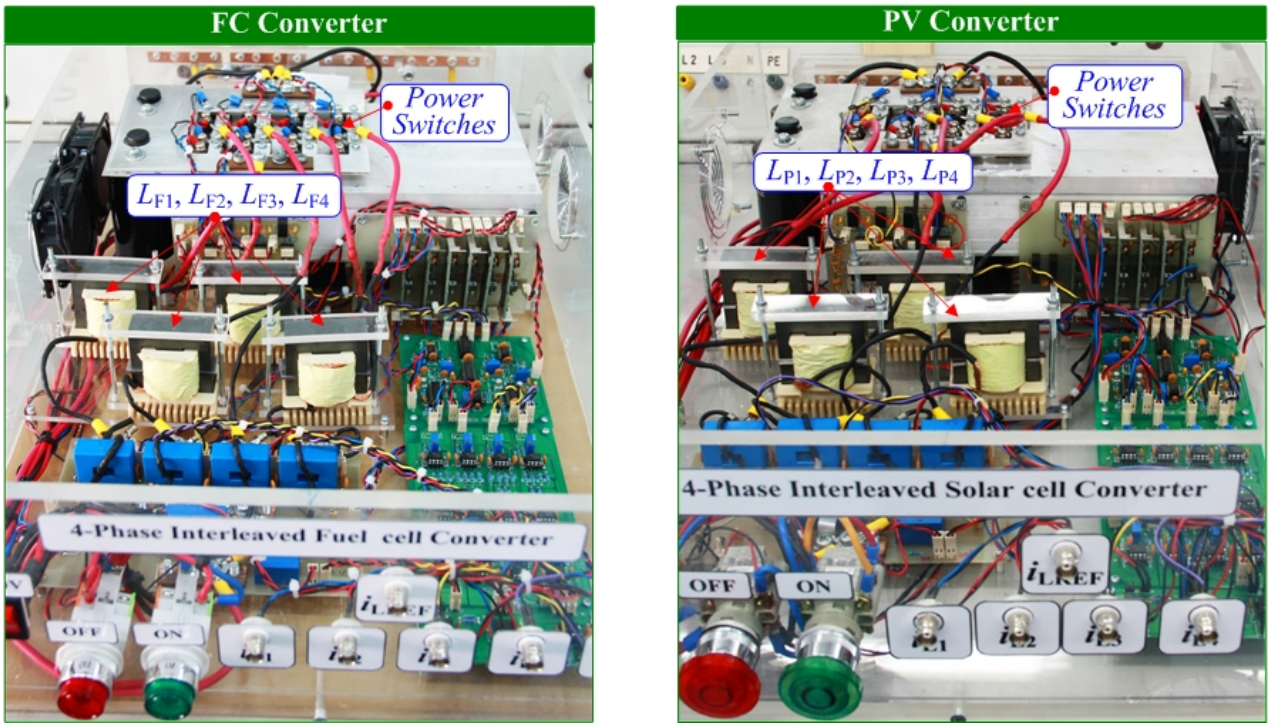

Fig. II.3.21. Photograph of the implemented 4-phase interleaved power converters for an FC and a PV.

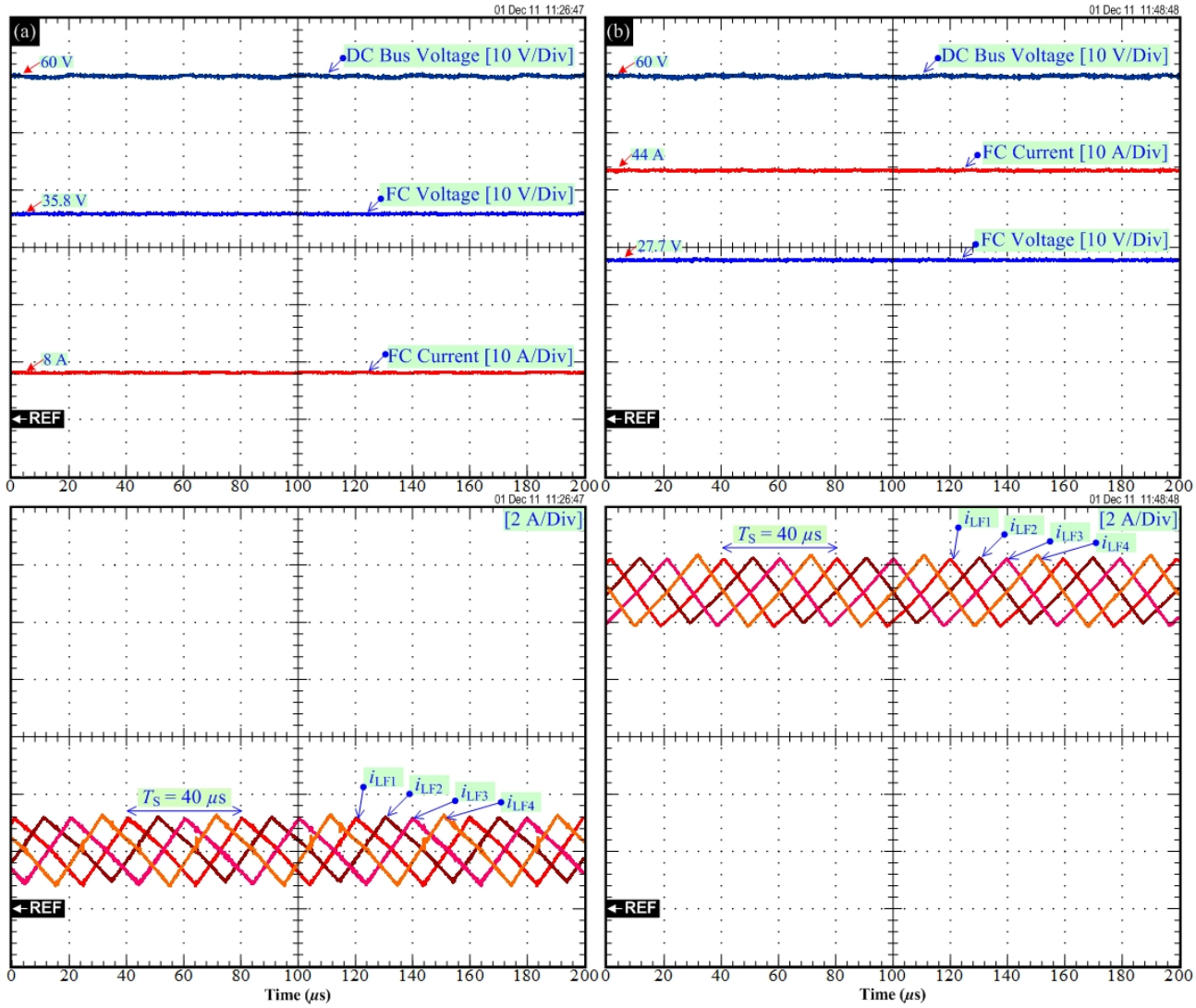

Fig. II.3.22. Experimental Result: steady-state waveforms of the FC interleaved converter system at an FC current of (a) 8 A and (b) 44 A.

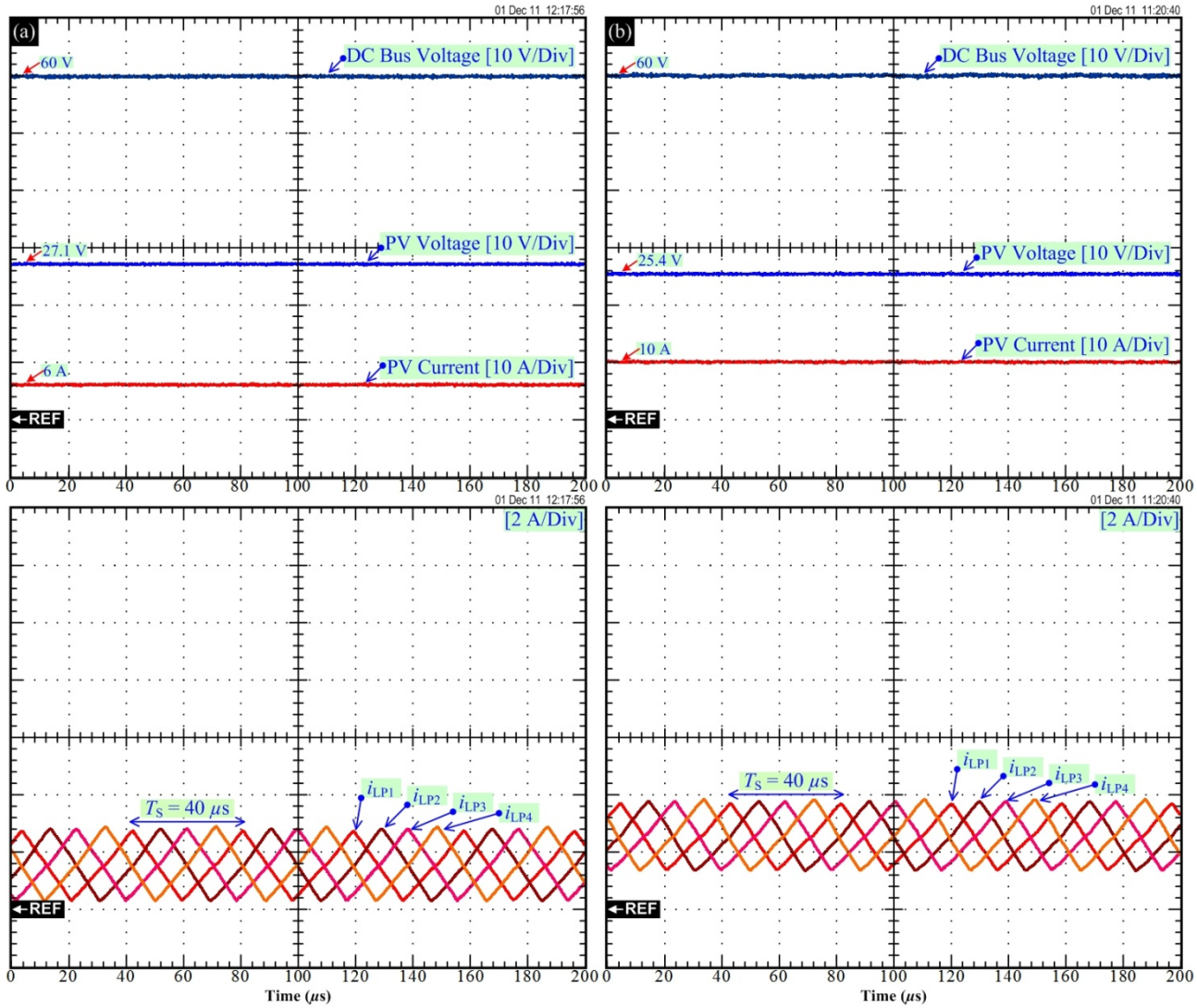

Fig. II.3.23. Experimental Result: steady-state waveforms of the PV interleaved converter system at a PV current of (a) 6 A and (b) 10 A.

Finally, the prototype 4-phase interleaved bidirectional converter for a supercapacitor storage device is shown in Fig. II.3.24. The oscilloscope waveforms in Figs. II.3.25 and II.3.26 portray the steady state characteristics of the 4-phase interleaved converter connected with the Maxwell supercapacitor [100 F, 500 A, and 32 V] (refer to Fig. II.2.33) at different SC current operations. It demonstrates the dc bus voltage, the SC voltage, the SC current, the first, second, third and forth inductor currents. Fig. II.3.25(a) and (b) presents the characteristics at the average SC current of +6 A and +16 A (discharging), respectively; Fig. II.3.26(a) and (b) presents the characteristics at the average SC current of –8 A and –20 A (charging), respectively. One again can observe that the SC current are the sum of the inductor currents. So, the SC ripple current of the four-cell interleaved converter is nearly zero. It means that the SC mean current is close to the SC rms current.

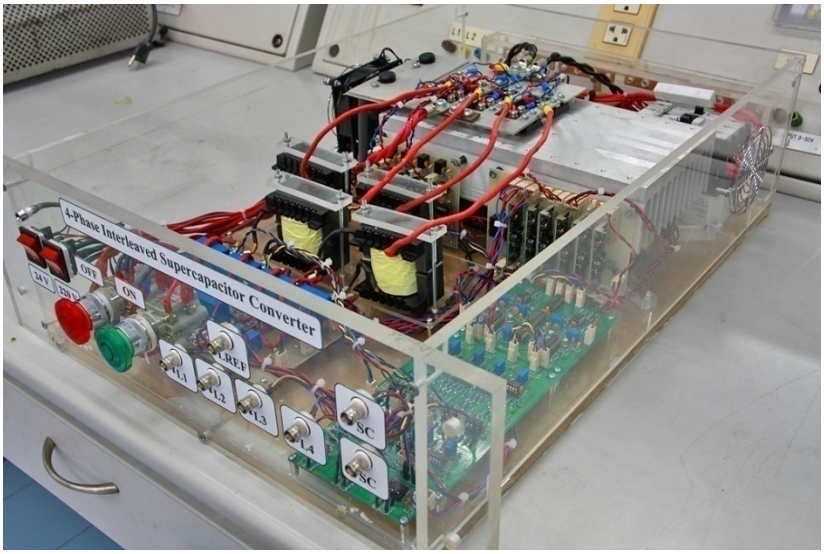

Fig. II.3.24. Photograph of the implemented 4-phase interleaved bidirectional converter for a supercapacitor.

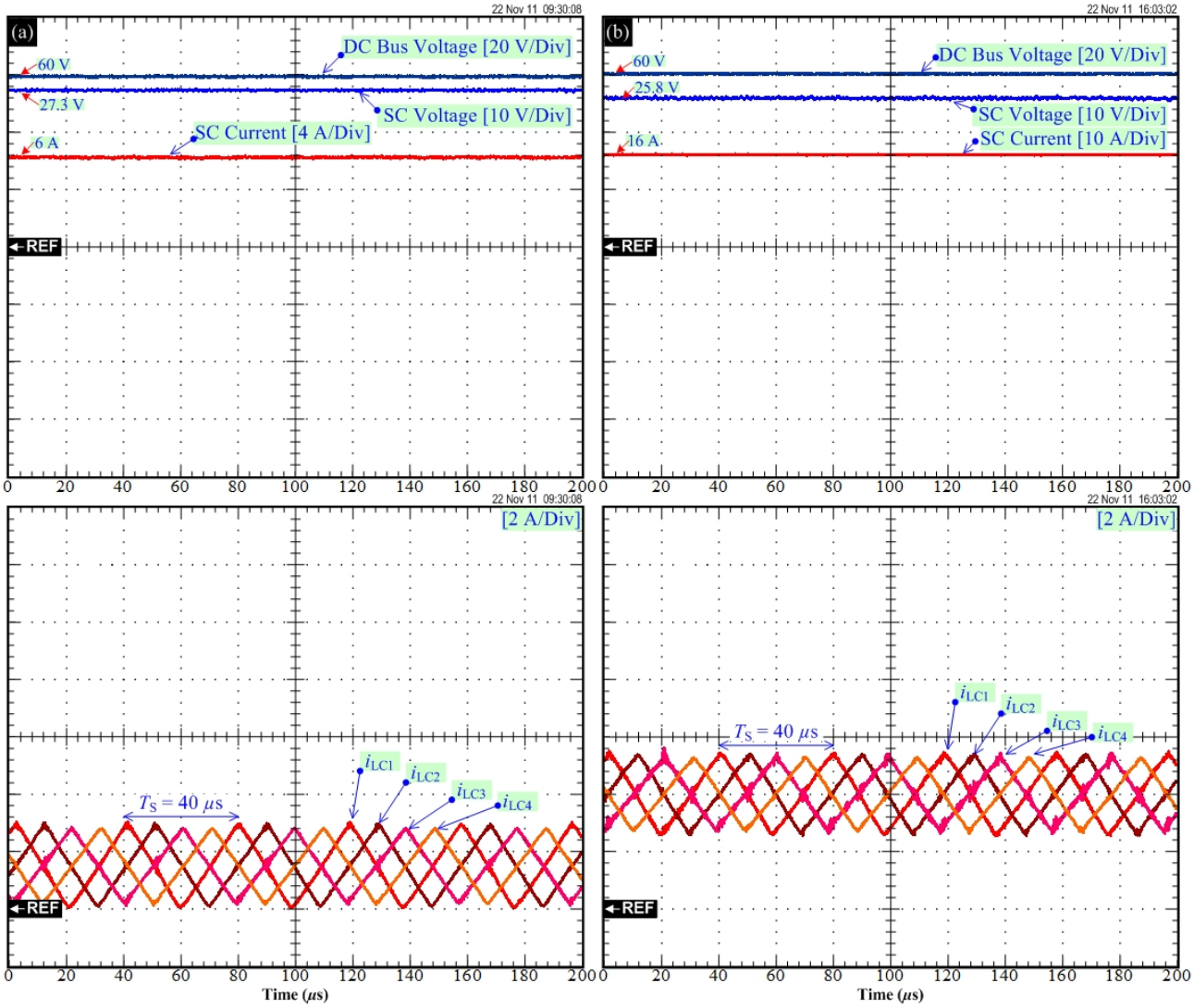

Fig. II.3.25. Experimental Result: steady-state waveforms of the SC interleaved converter system at a SC current of (a) +6 A and (b) +16 A.

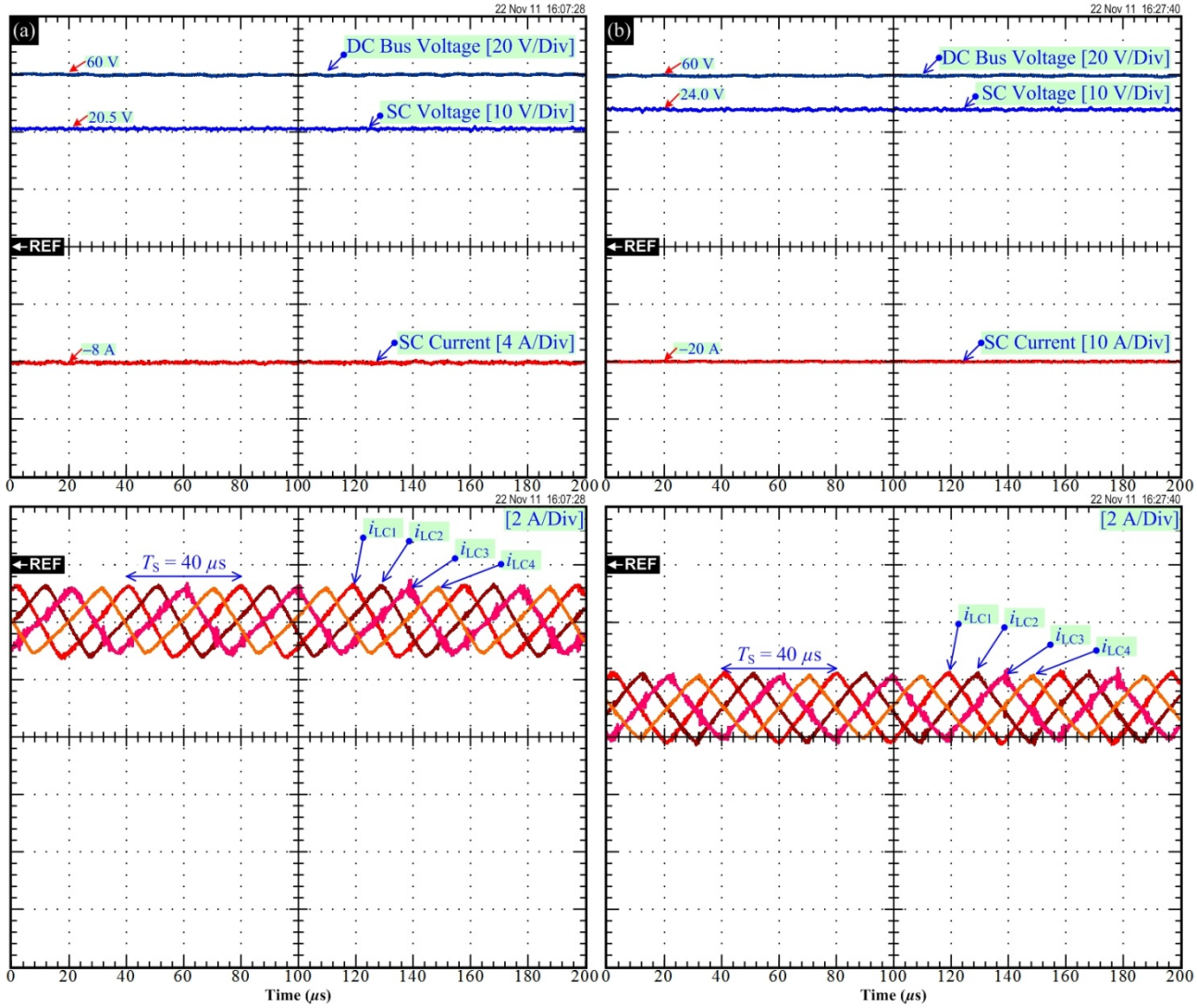

Fig. II.3.26. Experimental Result: steady-state waveforms of the SC interleaved converter system at a SC current of (a) –8 A and (b) –20 A.

To observe the dynamic performance of the SC interleaved 2-quadrant converter, Figs.II.3.27 and 28 present waveforms that are obtained during the large step of the input SC power setpoint. The data show the input SC power reference p_{SCREF}, the input SC power response p_{SC}, the SC voltage v_{SC}, and the SC current i_{SC}. The SC converter interfaces between the 60 V dc bus and the SC bank (100 F, 32 V, see Fig.II.2.33). One can observe the high dynamic response of the SC storage source from –100 W to +100 W in 0.4 ms and –700 W to +700 W in 0.6 ms. Unquestionably, the fast response of SC power source can function with the FC or PV main generator to improve the slow dynamics of the whole system.

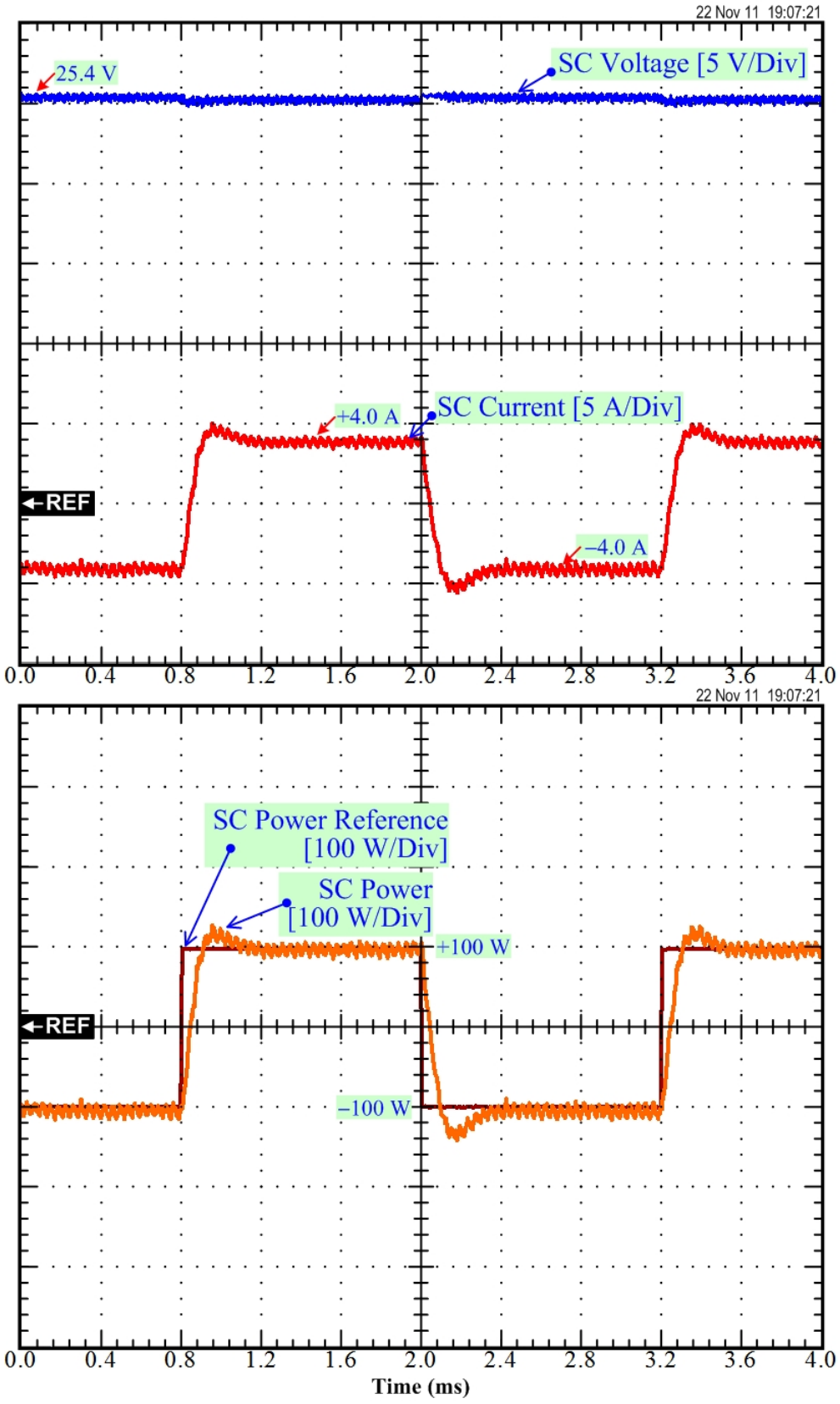

Fig. II.3.27. Experimental Result: Dynamic performance at an input SC power reference p_{SCREF} step from −100 to +100 W and vice versa.

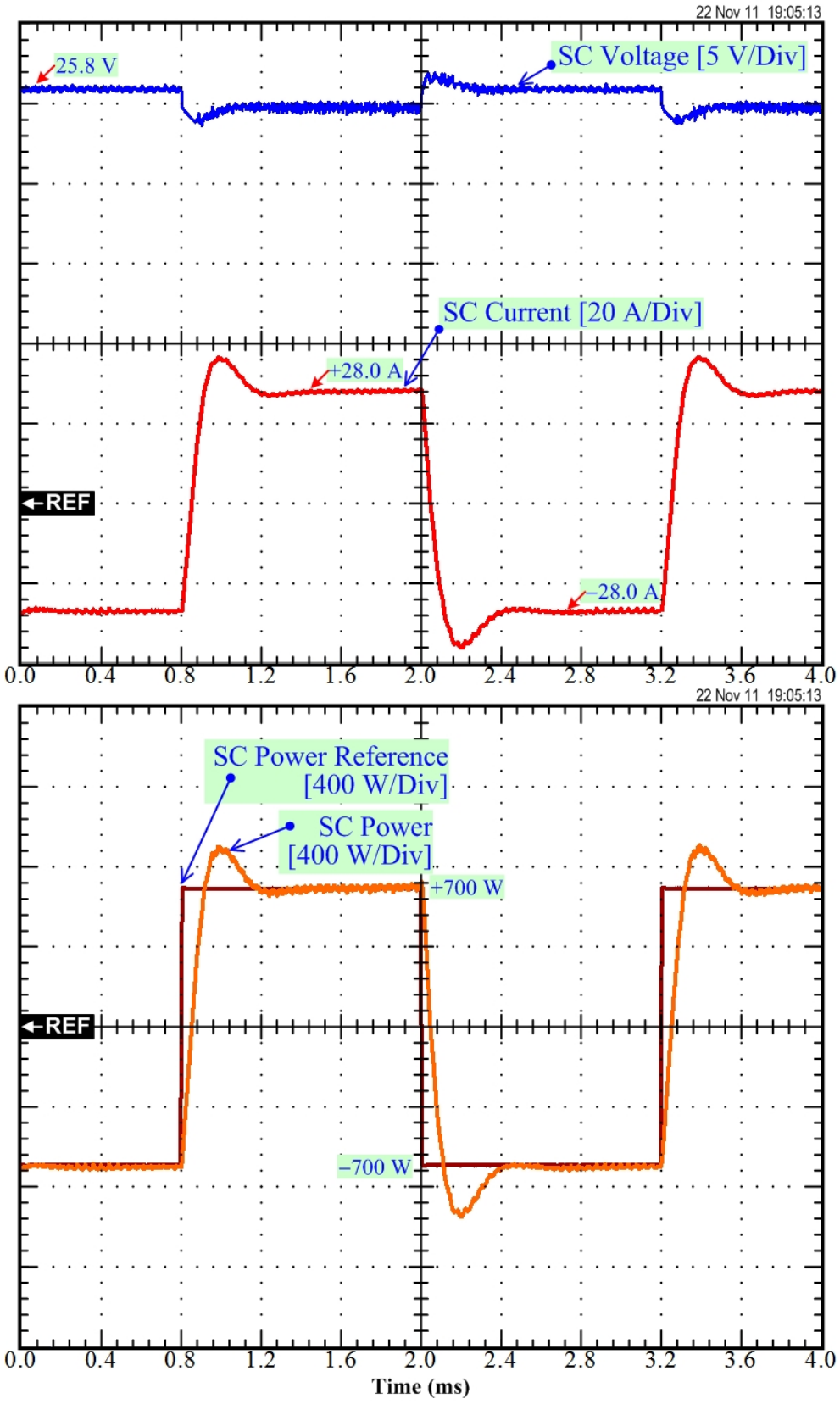

Fig. II.3.28. Experimental Result: Dynamic performance at an input SC power reference p_{SCREF} step from −700 to +700 W and vice versa.

II.3.2.3 Three Level Converter [Tho12a]

Recently, multilevel converters (transformer-less) have been studied for high-power applications due to their ability to meet the increasing demand for power ratings and higher efficiencies when compared with conventional topologies. In particular, multilevel converters for ac/dc and dc/ac conversions [Fig. II.3.29(a)] have been developed for many years [Nab81], [Por06], [Fre10]. Since Nabae *et al*. [Nab81] proposed the topology neutral-point-clamped inverter in 1981, the advantages of multilevel converters have become well-known. Later, Portillo *et al*. [Por06] proposed a three-level, back-to-back power converter for three-phase wind turbine applications, and Freitas *et al*. [Fre10] studied a three-level, three-leg ac–dc–ac converter for single-phase applications.

In this section, a three-level step-up converter that was adapted and modified from the three-level ac/dc converter [transformer-less, see Fig. II.3.29(b)] is proposed to solve the problems associated with the abovementioned modified boost converters. The start-up time of an FC system is typically more than 2 min. The start-up sequence begins with the water circulating pump wetting the FC, the solenoid valve opening to supply fuel (hydrogen), and the blower starting to feed reaction air. Once the open circuit voltage of the FC is verified, the converter can be connected to the FC. This start-up sequence takes approximately 2 min to complete. To avoid start-up problems when the converter is connected to the FC because a high inrush current flows through the inductor L, diode D_1, capacitor C_1, capacitor C_2, and diode D_4, a *soft-start circuit* is proposed, as depicted in Fig. II.3.29(b).

In comparison with a conventional boost converter, this circuit involves more devices, including four power switches (S_1, S_2, S_3, and S_4) and two output capacitors (C_1 and C_2). By cascading the capacitor voltage v_{C1} and the capacitor voltage v_{C2}, a high output voltage v_{Bus} is easily achieved. In addition, there is low voltage stress on the power switch, diode, and output capacitors in comparison with conventional boost converters. Power switches with low voltage ratings are used to reduce the conduction loss, and as a result, the overall efficiency is significantly improved. This allows us to use lower-voltage-rated switches with better switching and conduction performance than the switches rated for the full blocking voltage. Therefore, the converter's overall performance, including the cost and efficiency, can be significantly better than two-level converters, especially when the switching frequency is above 20 kHz or metal–oxide–semiconductor field-effect transistors (MOSFETs) are used.

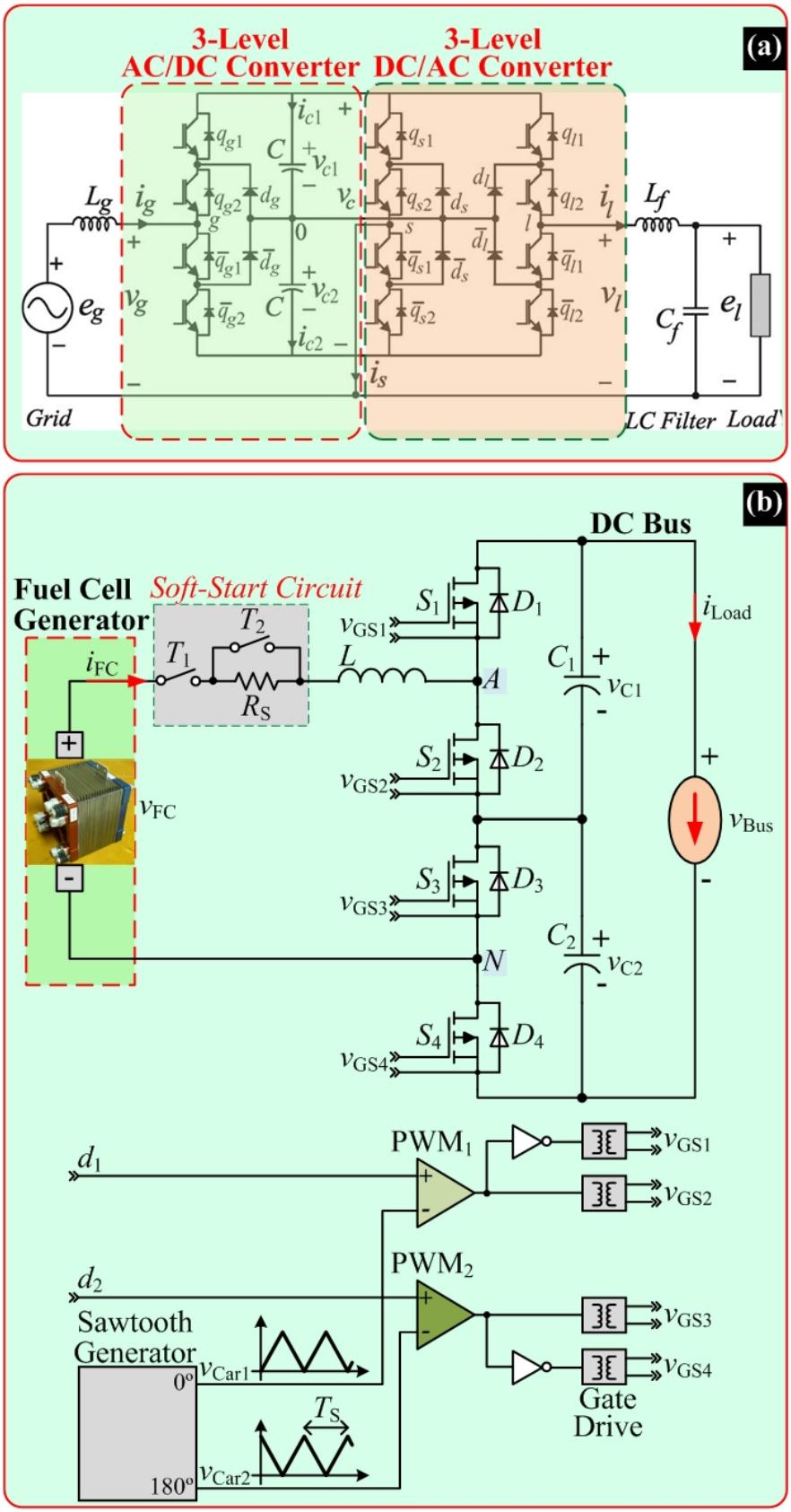

Fig. II.3.29. Three-level converters: (a) ac-dc and dc-ac three-level converter, (b) proposed dc-dc three level boost converter and its switching functions for FC applications, where v_{FC} and i_{FC} are the FC voltage and current, respectively. i_{Load} is the load current. v_{Bus} the dc bus voltage.

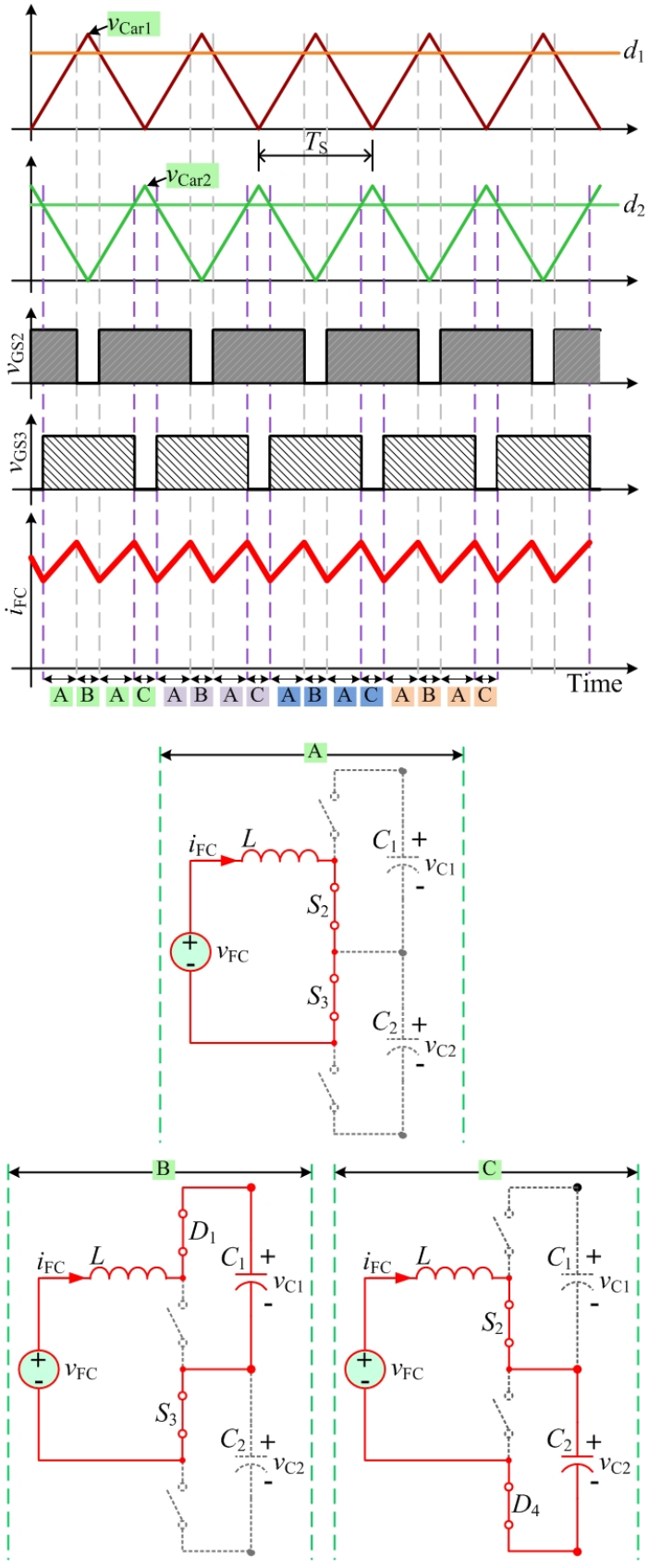

Fig. II.3.30. Key waveforms and operational modes of the three-level boost converter in continuous conduction mode at $d_1 = d_2 = 0.8$.

The switching functions are generated by the pulsewidth modulators PWM_1 and PWM_2, shown in Fig. II.3.30, where T_S is the switching period. The modulation signals d_1 and d_2 (> 0.5) are duty cycles generated by a control circuit (the current control or power control loop presented hereafter). The carrier signals are triangular signals v_{Car1} and v_{Car2} shifted by π (called the interleaving technique) and running at the same switching frequency f_S (= $1/T_S$).

The proposed converter operating in continuous conduction mode (CCM) is considered. According to *Remark 1*, the FC must be operated in CCM with a small ripple current to avoid using an input L-C filter. The switching sequences and key waveforms of the converter in CCM are illustrated in Fig. II.3.30. The output capacitors C_1 and C_2 are assumed to be large enough so that the output voltages v_{C1} and v_{C2} across them are assumed to be constant during the entire switching cycle and become $v_{Bus} = v_{C1} + v_{C2}$.

From the average model of a traditional boost converter [Sha10], the circuit can be described by the following set of equations:

$$L\frac{d\bar{i}_{FC}}{dt} = \bar{v}_{FC} - r_L \cdot \bar{i}_{FC} - (1-d_1)\cdot \bar{v}_{C1} - (1-d_2)\cdot \bar{v}_{C2} \tag{2.28}$$

$$C_1\frac{d\bar{v}_{C1}}{dt} = (1-d_1)\cdot \bar{i}_{FC} - i_{Load} \tag{2.29}$$

$$C_2\frac{d\bar{v}_{C2}}{dt} = (1-d_2)\cdot \bar{i}_{FC} - i_{Load} \tag{2.30}$$

where r_L is the series resistance of inductor L. Note that r_L also represents the static losses in the converter. The filter capacitors are assumed to be identical, i.e., $C_1 = C_2 = C$, and $d_1 = d_2 = d$ and $v_{C1} = v_{C2} = v_{Bus}/2$. From (2.28), the differential equation can be written as follows:

$$L\frac{d\bar{i}_{FC}}{dt} = \bar{v}_{FC} - r_L \cdot \bar{i}_{FC} - (1-d)\cdot \bar{v}_{Bus}\,. \tag{2.31}$$

The input power p_{FC} is given versus v_{FC} and i_{FC} by the following differential equation:

$$\bar{p}_{FC} = \bar{v}_{FC} \cdot \bar{i}_{FC} \tag{2.32}$$

$$\frac{d\bar{p}_{FC}}{dt} = v_{FC}\left.\frac{d\bar{i}_{FC}}{dt}\right|_{\bar{v}_{FC}=\text{Constant}}. \tag{2.33}$$

To regulate an FC current or power based on the flatness principle introduced in Appendix, the FC power p_{FC} is assumed to be the flat output component. Thus, we define a flat output as y =

p_{FC}, a control input variable as $u = d$, and a state variable as $x = i_{FC}$. The state variable x can be written as

$$x = \frac{p_{FC}}{v_{FC}} = \varphi(y). \tag{2.34}$$

From (2.31) and (2.33), the control variable u can be calculated from the flat output y and its time derivative $\dot{y}$, as follows:

$$u = 1 + \left(\dot{y} \cdot \frac{L}{v_{FC}} + r_L \cdot i_{FC} - v_{FC} \right) \cdot \frac{1}{v_{Bus}} = d = \psi(\dot{y}). \tag{2.35}$$

It is clear that $x = \varphi(y)$ and that $u = \psi(\dot{y})$. Consequently, the mathematical model of the converter can be assumed to be a flat system [Zan11], [Sha10].

The input power reference for the converter is represented by y_{REF} (= p_{FCREF}). A linearizing feedback control law that provides exponential asymptotic tracking of the trajectory is given by the following expression [Tho10b], [Tho10c]:

$$(\dot{y} - \dot{y}_{REF}) + K_{11}(y - y_{REF}) + K_{12} \int (y - y_{REF}) d\tau = 0 \tag{2.36}$$

where K_{11} and K_{12} are the controller parameters. Then,

$$\dot{y} = \dot{y}_{REF} + K_{11}(y_{REF} - y) + K_{12} \int (y_{REF} - y) d\tau . \tag{2.37}$$

Inserting the term for $\dot{y}$ from (2.37) into (2.35) gives the equation for the closed-loop static-state feedback duty cycle d (called the *inverse dynamic equation*). Evidently, the control system is stable for $K_{11}, K_{12} > 0$.

The FC power is measured by using (2.32), which is associated with a first-order filter that is used to reduce the harmonics caused by power-electronic switching. Based on the power-electronic constant switching frequency ω_S (PWM) and the cascade control structure, the outer control loop (here, the input power control) must operate at a cutoff frequency $\omega_P << \omega_F$ (the cutoff frequency of the first-order filter) $<< \omega_S$. Once the flat outputs are stabilized, the whole system is exponentially stable because all the variables of the system are expressed in terms of the flat outputs [Tho10c].

Next, voltage balancing controller functions are used to eliminate the difference between the voltages v_{C1} and v_{C2}. The duty cycles d_1 and d_2 are determined as follows:

$$\left.\begin{aligned} d_1 &= d - \vartheta \\ d_2 &= d + \vartheta \end{aligned}\right\} \tag{2.38}$$

where d is the main duty cycle generated by the power controller (refer to (2.35)) and ϑ represents a correction term, which is used to balance the voltages.

A proportional controller is sufficient as long as the gain is high enough to introduce only a small static error. Therefore, voltage balancing control can be expressed by the following function:

$$\vartheta = K_{\mathrm{V}}\left(\frac{v_{\mathrm{Bus}}}{2} - v_{\mathrm{C2}}\right) \tag{2.39}$$

where K_{V} is the controller parameter.

The FC power reference p_{FCREF} must be restricted to an interval with a maximum of p_{FCMax} (corresponding to the rated power of the FC) and a minimum of p_{FCMin} (set to 0 W) and be limited in dynamics; these limitations ensure safe operation of the FC with respect to the constraints that are associated with the FC (i.e., the prevention of fuel starvation in an FC stack [Tho09d], [Tho09f]). Thus, to limit transient FC power, a low-pass filter (second order) is employed such that the power demand p_{FCDEM} from the external loop is always limited (desired trajectory planning) as follows:

$$p_{\mathrm{FCREF}}(t) = p_{\mathrm{FCDEM}}(t)\cdot\left(1 - e^{-\frac{t}{\tau_1}} - \frac{t}{\tau_1}e^{-\frac{t}{\tau_1}}\right) \tag{2.40}$$

where τ_1 is the control parameter. The nonlinear control law based on the differential flatness of the FC power as detailed above is presented in Fig. II.3.31.

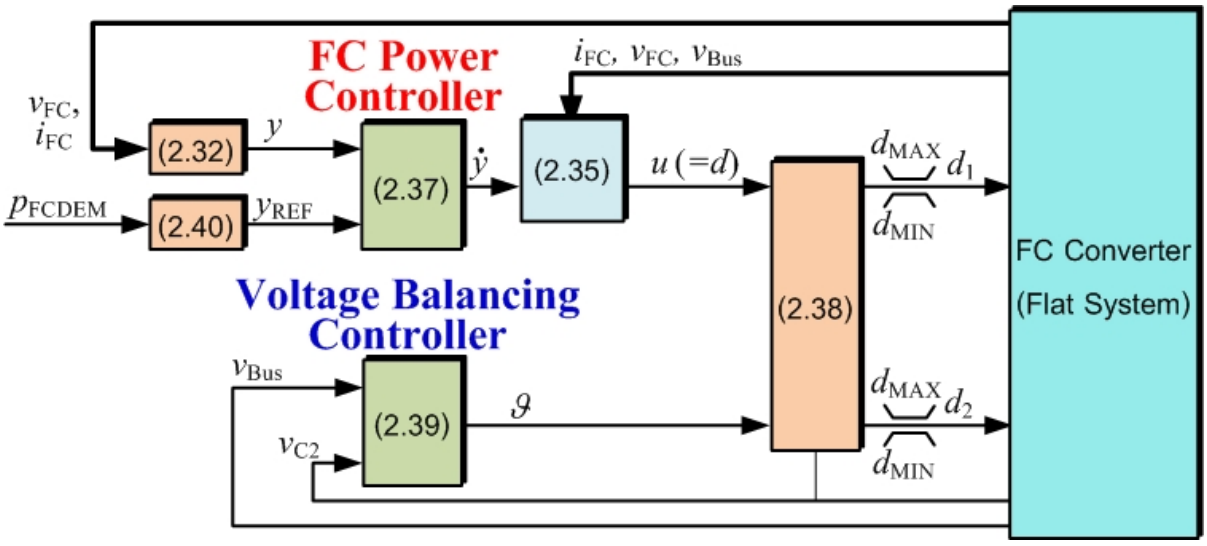

Fig. II.3.31. Proposed FC power control scheme for the three-level converter.

A small-scale test bench was implemented in the laboratory, as presented in Fig. II.3.32. The parameters of the three-level boost converter and the semiconductor components are described in this section. The inductor L is obtained by means of a ferrite core; its inductance is 223 μH, and its series resistance R_{L1} is 0.14 Ω. The capacitors C_1 and C_2 are obtained by means of electrolytic capacitors with capacitances of 1,000 μF each. The switches S_1, S_2, S_3, and S_4 are IRFP2640N power MOSFET transistors (250 V, 38 A).

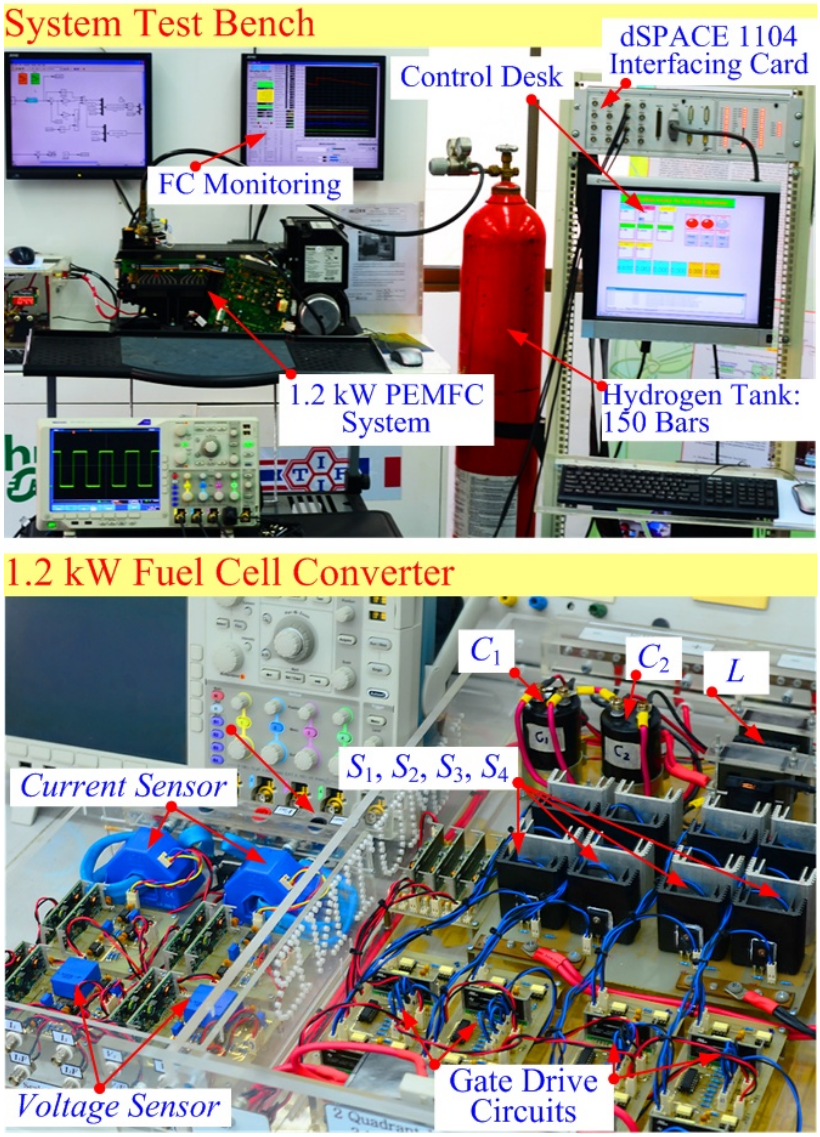

Fig. II.3.32. Test bench system for the three level FC converter.

The FC power control loop, the voltage balancing control, and the PWM generation algorithm were implemented in the mathematical environment of MATLAB–Simulink using a real-time dSPACE DS1104 card (see Fig. II.3.32), the fourth-order *Runge–Kutta* integration algorithm, and a sampling time of 20 μs. The switching frequency f_S was set to 10 kHz.

Measurements of the FC current i_{FC}, the FC voltage v_{FC}, the dc bus voltage v_{Bus}, and the output voltage v_{C2} were collected with zero-flux Hall effect sensors. The nonlinear controller gains used were K_{11} = 141.4 rd·s^{-1} and K_{12} = 10 000 rd^2·s^{-2}. As a result, the cutoff frequency ω_P of the closed-loop FC power was equal to 100 rd·s^{-1}, which is lower than the cutoff frequency ω_F of the measured power filter of 1 000 rd·s^{-1} (T_F = 1 ms), so that the system was exponentially stable. The voltage balancing controller gain was K_V = 0.6. The parameter τ_1 for the FC power dynamic (desired trajectory) was 5 s. This value has experimentally been found to be the highest power slope of our FC system at which no fuel starvation occurs.

To illustrate the switching characteristics of the proposed converter, the oscilloscope waveforms in Fig. II.3.33 show the steady-state waveforms for FC power regulation at the reference power of 500 W. This figure shows the FC voltage v_{FC} (CH1), the FC current i_{FC} (CH2), the gate drive signal for S_2, v_{GS2} (CH3), and the gate drive signal for S_3, v_{GS3} (CH4). The power switching devices, S_2 and S_3 (individual interleaved power stages), operate at 10 kHz, which is the same frequency as the classical boost converter design, but the effective input FC current ripple frequency is 20 kHz; as a result, the FC ripple current is reduced.

The waveforms that were obtained as the FC power reference trajectory p_{FCREF} increased are presented in Fig. II.3.34. The data show the FC power reference trajectory p_{FCREF} (CH1), the measured FC power p_{FC} (CH2), the FC voltage v_{FC} (CH3), and the FC current i_{FC} (CH4). In the initial state, the FC reference power is equal to 200 W, the measured FC power is equal to 200 W, the FC voltage is equal to 36.4 V, and the FC current is equal to 5.5 A. At t = 5 s, the FC power reference trajectory slowly increases to a final constant power of 500 W. The measured FC power follows its reference perfectly, and there is no fuel starvation phenomenon in the FC system because the dynamics of the FC power reference trajectory are limited, as described in (2.40).

Finally, the waveforms obtained as the FC power reference trajectory p_{FCREF} decreased are presented in Fig. II.3.35. The data show the dc bus voltage v_{Bus}, the output capacitor voltage v_{C1}, the output capacitor voltage v_{C2}, the FC power reference trajectory p_{FCREF}, the measured FC power p_{FC}, the FC voltage v_{FC}, and the FC current i_{FC}. In the initial state, the FC power reference is equal to 500 W, the measured FC power is equal to 500 W, the FC voltage is equal to 33.3 V, the FC current is equal to 15.0 A, the dc bus voltage is equal to 118 V, and the output capacitor voltages (v_{C1} and v_{C2}) are equal to 59.0 V. At t = 10 s, the FC power reference trajectory slowly decreases to a final constant power of 200 W. Again, the measured FC power follows its reference perfectly. It shows the behavior of the balancing system associated with the power reference variation for the transient state. This result shows that the voltage balancing control is still efficient for a transient state.

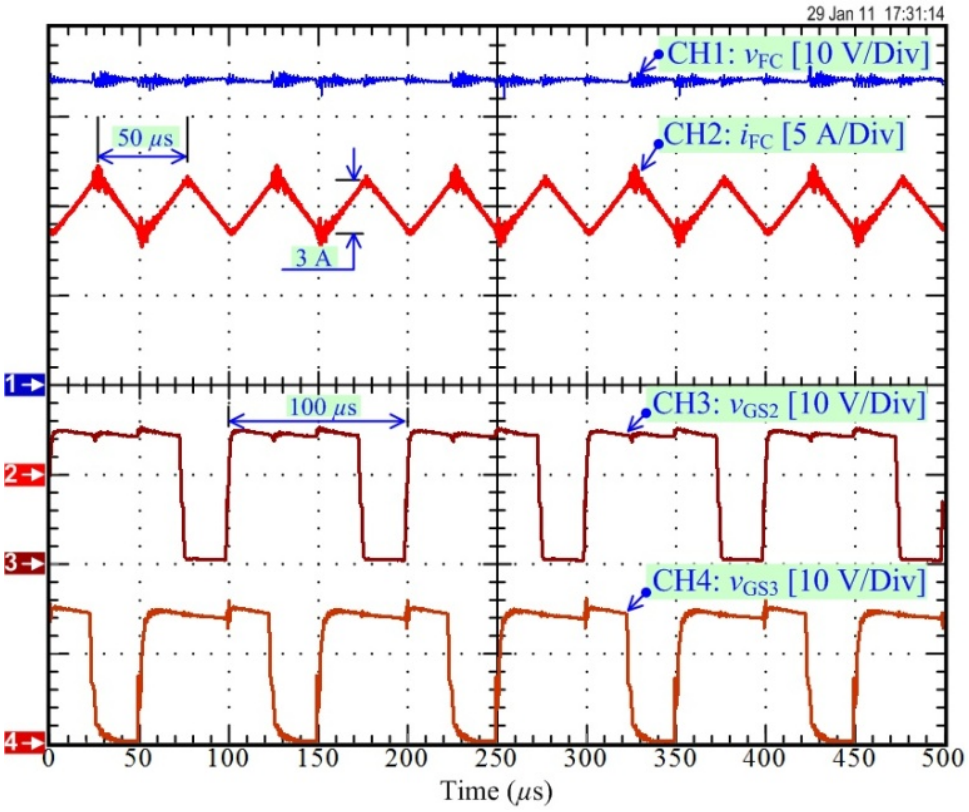

Fig. II.3.33. Experimental results: FC power control characteristics of the prototype system at p_{FCREF} = 500 W, v_{Bus} = 120 V, v_{C1} = 60 V, v_{FC} = 34.0 V, and i_{FC} = 14.7 A.

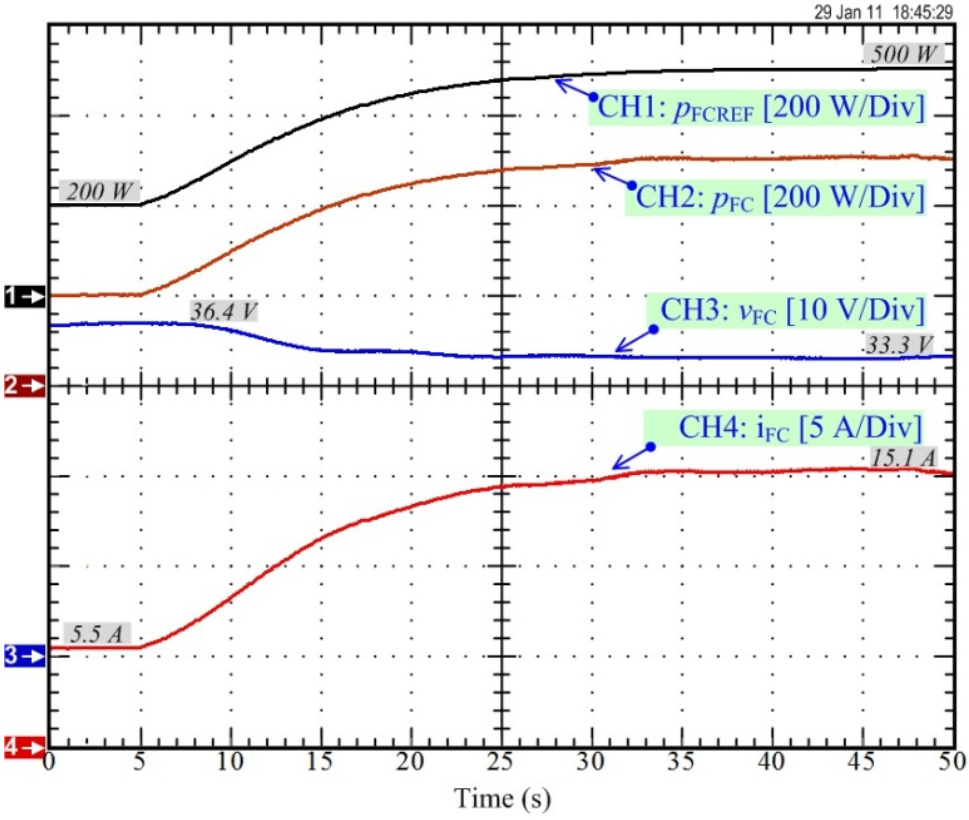

Fig. II.3.34. Experimental results: Converter response during the FC power reference trajectory increases from 200 W to 500 W.

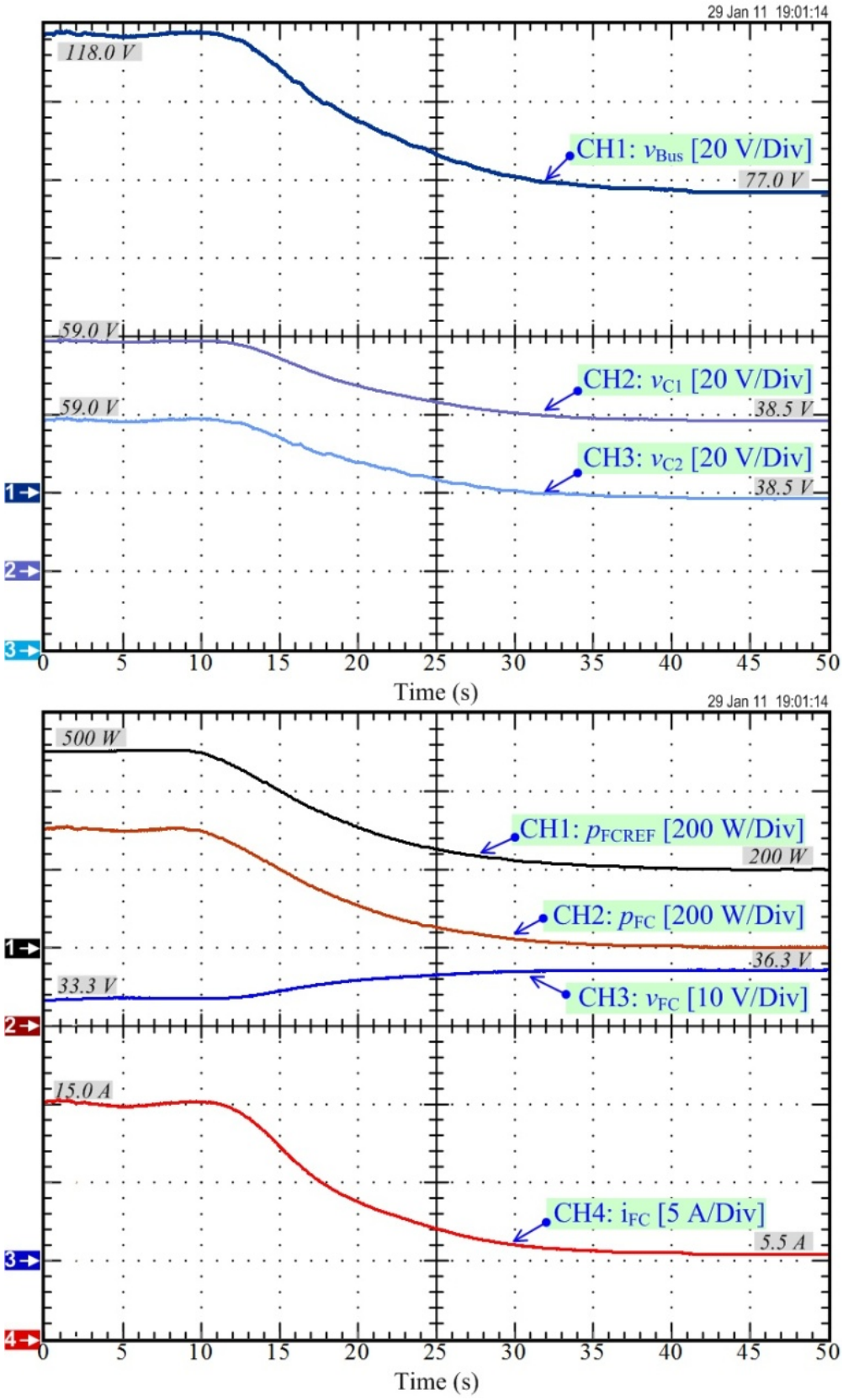

Fig. II.3.35. Experimental results: Converter response during the FC power reference trajectory decreases from 500 W to 200 W.

II.3.3 Hybrid Power Plants

II.3.3.1 Fuel cell/battery hybrid power source [Tho08b]

A. System Description

Refer to Fig. II.3.3. Configuration 1: Single Source/Single Energy Storage Device, a FC/battery hybrid source have operated by connecting batteries directly to a dc link [for example, dc link voltage (battery voltage) of the Honda Hybrid Insight is 144 V] and interfacing FC to dc link by step-up unidirectional converter (Fig. II.3.10) because v_{FC} is normally lower than dc bus voltage. The system detail is displayed in Fig. II.3.36. Note that a resistive brake (R_B) is a protection device to prevent overvoltage at the dc bus.

When an FC operates, its fuel (hydrogen and oxygen) flows are controlled by a "fuel cell processor," which receives current demand. This current demand is the FC current reference i_{FCREF} coming from the hybrid control algorithm detailed hereafter. The fuel flows must be adjusted to match the reactant delivery rate to the usage rate by the FC processor. For this reason, the inner FC current control loop is obligatory and the hybrid control algorithm demands energy from the FC to dc link by generating i_{FCREF} [Tho07], which is sent to the FC processor synchronously (Fig. II.3.36).

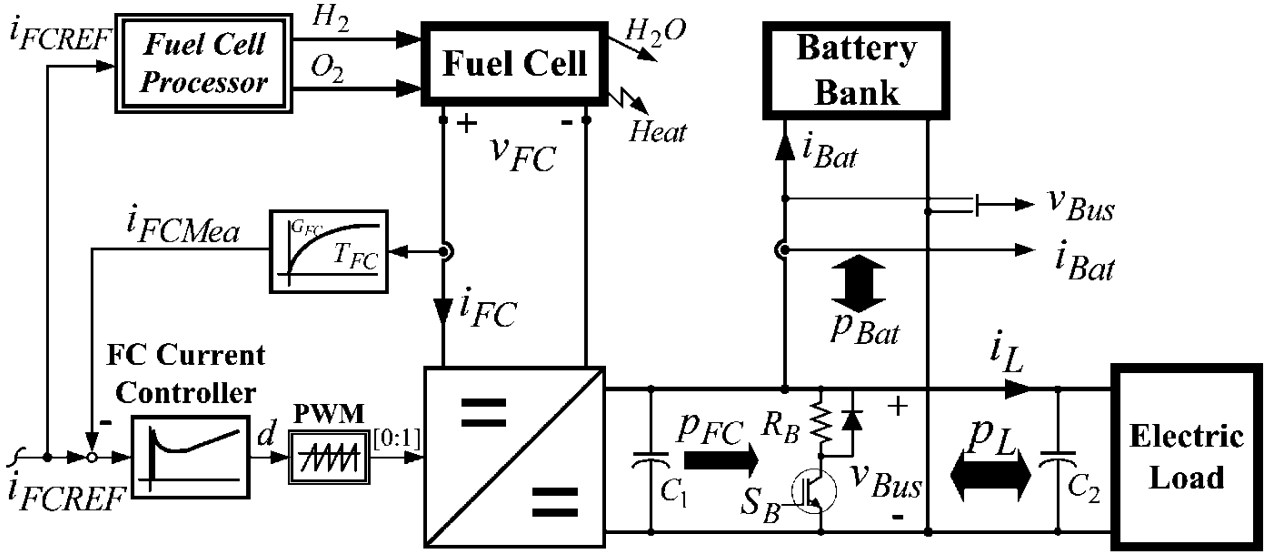

Fig. II.3.36. Structure of FC/battery hybrid power source (p_{FC}, v_{FC} and i_{FC} are the FC power, voltage, and current. Note that it has been assumed that there are no losses in FC converter. p_L , i_L, and p_{Bat} are the load power, current, and the battery power, respectively.

B. Energy Management

To manage energy exchanges between the dc link, the main source, and the storage device, one may define three operating modes (or states):

1) Charge mode: In this, the main source supplies energy to the storage device and to the load.
2) Discharge mode: Here, both the main source and the storage device supply energy to the load.
3) Recovery mode: In this, the load supplies energy to the storage device.

This method has already been investigated earlier, for example, in [Jia05], where an unregulated voltage FC/battery hybrid source was investigated. The problem of such a control strategy is well known. The definition of system states (used state machine) implies control algorithm permutations, which may lead to a phenomenon of chattering when the system is operating near a border between two states.

The proposed control scheme hereafter is not based on a state definition, so that it presents no chattering problem. Rather, one takes advantage of a battery bank, which is directly connected to a dc link for supplying transient energy demand and peak loads required during motor acceleration and deceleration, as if this device is a standard power supply. In addition, the FC, as a slow dynamic device, functions to supply energy to a battery bank in order to keep it charged, although it is evidently the main power energy source of the system.

The proposed control strategy is a cascade control structure composed of three loops. The outer loop is the battery SOC controller that links the battery SOC to the battery charging reference current i_{BatREF}. The middle loop controls the battery charging current and links i_{BatREF} to the FC current reference i_{FCREF}. The inner loop is the FC current control, already explained in the previous section.

C. Performance Validation

1) Test Bench Description

The small-scale test bench is presented in Fig. II.3.37. The storage device is obtained by means of four aged lead-acid batteries 7.78 Ah (33 Ah at name plate), 12 V connected in series. The PEMFC system (Fig. II.2.3) was constructed by the ZSW company. It is composed of 23 cells of

100 cm^2 in series. It is supplied with pure hydrogen from bottles under pressure and with clean, dry air from a compressor.

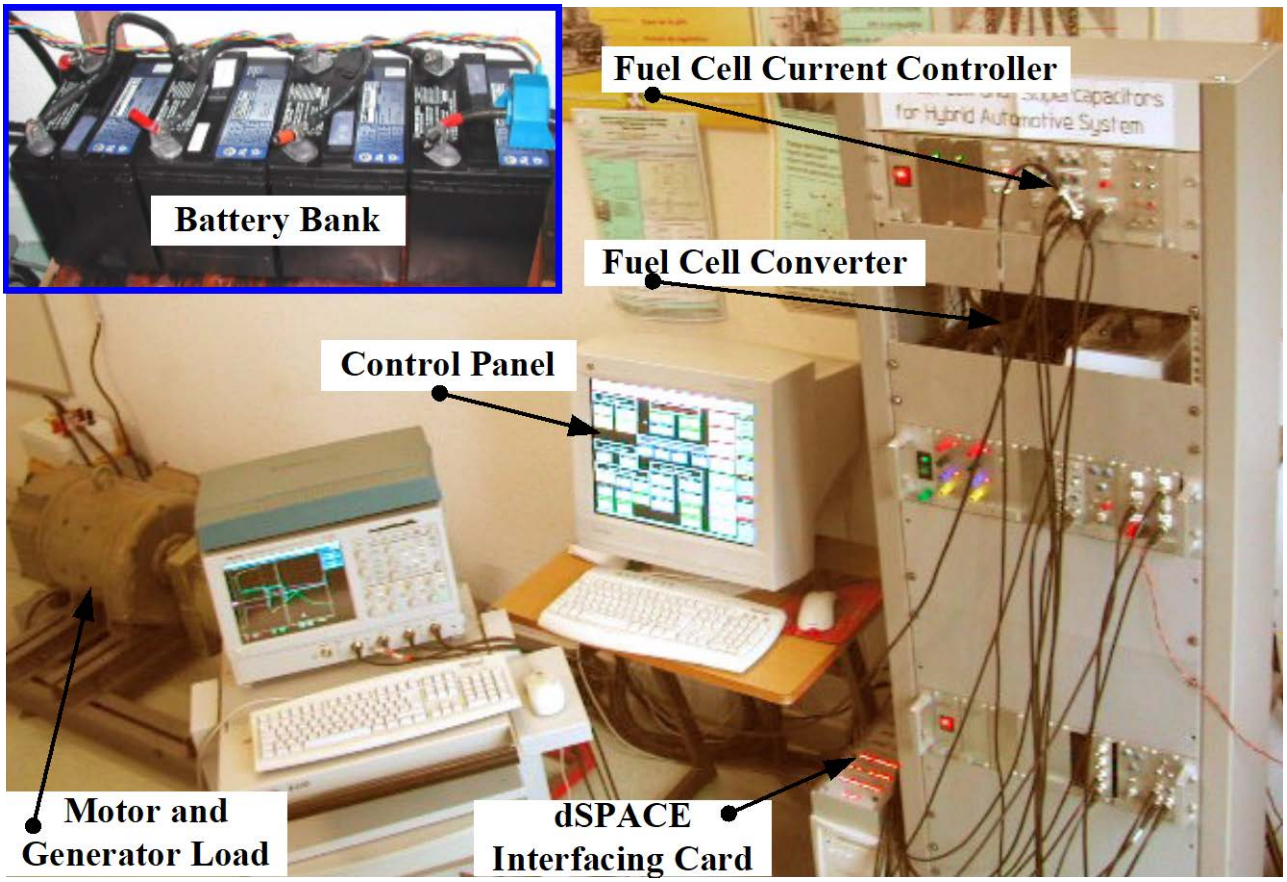

Fig. II.3.37. Hybrid source test bench.

2) Control Description

The measurements of the FC current i_{FC}, the battery current i_{Bat}, and the dc link voltage v_{Bus} are realized by means of zero-flux Hall effect sensors. The parameters associated with the battery *SOC* regulation loop can be seen in Table II.3.1. The parameters associated with the battery current control loop are detailed in Table II.3.2. The FC current absolute slope limitation (G_{SL}) is set to 4 $A \cdot s^{-1}$. This value has been experimentally determined as the highest current slope of this FC system, where no fuel starvation occurs.

The battery current control loop, which generates i_{FCREF}, has been implemented in the real time card dSPACE DS1104, through the mathematical environment of Matlab–Simulink, with a sampling frequency of 25 kHz. The ControlDesk software enables changes in the parameters of the control loops. It is employed to maneuver a dc motor drive as well.

TABLE II.3.1 BATTERY SOC REGULATION LOOP PARAMETERS

$SOCREF$	Q_{Bat}	I_{Batmax}	ΔSOC	V_{Busmax}	ΔV_{Bus}	G_{SOC}
100%	7.78 Ah	6 A	1%	61 V	2 V	6

TABLE II.3.2 BATTERY CURRENT REGULATION LOOP PARAMETERS

G_{SL}	I_{FCmax}	I_{FCmin}	G_{iBat}	G_{Bat}	T_{Bat}
4 $A.s^{-1}$	40 A	0 A	30	1	31.8 ms

3) Test Bench Results

The experimental tests shown below were carried out by connecting the dc link to an active load composed of a two-quadrant converter, loaded by a dc motor coupled with a dc generator. A motor functions with the cascade current–speed control method. A hysteresis and PI controller are selected for the motor current and speed loops, respectively, with a current limitation at ±60 A. Figs. II.3.38 and II.3.39 present waveforms obtained at the motor start: the dc bus and FC voltages, motor speed, FC, battery and load (motor) powers, FC, battery and motor currents and battery *SOC*. The initial state is zero for both the FC and battery currents and, 100% for the battery *SOC*.

In Fig. II.3.38, the final motor speed is 600 r/min, so that the final FC current is less than $I_{FCRated}$. One can observe the following:

- The battery supplies most of the power required during motor acceleration.
- The peak load power required during the motor start is about 320 W and the steady state load power is about 300 W, entirely supplied by the FC.
- The FC current increases with a limited slope, up to a level lower than 40 A.
- Simultaneously, the battery current, after a sharp increase during motor acceleration, decreases slowly to zero.
- The final battery *SOC* is lower than 100%, because of a small static error introduced by a P corrector of the battery SOC control loop.

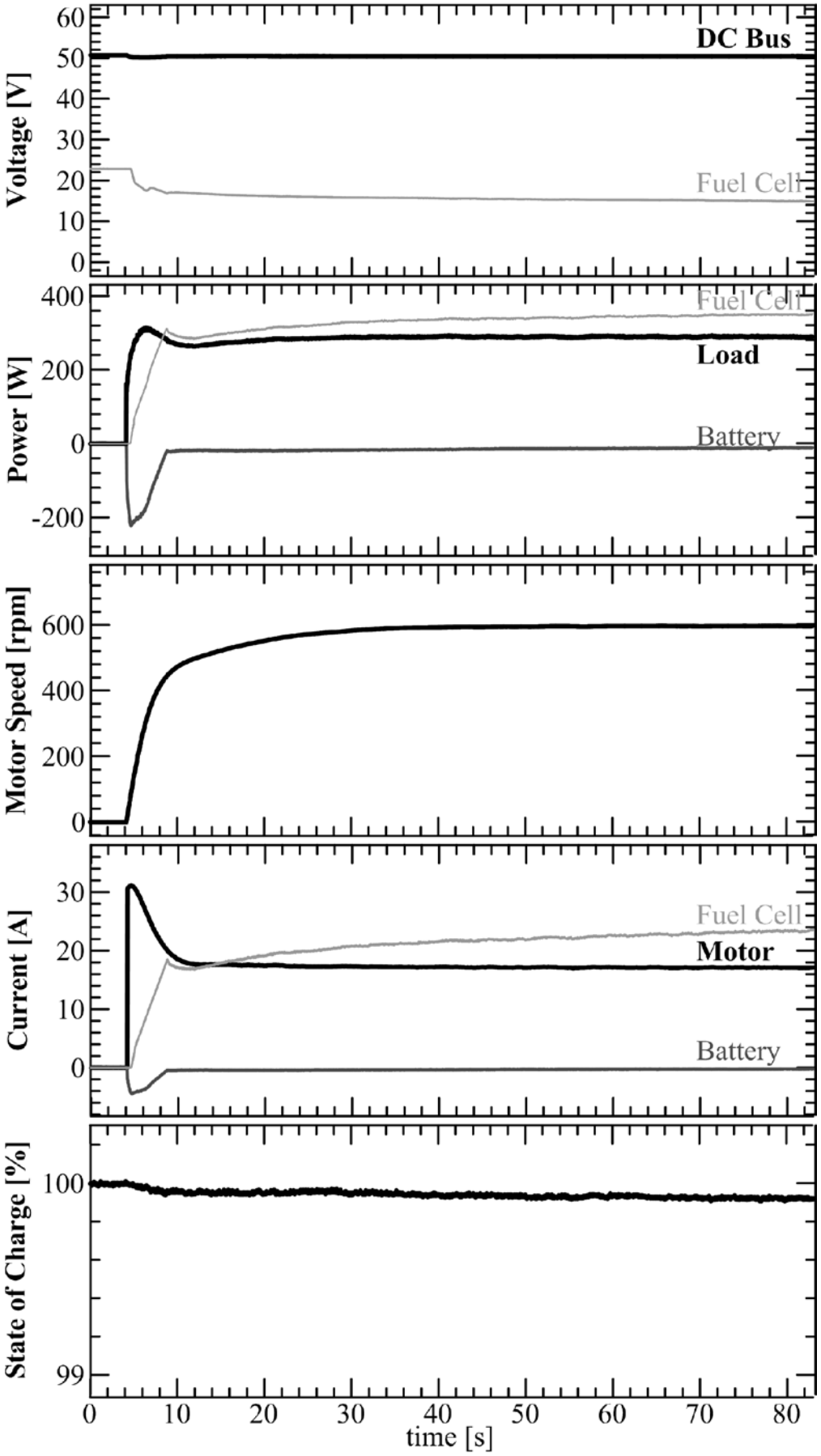

Fig. II.3.38. Experimental Result: Hybrid source response during starting motor to 600 r/min.

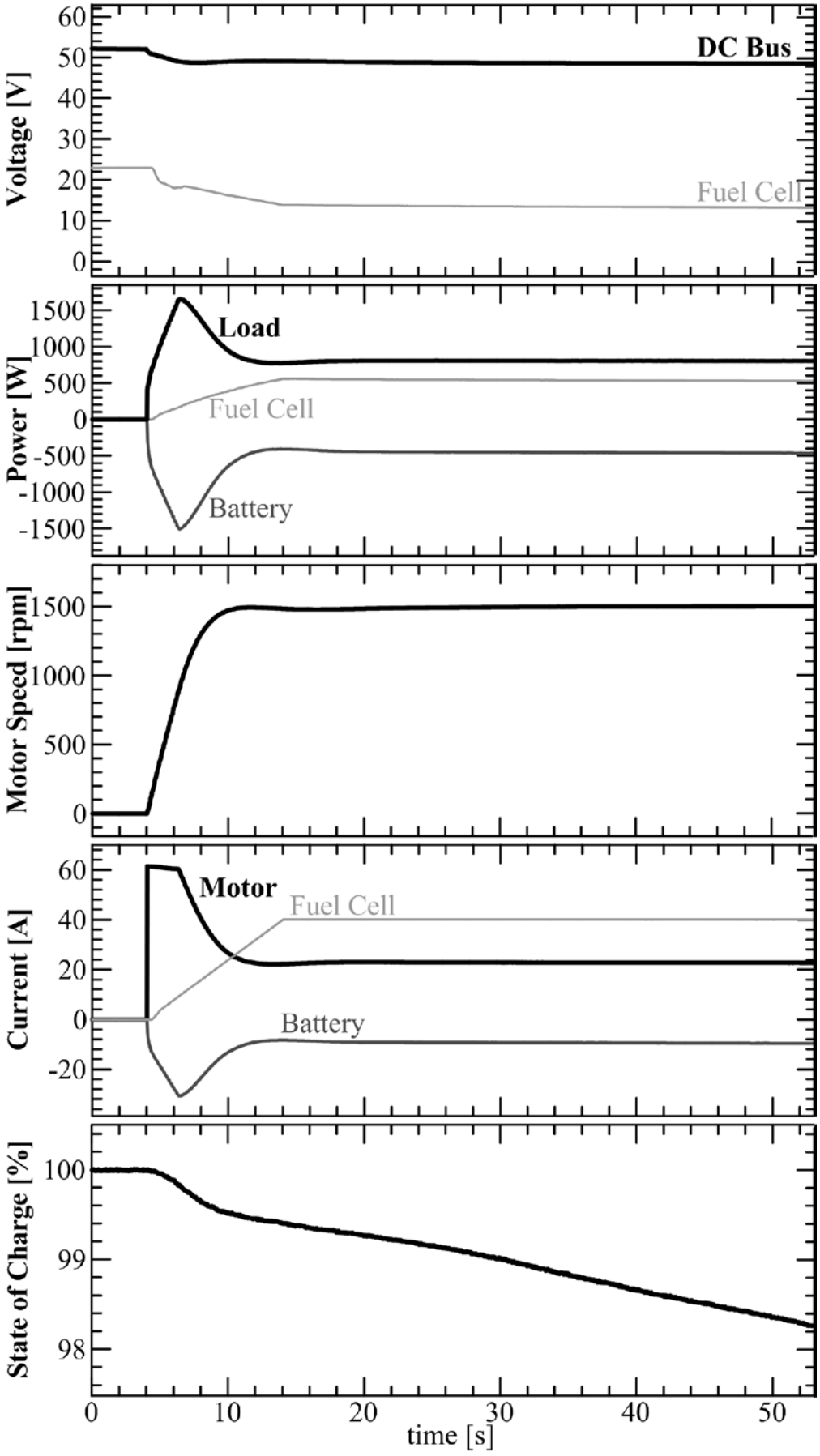

Fig. II.3.39. Experimental Result: Hybrid source response during starting motor to 1 500 r/min.

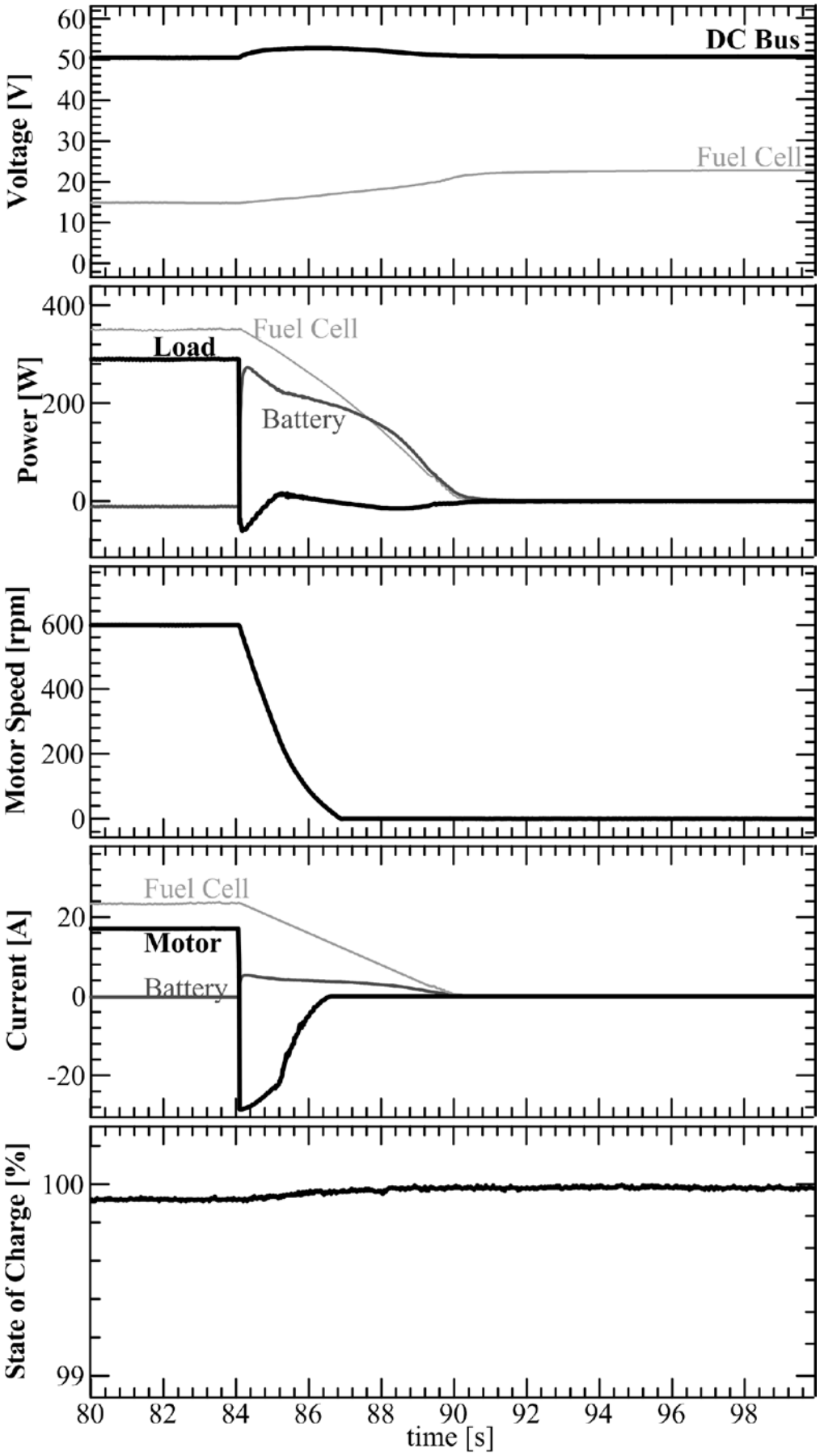

Fig. II.3.40. Experimental Result: Hybrid source response during braking motor from 600 r/min.

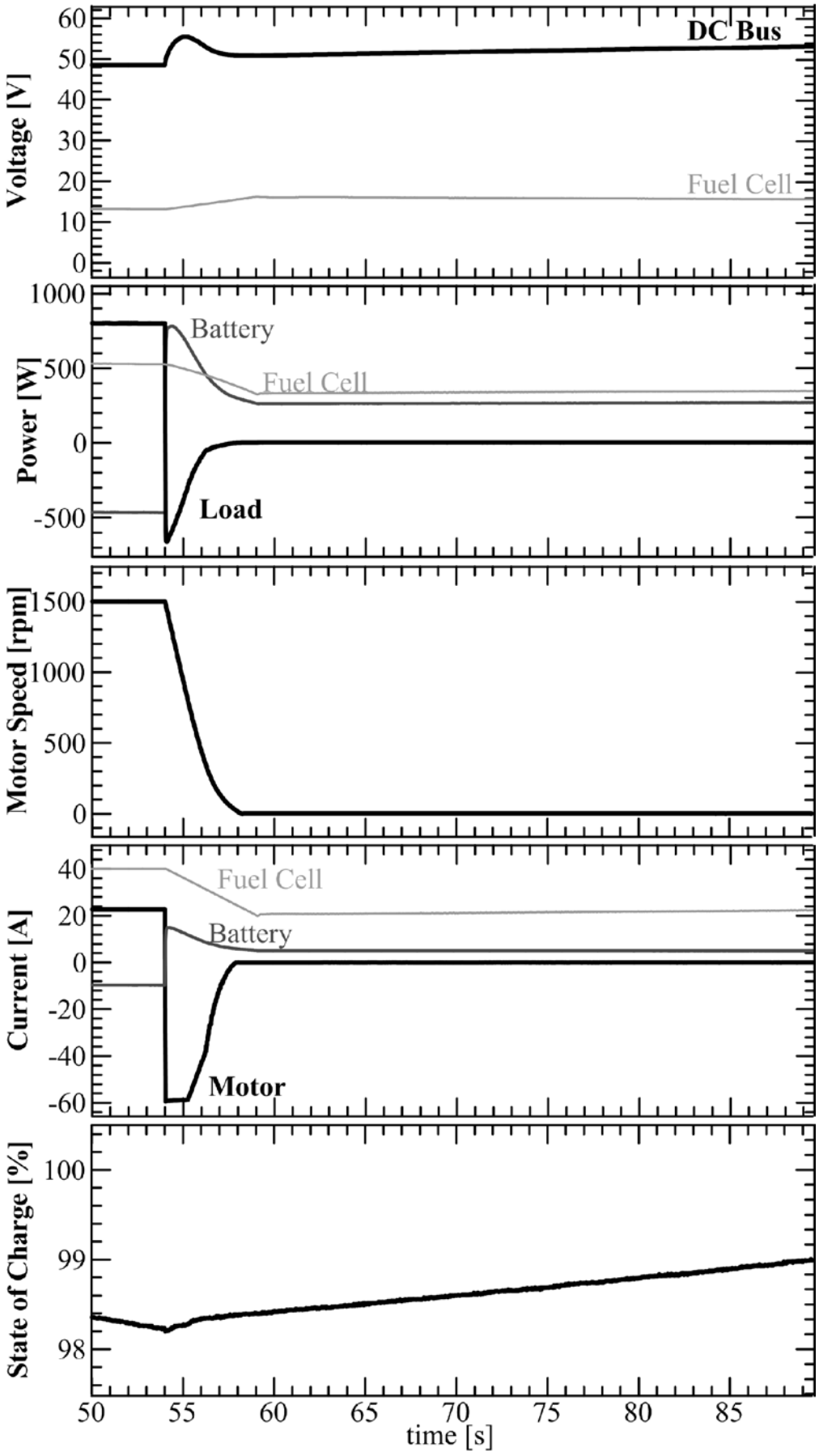

Fig. II.3.41. Experimental Result: Hybrid source response during braking motor from 1 500 r/min.

In the case of Fig. II.3.39, the final motor speed is 1 500 r/min, such that the final FC current is $I_{FCRated}$. Thus, the battery, which once again supplies most of the power required during motor acceleration, remains in a discharge state after the motor start. The final battery current is−10 A, because the steady-state load power (approximately 800 W) is greater than the FC rated power (500 W). Note that the FC current increases up to 40 A in 10 s (one can calculate, here, the slope limitation of 4 $A \cdot s^{-1}$) and the peak load power is about 1.7 kW, which is around three times that of the FC rated power.

Fig. II.3.40 presents waveforms obtained when reducing the motor speed to stop from 600 r/min. The initial state is zero for the battery current and nearly 100% for the battery *SOC*. The total load power for driving the motor is supplied solely by the FC. The final state is zero for the FC, battery and motor currents and 100% for the battery SOC. This shows that the battery, first, recovers the power supplied to the dc link by the FC and by the motor (a motor current is negative, known as a regenerative braking energy), and then, the battery is slightly charged by the FC up to 100%. The FC current immediately decreases with a limited slope, and in a second phase (the end of charging of the battery), slowly decreases to zero. The peak load power during motor brake is about −100 W, automatically recovered by the battery due to the connection at the directly dc link.

Finally, Fig. II.3.41 illustrates waveforms obtained when reducing the motor speed to stop from 1 500 r/min with a peak load power of about –700 W. The battery is more deeply charged than in the previous case, demonstrating the three phases:

- First, the battery recovers the power supplied to the dc link by the FC and the motor.
- Second, the battery recovers the reduced power supplied to the dc link by only the FC.
- Third, the battery is charged at a constant current by the FC.

During the first and second phases, the FC current reduces from a rated current 40 A with a constant slope 4 $A \cdot s^{-1}$. In the third phase, the FC current is nearly constant at around 22 A, to charge the battery at a maximum battery current (I_{Batmax}) around 6 A. After that, both the FC and battery current will reduce to zero when *SOC* will reach SOC_{REF}.

D. Conclusion

The main objective of this section is to propose a new control scheme for a hybrid power source supplied by a battery bank associated with a PEMFC, in order to manage the energy transfer from an FC to the dc link in high dynamic applications, especially for future electric vehicles. The important point here is to show the slow dynamics of the FC system because of mechanical delays. Hence, the control principle presents how to avoid the fast transition of the FC current, in order to prevent fuel starvation problems by controlling the FC current slope, and then, reducing mechanical stresses in the FC system (fuel pressure, water pressure in tubes, and stack). Experimental results, with small-scale devices of a 500 W, 40-A PEMFC and a 48 V, 33 Ah battery bank, authenticate the excellent performances of the proposed control algorithm during motor drive cycles.

II.3.3.2 Fuel cell/supercapacitor hybrid power source [Tho10b].

Refer to Fig. II.3.4. Configuration 2: Single Source/Single Energy Storage Device, one proposes a power electronics topology for the hybrid power-management system, as shown in Fig. II.3.42, in which multiphase dc/dc converters are connected at the output of the stack and the storage device, which are then connected in parallel to share the load at the dc bus. The number of parallel converter modules N (with interleaving switching technique) would depend upon the rated power of the stack and the supercapacitor module. Here, N is equal to 2 for the FC and supercapacitor converters (called two-phase converters).

This section presents the original control method based on the flatness properties for the FC/Supercapacitor hybrid power source. It will provide a significant contribution to the field of the multisource system, particularly in nonlinear power electronics applications.

For safety and high dynamics, the FC and supercapacitor converters are mostly controlled by inner current regulation loops, classically [Jia08]. The current controls of these converters are similar to a basic current control of parallel converters. Here, sliding-mode current control is implemented for each converter module. The dynamics of the current regulation loops are also supposed to be much faster than those of the outer control loops. These current control loops are supplied by two reference signals:

1) the supercapacitor current reference i_{SCREF} and

2) the FC current reference i_{FCREF}, generated by the energy-management algorithm presented hereafter.

Thus, the currents i_{SC} and i_{FC} are considered to follow their references i_{SCREF} and i_{FCREF} completely [Tel09].

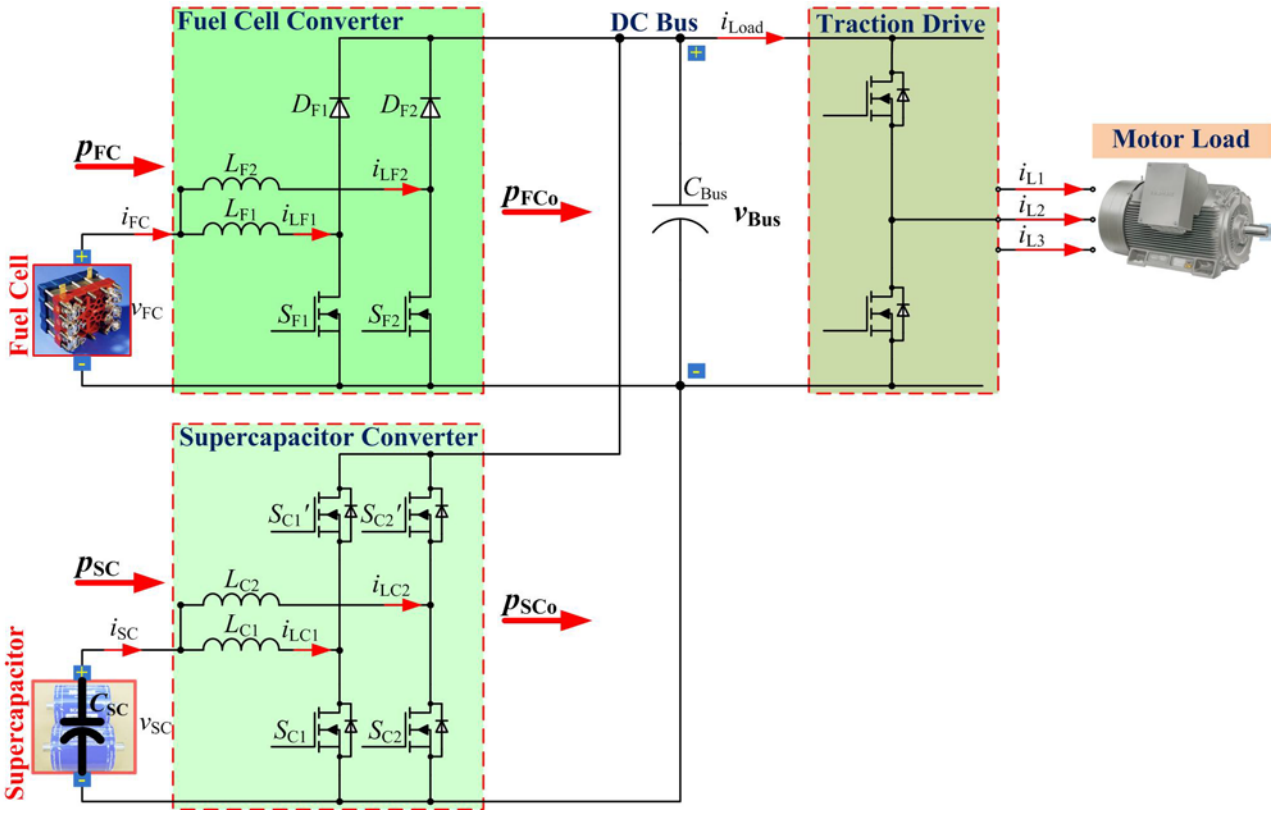

Fig. II.3.42. Topology of a multiconverter-based hybrid power-management system, where p_{Load} (= v_{Bus} × i_{Load}), v_{Bus}, and i_{Load} are the load power, the dc-bus voltage, and the dc-bus load current, respectively. p_{FC} (= v_{FC} × i_{FC}), v_{FC}, and i_{FC} are the FC power, voltage, and current, respectively. p_{SC} (= v_{SC} × i_{SC}), v_{SC}, and i_{SC} are the supercapacitor power, voltage, and current, respectively. p_{FCo} and p_{SCo} are the output powers to the dc link from the converters of FC and supercapacitor, respectively.

A. Modeling of the Hybrid Power Source

One supposes that the FC and supercapacitor currents follow their set-point values perfectly. Thus

$$i_{FC} = i_{FCREF} = \frac{p_{FC}}{v_{FC}} = \frac{p_{FCREF}}{v_{FC}} \tag{2.41}$$

$$i_{SC} = i_{SCREF} = \frac{p_{SC}}{v_{SC}} = \frac{p_{SCREF}}{v_{SC}} \tag{2.42}$$

Now, the FC generator and the supercapacitor storage device function as controlled current sources. We consider here that there are only static losses in these converters (called reduced order

model, see Fig. II.3.48), and r_{FC} and r_{SC} represent the static losses in the FC and supercapacitor converters (refer to Fig. II.3.46), respectively.

The dc-bus capacitive energy y_{Bus} and the supercapacitive energy y_{SC} can be written as

$$y_{Bus} = \frac{1}{2} C_{Bus} v_{Bus}^2 \tag{2.43}$$

$$y_{SC} = \frac{1}{2} C_{SC} v_{SC}^2 \tag{2.44}$$

The total electrostatic energy y_T stored in the dc-bus capacitor C_{Bus} and in the supercapacitor C_{SC} can also be written as

$$y_T = \frac{1}{2} C_{Bus} v_{Bus}^2 + \frac{1}{2} C_{SC} v_{SC}^2 \tag{2.45}$$

The dc-bus capacitive energy y_{Bus} is given versus p_{FCo}, p_{SCo}, and p_{Load} by the following differential equation:

$$\dot{y}_{Bus} = p_{FCo} + p_{SCo} - p_{Load} \tag{2.46}$$

where

$$p_{FCo} = p_{FC} - r_{FC}\left(\frac{p_{FC}}{v_{FC}}\right)^2 \tag{2.47}$$

$$p_{SCo} = p_{SC} - r_{SC}\left(\frac{p_{SC}}{v_{SC}}\right)^2 \tag{2.48}$$

$$p_{Load} = v_{Bus} \cdot i_{Load} = \sqrt{\frac{2y_{Bus}}{C_{Bus}}} \cdot i_{Load} \tag{2.49}$$

$$p_{SC} = v_{SC} \cdot i_{SC} = \sqrt{\frac{2y_{SC}}{C_{SC}}} \cdot i_{SC}. \tag{2.50}$$

B. Energy Management and Control Laws

As mentioned earlier, one must operate an FC at slow dynamics to improve its stack lifetime. Then, it can be compensated by faster dynamics from storage devices. The FC generator is

controlled as a lower dynamic power source. The supercapacitor is a higher dynamic power source, which provides the microcycles and the fast dynamic power supply.

In this kind of system, as depicted in Fig. II.3.42, there are two voltage variables or two energy variables to be regulated.

1) The dc-bus energy y_{Bus} is the most important variable.

2) It is the supercapacitor storage energy y_{SC} (charging supercapacitor).

Therefore, the proposed hybrid energy management is that its basic principle lies in using the supercapacitors (the faster energy source) to supply the energy required to achieve dc-bus voltage regulation (or dc-bus energy regulation) [Tho07]. Then, the FC, although obviously the main energy source of the system, functions as the generator (with dynamic limitations) that supplies energy for both the dc-bus capacitor C_{Bus} and the supercapacitors C_{SC} to keep them charged.

1) DC-Bus Energy Regulation

To prove that the system is flat, the dc-bus electrostatic energy y_{Bus} stored in C_{Bus} is assumed as the flat output component. Therefore, one defines a flat output $y_1 = y_{Bus}$, a control variable $u_1 = p_{SCREF}$, and a state variable $x_1 = v_{Bus}$.

From (2.43), the state variable x_1 can be written as

$$x_1 = \sqrt{\frac{2y_1}{C_{Bus}}} = \varphi_1(y_1) \tag{2.51}$$

From (2.46), the control variable u_1 can be calculated from the flat output y_1 and its time derivatives (inverse dynamics; see Fig. A1) as

$$u_1 = 2 \cdot P_{SCLimited} \cdot \left[1 - \sqrt{1 - \left(\frac{\dot{y}_1 + \sqrt{\frac{2y_1}{C_{Bus}}} \cdot i_{Load} - p_{FCo}}{P_{SCLimited}} \right)} \right] \tag{2.52}$$
$$= \psi_1(y_1, \dot{y}_1) = p_{SCREF}$$

where

$$P_{\text{SCLimited}} = \frac{v_{\text{SC}}^2}{4r_{\text{SC}}} \tag{2.53}$$

$P_{\text{SCLimited}}$ is the limited maximum power from the supercapacitor module.

So, it is apparent that $x_1 = \varphi_1(y_1)$ and $u_1 = \psi_1(y_1, \dot{y}_1)$ correspond with (A.6) and (A.7). Consequently the proposed reduced order model of the hybrid system can be considered as a flat system.

A desired reference trajectory for the dc-bus energy is represented by $y_{1\text{REF}}$. A feedback control law (refer to Fig. A1) achieving an exponential asymptotic tracking of the trajectory is given by the following expression [Pay08], [Na08]:

$$(\dot{y}_1 - \dot{y}_{1\text{REF}}) + K_{11}(y_1 - y_{1\text{REF}}) + K_{12}\int(y_1 - y_{1\text{REF}})d\tau = 0 \tag{2.54}$$

where the set of controller parameters (K_{11}, K_{12}) is chosen so that the roots of the closed-loop characteristic polynomial in the complex variable s

$$p(s) = s^2 + \lambda_1 s^1 + \lambda_0 \tag{2.55}$$

is a Hurwitz polynomial.

Obviously, the tracking error $e_1 = y_1 - y_{1\text{REF}}$ satisfies

$$\ddot{e}_1 + K_{11}\dot{e}_1 + K_{12}e_1 = 0 \tag{2.56}$$

An optimum choice of the design controller parameters is obtained by matching the characteristic polynomial p(s) to a desired characteristic polynomial with defined root locations.

One may set as a desired characteristic polynomial

$$p(s) = s^2 + 2\zeta\omega_n s + \omega_n^2 \tag{2.57}$$

$$K_{11} = 2\zeta\omega_n \tag{2.58}$$

$$K_{12} = \omega_n^2 \tag{2.59}$$

where, ζ and ω_n are desired dominant damping ratio and natural frequency.

It is noticeable that the control system is stable for K_{11}, $K_{12} > 0$ (ζ, $\omega_n > 0$). However, based on power electronic constant switching frequency f_S and cascade control structure, the outer control loop (here the dc-bus energy control) must operate at a cut-off frequency $f_E << f_C$ (a cut-off frequency of the supercapacitor current loop) << f_S. Once the flat outputs are stabilized, the whole system is stable because all the variables of the system are expressed in terms of the flat outputs.

2) Supercapacitive Energy Regulation

For total energy regulation (or supercapacitor energy regulation), a desired reference trajectory for the total energy is represented by y_{TREF}. Since the supercapacitor ES is an enormous size capacity, and the supercapacitor energy is defined as a slower dynamic variable than the dc-bus energy variable, a special control law of the total energy regulation is defined as

$$p_{FCDem} = P_{FCMin} \quad \text{if } y_{TREF} - y_T < -\Delta y \tag{2.60.1}$$

$$p_{FCDem} = \frac{f(p_{FC}, p_{Load}) - P_{FCMin}}{\Delta y} \cdot (y_{TREF} - y_T) + f(p_{FC}, p_{Load}) \quad \text{if } -\Delta y < y_{TREF} - y_T \le 0 \tag{2.60.2}$$

$$p_{FCDem} = \frac{P_{FCMax} - f(p_{FC}, p_{Load})}{\Delta y} \cdot (y_{TREF} - y_T) + f(p_{FC}, p_{Load}) \quad \text{if } 0 < y_{TREF} - y_T \le \Delta y \tag{2.60.3}$$

$$p_{FCDem} = P_{FCMax} \quad \text{if } \Delta y < y_{TREF} - y_T \tag{2.60.4}$$

where,

$$f(p_{FC}, p_{Load}) = 2 \cdot P_{FCLimited}\left(1 - \sqrt{1 - \frac{p_{Load}}{P_{FCLimited}}}\right) \tag{2.60.5}$$

$$P_{FCLimited} = \frac{v_{FC}^2}{4 \cdot r_{FC}} \tag{2.60.6}$$

$P_{FCLimited}$ is the limited maximum power from the FC converter. P_{FCMax} and P_{FCMin} are the maximum and minimum power of the FC stack, respectively. Δy is the regulation parameter.

The total energy control law generates the FC power demand p_{FCDem}, refer to (2.54)-(2.60). The FC, although clearly the main energy source of the system, function as the generator that supplies energy for both the dc bus capacitor C_{Bus} and the supercapacitors C_{SC} to keep them charged.

3) Conclusion of the Control Laws

The multivariable control of the FC/supercapacitor hybrid power source previously detailed is portrayed in Fig. II.3.43. The dc bus energy control law generates a supercapacitor power reference p_{SCREF} [or the control variable u_1; see (2.52)]. This signal is then divided by the measured supercapacitor voltage v_{SC} and limited to maintain the supercapacitor voltage within an interval [V_{SCMin}, V_{SCMax}] by limiting a supercapacitor charging current or discharging current, as presented in the block "SC Current Limitation Function" [Tho06b]. This results in the supercapacitor current reference i_{SCREF}. For the total energy control law [see (2.60)], it generates the FC power demand p_{FCDem}. It must be limited in slope, which enables the safe operation of the FC with respect to the dynamic constraints that are associated with the FC stack.

To obtain a natural linear function, a second-order delay (filter) $D_{FC}(s)$ is chosen for the limited FC power dynamics as

$$D_{FC}(s)=\frac{p_{FCREF}(s)}{p_{FCDem}(s)}=\frac{1}{\left(\frac{s}{\omega_{n1}}\right)^2+\frac{2\zeta_1}{\omega_{n1}}s+1} \tag{2.61}$$

where ω_{n1} and ζ_1 are the regulation parameters. Then, the FC power reference p_{FCREF} is divided by the measured FC voltage v_{FC}. This results in an FC current reference i_{FCREF}. For safety, the FC current reference i_{FCREF} must be limited in level, i.e., within an interval [maximum FC current I_{FCMax} (corresponding to a FC rated current), minimum FC current I_{FCMin} (set to 0 A)].

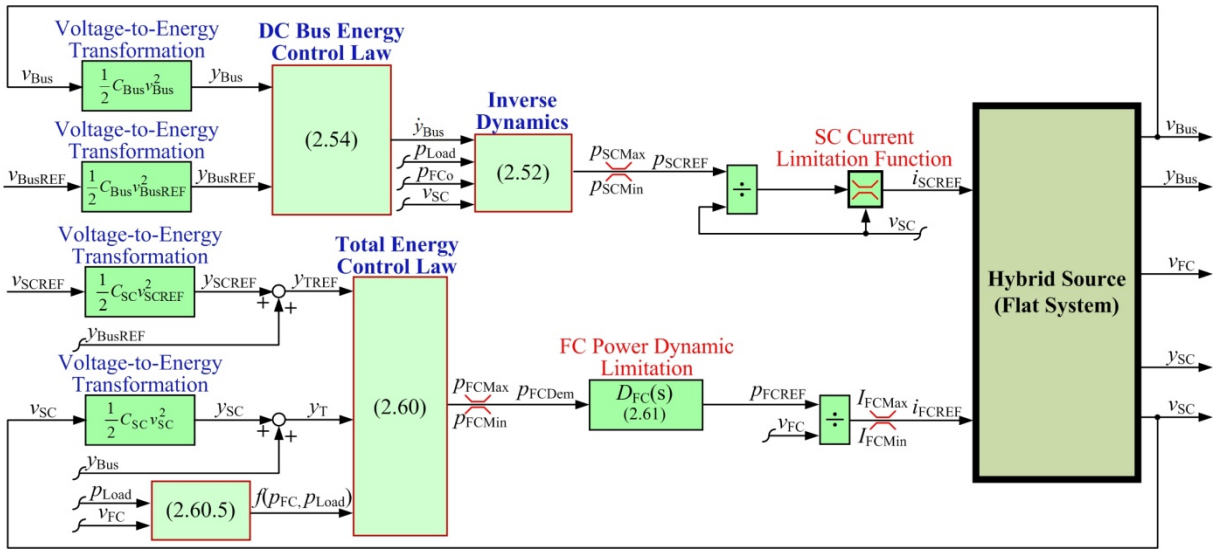

Fig. II.3.43. Proposed control scheme for the FC/supercapacitor hybrid source.

C. Performance Validation

1) Test Bench Description

To authenticate the proposed innovative control laws of the hybrid system, the small-scale test bench was implemented in a laboratory, as illustrated in Fig. II.3.44. The PEMFC system (500 W, 50 A, 10 V) was achieved by the Zentrum für Sonnenenergie und Wasserstoff-Forschung (ZSW) society, see Fig. II.2.4. It consists of 16 cells of 100 cm^2 in series. It is supplied using pure hydrogen from an aluminum tank under pressure of 150 bars and with clean and dry air from a compressor (50 W). The supercapacitor bank is obtained by means of two supercapacitor modules BMOD0500-P016 (developed and manufactured by Maxwell Technologies Inc.: 500 F, 16 V, 500 A) connected in series. The test bench was operated at around 25 ◦C at room temperature.

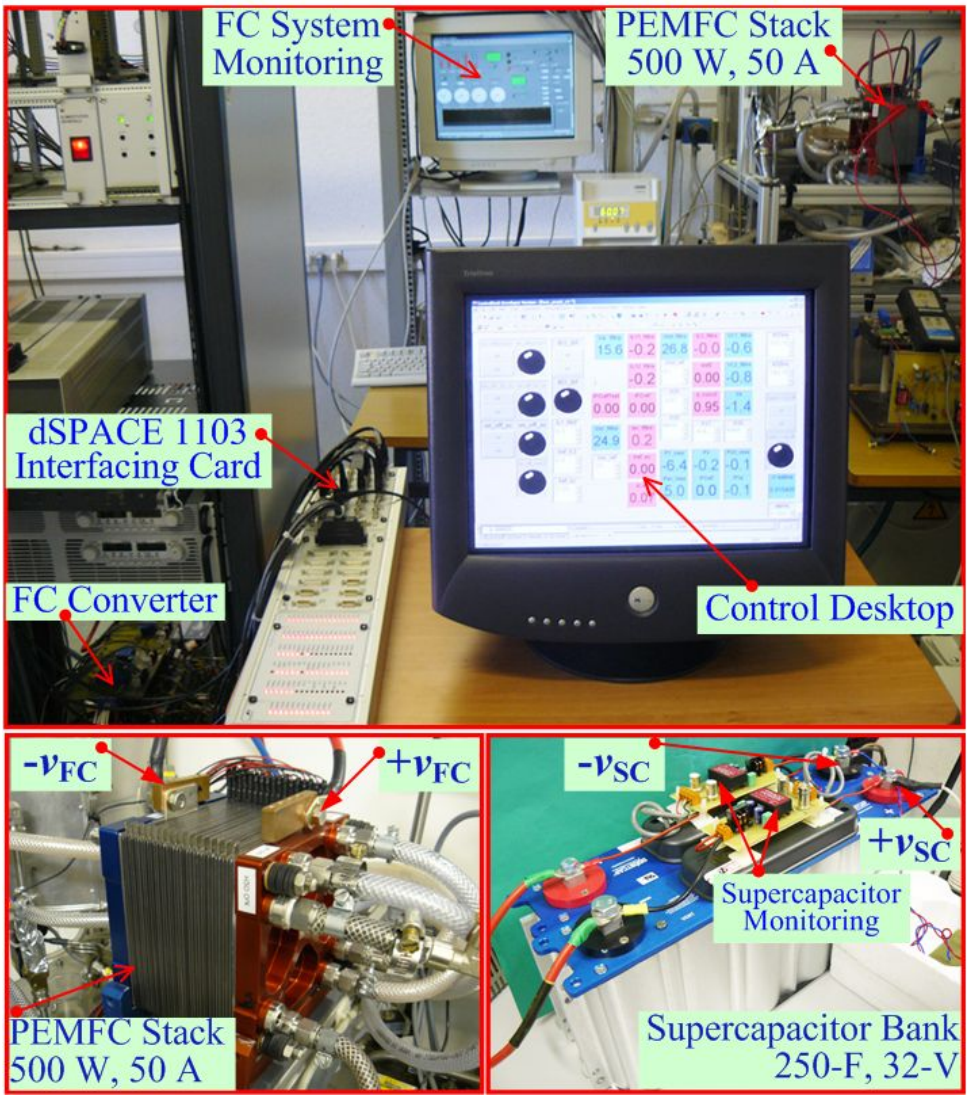

Fig. II.3.44. Test bench system at the Groupe de Recherche en Electrotechnique et Electronique de Nancy (GREEN).

The FC converter (two-phase parallel boost converters) and the supercapacitor converter (two-phase parallel bidirectional converters) (see Fig. II.3.46) are realized in the laboratory. The converter parameters and the semiconductor components are detailed in Table II.3.3.

TABLE II.3.3 CONVERTER PARAMETERS AND SEMICONDUCTOR DEVICES

Fuel Cell Converter:	
Inductors $L_{F1}=L_{F2}$	35 μH
MOSFETs $S_{F1}=S_{F2}$	IXFN230N10: 100 V, 230 A
Schottky diode $D_{F1}=D_{F2}$	STPS160H100TV: 100 V, 80 A
Supercapacitor Converter:	
Inductors $L_{C1}=L_{C2}$	140 μH
MOSFETs $S_{C1}=S_{C2}$ $=S_{C1}'=S_{C2}'$	STE110NS20FD: 200 V, 110 A

2) Control Description

Measurements of the FC current i_{FC}, the supercapacitor current i_{SC}, the load current i_{Load}, the dc-bus voltage v_{Bus}, the FC voltage v_{FC}, and the supercapacitor voltage v_{SC} are carried out by means of zero-flux Hall effect sensors. The two energy control loops and the two current control loops have been implemented in a real time card dSPACE DS1103 through the mathematical environment of MATLAB/Simulink with a sampling frequency of 25 kHz.

The parameters associated with the dc-bus energy regulation loop and the total energy regulation loop are shown in Tables II.3.4 and II.3.5, respectively. The parameters for the FC power dynamic delay are shown in Table III. This value has experimentally been determined as the highest power slope of our FC system, where no fuel starvation occurs. It must be noted here that, for the small-test bench, the FC maximum power p_{FCMax} is set at 320 W; in fact, the rated FC power considered here is 500 W.

TABLE II.3.4 DC-BUS ENERGY CONTROL LOOP PARAMETERS

v_{BusREF}	42	V
C_{Bus}	6200	μF
K_{11}	424	rad·s^{-1}
K_{12}	90×10^3	rad^2·s^{-2}
r_{FC}	0.015	Ω
r_{SC}	0.030	Ω
P_{SCMax}	+1500	W
P_{SCMin}	-1500	W
V_{SCMax}	32	V
V_{SCMin}	12.5	V
$I_{SCRated}$	100	A

TABLE II.3.5 TOTAL ENERGY CONTROL LOOP PARAMETERS

v_{SCREF}	25	V
C_{SC}	250	F
Δy	6.25×10^3	J
r_{FC}	0.015	Ω
P_{FCMax}	320	W
P_{FCMin}	0	W
I_{FCMax} (Rated)	50	A
I_{FCMin}	0	A
ζ_1	1	
ω_{n1}	0.5	rad·s^{-1}

3) Experimental Results

The experimental tests have been carried out by connecting the dc bus loaded by an electronic active load. Figs. II.3.45 and II.3.46 present waveforms that are obtained during the load cycles (motoring and regenerative braking modes). It shows the dc bus voltage, the FC voltage, the load power, the supercapacitor power, the FC power, the supercapacitor current, the FC current, and the supercapacitor voltage (or the supercapacitor state of charge *SOC*).

As illustrated in Fig. II.3.45, the initial state is in no-load power, and the storage device is full of charge, i.e., v_{SC} = 25 V. As a result, both FC and supercapacitor powers are zero. At t = 10 s, the load power steps to the final value of around +720 W (imitated vehicle acceleration). Synchronously, the final FC power increases with a limited slope (second order characteristics) to a limited maximum power of 320 W. Thus, the supercapacitor, which supplies most of the power that is required during stepped load, remains in a discharge state after constant power because the steady-state load power is greater than the FC limited maximum power. After that, at t = 70 s, the load power steps from +720 to +100W. Now, the supercapacitor voltage is equal to around 18.5 V; as a result, the supercapacitor is changing its state from discharging to charging. The FC power is

still at the limited maximum power of 320 W to supply the energy to the load and to charge the supercapacitor.

As illustrated in Fig. II.3.46, in the initial state, the load power is equal to +80 W, and the supercapacitor voltage is equal to 24.5 V, which is nearly fully charged. As a result, the FC power is 120 W to supply the energy for the load and to charge the supercapacitor. At t = 10 s, the load power steps to −400 W (imitated vehicle deceleration or regenerative braking), and the supercapacitor is deeply charged (recuperative braking energy), demonstrating the two phases.

1) First, the supercapacitor recovers the energy that is supplied to the dc bus by the FC and the load; synchronously, the FC power reduces with a limited slope (second-order characteristics) to zero.

2) Second, at t = 20 s, the supercapacitor absorbs the negative energy supplied only by the load. As a result, the supercapacitor is overcharged, i.e., $v_{SC} > v_{SCREF} = 25$ V.

After that, at t = 60 s, the load power steps from −400 to +80 W. Now, the supercapacitor voltage is equal to around 27 V (overcharged). As a result, the supercapacitor changes its state from charging to discharging. The FC power is still at the limited minimum power of 0 W. Therefore, the load power is supplied by only the supercapacitor power. After that, when v_{SC} reduces to v_{SCREF} of 25 V, the supercapacitor power will reduce to zero, and the FC power will increase to supply the energy for the load.

To illustrate the dynamic regulation of the dc-bus energy (voltage), the oscilloscope waveforms in Fig. II.3.47 portray the dc bus voltage (representing the flat output y_1) dynamics at a high load power demanded (disturbance). It shows the dc-bus ripple voltage (state variable x_1), the load power, the supercapacitor power, and the FC power. Once again, the supercapacitor supplies most of the power that is required during the high step load. The experimental results reveal only small perturbations on the dc-bus voltage waveform, which is of major importance by using the flatness-based control law for the dc-bus energy regulation in the proposed system.

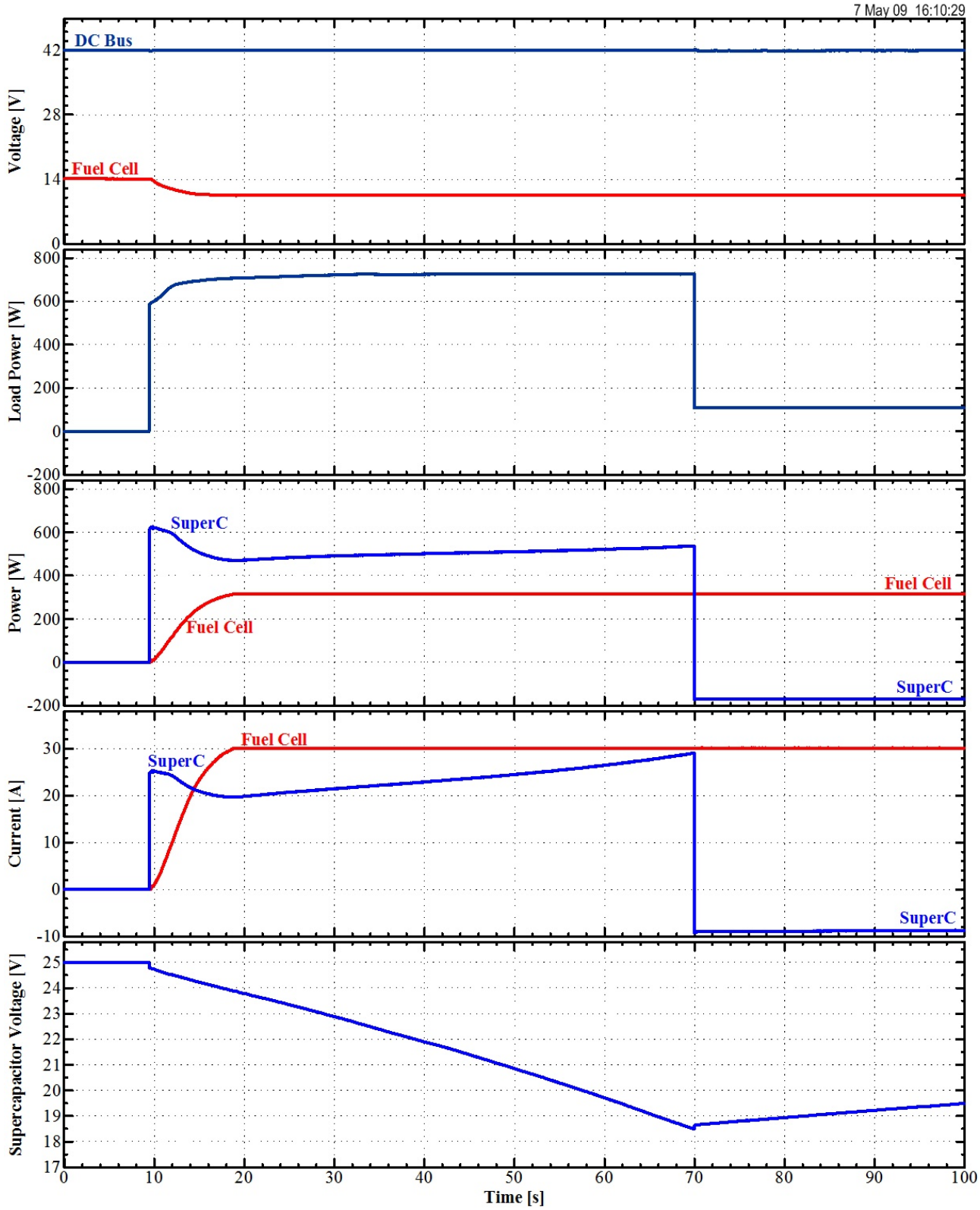

Fig. II.3.45. Experimental Result: Hybrid source response during step load from 0 to 720 W and from 720 to 100 W (motoring mode).

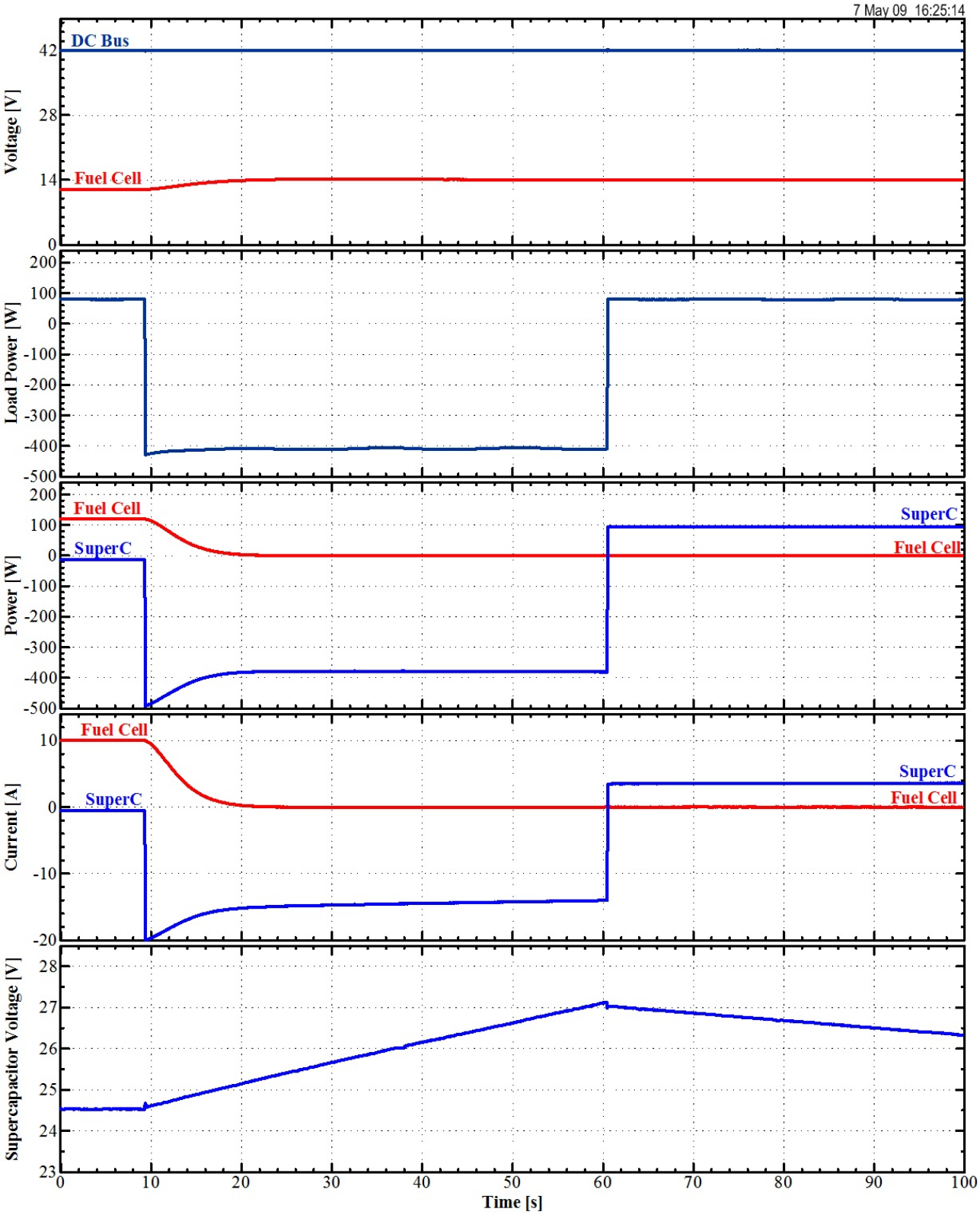

Fig. II.3.46. Experimental Result: Hybrid source response during step load from 0 to 720 W and from 720 to 100 W (motoring mode).

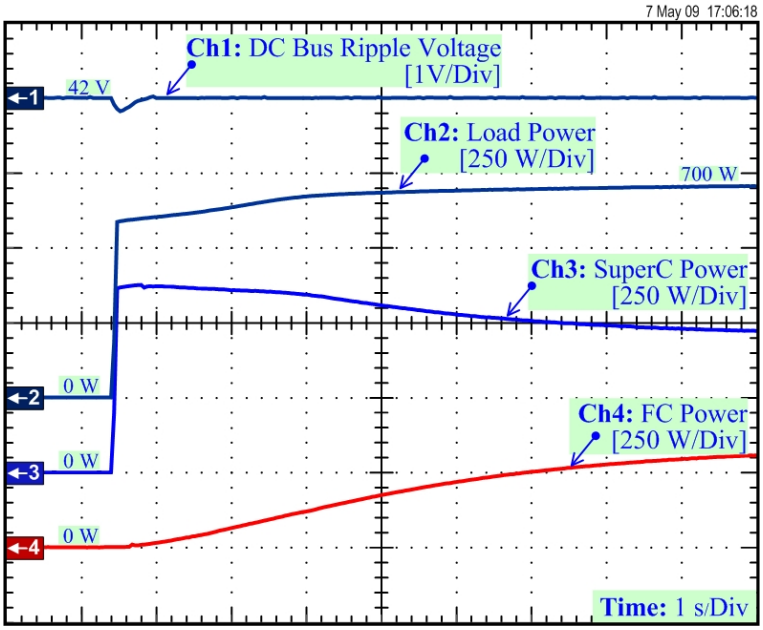

Fig. II.3.47. Experimental Result: Dynamic characteristic of the hybrid source during a step load from 0 to 700 W.

4) Performance Comparison Between the Flatness Control and the Classical Linear PI Control

To compare the performance of the flatness-based control, a traditional linear proportional–integral (PI) control method presented in [Tho07], [Tho14] is also detailed. Here, we briefly review this approach. A desired reference for the dc-bus energy is represented by y_{BusREF} ($y_{1\mathrm{REF}}$). A linear feedback PI control law is given by the following expression:

$$p_{\mathrm{SCREF}} = K_{\mathrm{P}}\left(y_{\mathrm{BusREF}} - y_{\mathrm{Bus}}\right) + K_{\mathrm{I}}\int_0^t \left(y_{\mathrm{BusREF}} - y_{\mathrm{Bus}}\right)d\tau \tag{2.62}$$

where K_{P} and K_{I} are the set of controller parameters.

Therefore, because the supercapacitor current loop is much faster than the dc link voltage loop [so that it can be considered as a pure unity gain], the open-loop transfer function associated with the dc link voltage regulation can be written as

$$\frac{y_{\mathrm{Bus}}(s)}{y_{\mathrm{BusREF}}(s)} = \overbrace{\left(K_P + \frac{K_{\mathrm{I}}}{s}\right)}^{\mathrm{PI-Controller}} \cdot \overbrace{\frac{1}{s}}^{y_{\mathrm{Bus}}/p_{\mathrm{SC}}} \cdot \overbrace{\frac{1}{T_{\mathrm{p}}s+1}}^{p_{\mathrm{SC}}/p_{\mathrm{SCREF}}} \tag{2.63}$$

where T_{P} is the time constant of an equivalent first-order delay of the supercapacitor power regulation loop (or the supercapacitor current regulation loop). Thus, the linear control law of the dc link stabilization previously detailed is portrayed in Fig. II.3.48. It is similar to the nonlinear control

law (see Fig. II.3.49), where the PI controller also generates a supercapacitor power reference p_{SCREF}.

To compare the performance of the flatness-based control and the linear PI control laws, the simulation was implemented. Simulations with MATLAB/Simulink were performed using a reduced-order model of the power plant. To give a reasonable comparison between the methods, the parameters of the linear PI controller K_P and K_I were tuned to obtain the best possible performance, and this result is compared with the flatness-based control. Then, K_P = 600W· J^{-1}, and K_I = 100 000 W· $(J \cdot s)^{-1}$; therefore, the desired phase margin *PM* is equal to 60°. If K_P = 720 W· J^{-1} and K_I = 200 000 W· $(J \cdot s)^{-1}$, then the desired phase margin PM is equal to 50°.

Finally, Fig. II.3.49 shows simulation results obtained for both controllers during the large load step. It is similar to the test bench results illustrated in Fig. II.3.47. The flatness-based control shows good convergence of the dc-bus voltage regulation to its desired reference of 42 V. Although the dynamic response of the linear control law could be improved (by reducing the phase margin *PM*) relative to that shown in the figures, this enhancement came at the expense of a reduced stability margin (see Fig. II.3.49). From these results, we conclude that the flatness based control provides better performance than the classical PI controller.

D. Conclusion

There is an essential need for an efficient ES system that is affordable and has a drive cycle life for future FC vehicles. This section has focused on the dynamic performance by taking account of the intrinsic energetic characteristics of these sources (i.e., energy and power densities and typical operating dynamics) in the energy-management strategy. Hence, the control approach, based on the differential flatness control, presents the robustness, stability, and efficiency of the FC/supercapacitor hybrid power source. The control laws illustrate how to circumvent the fast transition of the FC power and then reducing the FC stack stress. As a result, the hybrid source lifetime is theoretically increased. To ensure the energy-efficient operation of the FC stack, the output current ripple of the FC stack is minimized by parallel boost converters with interleaving switching technique for a high-frequency ripple (25-kHz pulse width modulation) by the supercapacitor for a low-frequency ripple (e.g., 100 for single systems).

Experimental results in the GREEN laboratory (Université de Lorraine) carried out using a small-scale test bench, which employs a PEMFC (500 W, 50 A), and a storage device of supercapacitor bank (292 F, 30 V) corroborate the excellent performances during load cycles.

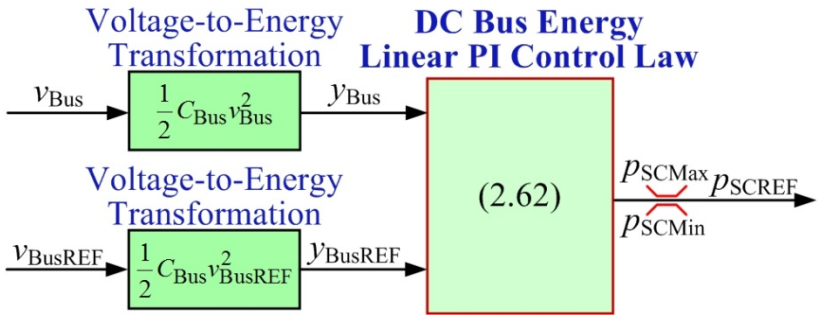

Fig. II.3.48. DC link stabilized FC/supercapacitor hybrid source based on linear PI control law.

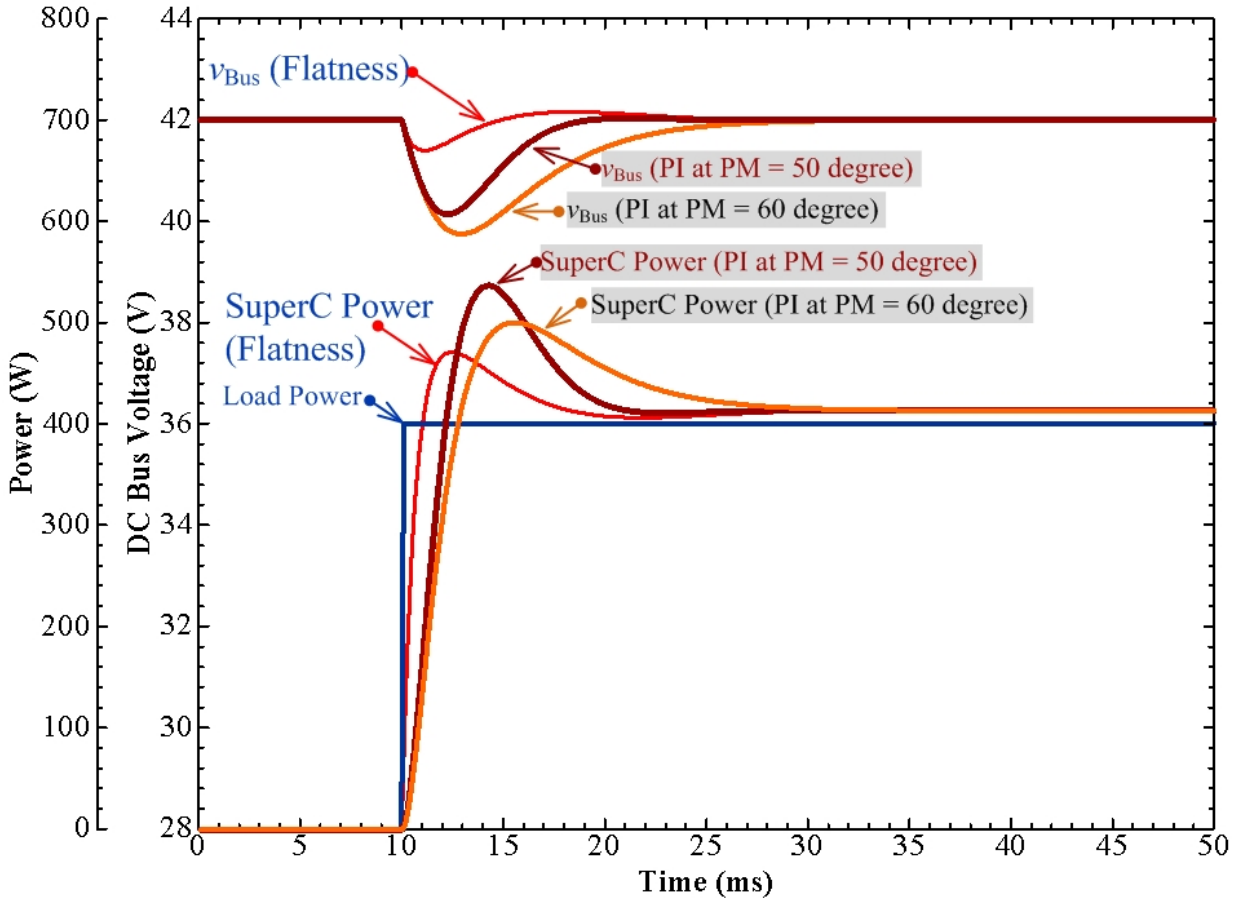

Fig. II.3.49. Simulation Result: Comparison of the flatness-based control law with a linear PI control law. Response to a large load step from 0 to 400 W at t = 10 ms.

II.3.3.3 Fuel cell/battery/supercapacitor hybrid power source

Presented here is a perfect hybridization of the batteries and supercapacitors as energy storage devices with a PEM fuel cell as a main source. It deals with the conception and the achievement of a regulated dc bus voltage hybrid power. Its interest is focused on an energy management in system. To authenticate the proposed hybrid structure, a small-scale hardware system is realized by analog circuits and numerical calculation (dSPACE). Experimental and simulations results will illustrate the system performances.

A. System Description

There are many possible structures to connect a main source and two storage devices with the utility dc bus. The total mass, volume, cost and efficiency (optimization) of the propulsion system are investigated. Refer to Fig. II.3.6, configuration 4: Single Source/Two Energy Storage Devices, one of the good solutions is depicted in Fig. II.3.50. It is composed of a unidirectional converter (step-up converter) for a FC stack, bidirectional (2-quadrant) converters for battery and supercapacitor modules. It is the most sufficient configuration when comparing mass, volume and cost, as detailed in [Sch07[,[Ste07].

For reasons of safety and dynamics, these converters are primarily controlled by inner current regulation loops, classically. These current control loops are supplied by three reference signals: i_{SCREF}, i_{BatREF}, and i_{FCREF}, generated by the energy management algorithm presented hereafter. The dynamics of the current regulation loops are also supposed to be much faster than those of the outer voltage control loops, detailed hereafter. Thus, the currents i_{SC}, i_{Bat}, and i_{FCREF} are considered to follow perfectly their references i_{SCREF}, i_{BatREF}, and i_{FCREF}.

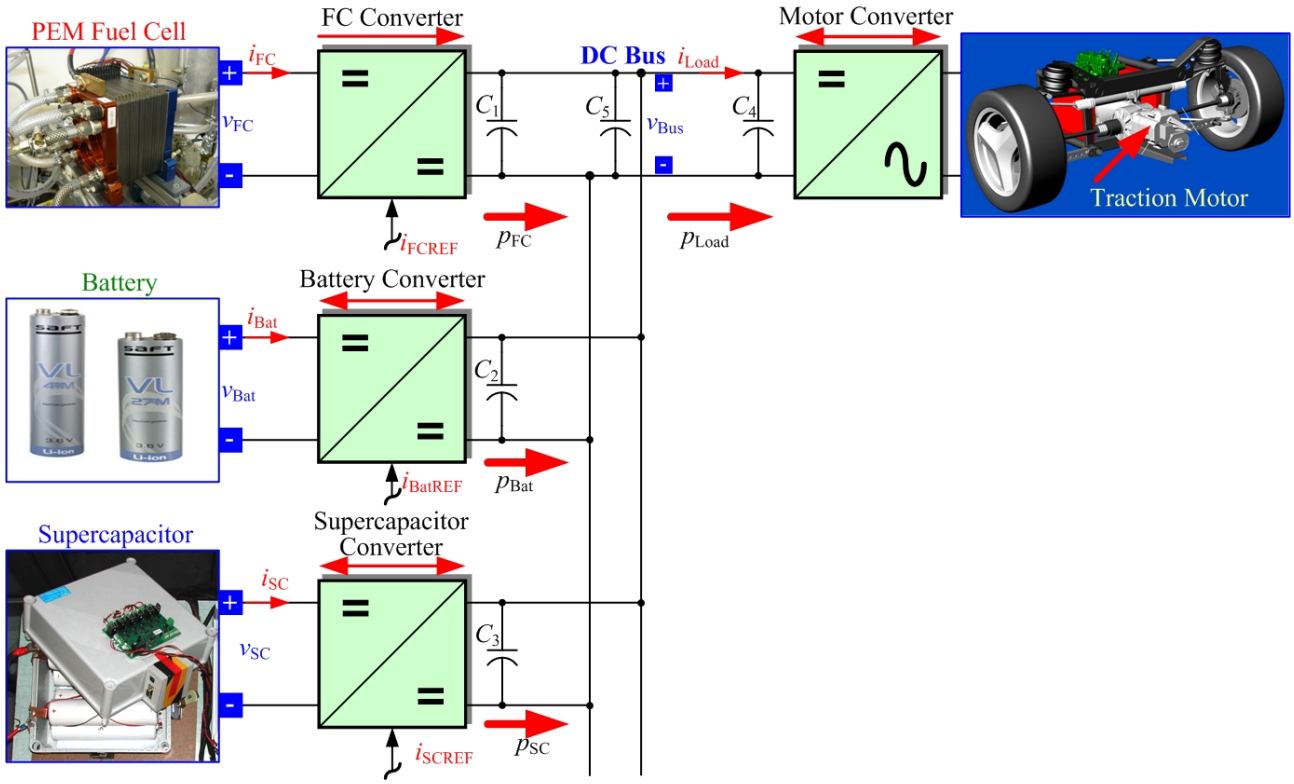

Fig. II.3.50. Proposed structure of fuel cell/battery/supercapacitor hybrid power source. p_{FC} (= $v_{FC} \cdot i_{FC}$), v_{FC} and i_{FC} are the FC power, voltage, and current. P_{Bat} (= $v_{Bat} \cdot i_{Bat}$), v_{Bat} and i_{Bat} are the battery power, voltage, and current. P_{SC} (= $v_{SC} \cdot i_{SC}$), v_{SC} and i_{SC} are the supercapacitor power, voltage, and current. P_{Load} (= $v_{Bus} \cdot i_{Load}$), v_{Bus} and i_{Load} are the load power, dc bus voltage, and load current, respectively. i_{FCREF}, i_{BatREF}, and i_{SCREF} are the current reference signals for FC, battery, and supercapacitor current control loops, respectively.

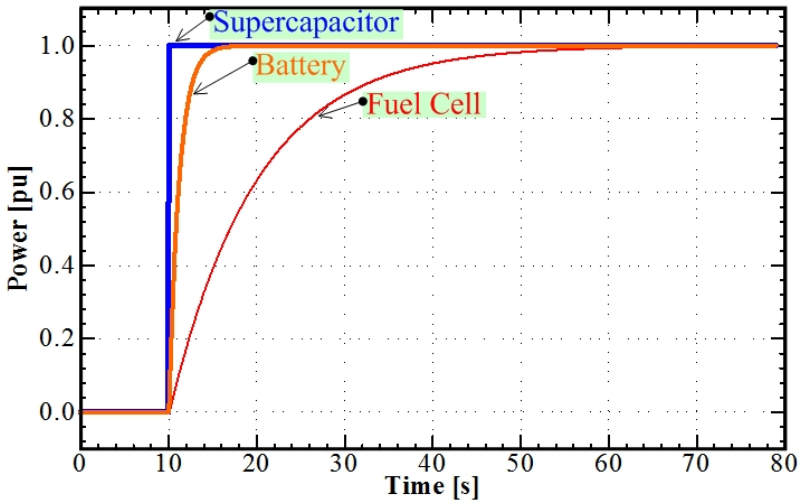

Fig. II.3.51. Dynamic classification of the embedded sources.

B. Energy Management of Hybrid Power Source

To manage the energy exchanges between the sources and the load at dc bus, three operating modes (or states) can be identified here again:

1) **Charge mode**, in which the main source supplies energy to the storage devices and to the load.
2) **Discharge mode**, in which main source and storage devices supply energy to the load.
3) **Recovery mode**, in which the load supplies energy to the storage devices.

As mentioned earlier, FC has slow dynamics. It can be compensated by faster dynamics from storage devices. Batteries have the best energy density but a bad power density. Contrary to batteries, supercapacitors have lower energy density (1000 times lower) but higher power density (100 times higher) and provide very fast dynamic cycles (close to 1ms).

Furthermore, battery lifetime depends on many factors: the operating temperature; the number and the depth of discharge cycles; rate and eventually the amount and number of rest in a discharged state and overcharge. To optimize the lifetime of the batteries, it is advisable to limit the battery current slope in order to ensure a longer battery lifetime. On the other hand, supercapacitors can provide more cycles than batteries (virtually infinite cycles) and are well suited to very fast dynamic cycles.

The energy management strategy based on a dynamic classification, as portrayed in Fig. II.3.51, aims at distributing the global power mission of the vehicle into the sources in such away that each source is optimally used. According to the three points mentioned above embedded energy sources can be classified as illustrated in Fig. II.3.51. Note that the power unit in Figure is the normalized unit (or per-unit [pu]). So, the defined dynamic classification is obtained from our simulation result. FC generator is controlled as the lowest dynamic power source. The FC current or power slope must be limited to avoid the fuel starvation problem. Normally, the FC limited current or power slope has been experimentally determined as the highest slope of operated FC system, where no fuel starvation occurs. Supercapacitor is the highest dynamic power source, which provides the micro-cycles and the fast dynamic power supply. Battery is between FC and supercapacitor in the dynamic classification.

Thounthong *et al*. [Tho07] who studied a FC/supercapacitor hybrid source have proposed the hybrid energy management by regulating a dc bus voltage. Therefore, the proposed hybrid energy management here is shown in Fig. II.3.52. Its basic principle here lies in using the supercapacitors (the fastest energy source), for supplying energy required to achieve the dc link voltage regulation.

The batteries are controlled as the power source (with dynamic limitations, F_2) that supplies energy to the supercapacitors to keep them charged. Then, the FC, although obviously the main energy source of the system, is functioned as the generator (with dynamic limitations, F_1) that supplies energy to the batteries to keep them charged.

Consequently, the supercapacitor converter is driven to realize a classical dc bus voltage regulation. The battery converter is driven to maintain the supercapacitors at a given state-of-charge, here the supercapacitor voltage regulation. Then, the FC converter is also driven tomaintain the batteries at a given state-of-charge, here the battery voltage regulation. As a result, the hybrid system composes of three-controlled variables:

- the dc bus voltage v_{Bus},
- the supercapacitor voltage v_{SC}, and
- the battery voltage v_{Bat}.

and three-control variables:

- the supercapacitor current reference i_{SCREF},
- the battery current reference i_{BatREF}, and
- the FC current reference i_{FCREF}.

1) DC Bus Voltage Control Loop

The dc bus voltage control loop considers a dc bus capacitive energy y_{Bus} as state variable, and the supercapacitor delivered power as command variable, to obtain a natural linear transfer function for the system. If the losses in the FC, battery, and supercapacitor converters are neglected, the dc link capacitive energy is given versus supercapacitor power p_{SC}, battery power p_{Bat}, FC power p_{FC} and load power p_{Load} by the following differential equation:

$$\frac{dy_{Bus}}{dt} = p_{SC} + p_{Bat} + p_{FC} - p_{Load} \tag{2.64}$$

which shows that the transfer function "y_{Bus}/p_{SC}" is a pure integrator [Tho07]. The dc bus energy measurement is carried out by means of the following classical calculation:

$$y_{Bus} = \frac{1}{2} \cdot C_{Bus} \cdot v_{Bus}^2 \tag{2.65}$$

where C_{Bus} is the total capacitance of capacitors at the dc bus (refer to Fig. II.3.52, $C_{Bus} = C_1 + C_2 + C_3 + C_4 + C_5$). It enables the generation of both bus energy reference and bus energy measurement, through dc bus voltage reference v_{BusREF} and dc bus voltage v_{Bus}, respectively. Supercapacitor power reference p_{SCREF} is generated by means of a proportional–integral (PI)-controller. So, a first-order filter is used for y_{Bus} to reduce harmonics due to switching. p_{SCREF} is then divided by the measured supercapacitor voltage v_{SCMea}, and limited to maintain supercapacitor voltage within an interval $[V_{SCMin}, V_{SCMax}]$. The upper value V_{SCMax} of this interval corresponds to the maximum voltage of the storage device, and the lower value V_{SCMin}, traditionally equal to $V_{SCMax}/2$, to a level under which supercapacitor discharge becomes ineffective. This results in the supercapacitor current reference i_{SCREF}.

The supercapacitor current–voltage saturation function called “SuperC Limitation Function” as portrayed in Fig. II.3.52, consists of limiting the reference i_{SCREF} to the interval [maximum charging current I_{SCMin} (negative value), maximum discharging current I_{SCMax} (positive value)] defined, versus the measured supercapacitor voltage v_{SCMea} as follows:

$$\begin{cases} I_{SCMin} = -I_{SCRated} \cdot \boldsymbol{min}\left(1, \dfrac{V_{SCMax} - V_{SCMea}}{\Delta v}\right) \\ I_{SCMax} = +I_{SCRated} \cdot \boldsymbol{min}\left(1, \dfrac{V_{SCMea} - V_{SCMin}}{\Delta v}\right) \end{cases} \tag{2.66}$$

where, $I_{SCRated}$ and Δv are the regulation parameters.

2) Supercapacitor Voltage Control Loop

As presented in Fig. II.3.52, a proportional (P)-controller is sufficient for the supercapacitor voltage control loop, as far as the proportional gain is high enough to introduce only a little static error. So, a first-order filter is used for supercapacitor voltage measurement, to reduce switching harmonics. The output signal from the regulator must be limited in level and slope, to respect constraints associated with the battery. Then the battery reference signal i_{BatREF} that drives the battery converter through the battery current control loop is then kept within an interval [maximum discharging current I_{BatDis} (positive value), maximum charging current I_{BatCh} (negative value)]. Moreover, the “Battery Current Slope Limitation” at a delay F_2 enables safe operation of the battery, even during transient power demand. To obtain a natural linear transfer function, a second-order delay (filter) F_2 is chosen for the battery current dynamics as follow:

$$F_2(s) = \frac{1}{\left(\frac{s}{\omega_{n2}}\right)^2 + \frac{2 \cdot \zeta_2}{\omega_{n2}} s + 1} \tag{2.67}$$

Where ω_{n2} and ζ_2 are the regulation parameters. So, a delay F_2 of the battery dynamics must be faster than a delay F_1 of the FC dynamics, refer to Fig. II.3.51 and 52.

3) Battery Voltage Control Loop

The proposed battery voltage control loop is also portrayed in Fig. II.3.52. The simple method to charge the battery is the constant current–constant voltage (CCCV) charging as depicted in Fig. II.3.53, where Q_{Bat} is the battery capacity. The battery current is constant (maximum battery charging current I_{BatMax} is set around $Q_{Bat}/5$–$Q_{Bat}/10$; for a Li-ion battery, it can be set at $I_{BatMax} = Q_{Bat}$) when the actual battery voltage v_{Bat} is far from the battery voltage reference v_{BatREF} and reduced current when v_{Bat} is near v_{BatREF} and zero when v_{Bat} is equal to v_{BatREF}. Note here that a similar structure of the battery charging algorithm based on battery state-of- charge SOC has been reported in [Tho08b]. So, the main problem is that the battery capacity Q_{Bat} is not constant. It is dependent on many factors as follows [Tho08b]:

- the depth of discharge,
- discharge rate,
- cell temperature,
- charging regime,
- dwell time at low and high SOC,
- battery maintenance procedures,
- current ripple, and
- amount and frequency of overcharge.

As a result, the battery voltage is here considered as a battery *SOC*. According to the proposed battery charging algorithm here, a P-controller is enough to generate a battery charging current. This signal must be limited within an interval [maximum charging current I_{BatMax} (equal to $-1 \cdot I_{BatCh}$), maximum discharging current I_{BatMin} (equal to $-1 \cdot I_{BatDis}$). The measured battery current must be inversed because the definition of battery current is negative for charging current.

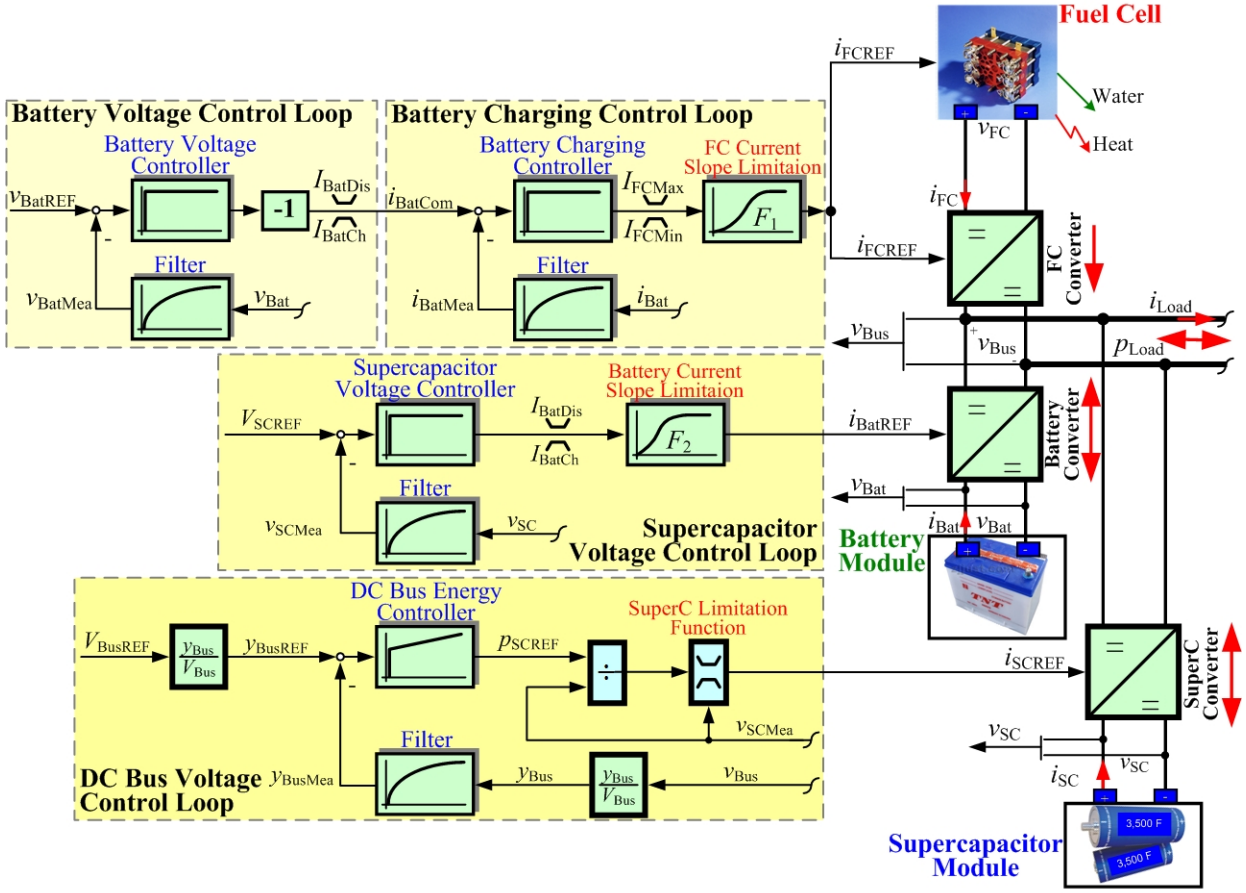

Fig. II.3.52. Proposed energy management of the fuel cell/battery/supercapacitor hybrid power source.

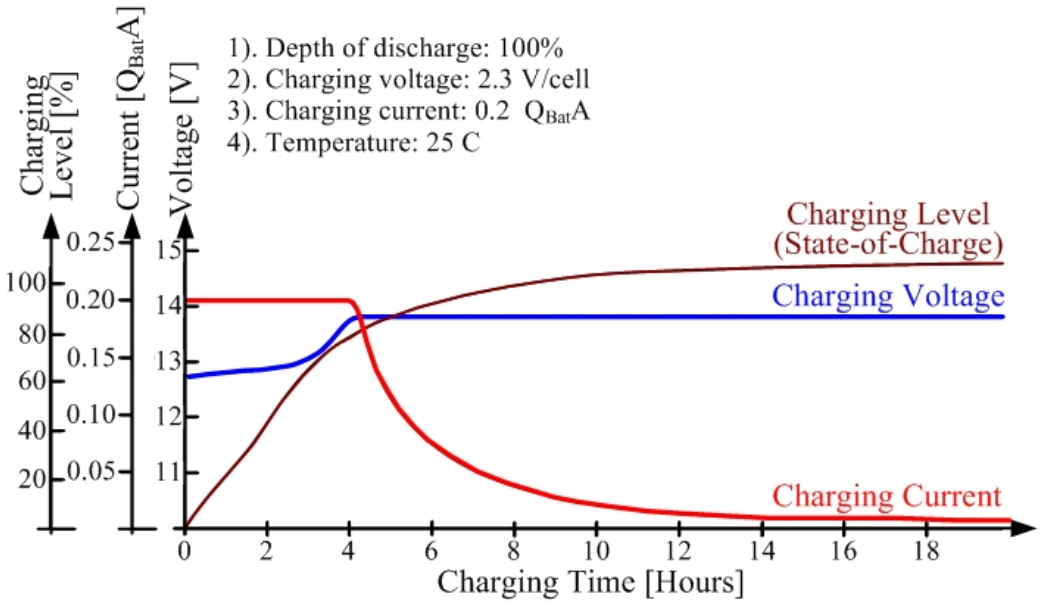

Fig. II.3.53. Constant current–constant voltage charging of a lead-acid battery.

4) Battery Charging Control Loop

The battery charging control loop receives i_{BatCOM} from a battery voltage regulation loop as illustrated in Fig. II.3.52. A P-controller is sufficient to generate the FC current reference i_{FCREF}. It must be limited in level, within an interval [maximum FC current I_{FCMax} (corresponding to a FC rated current), minimum FC current I_{FCMin} (set to 0 A)] and limited in slope, which enables the safe operation of the FC in order to respect constraints associated with the FC, as far as the proportional gain is high enough to introduce only a small static error.

A first-order low-pass filter is used for the battery current measurement to reduce ripple current coming from the switching frequency. Moreover, the "*FC Current Slope Limitation*" at a delay F_1 enables safe operation of the FC. To obtain a linear transfer function, a second-order delay (filter) F_1 is also chosen for the FC current dynamics as:

$$F_1(s) = \frac{1}{\left(\frac{s}{\omega_{n1}}\right)^2 + \frac{2\cdot\zeta_1}{\omega_{n1}}s + 1} \tag{2.68}$$

where, ω_{n1} and ζ_1 are the regulation parameters.

C. Performance Validation

1) Test Bench Description

A PEM fuel cell system (500W, 50A) studied here was constructed by the Zentrum für Sonnenenergie und Wasserstoff- Forschung (ZSW) Company, Germany (refer to Fig. II.2.4). It is composed of 16 cells in series with area of 100 cm^2. It is supplied with pure hydrogen from bottles under pressure and with clean, dry air from a compressor. Storage devices are obtained by means of two lead-acid batteries (68 Ah, 12 V) connected in series, and twelve supercapacitors (3500 F, 2.5 V, 500A) developed and manufactured by the SAFT Company, France connected in series. In addition, a small-scale test bench in our laboratory is presented in Fig. II.3.54.

The FC converter is a classical boost converter. The battery and supercapacitor converters are bidirectional (2-quadrant) converters. The load at dc link is only a traction motor drive of 2 kW coupled with a small-inertia flywheel. The dc bus studied here is 42V (PowerNet). For the supercapacitor, battery, and FC current control loops, they have been realized by analog circuits to function at high bandwidth. For the dc bus voltage, the supercapacitor voltage, the battery voltage,

and the battery charging regulation loops have been implemented in the real time card dSPACE DS1104, through the mathematical environment of Matlab–Simulink, with a sampling frequency of 25 kHz. The ControlDesk^{TM} software enables changes in the parameters of the control loops. The measurements of the dc bus voltage v_{Bus}, the supercapacitor voltage v_{SC}, supercapacitor current i_{SC}, the battery voltage v_{Bat}, the battery current i_{Bat}, and the FC current i_{FC} have been realized by means of zero-flux Hall effect sensors.

The voltage reference signals are set as follows:

- V_{BusREF} = 42 V,
- V_{BatREF} = 25 V,
- V_{SCREF} = 26 V.

For the minimum and maximum controlled parameters are set as follows:

- $I_{SCRated}$ = 200 A,
- V_{SCMin}= 15 V,
- V_{SCMax} = 30 V,
- Δv= 0.5 V,
- I_{BatCh} = –6 A,
- I_{BatDis} = +20 A,
- I_{BatMax} = +6 A,
- I_{BatMin} = –20 A,
- I_{FCMin} = 0 A,
- I_{FCMax} = 25 A.

Note here that for safety reasons the maximum FC current I_{FCMax} is set at 25 A (around 280 W) in place of 50 A (rated current).

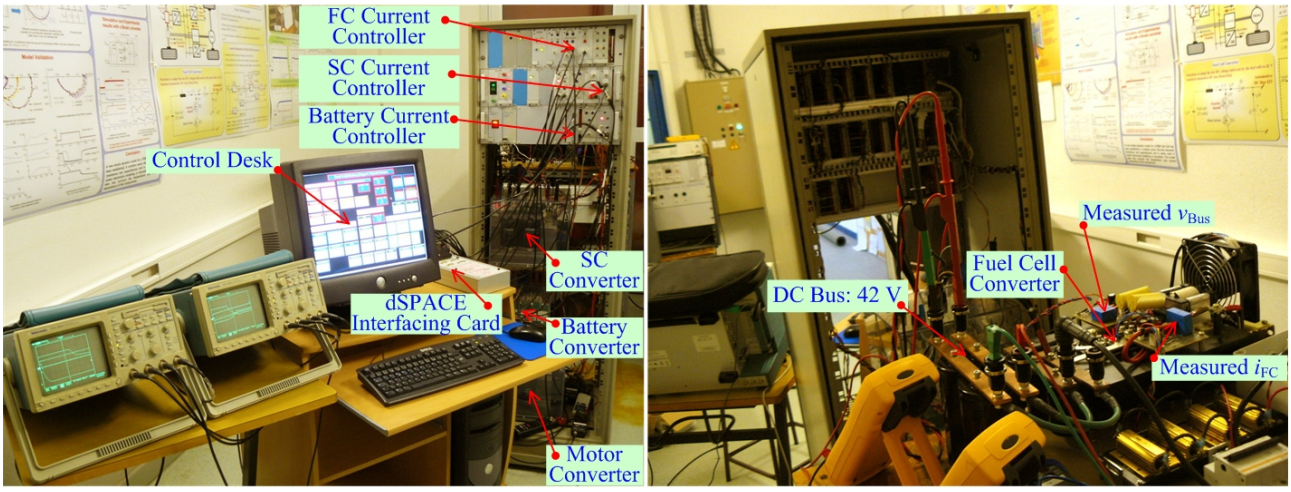

Fig. II.3.54. Test bench FC/SC/Battery hybrid power plant at the Groupe de Recherche en Electrotechnique et Electronique de Nancy (GREEN).

2) Experimental Results

Figs. II.3.55 and 56 portray waveforms obtained during a motor drive cycle. They present the dc bus, supercapacitor, battery, and FC voltages; supercapacitor, battery, and FC currents; load (or approximately as a motor power), supercapacitor, battery, and FC powers; and motor speed.

As portrayed in Fig. II.3.55, the initial state is zero for the load, supercapacitor, battery, and fuel cell powers. It means that the supercapacitor and battery modules are full of charge. One can observe the supercapacitor voltage is equal to the supercapacitor voltage reference of 26 V, and battery voltage is equal to the battery voltage reference of 25 V. At t = 4 s, the motor starts to the final speed of 800 rpm, so that the steady-state load power supplies by the FC, battery, and supercapacitor sources. It can be observed the following:

- The supercapacitor module supplies most of the transient power required during motor acceleration.
- The supercapacitor power is the fastest dynamics; the battery power is in the middle dynamics; then the FC power is the slowest dynamics.
- Synchronously, the supercapacitor power, after a sharp increase (discharging) during motor acceleration, decreases slowly to a constant discharge at around 160W.
- The steady-state load power is approximately 600W, totally supplied by the FC, battery, and supercapacitor sources. The FC operates at a maximum current of 25A, and the battery module is in the state of discharge with the constant discharging current I_{BatDis} of 20A.

As a final test, Fig. II.3.56 presents waveforms obtained at motor braking from an initial speed of 800 rpm to stop at t = 4 s. One can scrutinize the regenerative braking energy from the traction motor supplies back to the dc bus, demonstrating four phases as follows:

- First, the supercapacitor recovers the energy supplied to the dc link by the FC, the battery, and the motor regenerative braking.
- Second, the FC supplies power for charging the supercapacitor and battery storage devices.
- Third,when the supercapacitor module is nearly full of charge, the FC power slowly reduces to charging only the battery module.
- Fourth, the supercapacitor module is full of charge (V_{SCREF} = v_{SC}). Consequently, the FC supplies energy for only charging the battery.

Excellently, only little perturbations on the dc bus voltage can be seen during motor start/stop and the dynamics of FC and battery powers are reduced, which is of major importance in the proposed energy management hybrid power source.

D. Conclusion

The key objective of this section is to propose an original control algorithm for a dc distributed generation supplied by a fuel cell main source, and the perfect storage devices: supercapacitors and batteries. The combined utilization of batteries and supercapacitors is the perfect hybridization system of a high energy and high power density. The study mainly focuses on the FC, battery and supercapacitor taking account of the intrinsic energetic characteristics of these sources (i.e. energy and power densities, typical operating dynamics) in the energy management strategy. Hence, the control principle presents how to stay away from the fast transition of the FC and battery powers, and then reducing the FC and battery stresses. As a result, hybrid power source will increase its lifetime.

Experimental results in our laboratory carried out using a small scale test bench, which employs a PEMFC (500 W, 50 A), and storage devices composed of supercapacitor bank (292 F, 30 V) and lead-acid battery module (68 Ah, 24 V), corroborate the excellent performances of the proposed energy management during a motor drive cycle. During motor starts/stops or other significant steps in load, the storage elements provide the balance of energy needed during the momentary load transition period; and also absorbs excess energy from regenerative braking.

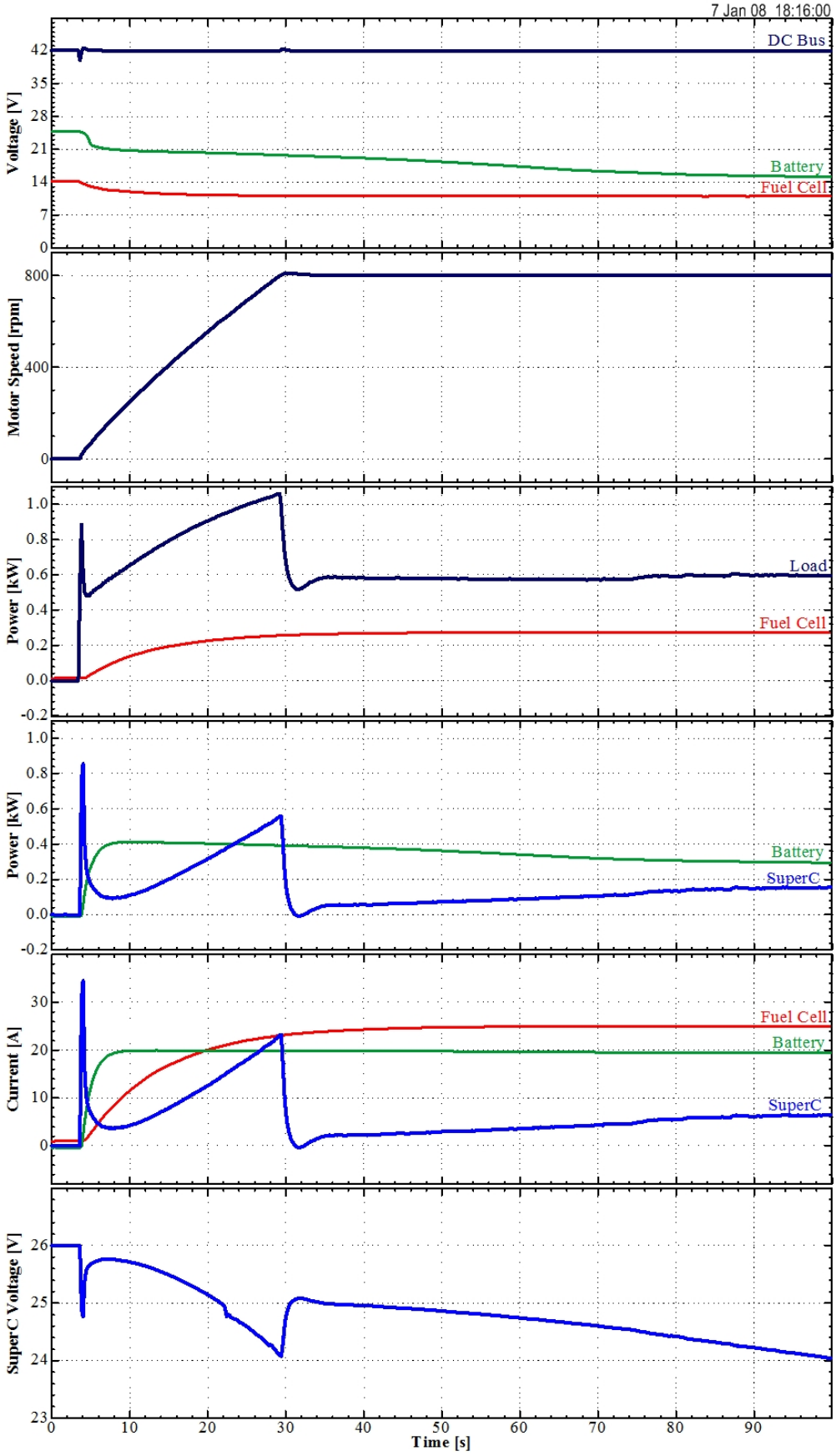

Fig. II.3.55. Experimental Result: Hybrid source response during motor starting to a final speed of 800 rpm.

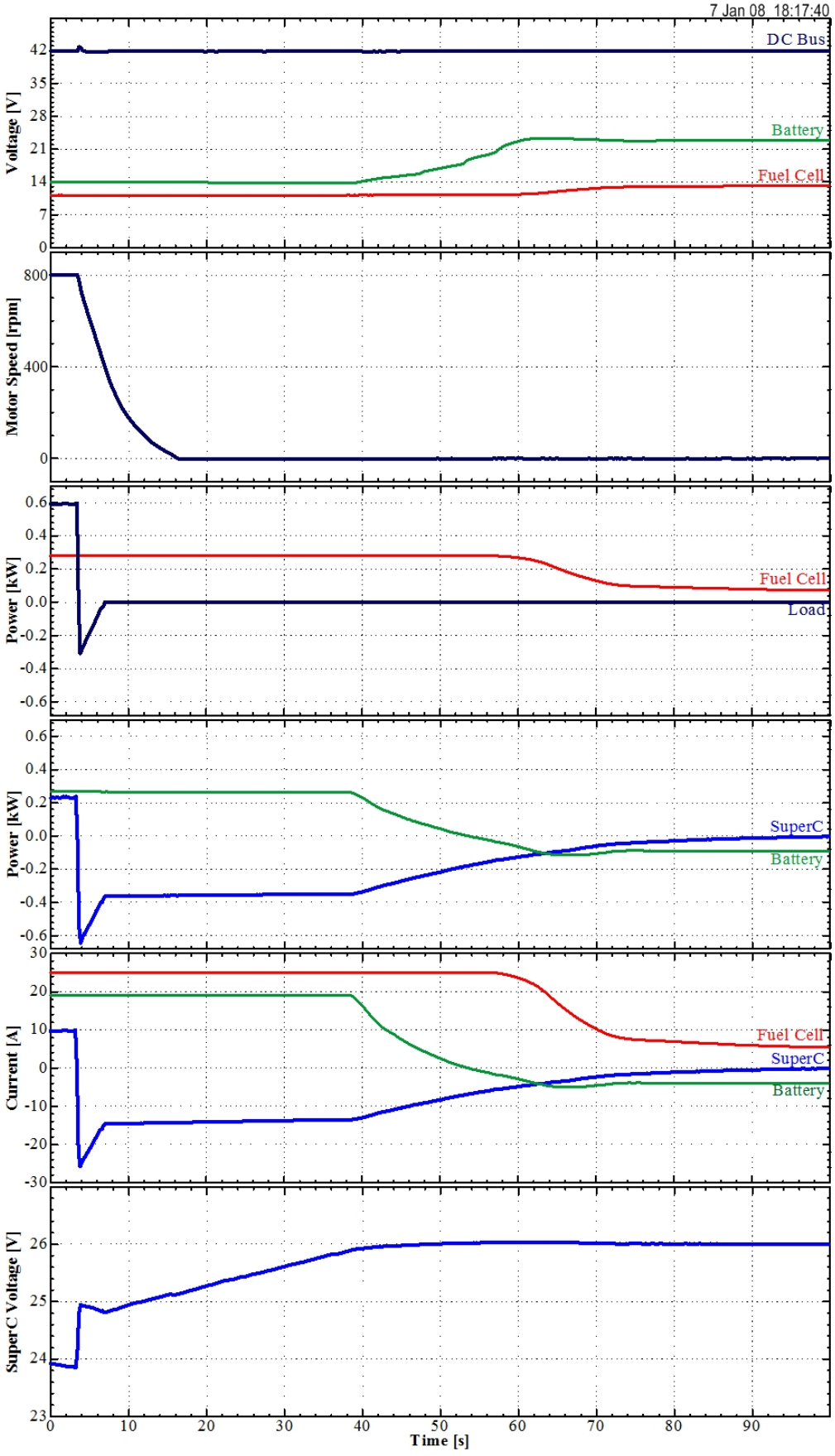

Fig. II.3.56. Experimental Result: Hybrid source response during motor braking from an initial speed of 800 rpm to stop.

II.3.3.4 Photovoltaic/supercapacitor hybrid power source [Tho11b]

A. System Description

In this section, we now study an uncomplicated design of a control system of the PV/SC power plant based upon the physical structure of the model. Fig. II.3.57 depicts the proposed hybrid source structure. The PV converter combines four-phase parallel boost converters with interleaving, and the SC converter employs four-phase parallel bidirectional converters with interleaving. The main contribution of this section is to present the differential flatness-based control approach of a solar power generation system with an SC storage device. In particular, we do not restrict ourselves to linear control techniques at an equilibrium point. This is the novel work in this domain.

For safety and dynamics, the PV and SC converters are primarily controlled by inner current regulation loops (or power regulation loops). These power control loops are supplied by two reference signals: the SC power reference p_{SCREF} and the PV power reference p_{PVREF}, generated by the control laws presented later.

For the PV power control, a PV power reference p_{PVREF} is divided by the measured photovoltaic voltage v_{PV}, resulting in a PV current reference i_{PVREF}. For the SC power control loop, an SC power reference p_{SCREF} is divided by the measured SC voltage vSC and limited to maintain the SC voltage within an interval [V_{SCMin}, V_{SCMax}], by the *SC current limitation function*. This calculation results in an SC current reference i_{SCREF}.

B. Energy Management

In the proposed system depicted in Fig. II.3.57, there are two voltage variables (or two energy variables) to be regulated.

1) The dc-bus energy y_{Bus} is the most important variable.

2) The SC storage energy y_{SC} is the next most important.

Therefore, we propose utilizing SCs, which are the fastest energy source in the proposed system, to supply the energy for the dc bus. In fact, we plan to functionalize the PV array by supplying energy only for charging the SC C_{SC}. However, during charging, the energy from the PV cell flows through the dc bus to the SC bank. For this reason, the PV array is mathematically operated to supply energy for both the dc-bus capacitor C_{Bus} and the SC C_{SC} to keep them charged.

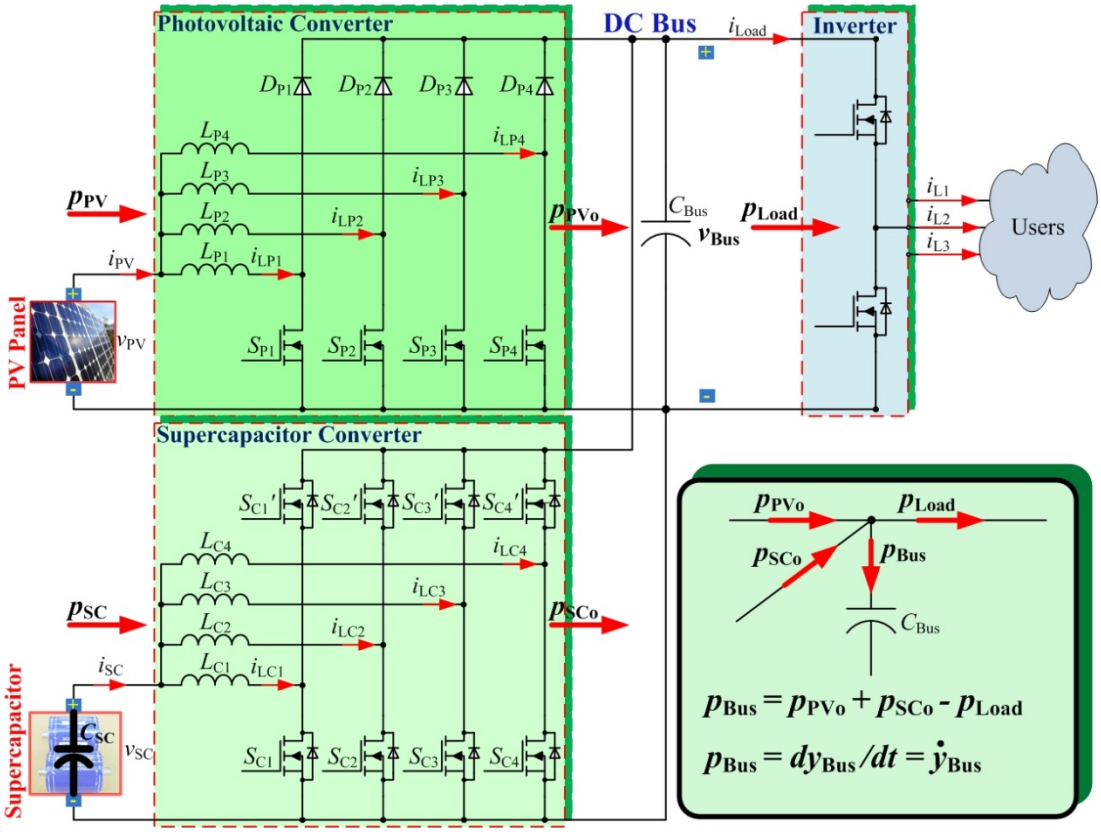

Fig. II.3.57. Proposed circuit diagram of the distributed generation system supplied by a PV and SC, where p_{Load} (= v_{Bus} × i_{Load}), v_{Bus}, and i_{Load} are the load power, the dc-bus voltage, and the dc-bus load current, respectively. p_{PV} (= v_{PV} ×iPV), v_{PV}, and i_{PV} are the PV power, voltage, and current, respectively. p_{SC} (= v_{SC} × i_{SC}), v_{SC}, and i_{SC} are the SC power, voltage, and current, respectively. p_{PVo} and p_{SCo} are the output powers to the dc link from the converters of the PV array and the SC, respectively.

In Fig. II.3.58, the proposed control algorithm of the renewable energy power plant, as detailed above, is depicted. The dc-bus energy control law generates a SC power reference p_{SCREF} [= u_1]. The total energy control law (or the supercapacitor energy control) generates a PV power demand p_{PVDEM} (= u_2). This signal must be saturated at the maximum power point by MPPT. It should be concluded here that, in this application, the PV does not always operate at its MPP in a stand-alone (grid-independent) scenario, as depicted in Fig. II.3.57.

C. Performance Validation

1) Power Plant Description for a Test Bench

To validate the performance of the modeling and control system, the small-scale test bench of the hybrid power plant was implemented in our laboratory, as presented in Fig. II.3.59. The prototype 0.8-kW PV converter and the 2-kW SC converter (refer to Fig. II.3.59) were implemented in the laboratory. Specifications of the PV module and storage device are detailed in Table II.3.6.

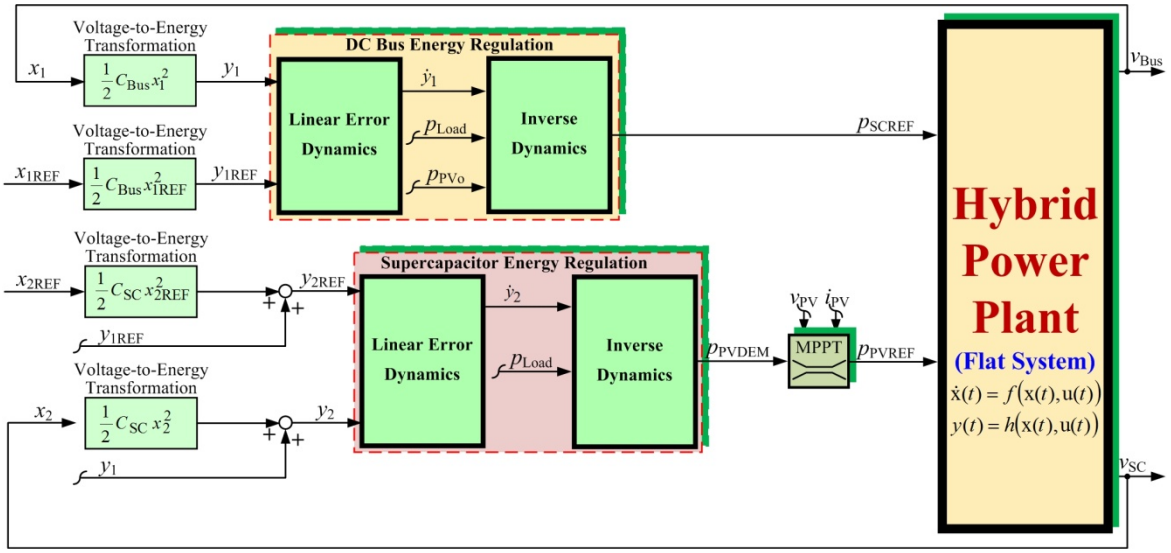

Fig. II.3.58. Multivariable control of a PV/SC hybrid power plant based on a differential flatness approach.

2) Control Description

The parameters associated with the dc-bus energy regulation loop are summarized in Table II.3.7. The parameters associated with the supercapacitor energy regulation loop are detailed in Table II.3.8. For the low-scale test bench, the dc bus voltage reference v_{BusREF} (= x_{1REF}) was set to 60 V and the supercapacitor voltage reference v_{SCREF} (= x_{2REF}) was set to 25 V (the nominal value of the supercapacitor bank).

The constant switching frequency ω_S of the PV and SC converters was 25 kHz (157,080 rad·s^{-1}). The controller gains used were K_{11} = 450 rad·s^{-1} and K_{12} = 22,500 rad^2·s^{-2} so that the system damping ratio ζ was equal to 1.5 and the natural frequency ω_n was equal to 150 rad·s^{-1}. As a result, the cutoff frequency (ω_E) of the closed-loop dc-bus energy was equal to 60 rad·s^{-1}. This value was lower than the cutoff frequency (ω_C) of the supercapacitor power loop of 450 rad·s^{-1} (equivalent to a first-order delay with a time constant T_C of 2.2 ms) so that the system was asymptotically stable. The controller gain of the closed-loop supercapacitive energy was K_{21} = 0.1 W·J^{-1} so that the cutoff frequency (ω_{SC}) of the closed-loop supercapacitive energy was equal to 0.1 rad·s^{-1} in which $\omega_{SC} << \omega_E$, in order to guarantee the asymptotic stability of the whole system.

The PV and SC current regulation loops and the electronic protections were realized by analog circuits. The two energy-control loops, which generate current references i_{PVREF} and i_{SCREF}, were implemented in the real-time card dSPACE DS1104 platform (see Fig. II.3.59) using the fourth-order *Runge–Kutta* integration algorithm and a sampling time of 80 μs within the mathematical environment of Matlab–Simulink.

Fig. II.3.59. Photograph of a test bench power plant. (a) solar cell panels, (b) SC bank, and (c) test bench.

TABLE II.3.6 SPECIFICATIONS OF PHOTOVOLTAIC SOURCE AND STORAGE DEVICE

Photovoltaic Array (by Ekarat Solar Company):		
Number of Panels in Parallel	4	
Panel Open Circuit Voltage	33.5	V
Panel Rated Voltage	26	V
Panel Rated Current	7.7	A
Panel Rated Power	200	W
Array Rated Power	800	W
Supercapacitor Bank (by Maxwell Technologies Comp):		
(Cell Model: BCAP1200)		
Number of Cells in Series	12	
Cell Capacity	1,200	F
Cell Maximum Voltage	2.7	V
Bank Capacity (C_{SC})	100	F
Bank Maximum Voltage	32	V

TABLE II.3.7 DC-BUS ENERGY CONTROL LOOP PARAMETERS

v_{BusREF}	60	V
C_{Bus}	12200	μF
K_{11}	450	rad·s^{-1}
K_{12}	22,500	rad^2·s^{-2}
r_{PV}	0.12	Ω
r_{SC}	0.10	Ω
V_{SCMax}	32	V
V_{SCMin}	15	V
$I_{SCRated}$	150	A

TABLE II.3.8 SUPERCAPACITIVE ENERGY CONTROL LOOP PARAMETERS

v_{SCREF}	25	V
C_{SC}	100	F
K_{21}	0.1	$W \cdot J^{-1}$
p_{PVMax} (Rated)	800	W
I_{PVMax} (Rated)	30.8	A
I_{PVMin}	0	A
ΔI_{PV}	0.1	A
Δt	6	ms

3) Experimental Results

Because flatness-based control is model-based, it may have some sensitivity to error in model parameters. To authenticate its robustness, the flatness-based control was tested with the exact model parameters (r_{PV} = 0.12 Ω, r_{SC} = 0.10 Ω) and the erroneous parameters case (r_{PV} = 0.001 Ω, r_{SC} = 0.001 Ω). For the sake of the dc bus voltage stabilization and robust control system, the oscilloscope waveforms in Fig. II.3.60 show the comparison (robustness) between the accurate parameters and the error parameters. It portrays the dynamic characteristics that are obtained during the large load step. It shows the dc bus voltage, the load power (disturbance), the SC power, and the SC voltage. The initial state is in no-load power, the SC storage device is full of charge, i.e., the SC voltage = 25 V (v_{SCREF} = 25 V), and the dc bus voltage is regulated at 60 V (v_{BusREF} = 60 V); as a result, the PV and SC powers are zero. At t = 20 ms, the large load power steps from 0 W to a constant value of 400 W (positive transition). Because during the transient state the PV power is limited by MPPT estimation, the supercapacitor supplies the transient load power demand. One can scrutinize the similar waveforms in Fig. II.3.60(a) and Fig. II.3.60(b). The dc bus voltage (dc link stabilization) is minimally influenced by the large load power step. Clearly the performance of the control system is minimally affected by the model parameter error considered. Experimental testing demonstrates that errors in these parameters had relatively little effect on regulation performance, and we conclude that the nonlinear differential flatness-based approach provides a robust controller in this application.

Finally, for the sake of the dc bus voltage stabilization and load profile (load cycles), Fig. II.3.61 presents waveforms that are obtained during the load cycles measured on December 18, 2009 at an ambient temperature of around 25 degree Celsius. In Figure, the dc bus voltage, the PV voltage, the load power (disturbance), the SC power, the PV power, the SC current, the PV current, and the SC voltage are shown. In the initial state, the small load power is equal to 100 W, and the storage device is full of charge, i.e., v_{SC} = 25 V; as a result, the SC power is zero, and the PV source

supplies 100 W of power for the load. At 09:00:50, the load power steps to the final constant power of around 450 W (positive load power transition). We observe the following phenomena:

- The supercapacitor supplies most of the transient power that is required during the step load.
- Simultaneously, the PV power increases to a MPP around 250 W, which is limited by the MPPT.
- Concurrently, the supercapacitor remains in a discharge state after the load step because the steady-state load power (approximately 450 W) is greater than the power supplied by the PV array.

After that phase, one can again observe that the power plant is always energy balanced ($p_{Load} = p_{PV} + p_{SC}$) by the proposed original control algorithm. One can observe that the dc-bus voltage waveform is asymptotically stable during the large load cycles, which is of major importance when employing supercapacitors to improve the dynamic performance of the whole system using the proposed control law.

D. Conclusion

The main contribution of this paper is to model and control a PV/SC hybrid power plant. The prototype power plant is composed of a PV array (800W, Ekarat Solar) and an SC module (100 F, 32 V, Maxwell Technologies). A compact topology, suitable for high-power applications, is proposed. Its working principle, analysis, and design procedure are presented. The PV array is the main source, and the SC functions as a storage device (or an auxiliary source) to compensate for the uncertainties of the PV source in the steady state and the transient state. An SC can advance the load, following the characteristics of the main sources, by providing a stronger power response to changes in the system load. Adding energy storage to the distributed power systems improves power quality and efficiency.

We propose a simple solution to the dynamic, stabilization, and robustness problems in the nonlinear power electronic system. And also, there are no operating points comparable with a classical linear control. This is a novel concept for this kind of application. However, the proposed control lawneeds a load current measurement to estimate the load power. For future work, a load observer will be used to avoid a measurement of a load current, as was explored in [Gen09].

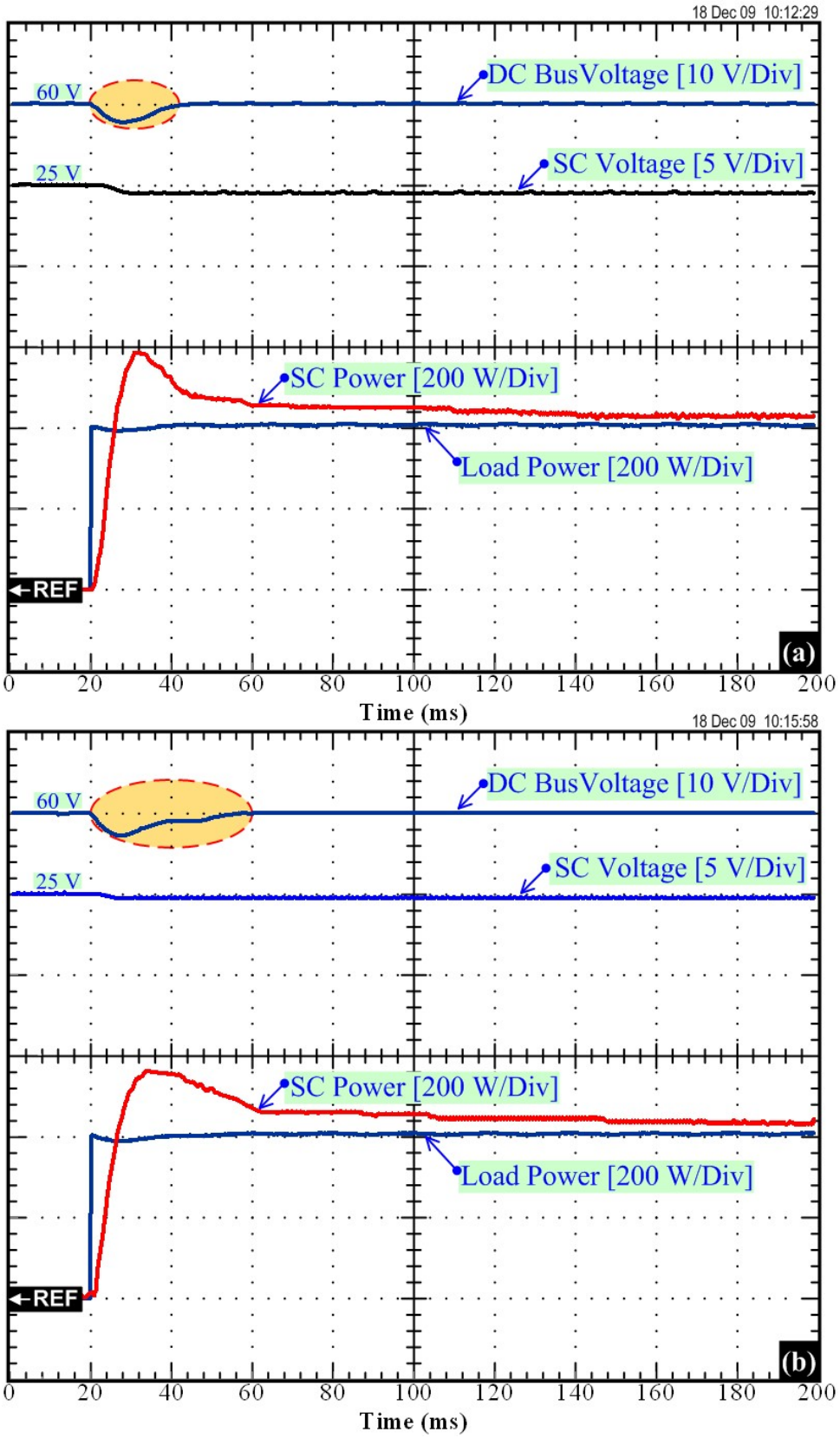

Fig. II.3.60. Experimental Result: Comparison of the DC link stabilization of the power plant during a large load step. (a) exact model (r_{PV} = 0.12 Ω, r_{SC} = 0.10 Ω). (b) error model (robustness) (r_{PV} = 0.001 Ω, r_{SC} = 0.001 Ω).

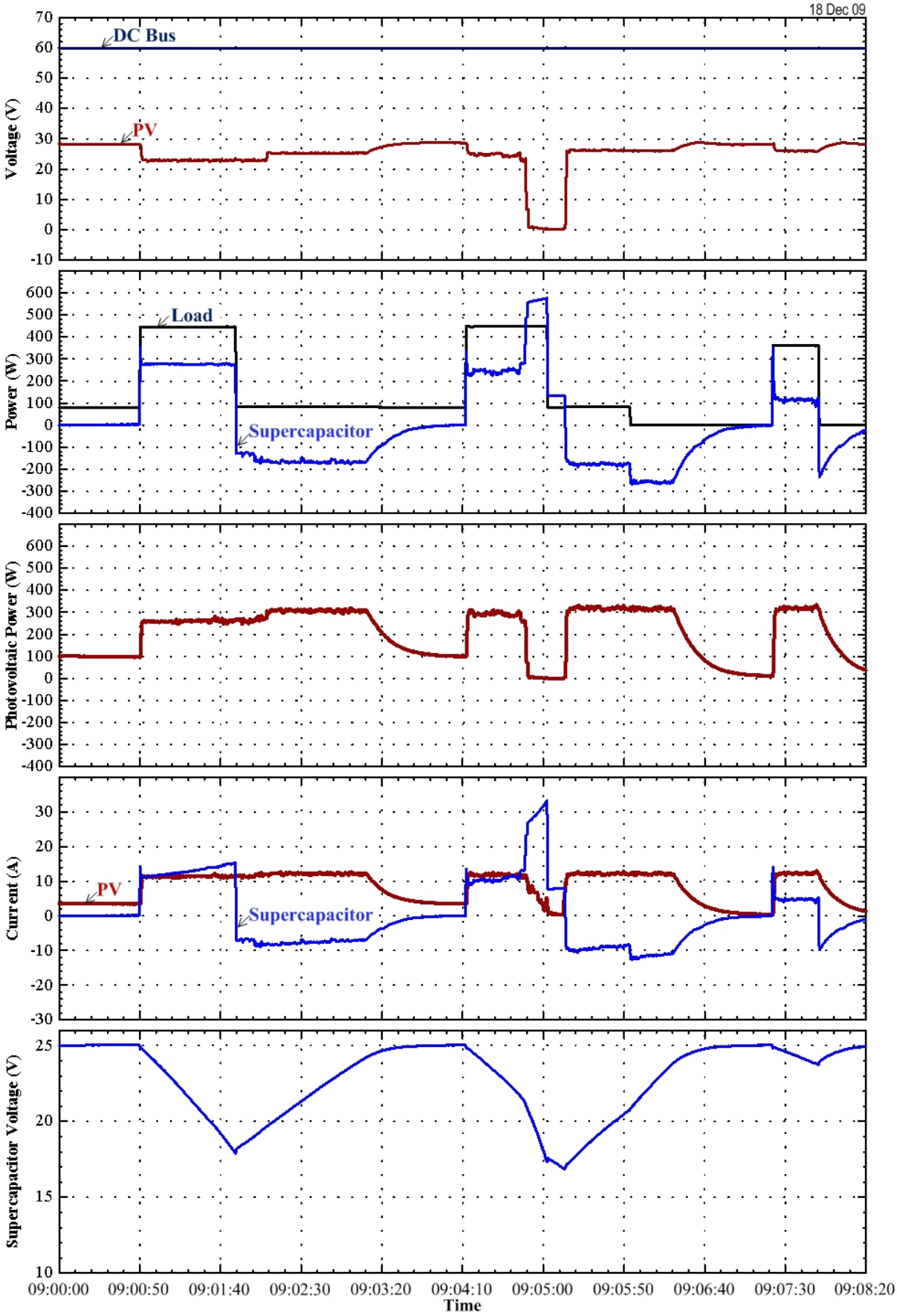

Fig. II.3.61. Experimental Result: Power plant response during load cycles.

II.3.3.5 Fuel cell/photovoltaic/supercapacitor hybrid power source [Tho11a]

A. System Description

A combination of PV and FC sources forms a good pair with promising features for distributed generation applications. Obviously, the slow response of the PEMFC [Rav11], [Azi11] needs to be compensated with a supercapacitor or a battery. A supercapacitor storage device is preferable due to its high power density, high dynamics, and long lifetime [Wed11].

The fast response, efficiency, and stability of the operation of hybrid power plants are of particular interest. In this work, a hybrid power generation system is studied, consisting of the following main components: a PV, PEMFC, and an SC as a high-power density device, see Fig. II.3.62. In this study, a novel framework is proposed for the nonlinear system based flatness control approach of a solar-hydrogen power generation system with a supercapacitor storage device.

We consider that the PV, FC, and SC currents follow their reference values perfectly. This is a classical assumption used in the cascade control structure in order to estimate the external control loop. However, the assumption error will be compensated by the intelligent external control loop. Then, the inner control loops of the PV, FC and SC powers can be approximated as a unity gain. The PV power reference is defined as p_{PVREF}, the FC power reference p_{FCREF}, and the SC power reference p_{SCREF}.

B. Energy Management of Hybrid Power Source

The main control objectives are stability, high overall efficiency, and fast response. As for supplying energy to the load demanded and the charging storage device, the multivariable control here involves set-point control of the dc-bus voltage v_{Bus} (representing the dc-bus energy y_{Bus}, called "*DC link stabilization*") and set-point control of the SC voltage v_{SC} (representing the supercapacitive energy y_{SC}).

The principle behind the proposed hybrid energy management lies in using the SCs (the fastest energy source) to supply the energy required to achieve the dc grid voltage regulation (or the dc bus energy regulation) [Tho07]. Then, the PV and FC, although clearly the main energy source of the system, function as the generator that supplies energy for both the dc bus capacitor C_{Bus} and the C_{SC} to keep them charged.

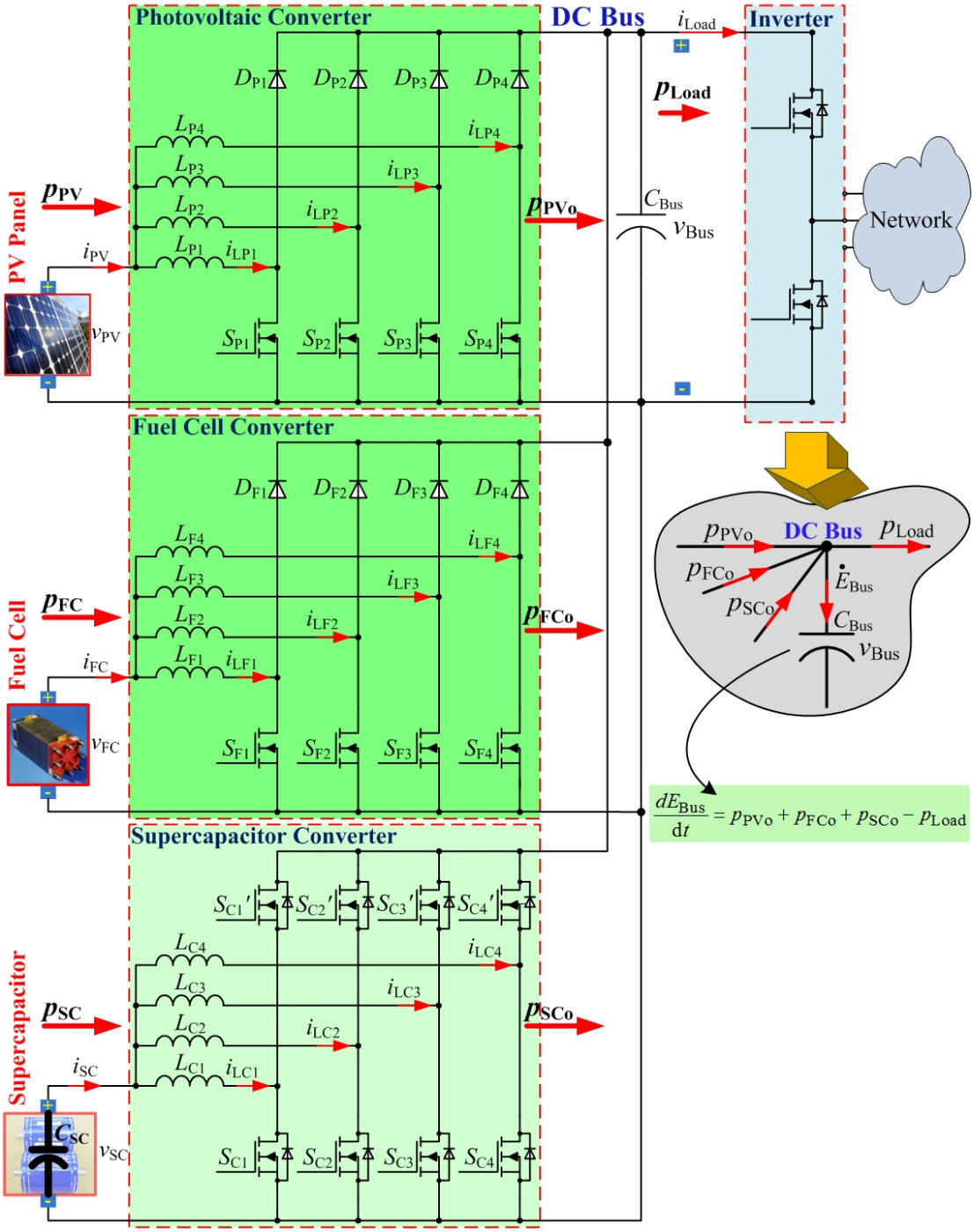

Fig. II.3.62. Proposed circuit diagram of power plant supplied by an FC, a PV and SC.

C. Performance Validation

1) Test Bench Description

To authenticate the performance of the modeling and control system, a test bench was implemented. The small-scale test bench of the renewable power plant was implemented in our laboratory, as presented in Fig. II.3.63. Moreover, the test bench diagram may be seen in Fig.

II.3.64. The prototype FC converter of 1 kW, the PV converter of 0.8 kW, and the SC converter of 2 kW (refer to Fig. II.3.63) were realized in the laboratory. Specifications of the real power sources and storage device are detailed in Table II.3.8. Note that the PV panel is installed on the roof of the laboratory building (Fig. II.3.63). It means that the PV energy production is directly from the sun.

Fig. II.3.63. Photograph of the experimental setup at the Renewable Energy Research Centre (RERC), Bangkok.

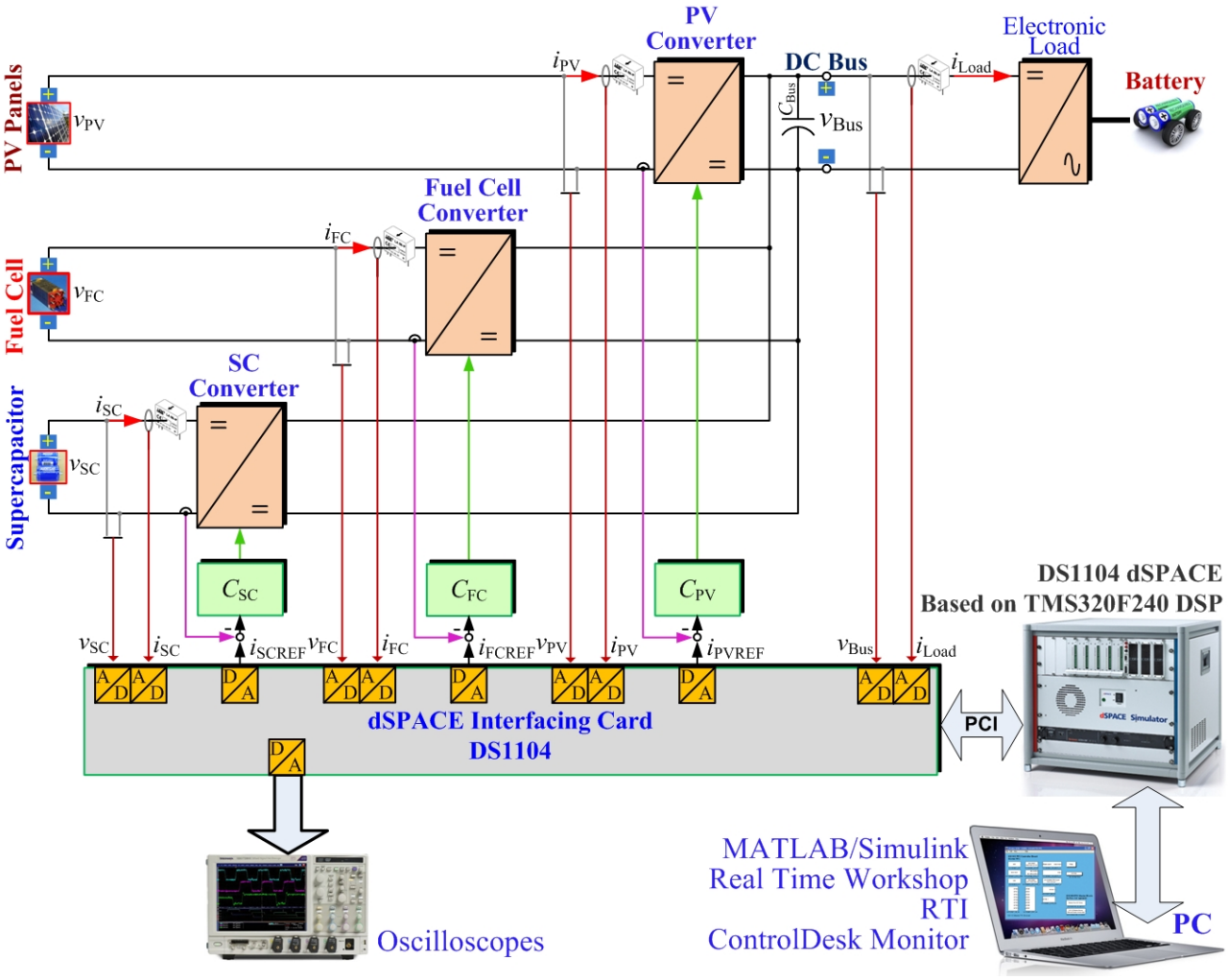

Fig. II.3.64. Test bench diagram.

TABLE II.3.8 SPECIFICATIONS OF POWER SOURCES AND STORAGE DEVICE

Fuel Cell System (by Ballard Power Systems Inc):		
Rated Power	1,200	W
Rated Current	46	A
Rated Voltage	26	V
Photovoltaic Array (by Ekarat Solar Company):		
Number of Panels in Parallel	4	
Panel Open Circuit Voltage	33.5	V
Panel Rated Voltage	26	V
Panel Rated Current	7.7	A
Panel Rated Power	200	W
Array Rated Power	800	W
Supercapacitor Bank (by Maxwell Technologies Comp): (Cell Model: BCAP1200)		
Number of Cells in Series	12	
Cell Capacity	1,200	F
Cell Maximum Voltage	2.7	V
Bank Capacity (C_{SC})	100	F
Bank Maximum Voltage	32	V

2) Control Description

Measurements of the FC current i_{FC}, the PV current i_{PV}, the SC current i_{SC}, the load current i_{Load}, the DC link voltage v_{Bus}, the FC voltage v_{FC}, the PV voltage v_{PV}, and the SC voltage v_{SC} are collected with zero-flux Hall effect sensors. The FC, the PV and the SC current regulation loops were realized by analog circuits to function at a high bandwidth. Parameters associated with the DC bus energy regulation loop and the SC energy regulation loop can be seen in Tables II.3.9 and 10, respectively. The FC power dynamic delay is shown in Table I.3.10; this value was experimentally determined as the highest power slope of the FC system, where no fuel starvation occurs. It must be noted here that, for the small-test bench, the FC maximum power p_{FCMax} is set at 500W; but, the rated FC power considered here is 1200 W. Further, these two energy control loops, which generate current references i_{FCREF}, i_{PVREF} and i_{SCREF} are implemented on the real time card dSPACE DS1104 through the mathematical environment of Matlab–Simulink with a sampling frequency of 25 kHz.

TABLE II.3.9 DC BUS ENERGY CONTROL LOOP PARAMETERS.

Parameter	Value	
v_{BusREF}	60	V
C_{Bus}	12200	μF
K_{11}	450	$rad \cdot s^{-1}$
K_{12}	22,500	$rad^2 \cdot s^{-2}$
r_{FC}	0.14	Ω
r_{PV}	0.12	Ω
r_{SC}	0.10	Ω
V_{SCMax}	32	V
V_{SCMin}	15	V
$I_{SCRated}$	150	A

TABLE II.3.10 SUPERCAPACITOR ENERGY CONTROL LOOP PARAMETERS.

Parameter	Value	
v_{SCREF}	25	V
C_{SC}	100	F
K_{21}	0.1	$W \cdot J^{-1}$
p_{PVMax} (Rated)	800	W
p_{PVMin}	0	W
I_{PVMax} (Rated)	28	A
I_{PVMin}	0	A
p_{FCMax}	500	W
p_{FCMin}	0	W
I_{FCMax} (Rated)	46	A
I_{FCMin}	0	A
ζ_1	1	
ω_{n1}	0.4	$rad \cdot s^{-1}$

3) Experimental Results

The studied DC bus of 60V is only connected to an electronic load. To validate the dynamics of the power (current) regulation loops for each power source, Figs. II.3.65–67 present waveforms that are obtained during the stepped power demand. Fig. II.3.65 illustrates the FC power demand, power response, voltage and current. Fig. II.3.66 contains the PV power demand, power response, voltage and current. Finally, Fig. II.3.67 illustrates the SC power demand, power response, voltage and current. The SC power dynamics are very fast. The SC can supply power from 0 to 400W in 50 ms. It is clear that the fast response of the SC storage device can be operated with the FC and PV main generators in order to improve system performance. The data in Fig. II.3.65 also confirm that the FC is controlled to avoid the fuel starvation phenomenon.

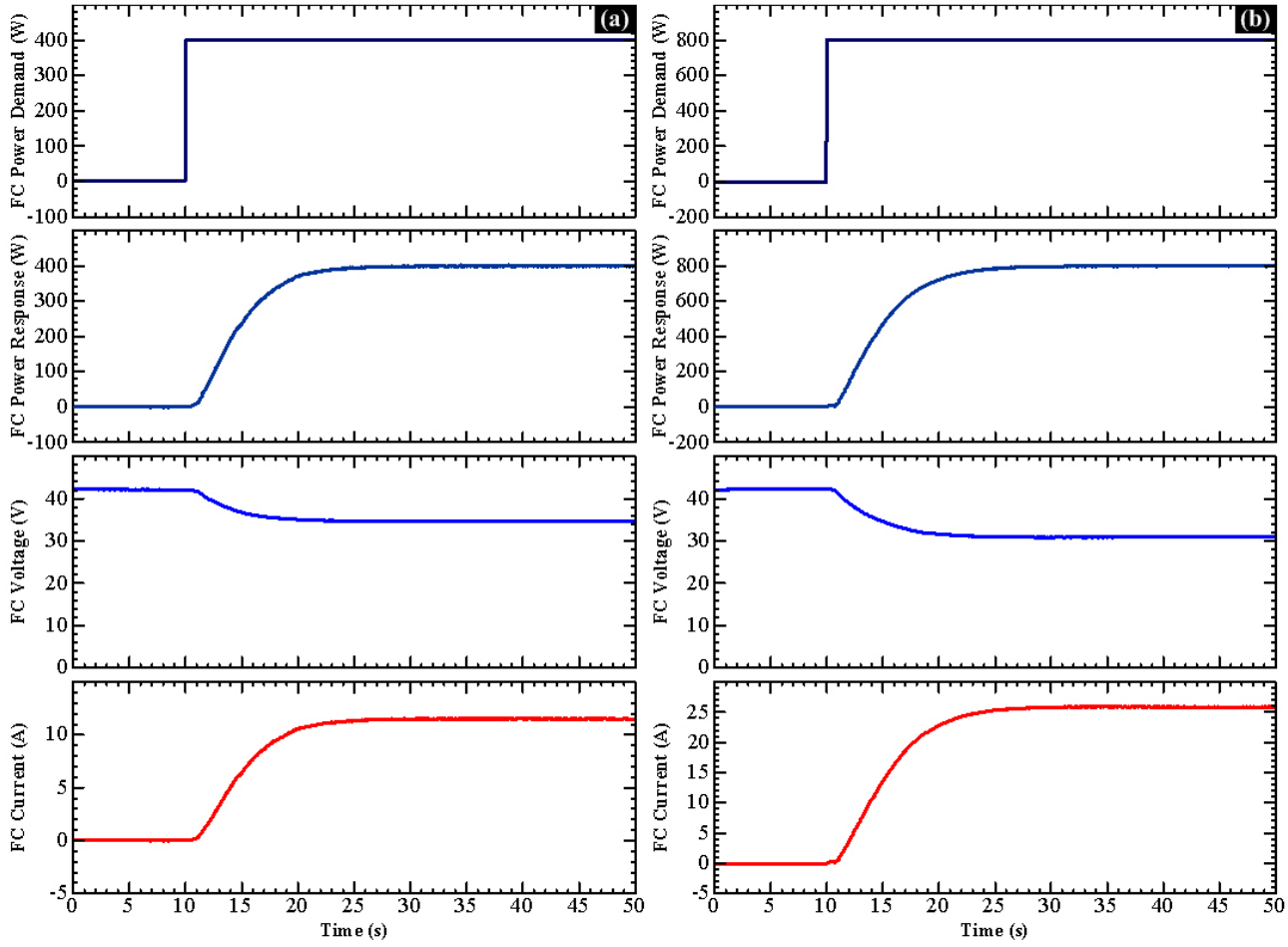

Fig. II.3.65. Experimental Result: Dynamic identification of FC power control loop, (a) p_{FCSet}: 0 – 400 W, (b) p_{FCSet}: 0 – 800 W.

Because flatness-based control is model-based, it may have some sensitivity to errors in the model parameters. To authenticate its robustness, the flatness-based control was tested with the exact model parameters (r_{FC} = 0.14 Ω, r_{PV} = 0.12 Ω, r_{SC} = 0.10 Ω) and in the lossless parameters

case (r_{FC} =0 Ω, r_{PV} = 0 Ω, r_{SC} =0 Ω). In the case of no losses, this leads to a drastically less complex estimation of the control law. Comparisons (robustness) between the accurate parameters and the error parameters are given in Fig. II.3.68. They generate waveforms that are obtained during the large load step from 0 to 500 W and show the DC bus voltage, the load power (disturbance), the SC power, and the SC voltage (storage *SOC*). Because the power of the FC and the PV are slow responses, the SC supplies the transient load power demand. The DC bus voltage (DC link stabilization) is minimally influenced by the large step in load power. Clearly the performance of the control system is hardly affected by the considered error in model parameters. Experimental testing demonstrates that errors in these parameters have relatively little effect on regulation performance. It is therefore conclude that the non-linear differential flatness-based approach provides an absolutely robust controller in this application.

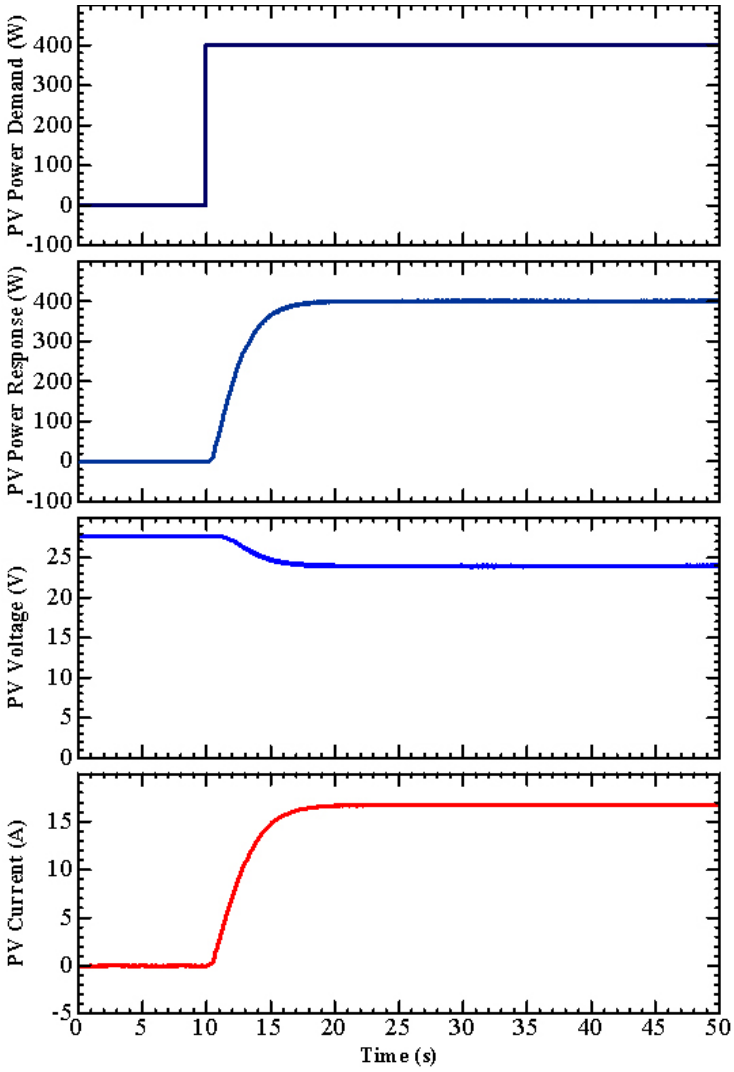

Fig. II.3.66. Experimental Result: Dynamic identification of PV control loop.

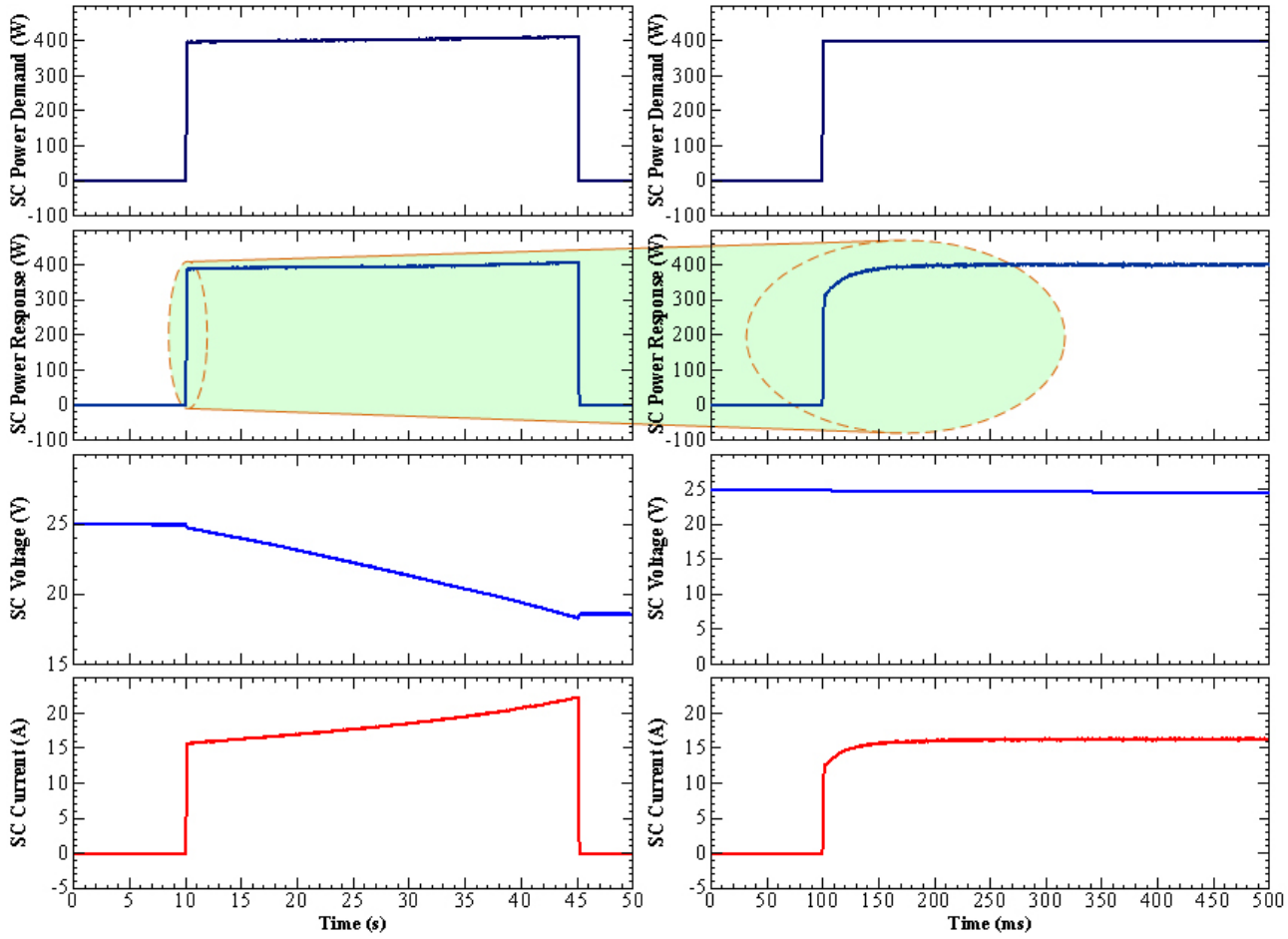

Fig. II.3.67. Experimental Result: Dynamic identification of SC power control loop.

Waveforms obtained during the large load cycle are presented in Fig. II.3.69. The data show the DC bus voltage, the FC voltage, the PV voltage, the load power, the SC power, the FC power, the PV power, the SC current, the FC current, the PV current, and the SCvoltage (or the SC *SOC*). In the initial state, the small load power is equal to 100 W, and the storage device is fully charge, i.e., v_{SC} = 25 V; as a result, both the FC and SC powers are zero, and the PV source supplies power for the load of 100 W. At t = 40 s, the load power steps to the final constant power of around 900W (positive load power transition). The following observations are made:

- The SC supplies most of the 900W power that is required during the transient step load.
- Simultaneously, the PV power increases to a maximum power point (MPP) of around 300 W, which is limited by the maximum power point tracker (MPPT).
- Concurrently, the FC power increases with limited dynamics to a maximum power of 500 W.

- The input from the SC, which supplies most of the transient power that is required during the stepped load, slowly decreases and the unit remains in a discharge state after the load step because the steady-state load power (approximately 900W) is greater than the total power supplied by the FC and photovoltaic array.

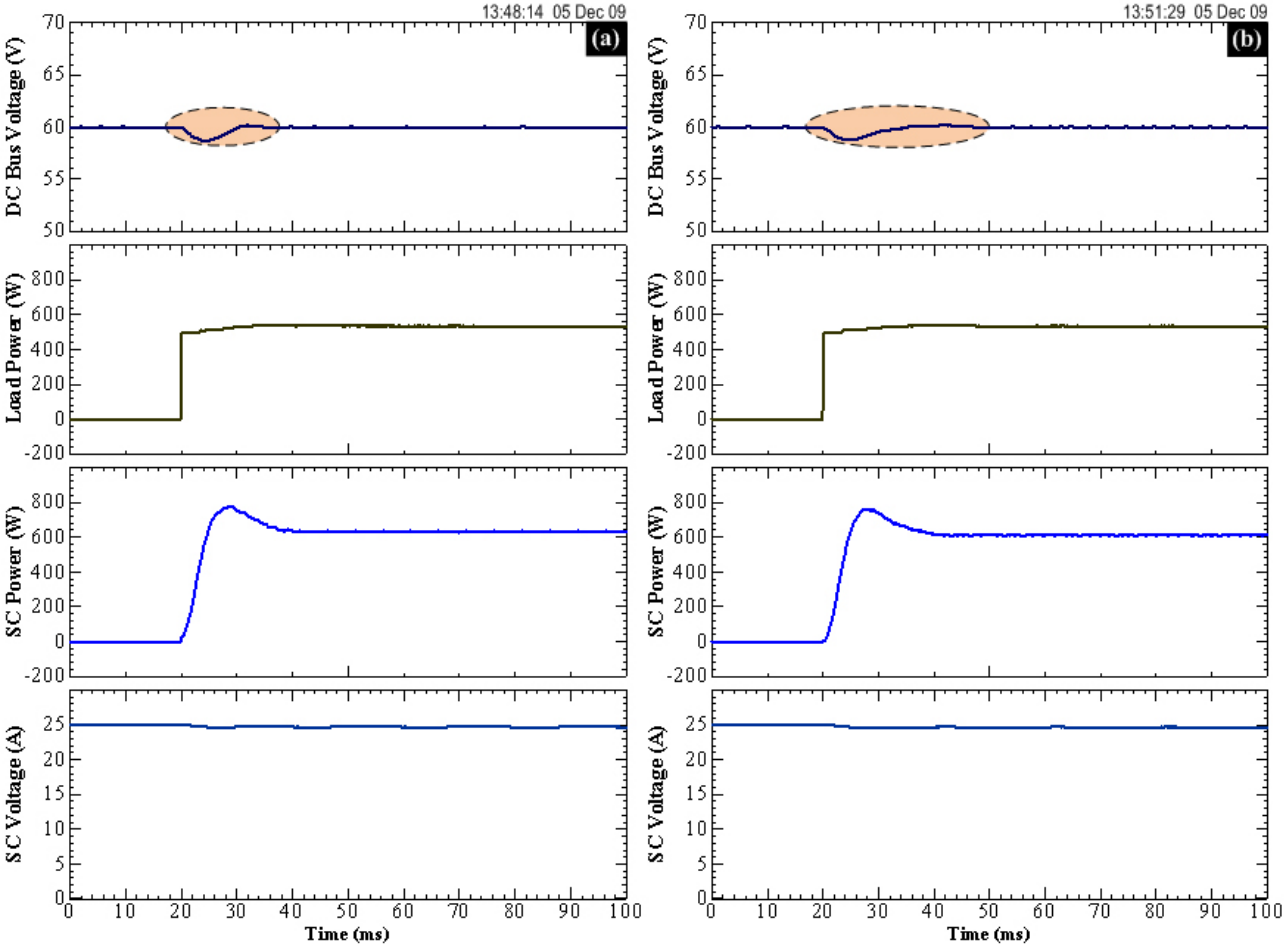

Fig. II.3.68. Experimental Result: Comparison of d.c. link stabilization of hybrid energy source during large load step.
(a) exact model (r_{FC} = 0.14 Ω, r_{PV} = 0.12 Ω, r_{SC} = 0.10 Ω) and
(b) error model (robustness) (r_{FC} =0 Ω, r_{PV} =0 Ω, r_{SC} =0 Ω).

At t = 100 s, the SC voltage is equal to 19 V. As a result, the SC supplies its stored energy y_{SC} to the DC bus. This energy y_{SC_Supply} is estimated to be:

$$y_{SC\_Supply} = \frac{1}{2}C_{SC}v_{SC}^2(t=40\,s) - \frac{1}{2}C_{SC}v_{SC}^2(t=100\,s) = 13.20 \quad \text{kJ} \tag{2.69}$$

The load power is reduced from the high constant power of 900 W to the low constant power of 100W (negative load power transition). As a result, the SC changes from discharging to charging and demonstrates the following four phases:

- First, the FC and photovoltaic array still supply their constant maximum powers to drive the load and to charge the supercapacitor.
- Second, at t = 110 s, the supercapacitor is approaching full charge, i.e., v_{SC} = 23 V. Consequently, the FC power is reduced with limited power dynamics.
- Third, at t = 120 s, the supercapacitor is nearly fully charged, i.e., v_{SC} = 24 V. As a result, the photovoltaic power is reduced.
- Fourth, at t = 160 s, the supercapacitor is fully charged, i.e., v_{SC} = v_{SCREF} = 25 V. After slowly decreasing, the photovoltaic power remains at a constant power of 100W for the load power demanded. Furthermore, the FC and SC powers are zero.

It is evident that the DC bus voltage waveform is stable during the large load cycle, which is critically important when employing supercapacitors to improve the dynamic performance of the whole system using the proposed control law.

Finally, Fig. II.3.70 presents waveforms that are obtained during the long load cycles measured on 5 December, 2009. The waveforms are similar to the test bench results in Fig. II.3.69. During the experiment, the FC maximum power was set to 500 W, and the PV maximum power (depending on solar radiation, weather conditions and temperature) was limited by the MPPT. For example, at 15:01:40, the PV maximum power was approximately equal to 180W; at 15:02:30, the PV maximum power was about 180W; at 15:03:20, the PV maximum power was around 180W; and from 15:05:50 to 15:08:20, the PV maximum power was reduced to 0W, because of the cloudy conditions. In particular, it was found that the power plant was always energy balanced $p_{Load} \approx p_{FC} + p_{PV} + p_{SC}$ by the proposed original control algorithm.

The important variable necessary to balance the energy in this complex system is the DC bus energy or voltage. From the experimental validations, the DC bus voltage is automatically controlled at the constant set-point, i.e., v_{Bus} = 60 V. This experiment confirms that the energy in the system is well managed. The FC and PV powers are limited at their maximum powers, and the FC power dynamics are controlled; as a result, there is no fuel starvation problem and the fuel cell stack lifetime is increased [You09], [Has09], [Ett09].

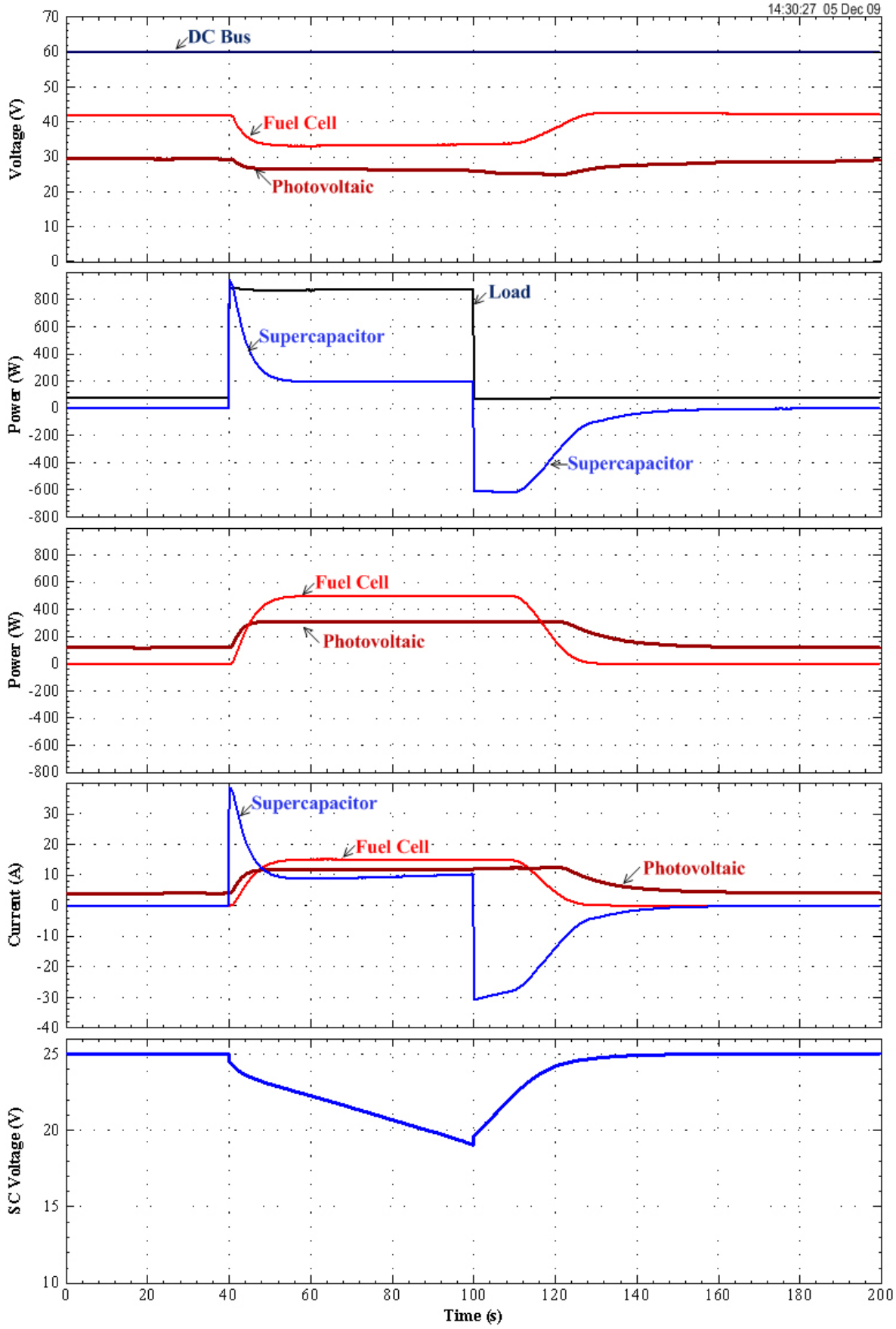

Fig. II.3.69. Experimental Result: Hybrid source response during load cycle.

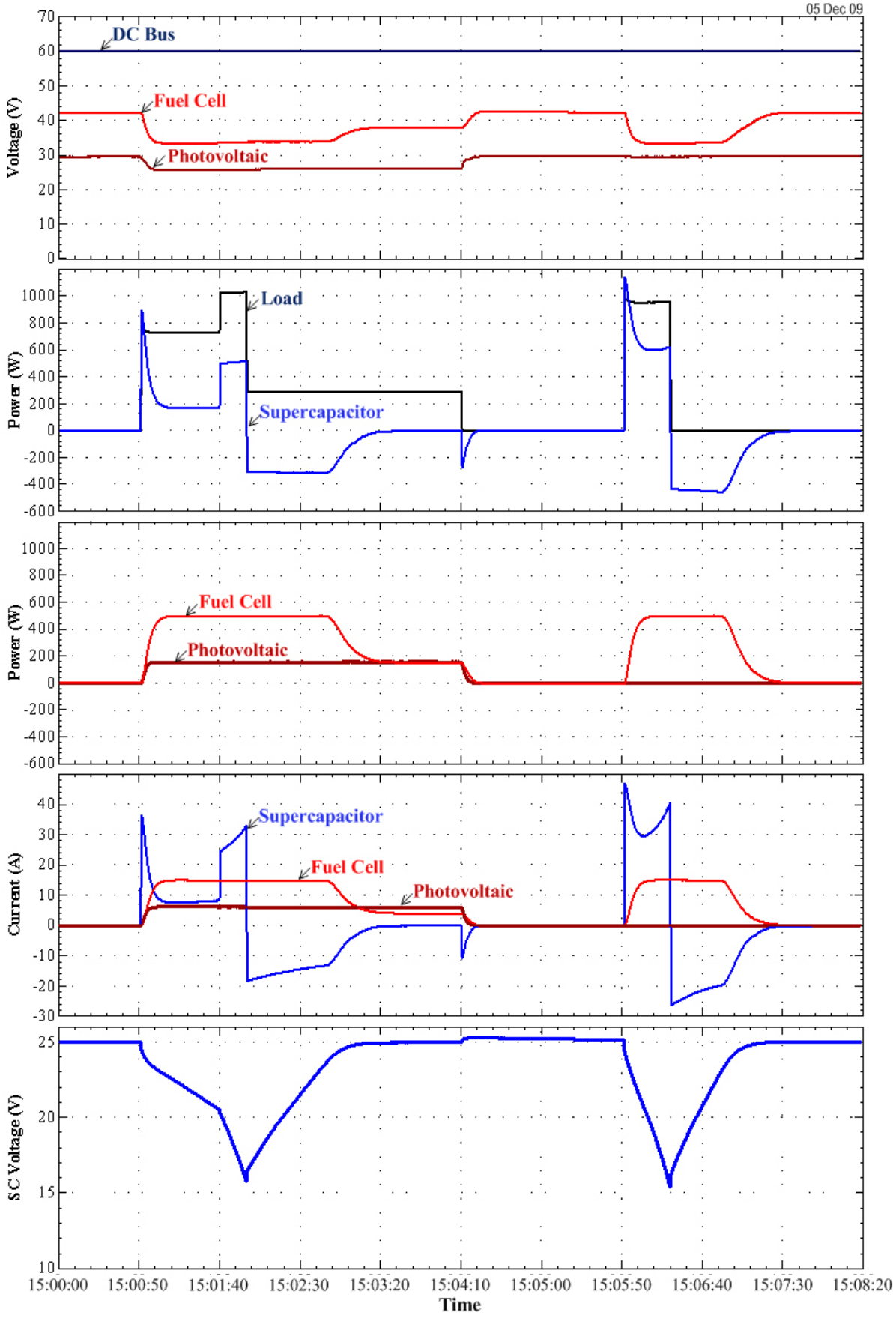

Fig. II.3.70. Experimental Result: Hybrid source response during long load cycles.

D. Conclusion

Energy management of multi-power sources has been proposed in this section as a solution for a hybrid energy system that uses renewable energy from PV, FC and a SC as an energy storage device. A SC can advance the load, following the characteristics of the main sources by providing a stronger power response to changes in the system load. During essential steps in the load, the SC provides the energy balance needed during load transition periods. Adding energy storage to the distributed power systems improves power quality and efficiency.

Experimental verification with a small-scale hybrid test bench (Nexa Ballard fuel cell power generator: 1.2 kW, 46A; Ekarat PV power module: 800 W, 31 A; Maxwell supercapacitor storage device: 100 F, 32 V) has demonstrated the excellent performance of the whole system, and has validated the proposed energy management principle.

III.1 Research Perspective

Since 2003, I have done a lot of works on DC/DC converter for FC, PV, battery, and supercapacitor sources, and energy managements for dc distributed system based on a classic linear control and a differential flatness approach for hybrid systems: FC/SC, FC/Battery, FC/Battery/SC, PV/SC, etc… So, there are five main topics of my works for maybe next 15 years:

1). AC/DC converter (Power Factor Correction PFC).
2). DC/DC converter.
3). DC/AC converter (Inverter) with grid connection.
4). Energy management of hybrid system for DC grid.
5). Electrical Machine Drives.

In power electronic systems there has been a continuous trend towards a higher system power density in the last decades and due to environmental concerns and rising energy costs, also the efficiency of the systems became an important system performance criteria, over the past years besides costs. For meeting these demands, the development of power semiconductors is a crucial enabling factor besides passive components, control, cooling and EMC.

With the recent technological progress in manufacturing power devices based on wide band gap materials as e.g. silicon carbide (SiC) or gallium nitride (GaN), the operating voltage range, the switching speed and/or specific on-resistance have been and will be improved significantly compared to silicon power devices (Fig. III.1 and 2). In case these new devices are applied in power electronic systems, the improvements on the device level will impact also the system performance, which is usually measured by power density, efficiency, weight, reliability, and costs.

Why SiC MOSFETs for Future Project?

To appreciate the capabilities of SiC MOSFETs it's useful to compare them to their Si counterparts. SiC devices can block 10x more voltage than silicon, have a higher current density, can transition between the on and off states 10x faster, and have lower on-state resistance. For example, a 900 volt SiC MOSFET can provide the same on-state resistance as Si MOSFETs in a chip size 35x smaller (Fig. III.1).

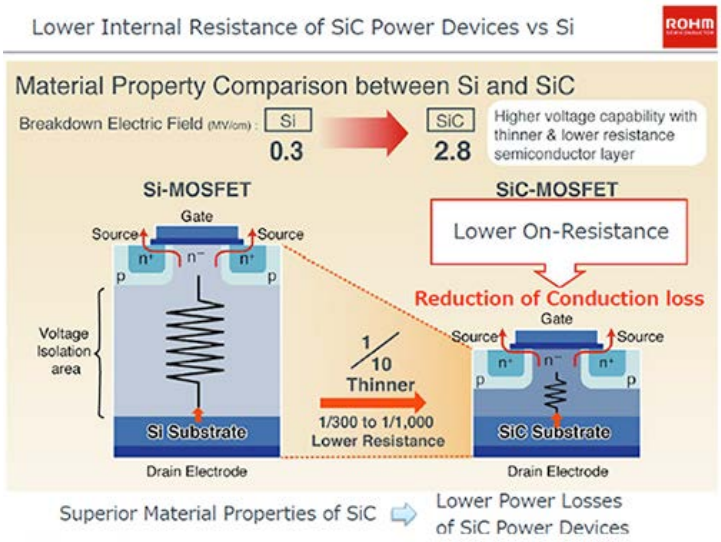

Fig. III.1. SiC MOSFETs (right) offer lower on-state resistance and higher voltage capability, compared to Si devices.

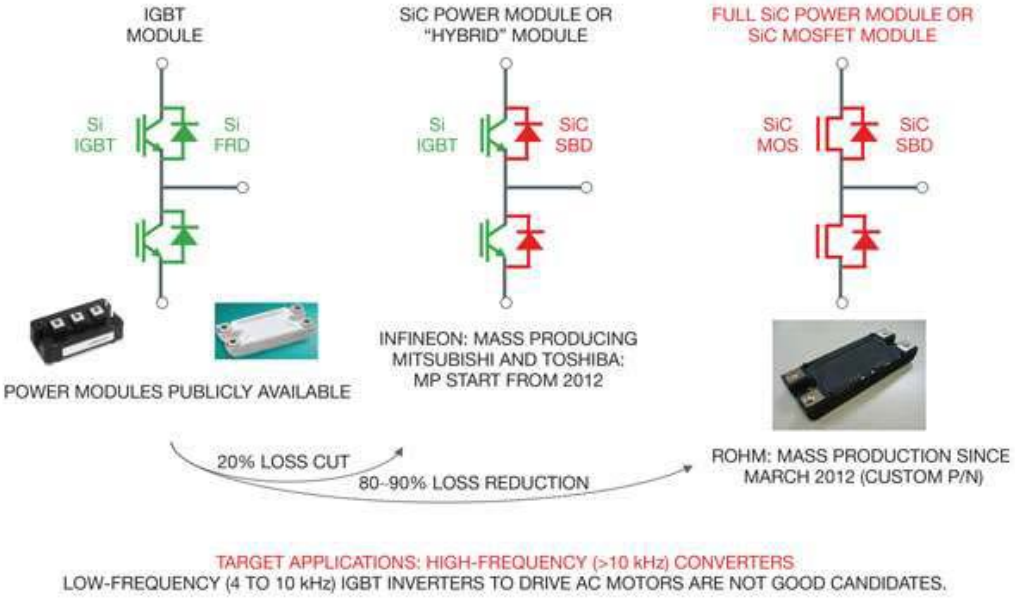

Fig. III.2. An all-SiC module greatly reduces power losses by eliminating any Si lossy components.

Gallium nitride (GaN)?

Gallium nitride transistors have emerged as a high-performance alternative to silicon-based transistors, thanks to the technology's ability to be made allow smaller device sizes for a given on-resistance and breakdown voltage than silicon. GaN transistors borrowed the same nomenclature as their silicon transistor: gate, drain and source, as shown Fig. III.3.

The power electronics industry reached the theoretical limit of silicon MOSFETs and now must go to another semiconductor material whose perfromance matches today's newer systems. The new material is gallium nitride (GaN) a high electron mobility (HEMT) semiconductor, whaich is poised to usher in new power devices that are superior to the present state of the art. Although GaN is young in its life cycle, it will certainly see significant improvements in the years to come.

GaN has a higher critical electric field strength than silicon. Its higher electron mobility enables a GaN device to have a smaller size for a given on-resistance and breakdown voltage than a silicon semiconductor. Compared to silicon devices, this also allows devices to be physically smaller and their electrical terminals closer together for a given breakdown voltage requirement.

Fig. III.4 is future projection of the GaN devices. When originally introduced in 2010, devices were rated at 40 to 200 V and 500 Mhz switching speed. Recent introductions raised the speed up to 3 GHz for devices rated at 40 V, 65 V and 100 V and on-resistance ranging from 125 mΩ to 530 mΩ. The company also expects GaN transistors to eventually operate at 600 V and it expects more functions per chip.

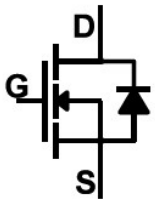

Fig. III.3 - Enhancement mode GaN has a circuiut schematic similar to silicon MOSFETs with Gate (G), Drain (D), and Source (S).

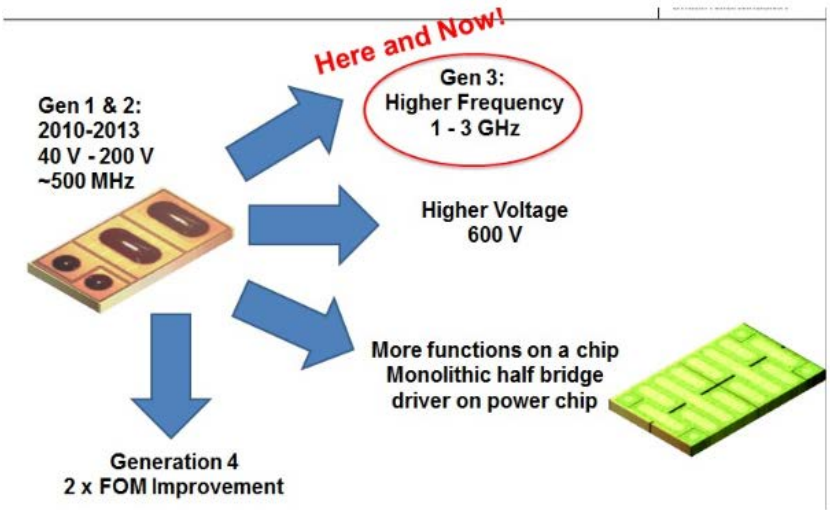

Fig. III.4 - The future of GaN transistors indicates the development of faster and higher voltage devices.

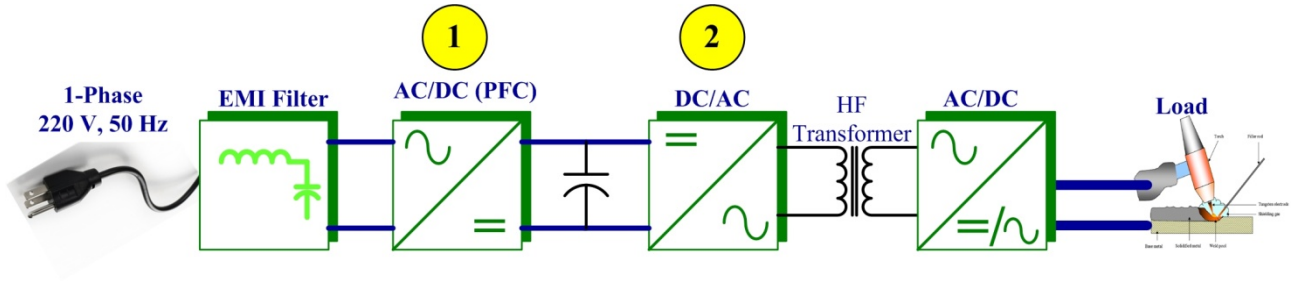

Fig. III.5. Future project: optimization of electric appliances: AC/DC (PFC) converter and DC/AC converter.

1). AC/DC converter (Power Factor Correction, PFC)

Based on the current project with the D.Enterprises Co.,Ltd. (Thai company, www.plang-daichi.com), I have worked with the company to design and implement a new TIG welding machine, see Fig. III.5. In this system, there are two-main circuits: a AC/DC power factor correction (PFC) and a DC/AC full-bridge with a high-frequency transformer.

Active Power Factor Correct ion (PFC) is widely used in today' s power supplies. Government regulations and customer requirements must be satisfied when designing these circuits. Increasingly, efficiency and power density are dominating the design tasks for a typical ac-dc converter. Designers also are being chal lenged to speed the design process and eliminate risk.

As advances occur within the semiconductor market, it isn't always clear what the expected advantage is or how it will benefit a specific application. Often, the designer must change the design to fully realize the benefit of next generation silicon. Engineers want less work, not more.

PFC Background

At power levels above approximately 200 W, most active PFC designs are continuous conduction mode (CCM) boost converters. It should be apparent that critical and discontinuous conduction mode converters suffer from large peak-to-peak current levels because the inductor current swings to zero each switching cycle. Fig. III.6 shows the three main conduction modes for a boost converter. The CCM not only limits peak current stress, but also will be easier to filter.

Along with the benefits of using CCM, certain drawbacks exist, the most notable being the losses and EMI generation associated with the turn-off of the boost diode. Fig. III.7 shows the typical MOSFET and diode currents for a CCM boost converter using an ultrafast high-voltage silicon rectifier. Note that the reverse recovery current of the diode shows up in the MOSFET drain

current. This current will cause significant power dissipation in the MOSFET, along with increased EMI.

However, large portion of system loss are in the diode bridge and can not be avoided even with zero voltage switching on the Boost stage. This inherently limits the peak efficiency of the conventional PFC stage. A rectifier diode has typical 1-V forward voltage drop and there are 2 diodes in the current path, which could account for 2% of total efficiency loss. A well-designed PFC stage can probably achieve efficiency about 97 to even 98%, but efficiency higher than 98% becomes very challenging for standard PFC due to the fixed diode bridge loss.

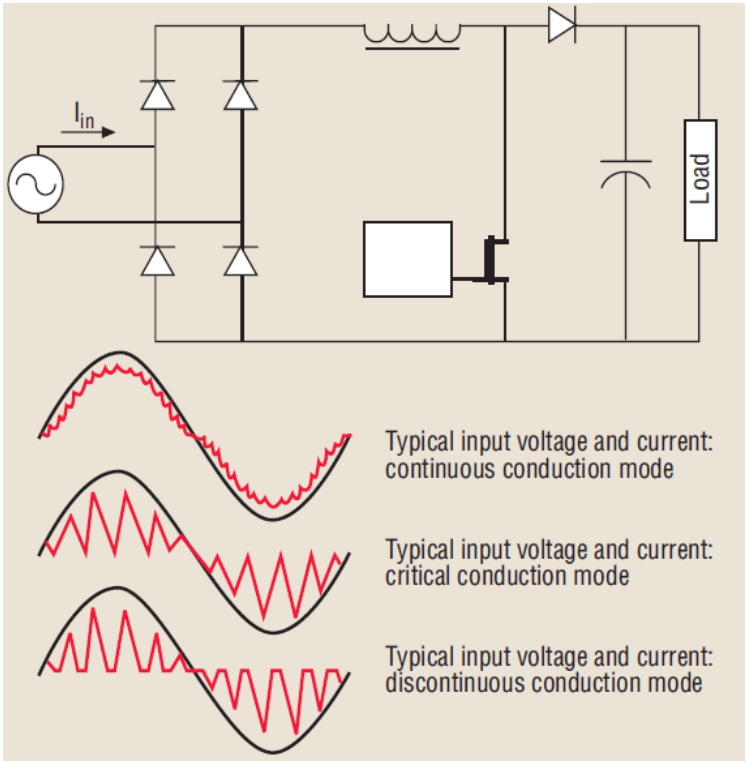

Fig. III.6. Comparison of conduction modes for a classic boost PFC converter.

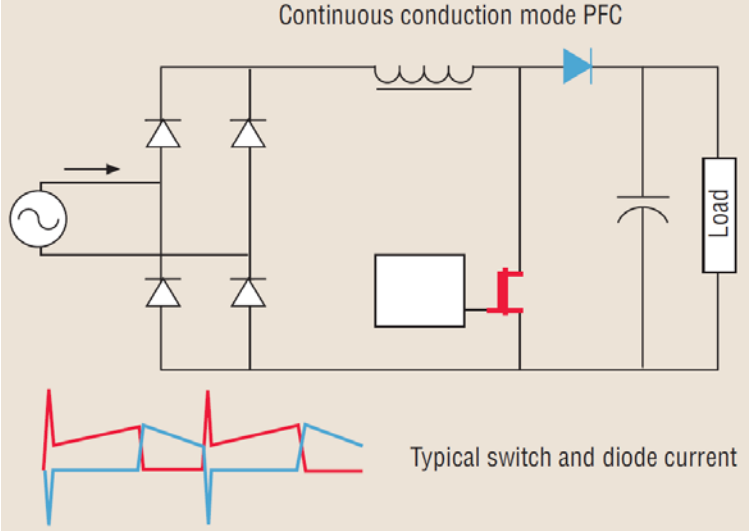

Fig. III.7. Typical MOSFET and diode current waveforms in a classic boost PFC converter.

Fig. III.8. shows the topologies of a Bridgeless Totem-Pole PFC (BTPPFC). It can be considered as a conventional boost PFC in which one half of the diode bridge is replaced by active switches S1 and S2 in a half bridge configuration, hence the name “totem pole”. The diode D1/D2 forms the slow 50/60Hz line frequency leg which can either be slow AC rectifier diodes or can be replaced by low-Rds(on) synchronous MOSFETs for improved efficiency, as shown in Fig.III.6(b).

The BTPPFC overcomes many issues which existed in the classic PFC and has the following advantages:

- **Improved efficiency:** main current only flows through two switches at a time. S1/S2 are driven synchronously with complimentary PWM signals and the S3/S4 on the slow line frequency legs can be low Rds(on) Si MOSFETs to further reduce the conduction loss.

- **Lower part counts, higher power density and lower BOM cost.** It uses fewer parts and has a simpler circuit: It needs only one inductor and neither SiC diodes nor AC return diodes are required.

- **Bidirectional power flow.** BTPPFC is inherently capable of bidirectional operation,which is ideal applications which may require power flow in both directions, such as Energy Storage System (ESS) and on-board bidirectional battery chargers (OBBC).

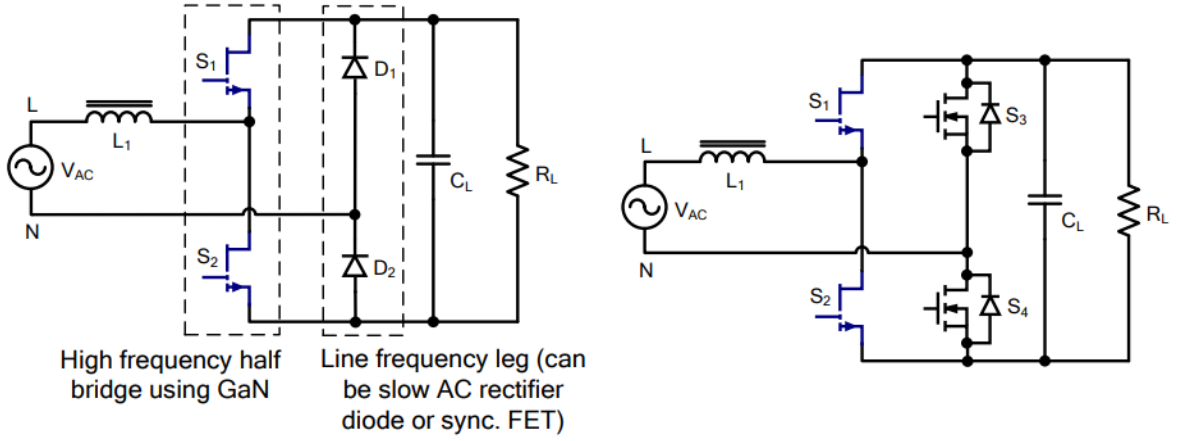

(a) BTPPFC circuit (b) Replace D1/D2 with synchronous MOSFETs

Fig. III.8. Future studies of a Bridgeless Totem-Pole PFC circuit using SiC or GaN.

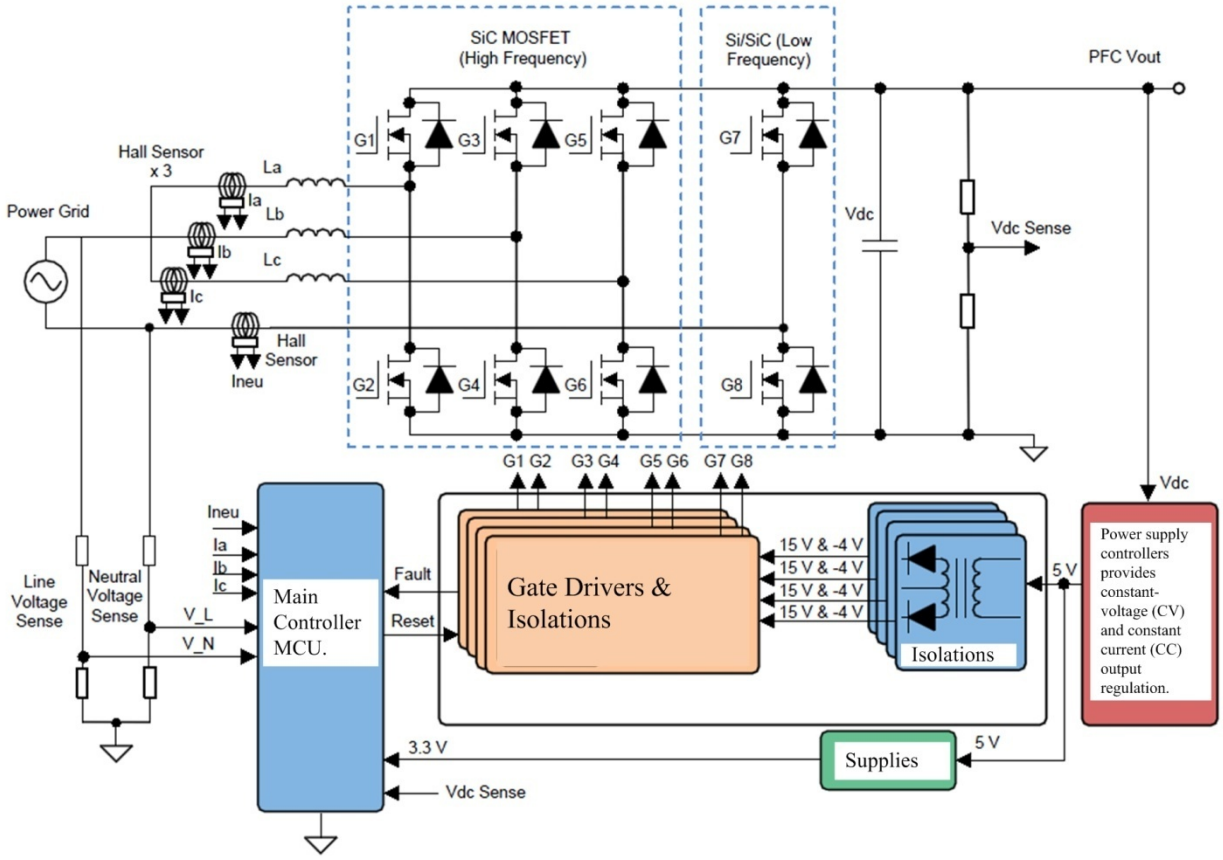

Fig. III.9. Future studies of a multiphase interleaved Bridgeless Totem-Pole PFC (3-phase interleaved, for example).

Moreover, for the future study of AC/DC with PFC, it is not only to use in a welding machine, also it may apply for other equipments, such as inverter, vacuum cleaners, refrigerators, air conditioners, and washers. For higher power applications, futures works on multiphases interleaving PFC (Fig. III.9) and operates in continuous conduction mode (CCM) to achieve a

higher efficiency (> 98%) at a 220-V input voltage and full power over than 5 kW. The power stage will be implemented with silicon carbide (SiC) MOSFETs driven by a microcontroller (MCU) with SiC-isolated gate drivers.

2) DC/DC converter (DC/AC + AC/DC)

Refer to Fig. III.10, the circuit (DC/AC conversion) is usually a phase shifted full bridge (PSFB) converter. It functions to convert a high voltage bus (360 V, for example) to a low voltage bus (10 – 80 V, for example in welding machines or low voltage battery charger). PSFB stage provides voltage translation as well as isolation from the line voltage, since this topology includes a transformer. PSFB DC-DC converters are used frequently to step down high DC bus voltages and/or provide isolation in medium to high power applications like welding machines, server power supplies, telecom rectifiers, battery charging systems, and renewable energy systems, such PV or FC. A PSFB converter consists of four power electronic switches (like MOSFETs or IGBTs) that form a full-bridge on the primary side of the isolation transformer and diode rectifiers or MOSFET switches for synchronous rectification (SR) on the secondary side. This circuit can be controlled in various modes like voltage mode control, average current mode control or peak current mode control, classically. For the future works on PSFB, some new control algorithms may study such differential flatness approach for higher performance.

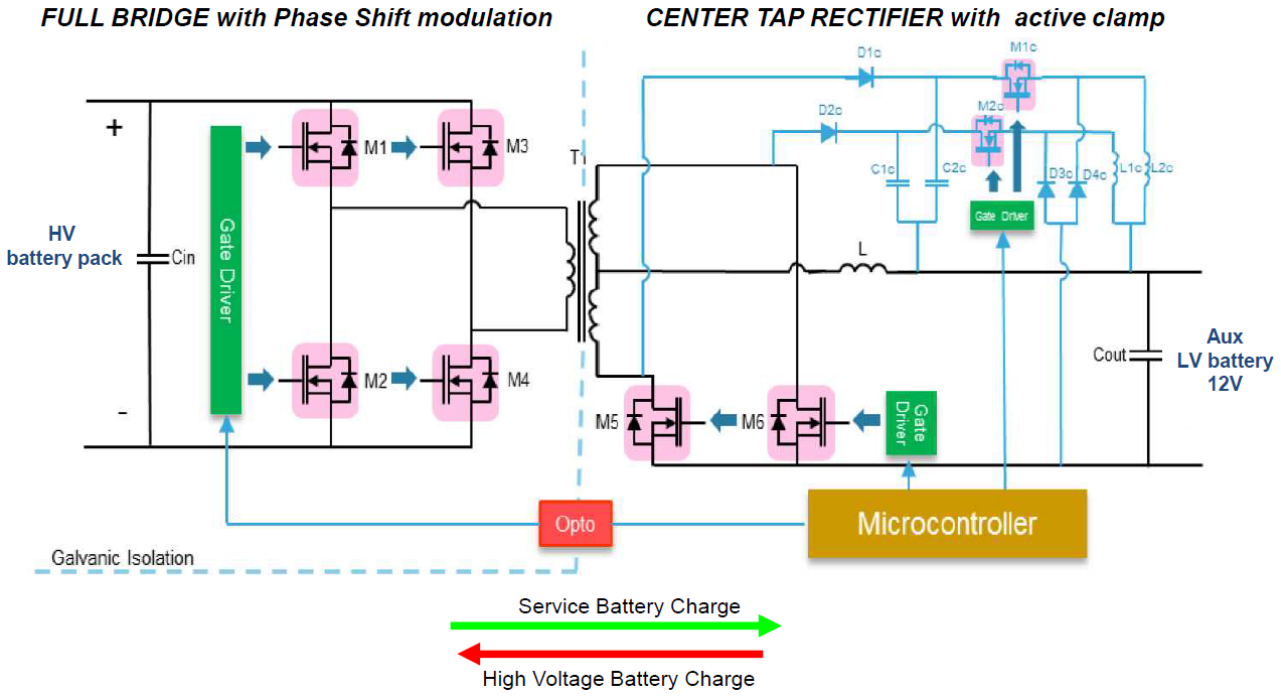

Fig. III.10. Future studies of Bidirectional DC-DC converter.

3) DC/AC converter

Control, robustness, stability, efficiency, and optimization of power electronics systems (nonlinear systems) remain the focus of most of the research. Fig. III.11 shows the diagram of a three-phase grid-connected converter with an output *L*-type filter. Several researchers have studied different topologies and control algorithms for this structure. The classic control is a vector control (decoupling control), shown in Fig.III.12. To improve the system performance, the differential flatness estimation may apply for this system, Fig. III.13. Moreover, online real time loss estimation in this system is also important. So, some observers should be studied in the future works. As, we know that the PV system may operate for more than 25 years; then, to improve the system efficiency just 1% for the big system, it is a great work.

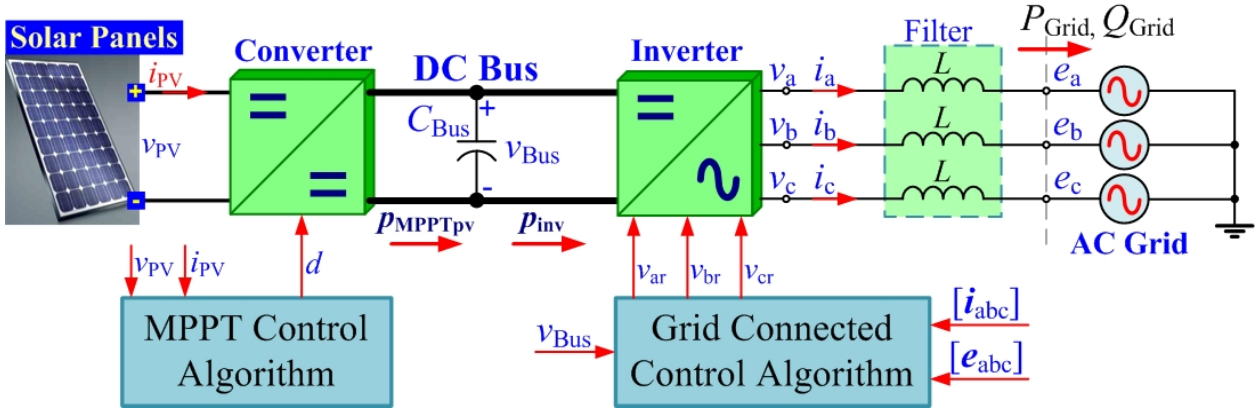

Fig. III.11. Concept of three-phase inverter for grid connection.

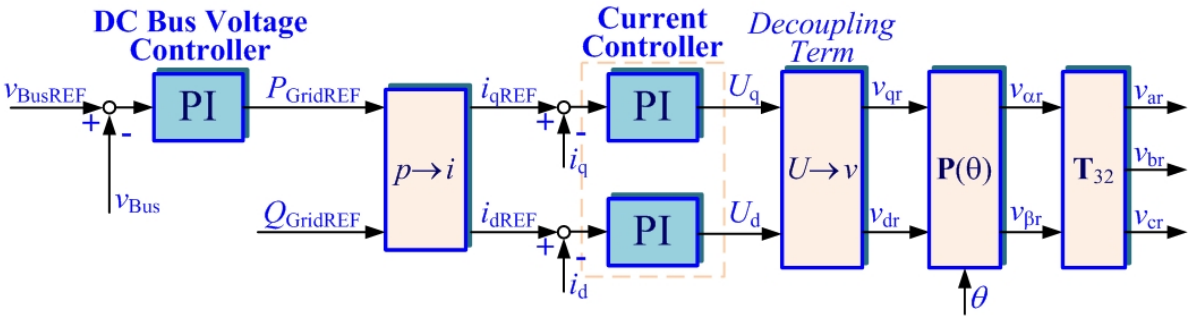

Fig. III.12. Classic vector control (decoupling control) of the three-phase grid-connected inverter [Sve99].

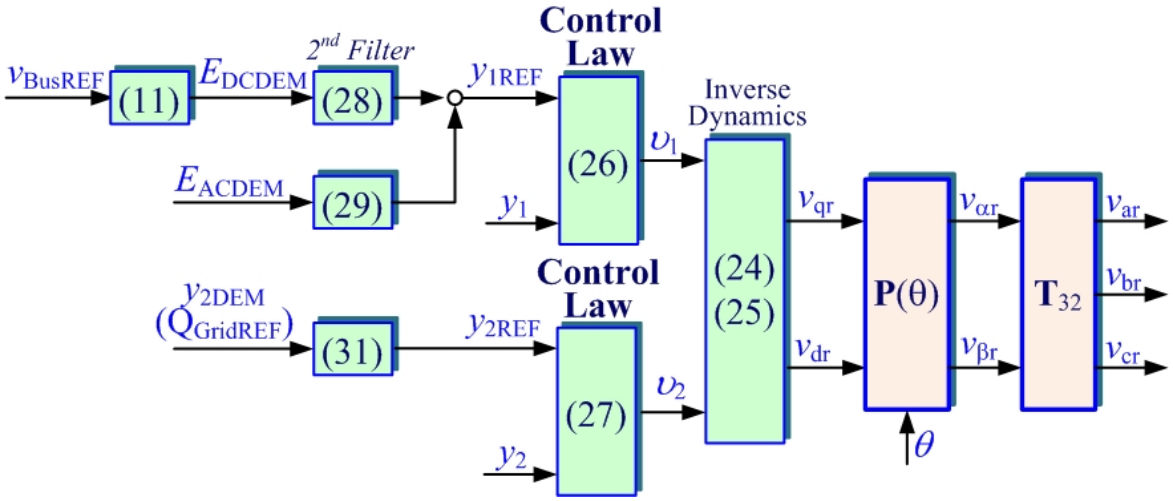

Fig. III.13. Proposed differential flatness control of the three-phase grid-connected inverter.

4). Energy management of hybrid system for DC grid

I have worked a lot of using the supercapacitor for FC and/or PV hybrid systems. Working with SC, it is simple to charge or discharge, because it can charge or discharge with very high current: +/– 500 A, for example, and the SC state-of-charge is simple by observing its voltage. However, the supercapacitor is low energy density comparative with modern Li-Ion battery. In the future, the combination between Li-Ion battery and supercapacitor will be studied. Nevertheless, there are many tasks to work with battery:

1). Current limitation for charging and discharging of battery is the constraints.
2). The battery state-of-charge is very complex.
3). The battery state-of-health is also very complex.

5). Electrical Machine Drives

Currently, I have worked with Prof. Noureddine TAKORABET and Prof. Babak NAHIDMOBARAKEH (GREEN lab) and Dr. Sisuda CHAITHONGSUK (Thai colleague). They have designed a new type of permanent magnet synchronous machine. The surface of the studied rotor can be smooth [Fig. III.14(a)] or grooved with equal and equidistant grooves [Fig. III.14(b)] or using proposed PWM technique [Fig. III.14(a)]. The new rotor surface is a PWM technique for low speed applications. The use of PWM technique grooves on the surface rotor allows reducing a given set of harmonics and consequently the torque ripples. Based on my experiences on power electronics and control, I have worked with this team for the machine drives: sensor control or sensorless control. The differential flatness approach may apply for this system.

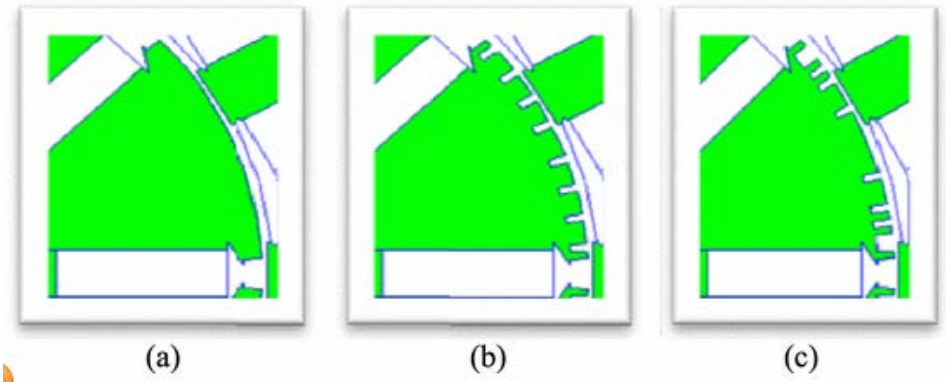

Fig. III.14. Shape of different topologies of the rotor. (a) Smooth. (b) Equidistant. (c) PWM.

Actually, the drive of Permanent Magnet Assisted Synchro-Reluctances Machines is one of the target topics I will develop in the future. A new PhD thesis is launched in cooperation with Prof. Babak NAHID MOBARAKEH and Prof. Noureddine TAKORABET on the control of electric machines for electric vehicles. The thesis of Songklod SRIPRANG on the Design and Control of PM Assisted Synchro-Reluctance Machines is new step towards this objective. In this thesis, the aim is to improve the power factor of synchro reluctance machines by adding Ferrite magnets of electric vehicle applications. This may avoid the use of rare earth magnets which are expensive and whose market is unstable. In addition, the development of nonlinear control laws to achieve target performances on the EV power train. Moreover, the control law should show fault-tolerance properties with respect to mechanical sensor failure.

III.2 Conclusion

This document is written in order to obtain L'Habilitation à Diriger des Recherches (HDR) for Université de Lorraine (UL). It composes of three parts. For Part I, it is a long curriculum vitae including the synthesis of lecture activities at King Mongkut's University of Technology North Bangkok (KMUTNB). My main lectures are the power electronics and the microcontrollers for undergraduate level since 2005. For the administrative experiences, I was a Head of department of Teacher Training in Electrical Engineering, KMUTNB during Jan. 2009 – Dec. 2012; since Jan. 2013, I am a Deputy Director for Research Promotion and Innovation Science and Technology Research Institute, KMUTNB.

For Part II, it is a synthesis of my thirteen years research works after my PhD thesis from INPL. My research works have continued from my PhD thesis. There are two main topics: 1) DC/DC converter for FC or PV or battery of SC, 2) energy management of hybrid systems: FC/SC,

FC/SC/Baterry, etc. Including my PhD publications, I have published at least 96 international journal papers in ISI Web of Science and 95 international journal and conference papers in Scopus database with *Citations: 2 104 times* (without self-citations) and *H-index: 22* (without self-citations) [up-date: 14 September 2018]. Number of citations may guarantee my research contributions and impacts in the domain of my works on power electronics applications. Moreover, Refer to Part I (long CV), I have received at least three international awards:

1) year 2009: *First Prize Paper Award* by the Industrial Automation and Control Committee of the IEEE Industry Applications Society, Oct. 2009 IAS Annual Meeting, Texas-USA,
2) year 2015: *Outstanding Paper Award: 3rd PRIZE* by the 37th IEEE International Telecommunications Energy Conference, Osaka, Japan on 17-23 Oct. 2015,
3) year 2010: *ICEM Best Poster Presentation Award* by the XIX IEEE International Conference on Electrical Machines (ICEM2010), Rome-Italy, 6-8 September 2010.

For national awards, I have received many awards.

1. The biggest one is *TRF-CHE-Scopus Researcher Awards*, Engineering & Multidisciplinary Technology in year 2017 by Scopus and The Thailand Research Fund (TRF) and The Commission on Higher Education (CHE).

2. The second one is *TRF-CHE-Scopus Young Researcher Awards*, Engineering & Multidisciplinary Technology in year 2012 by Scopus and The Thailand Research Fund (TRF) and The Commission on Higher Education (CHE).

In Final, the research perspective is present in Part III. There are at least five main subjects to further works: AC/DC, DC/DC, and DC/AC converters; hybrid systems; and PMSM drives. These works are strong cooperation with Thai companies and European Institutions (Université de Lorraine, Politecnico di Milano, and University Birmingham). These will make a sustainable development, particularly for Thailand.

@@@ END @@@

[Adz08] K. P. Adzakpa, K. Agbossou, Y. Dubé, M.Dostie, M. Fournier, and A. Poulin, "PEM fuel cells modeling and analysis through current and voltage transient behaviors," *IEEE Trans. Energy Convers.*, vol. 23, no. 2, pp. 581–591, June 2008.

[Agb04] K. Agbossou, M. Kolhe, J. Hamelin, and T. K. Bose, "Performance of a stand-alone renewable energy system based on energy storage as hydrogen," *IEEE Trans. Energy Convers.*, vol. 19, pp. 633–640, Sept. 2004.

[Agl09] G. S. Aglietti, S. Redi, A. R. Tatnall, and T. Markvart, "Harnessing high-altitude solar power," *IEEE Trans. Energy Convers.*, vol. 24, no. 2, pp. 442–451, June 2009.

[Agr09] S. K. Agrawal, K. Pathak, J. Franch, R. Lampariello, and G. Hirzinger, "A differentially flat open-chain space robot with arbitrarily oriented joint axes and two momentum wheels at the base," *IEEE Trans. Autom. Control*, vol. 54, no. 9, pp. 2185–2191, Sep. 2009.

[Amo00] A. Al- Amoudi and L. Zhang, "Application of radial basis function networks for solar-array modelling and maximum power-point prediction," *IEE Proc.-Gener. Transm. Distrib.*, vol. 147, no. 5, pp. 310–316, Sept. 2000.

[And08] J. M. Andujar, F. Segura, and M. J. Vasallo, "A suitable model plant for control of the set fuel cell-DC/DC converter," *Renewable Energy*, vol. 33, pp. 813–826, Apr. 2008.

[Asc08] H. Aschemann and D. Schindele, "Sliding-mode control of a high-speed linear axis driven by pneumatic muscle actuators," *IEEE Trans. Ind. Electron.*, vol. 55, no. 1, pp. 3855–3864, Nov. 2008.

[Azi11] T. Azib, O. Bethoux, G. Remy, and C. Marchand, "Saturation management of a controlled fuel-cell/ultracapacitor hybrid vehicle," *IEEE Trans. Veh. Technol.*, vol. 60, no. 9, pp. 4127–4138, Nov. 2011.

[Bau09] J. Bauman and M. Kazerani, "An analytical optimization method for improved fuel cell–battery–ultracapacitor powertrain," *IEEE Trans. Veh. Technol.*, vol. 58, no. 7, pp. 3186–3197, Sept. 2009.

[Ber09a] A. Bergen, L. Pitt, A. Rowe, P. Wild, and N. Djilali, "Experimental assessment of a residential scale renewable–regenerative energy system," *J. Power Sources*, vol. 186, pp. 158–166, 2009.

[Ber09b] J. Bernard, S. Delprat, F. N. Büchi, and T. M. Guerra, "Fuel-cell hybrid powertrain: toward minimization of hydrogen consumption," *IEEE Trans. Veh. Technol.*, vol. 58, no. 7, pp. 3168–3176, Sept. 2009.

[Bit04] O. Bitsche and G. Gutmann, "Systems for hybrid cars," *J. Power Sources*, vol. 127, pp. 8–15, Mar. 2004.

[Bre07] J. J. Brey, C. R. Bordallo, J. M. Carrasco, E. Galvan, A. Jimenez, and E. Moreno, "Power conditioning of fuel cell systems in portable applications," *Int. J. Hydrogen Energy*, vol. 32, pp 1559–1566, July–Aug. 2007.

[Cas92] M. A. Casacca and Z. M. Salameh, "Determination of Lead-Acid Battery Capacity via Mathematical Modeling Techniques", *IEEE Trans. Energy Convers.*, vol. 7, no. 3, pp. 442–446, Sep. 1992.

[Che10] L. R. Chen, C. H. Tsai, Y. L. Lin, and Y. S. Lai, "A biological swarm chasing algorithm for tracking the PV maximum power point," *IEEE Trans. Energy Convers.*, vol. 25, no. 2, pp. 484–493, Jun. 2010.

[Cho04] W. Choi, G. Joung, P. N. Enjeti, and J. W. Howze, “An experimental evaluation of the effects of ripple current generated by the power conditioning stage on a proton exchange membrane fuel cell stack,” *Trans. ASME, J. Mater. Eng. Perform.*, vol. 13, pp. 257–264, June 2004.

[Cho06a] S. R. Choudhury and R. Rengaswamy, “Characterization and fault diagnosis of PAFC cathode by EIS technique and a novel mathematical model approach,” *J. Power Sources*, vol. 161, pp. 971–986, Oct. 2006.

[Cho06b] W. Choi, J. W. Howze, and P. Enjeti, “Fuel-cell powered uninterruptible power supply systems: Design considerations,” *J. Power Sources*, vol. 157, pp. 311–317, June 2006.

[Col07] M. Coleman, C. K. Lee, C. Zhu, and W. G. Hurley, ‘‘State-of-charge determination from EMF voltage estimation: using impedance, terminal voltage, and current for lead-acid and lithium-ion batteries,’’ *IEEE Trans. Ind. Electron.*, vol. 54, no. 5, pp. 2550–2557, Oct. 2007.

[Coo09] A. Cooper, J. Furakawa, L. Lam, and M. Kellaway, “The UltraBattery—A new battery design for a new beginning in hybrid electric vehicle energy storage,” *J. Power Sources*, vol. 188, pp. 642– 649, 2009.

[Cor04] J. M. Corrêa, F. A. Farret, L. N. Canha, and M. G. Simões, “An electrochemical-based fuel-cell model suitable for electrical engineering automation approach,” *IEEE Trans. Ind. Electron.*, vol. 51, pp. 1103–1112, Oct. 2004.

[Cor05a] J. M. Corrêa, F. A. Farret, V. A. Popov, and M. G. Simões, “Sensitivity analysis of the modeling s used in simulation of proton exchange membrane fuel cells,” *IEEE Trans. Energy Convers.*, vol. 20, pp. 211–218, Jan./Mar. 2005.

[Cor05b] P. Corbo, F. E. Corcione, F. Migliardini, and O. Veneri, “Experimental study of a fuel cell power train for road transport application,” *J. Power Sources*, vol. 145, pp. 610–619, Aug. 2005.

[Cor06] P. Corbo, F. E. Corcione, F. Migliardini, and O. Veneri, “Experimental assessment of energy-management strategies in fuel-cell propulsion systems,” *J. Power Sources*, vol. 157, pp. 799–808, Jul. 2006.

[Cor08] P. Corbo, F. Migliardini, and O. Veneri, ―An experimental study of a PEM fuel cell power trainfor urban bus application, *J. Power Sources*, vol. 181, pp. 363–370, July 2008.

[Dan08] M. A. Danzer, J. Wilhelm, H. Aschemann, and E. P. Hofer, “Model-based control of cathode pressure and oxygen excess ratio of a PEM fuel cell system,” *J. Power Sources*, vol. 176, no. 2, pp. 515–522, Feb. 2008.

[Dol06] J. Dollmayer, N. Bundschuh, and U. B. Carl, “Fuel mass penalty due to generators and fuel cells as energy source of the all-electric aircraft,” *Aerosp. Sci. Technol.*, vol. 10, pp. 686–694, Dec. 2006.

[Ehn09] M. Ehsani, Y. Gao, S. E. Gay, and A. Emadi, “Modern Electric, Hybrid Electric, and Fuel Cell Vehicles: Fundamentals, Theory, and Design,” CRC Press; 2 edition, 557 pages, Sep. 2009.

[Ema08] A. Emadi, Y. J. Lee, and K. Rajashekara, “Power electronics and motor drives in electric, hybrid electric, and plug-in hybrid electric vehicles,” *IEEE Trans. Ind. Electron.*, vol. 55, pp. 2237–2245, June 2008.

[Esr07] T. Esram, and P. L. Chapman, “Comparison of Photovoltaic Array Maximum Power Point Tracking Techniques,” *IEEE Trans. Energy Convers.*, vol. 22, no. 2, pp. 439–449, June 2007.

[Ett09] F. Ettingshausen, J. Kleemann, M. Michel, M. Quintus, H. Fuess, C. and Roth, “Spatially resolved degradation effects in membrane-electrode-assemblies of vehicle aged polymer electrolyte membrane fuel cell stacks,” *J. Power Sources*, no. 194, no. 2, pp. 899–907, Dec. 2009.

[Fah04] B. Fahimi, A. Emadi, and R. B. Sepe, Jr., “Switched reluctance machine-based starter/alternator for more electric cars,” *IEEE Trans. Energy Convers.*, vol. 19, pp. 116–124, Mar. 2004.

[Fli95] M. Fliess, J. L´evine, Ph. Martin, and P. Rouchon, “Flatness and defect of nonlinear systems: Introductory theory and examples,” *Int. J. Contr*., vol. 61, no. 6, pp. 1327–1361, 1995.

[Fli99] M. Fliess, J. L´evine, Ph. Martin, and P. Rouchon, “A Lie–B¨acklund approach to equivalence and flatness of nonlinear systems,” *IEEE Trans. Automat. Contr*., vol. 44, no. 5, pp. 922–937, May 1999.

[Fre10] I. S. de Freitas, C. B. Jacobina, E. R. C. da Silva, and T. M. Oliveira, “Single-phase AC–DC–AC three-level three-leg converter,” *IEEE Trans. Ind. Electron*., vol. 57, no. 12, pp. 4075–4084, Dec. 2010.

[Fri04] W. Friede, S. Raël, and B. Davat, “Mathematical model and characterization of the transient behavior of a PEM fuel cell,” *IEEE Trans. Power Electron.*, vol. 19, no. 5, pp. 1234–1241, Sept. 2004.

[Fur06] T. Furuya, K. Kondo, and T. Yamamoto, “Experimental study on a PEMFC fed railway vehicle motor drive system,” in *Proc. 41st IEEE-IAS*, 8–12 Oct. 2006, pp. 1249–1252.

[Gay08] R. Gaynor, F. Mueller, F. Jabbari, and J. Brouwer, “On control concepts to prevent fuel starvation in solid oxide fuel cells,” *J. Power Sources*, vol. 180, pp. 330–342, May 2008.

[Gem03] R. S. Gemmen, “Analysis for the effect of inverter ripple current on fuel cell operating condition,” *Trans. ASME, J. Fluids Eng.*, vol. 125, pp. 576–585, May 2003.

[Gen09] A. Gensior, H. Sira-Ramirez, J. Rudolph, and H. Guldner, “On some nonlinear current controllers for three-phase boost rectifiers,,” *IEEE Trans. Ind. Electron*., vol. 56, no. 2, pp. 360–370, Feb. 2009.

[Gen11] A. Gensior, T. M. P. Nguyen, J. Rudolph, and H. Güldner, “Flatness based loss optimization and control of a doubly fed induction generator system,” *IEEE Trans. Control Syst. Technol*., vol. 19, no. 6, pp. 1457–1466, Nov. 2011.

[Gib10] T. L. Gibson and N. A. Kelly, “Solar photovoltaic charging of lithium-ion batteries,” *J. Power Sources*, vol. 195, no. 12, pp. 3928–3932, Jun. 2010.

[Gok02] L. U. Gökdere, K. Benlyazid, R. A. Dougal, E. Santi, and C. W. Brice, “A virtual prototype for a hybrid electric vehicle,” *Mechatronics*, vol. 12, pp. 575–593, May 2002.

[Gua02] M. Guay, “On the linearizability of nonisothermal continuous stirred-tank reactors,” *Automatica*, vol. 38, no. 2, pp. 269–278, Feb. 2002.

[Has09] J. Hasikos, H. Sarimveis, P. L. Zervas, and N. C. Markatos, “Operational optimization and real-time control of fuel-cell systems,” *J. Power Sources*, no. 193, no. 1, pp. 258–268, August 2009.

[Hel07] R. von Helmolt and U. Eberle, ‘‘Fuel cell vehicles: Status 2007,’’ *J. Power Sources*, vol. 165, no. 2, pp. 833–843, Mar. 2007.

[Hin09] M. Hinaje, I. Sadli, J-P. Martin, **P. Thounthong**, S. Raël, and B. Davat, “Online humidification diagnosis of a PEMFC using a static DC-DC converter,” *International Journal of Hydrogen Energy*, vol. 34, no. 6, pp. 2718–2723, Mar. 2009.

[Hoo03] G. Hoogers, Fuel Cell Technology Handbook. Boca Raton, FL: CRC Press, 2003.

[Ike98] T. Ikeya, N. Sawada, S. Takagi, J. Murakami, K. Kobayashi, T. Sakabe, E. Kousaka, H. Yoshioka, S. Kato, M. Yamashita, H. Narisoko, Y. Mita, K. Nishiyama, K. Adachi, and K. Ishihara, “Multi-step constant-current charging method for electric vehicle, valve-regulated, lead/acid batteries during night time for load-levelling,” *J. Power Sources*, vol. 75, no. 1, pp. 101–107, Sep. 1998.

[Jia05] Z. Jiang, L. Gao, and R. A. Dougal, “Flexible multiobjective control of power converter in active hybrid fuel cell/battery power sources,” *IEEE Trans. Power Electron*., vol. 20, no. 1, pp. 244–253, Jan. 2005.

[Jia08] S. Jain and V. Agarwal, “An integrated hybrid power supply for distributed generation applications fed by nonconventional energy sources,” *IEEE Trans. Energy Convers*., vol. 23, no. 2, pp. 622–631, Jun. 2008.

[Jun07] J. W. Jung and A. Keyhani, ‘‘Control of a fuel cell based Z-source converter,’’ *IEEE Trans. Energy Convers.*, vol. 22, no. 2, pp. 467–476, June 2007.

[Jur05] F. Jurado, “Novel fuzzy flux control for fuel-cell inverters,” *IEEE Trans. Ind. Electron.*, vol. 52, no. 6, pp. 1707–1710, Dec. 2005.

[Kak09] N. Kakimoto, H. Satoh, S. Takayama, and K. Nakamura, “Ramp-rate control of photovoltaic generator with electric double-layer capacitor,” *IEEE Trans. Energy Convers.*, vol. 24, no. 2, pp. 465–473, June 2009.

[Kei04] T. A. Keim, “Systems for 42 V mass-market automobiles,” *J. Power Sources*, vol. 127, pp. 16–26, Mar. 2004.

[Ko08] D. H. Ko, M. J. Lee, W. H. Jang, and U. Krewer, “Non-isothermal dynamic modelling and optimization of a direct methanol fuel cell,” *J. Power Sources*, vol. 180, pp. 71–83, May 2008.

[Kol09] M. Kolhe, “Techno-economic optimum sizing of a stand-alone solar photovoltaic system,” *IEEE Trans. Energy Convers.*, vol. 24, no. 2, pp. 511–519, June 2009.

[Lee06] J. Lee, J. Jo, S. Choi, and S. B. Han, “A 10-kW SOFC low-voltage battery hybrid power conditioning system for residential use,” *IEEE Trans. Energy Convers.*, vol. 21, pp. 575–585, June 2006.

[Lee08] Y. S. Lee, W. Y. Wang, and T. Y. Kuo, ‘‘Soft computing for battery state-of-charge (BSOC) estimation in battery string systems,’’ *IEEE Trans. Ind. Electron.*, vol. 55, no. 1, pp. 229–239, Jan. 2008.

[Lec04] D. Lecocq, ‘‘Tomorrow’s energy today with Axane,’’ *Fuel Cells Bull.*, vol. 2004, pp. 13–15, Mar. 2004.

[Luk08] S. M. Lukic, J. Cao, R. C. Bansal, F. Rodriguez, and A. Emadi, “Energy storage systems for automotive applications,” *IEEE Trans. Ind. Electron.*, vol. 55, pp. 2258–2267, June 2008.

[Mei08] M. Meiler, O. Schmid, M. Schudy, and E. P. Hofer, “Dynamic fuel cell stack model for realtime simulation based on system identification,” *J. Power Sources*, vol. 176, pp. 523–528, Feb. 2008.

[Mil09] N. W. Miller, D. Guru, and K. Clark, “Wind Generation,” *IEEE Ind. Appl. Mag.*, vol. 14, no. 4, pp. 54–61, March-April 2009.

[Kim08] M. Kim, Y. J. Sohn, W. Y. Lee, and C. S. Kim, “Fuzzy control based engine sizing optimization for a fuel cell/battery hybrid mini-bus,” *J. Power Sources*, vol. 178, pp. 706–710, Apr. 2008.

[Mei03] E. Meissner and G. Richter, “Battery monitoring and electrical energy management: Precondition for future vehicle electric power systems,” *J. Power Sources*, vol. 116, no. 1–2, pp. 79–98, Jul. 2003.

[Mei05] E. Meissner and G. Richter, “The challenge to the automotive battery industry: the battery has to become an increasingly integrated component within the vehicle electric power system,” *J. Power Sources*, vol. 144, no. 2, pp. 438–460, Jun. 2005.

[Mil06] A. R. Miller, J. Peters, B. E. Smith, and O. A. Velev, “Analysis of fuel cell hybrid locomotives,” *J. Power Sources*, vol. 157, pp. 855–861, July 2006.

[Mil07] A. R. Miller, K. S. Hess, D. L. Barnes, and T. L. Erickson, “System design of a large fuel cell hybrid locomotive,” *J. Power Sources*, vol. 173, pp. 935–942, Nov. 2007.

[Mit06] W. Mitchell, B. J. Bowers, C. Garnier, and F. Boudjemaa, “Dynamic behavior of gasoline fuel cell electric vehicles,” *J. Power Sources*, vol. 154, pp. 489–496, Mar. 2006.

[Moc09] J. P. Mock and S. A. Schmid, “Fuel cells for automotive powertrains—A techno-economic assessment,” *J. Power Sources*, vol. 190, pp. 133–140, 2009.

[Moh05] M. Mohr and F. W. Fuchs, “Comparison of three phase current source inverters and voltage source inverters linked with dc to dc boost converters for fuel cell generation systems,” in *Proc. EPE’05*, 11–14 Sept. 2005, pp. 1–10.

[Mon03] T. Montani, “Electric energy storage evaluation for urban rail vehicles,” in *Proc. EPE’03*, Toulouse, France, Oct. 2003.

[Mor09] V. Morio, F. Cazaurang, and P. Vernis, “Flatness-based hypersonic reentry guidance of a lifting-body vehicle,” Control Eng. Pract., vol. 17, no. 5, pp. 588–596, May 2009.

[Na07] W. K. Na, B. Gou, and B. Diong, ‘‘Nonlinear control of PEM fuel cells by exact linearization,’’ *IEEE Trans. Ind. Appl.*, vol. 43, no. 6, pp. 1426–1433, Nov./Dec. 2007.

[Na08] W. K. Na and B. Gou, “Feedback-linearization-based nonlinear control for PEM fuel cells,” *IEEE Trans. Energy Convers.*, vol. 23, no. 1, pp. 179–190, Mar. 2008.

[Nab81] A. Nabae, I. Takahashi, and H. Akagi, “A neutral-point clamped PWM inverter,” *IEEE Trans. Ind. Appl.*, vol. IA-17, no. 5, pp. 518–523, Sep. 1981.

[Neh06] M. H. Nehrir, C. Wang, and S. R. Shaw, “Fuel cells: promising devices for distributed generation,” *IEEE Power Energy Mag.*, vol. 4, pp. 47–53, Jan./Feb. 2006.

[Nel03] R. M. Nelms, D. R. Cahela, and B. J. Tatarchuk, “Modeling double-layer capacitor behavior using ladder circuits,” *IEEE Trans. Aerosp. Electron. Syst.*, vol. 39, no. 2, pp. 430–438, Apr. 2003.

[Nic03] L. Nicod, “Energy strategy and optimization on hybrid light rail vehicle,” in *Proc. EPE’03*, 2003.

[Noi12] P. Noiying, M. Hinaje, **P. Thounthong**, S. Raël, and B. Davat "Using electrical analogy to describe mass and charge transport in PEM fuel cell," *Renewable Energy*, vol. 44, pp. 128–140, Aug. 2012.

[Oga07] T. Ogawa, H. Yoshihara, S. Wakao, K. Kondo, and M. Kondo, "Energy consumption analysis of FC-EDLC hybrid railway vehicle by dynamic programming," in *Proc. EPE'07*, 2–5 Sept. 2007, pp. 1–10.

[Oru07] M. Ortúzar, J. Moreno, and J. Dixon, ''Ultracapacitor-based auxiliary energy system for an electric vehicle: implementation and evaluation,'' *IEEE Trans. Ind. Electron.*, vol. 54, no. 4, pp. 2147–2156, Aug. 2007.

[Oze07] S. Ozeri, D. Shmilovitz, S. Singer, and L. M. Salamero, "The mathematical foundation of distributed interleaved multiple systems," IEEE Trans. Circuits Syst. I, Reg. Papers, vol. 54, no. 3, pp. 610–619, Mar. 2007.

[Pag07] S. C. Page, A. H. Anbuky, S. P. Krumdieck, and J. Brouwer, "Test method and equivalent circuit modeling of a PEM fuel cell in a passive state," *IEEE Trans. Energy Convers.*, vol. 22, pp. 764–773, Sept. 2007.

[Paq08] M. Paquin and L. G. Fréchette, "Understanding cathode flooding and dry-out for water management in air breathing PEM fuel cells," *J. Power Sources*, vol. 180, pp. 440–451, May 2008.

[Pas07] S. Pasricha, M. Keppler, S. R. Shaw, and M. H. Nehrir, "Comparison and identification of static electrical terminal fuel cell models," *IEEE Trans. Energy Convers.*, vol. 22, pp. 746–754, Sept. 2007.

[Pat09] H. Patel and V. Agarwal, "MPPT scheme for a PV-fed single-phases-stage grid-connected inverter operating in CCM with only one current sensor," *IEEE Trans. Energy Convers.*, vol. 24, no. 1, pp. 256–263, March 2009.

[Pay08] A. Payman, S. Pierfederici, and F. Meibody-Tabar, "Energy control of supercapacitor/fuel cell hybrid power source," *Energy Convers. Manage.*, vol. 49, no. 6, pp. 1637–1644, Jun. 2008.

[Pay11] A. Payman, S. Pierfederici, F. Meibody-Tabar, and B. Davat "An Adapted Control Strategy to Minimize DC-Bus Capacitors of a Parallel Fuel Cell/Ultracapacitor Hybrid System," *IEEE Trans. Power Electron.*, vol. 26, no. 12, pp. 3843–3852, Dec. 2011.

[Per07] M. C. Pera, D. Candusso, D. Hissel, and J. M. Kauffmann, ''Power generation by fuel cells,'' *IEEE Ind. Electron. Mag.*, vol. 1, no. 3, pp. 28–37, Fall 2007.

[Por06] R. Portillo, M. M. Prats, J. I. León, J. A. Sánchez, J. M. Carrasco, E. Galván, and L. G. Franquelo, "Modeling strategy for back-to-back three-level converters applied to high-power wind turbines," *IEEE Trans. Ind. Electron.*, vol. 53, no. 5, pp. 1483–1491, Oct. 2006.

[Puk04] J. T. Pukrushpan, A. G. Stefanopoulou, and H. Peng, "Controlling fuel cell breathing," *IEEE Control Syst. Mag.*, vol. 24, no. 2, pp. 30–46, Apr. 2004.

[Rab09] T. Rabbani, S. Munier, D. Dorchies, P. Malaterre, A. Bayen, and X. Litrico, "Flatness-based control of open-channel flow in an irrigation canal using scada," *IEEE Control Syst. Mag.*, vol. 29, no. 5, pp. 22–30, Oct. 2009.

[Raj08] K. Rajashekara, J. Grieve, and D. Daggett, "Hybrid fuel cell power in aircraft," *IEEE Ind. Appl. Mag.*, vol. 14, no. 4, pp. 54–60, July-Aug. 2008.

[Rav11] A. Ravey, N. Watrin, B. Blunier, D. Bouquain, and A. Miraoui, "Energy- source-sizing methodology for hybrid fuel cell vehicles based on statistical description of driving cycles," *IEEE Trans. Veh. Technol*., vol. 60, no. 9, pp. 4164–4174, Nov. 2011.

[Rea09] A. J. del Real, A. Arce, and C. Bordons, "Optimization strategy for element sizing in hybrid power systems," *J. Power Sources*, vol. 193, pp. 315–321, 2009.

[Ro97] K. Ro, "Two-Loop Controller for Maximizing Performance of a Grid-Connected Photovoltaic-Fuel Cell Hybrid Power Plant," *PhD Thesis*, Virginia Polytechnic Institute and State University, Blacksburg, Virginia, USA, Apr. 1997.

[Rod05] P. Rodatz, G. Paganelli, A. Sciarretta, and L. Guzzella, "Optimal power management of an experimental fuel cell/supercapacitor powered hybrid vehicle," *Control Eng. Practice*, vol. 13, no. 1, pp. 41–53, Jan. 2005.

[Sad06] I. Sadli, **P. Thounthong**, J-P. Martin, S. Raël, and B. Davat, "Behaviour of a PEMFC supplying a low voltage static converter," *J. Power Sources*, vol. 156, no. 1, pp. 119–125, May 2006.

[Sal09] J. R. Salgado and M. A. D. Aguilar, "Market survey of fuel cells in Mexico: Niche for low power portable systems," *J. Power Sources*, vol. 186, pp. 455–463, 2009.

[Sal92] Z. M. Salameh, M. A. Casacca, and W. A. Lynch, "A Mathematical Model for Lead-Acid Batteries", *IEEE Trans. Energy Convers.*, vol. 7, no. 1, pp. 93–97, Mar. 1992.

[Sch07] E. Schaltz, S.J. Andreasen, P.O. Rasmussen, Design of propulsion system for a fuel cell vehicle, Proceedings of the European Power Electronics and Drives 2007, CDROM.

[Sch09] E. Schaltz, A. Khaligh, and P. O. Rasmussen, "Influence of battery/ultracapacitor energy-storage sizing on battery lifetime in a fuel cell hybrid electric vehicle," *IEEE Trans. Veh. Technol.*, vol. 58, no. 8, pp. 3882–3891, Oct. 2009.

[Sha10] A. Shahin, M. Hinaje, J. P. Martin, S. Pierfederici, S. Raël, and B. Davat, "High voltage ratio DC–DC converter for fuel-cell applications," *IEEE Trans. Ind. Electron*., vol. 57, no. 12, pp. 3944–3955, Dec. 2010.

[Sen09] T. Senjyu, M. Datta, A. Yona, and C. H. Kim, "A control method for small utility connected large PV system to reduce frequency deviation using a minimal-order observer," *IEEE Trans. Energy Convers.*, vol. 24, no. 2, pp. 520–528, June 2009.

[Sil08] P. S. P. da Silva and P. Rouchon, "Flatness-based control of a single qubit gate," *IEEE Trans. Autom. Control*, vol. 53, no. 3, pp. 775–779, Apr. 2008.

[Son09] E. Song, A. F. Lynch, and V. Dinavahi, "Experimental validation of nonlinear control for a voltage source converter," *IEEE Trans. Control Syst. Technol*., vol. 17, no. 5, pp. 1135–1144, Sep. 2009.

[Ste07] A. Stepanov, I. Galkin, L. Bisenieks, Implementation of supercapacitors in uninterruptible power supplies, Proceedings of the European Power Electronics and Drives 2007, CDROM.

[Sud98] S. D. Sudhoff, K. A. Corzine, S. F. Glover, H. J. Hegner, and H. N. Robey, Jr., "DC link stabilized field oriented control of electric propulsion systems," *IEEE Trans. Energy Convers*, vol. 13, no. 1, pp. 27–33, Mar. 1998.

[Suz08] M. Suzuki, N. Shikazono, K. Fukagata, and N. Kasagi, "Numerical analysis of coupled transport and reaction phenomena in an anode supported flat-tube solid oxide fuel cell," *J. Power Sources*, vol. 180, pp. 29–40, May 2008.

[Sve99] J. Svensson and M. Lindgren, “Influence of Nonlinearities on the Frequency Response of a Grid-Connected Vector-Controlled VSC,” *IEEE Trans. Ind. Electron.*, vol. 46, no. 2, pp. 319–324, Apr. 1999.

[Szu08] A. Szumanowski and Y. Chang, ‘‘Battery management system based on battery nonlinear dynamics modeling,’’ *IEEE Trans. Veh. Technol.*, vol. 57, no. 3, pp. 1425–1432, May 2008.

[Tan04] A. Taniguchi, T. Akita, K. Yasuda, and Y. Miyazaki, “Analysis of electrocatalyst degradation in PEMFC caused by cell reversal during fuel starvation,” *J. Power Sources*, vol. 130, pp. 42–49, May 2004.

[Tan11] C. P. Tang, P. T. Miller, V. N. Krovi, J.-C. Ryu, and S. K. Agrawal, “Differential-flatness-based planning and control of a wheeled mobile manipulator—Theory and experiment,” *IEEE/ASME Trans. Mechatronics*, vol. 16, no. 4, pp. 768–773, Aug. 2011.

[Tel09] S. Teleke, M. E. Baran, A. Q. Huang, S. Bhattacharya, and L. Anderson, “Control strategies for battery energy storage for wind farm dispatching,” *IEEE Trans. Energy Convers.*, vol. 24, no. 3, pp. 725–732, Sep. 2009.

[Tho06a] **P. Thounthong**, S. Raël, and B. Davat, “Test of a PEM fuel cell with low voltage static converter,” *J. Power Sources*, vol. 153, no. 1, pp. 145–150, Jan 2006.

[Tho06b] **P. Thounthong**, S. Raël, and B. Davat, “Control strategy of fuel cell/supercapacitors hybrid power sources for electric vehicle,” *J. Power Sources*, vol. 158, no. 1, pp. 806–814, Jul. 2006.

[Tho07] **P. Thounthong**, S. Raël, and B. Davat, “Control strategy of fuel cell and supercapacitors association for a distributed generation system,” *IEEE Trans. Ind. Electron.*, vol. 54, no. 6, pp. 3225–3233, Dec. 2007.

[Tho08a] **P. Thounthong**, B. Davat, and S. Raël, “Drive friendly,” IEEE POWER & ENERGY MAGAZINE, vol. 6, no. 1, pp. 69–76, Jan.-Feb. 2008.

[Tho08b] **P. Thounthong**, S. Raël, and B. Davat, “Control algorithm of fuel cell and batteries for distributed generation system,” *IEEE Trans. Energy Convers.*, vol. 23, no. 1, pp. 148–155, Mar. 2008.

[Tho09a] **P. Thounthong**, B. Davat, S. Raël, and P. Sethakul, “Fuel Cell High-Power Applications,” *IEEE Ind. Electron. Mag.*, vol. 3, no. 1, pp. 32–46, Mar. 2009.

[Tho09b] **P. Thounthong**, S. Raël, and B. Davat, “Analysis of Supercapacitor as Second Source Based on Fuel Cell Power Generation,” *IEEE Trans. Energy Convers.*, vol. 24, no. 1, pp. 247–255, Mar. 2009.

[Tho09d] **P. Thounthong**, B. Davat, S. Raël, and P. Sethakul, “FUEL STARVATION: Analysis of a PEM fuel-cell system,” *IEEE Ind. Appl. Mag.*, vol. 15, no. 4, pp. 52–59, Jul.-Aug. 2009.

[Tho09e] **P. Thounthong**, S. Raël, and B. Davat, “Energy management of fuel cell/battery/supercapacitor hybrid power source for vehicle applications,” *J. Power Sources*, vol. 193, no. 1, pp. 376–385, Aug. 2009.

[Tho09f] **P. Thounthong** and S. Raël, “The Benefits of Hybridization,” *IEEE Ind. Electron. Mag.*, vol. 3, no. 3, pp. 25–37, Sep. 2009.

[Tho09g] **P. Thounthong**, V. Chunkag, P. Sethakul, M. Hinaje, and B. Davat, "Comparative Study of Fuel-Cell Vehicle Hybridization with Battery or Supercapacitor Storage Device," *IEEE Trans. Veh. Technol.*, vol. 58, no. 8, pp. 3892–3904, Oct. 2009.

[Tho10a] **P. Thounthong** and B. Davat, "Study of a multiphase interleaved step-up converter for fuel cell high power applications," *Energy Convers. Manage.*, vol. 51, no. 4, pp. 826–832, Apr. 2010.

[Tho10b] **P. Thounthong**, S. Pierfederici, J-P. Martin, M. Hinaje, and B. Davat, "Modeling and Control of Fuel Cell/Supercapacitor Hybrid Source Based on Differential Flatness Control," *IEEE Trans. Veh. Technol.*, vol. 59, no. 6, pp. 2700–2710, Jul. 2010.

[Tho10c] **P. Thounthong**, S. Pierfederici, and B. Davat, "Analysis of Differential Flatness-Based Control for a Fuel Cell Hybrid Power Source," *IEEE Trans. Energy Convers.*, vol. 25, no. 3, pp. 909–920, Sep. 2010.

[Tho10d] **P. Thounthong** and S. Pierfederici, "A New Control Law Based on the Differential Flatness Principle for Multiphase Interleaved DC-DC Converter," *IEEE Trans. Circuits Syst. II, Exp. Briefs*, vol. 57, no. 11, pp. 903–907, Nov. 2010.

[Tho11a] **P. Thounthong**, V. Chunkag, P. Sethakul, S. Sikkabut, S. Pierfederici, and B. Davat, "Energy management of fuel cell/solar cell/supercapacitor hybrid power source," *J. Power Sources*, vol. 196, no. 1, pp. 313–324, Jan. 2011.

[Tho11b] **P. Thounthong**, "Model Based-Energy Control of a Solar Power Plant With a Supercapacitor for Grid-Independent Applications," *IEEE Trans. Energy Convers.*, vol. 26, no. 4, pp. 1210–1218, Dec. 2011.

[Tho12a] **P. Thounthong**, "Control of a Three-Level Boost Converter Based on a Differential Flatness Approach for Fuel Cell Vehicle Applications," *IEEE Trans. Veh. Technol.*, vol. 61, no. 3, pp. 1467–1472, Mar. 2012.

[Tho13] **P. Thounthong**, A. Luksanasakul, P. Koseeyaporn, and B. Davat, "Intelligent Model-Based Control of a Standalone Photovoltaic/Fuel Cell Power Plant With Supercapacitor Energy Storage," *IEEE Trans. Sustain. Energy*, vol. 4, no. 1, pp. 240–249, Jan. 2013.

[Tho14] **P. Thounthong**, P. Tricoli, and B. Davat, "Performance investigation of linear and nonlinear controls for a fuel cell/supercapacitor hybrid power plant," *Int. J. Electrical Power and Energy Systems*, vol. 54, no. 1, pp. 454–464, Jan. 2014.

[Too09] R. Toonssen, N. Woudstra, and A. H. M. Verkooijen, "Decentralized generation of electricity from biomass with proton exchange membrane fuel cell," *J. Power Sources*, vol. 194, no. 1, pp. 456–466, Oct. 2009.

[Uzu08] M. Uzunoglu and M. S. Alam, "Modeling and analysis of an FC/UC hybrid vehicular power system using a novel-wavelet-based load sharing algorithm," *IEEE Trans. Energy Convers.*, vol. 23, no. 1, pp. 263–272, Mar. 2008.

[Var06] S. Varigonda and M. Kamat, ''Control of stationary and transportation fuel cell systems: Progress and opportunities,'' *Comput. Chem. Eng.*, vol. 30, no. 10–12, pp. 1735–1748, Sept. 2006.

[Vil07] J. Villagra, B. A. Novel, H. Mounier, and M. Pengov, "Flatness-based vehicle steering control strategy with SDRE feedback gains tuned via a sensitivity approach," *IEEE Trans. Control Syst. Technol*., vol. 15, no. 3, pp. 554–564, May 2007.

[Wai05] R. J. Wai, R. Y. Duan, J. D. Lee, and L. W. Liu, “High-efficiency fuel-cell power inverter with soft-switching resonant technique,” *IEEE Trans. Energy Convers.*, vol. 20, pp. 485–492, June 2005.

[Wan04] M. G. Wanzeller, R. N. C. Alves, J. V. da Fonseca Neto, and W. A. dos Santos Fonseca, “Current Control Loop for Tracking of Maximum Power Point Supplied for Photovoltaic Array,” *IEEE Trans. Instrument and Measurement*, vol. 53, no 4, pp. 1304–1309, Aug. 2004.

[Wan06a] C. Wang, "MODELING AND CONTROL OF HYBRID WIND/PHOTOVOLTAIC/FUEL CELL DISTRIBUTED GENERATION SYSTEMS," PhD Thesis, MONTANA STATE UNIVERSITY, Bozeman, Montana, USA, July 2006.

[Wan06b] C. Wang, M. H. Nehrir, and H. Gao, “Control of PEM fuel cell distributed generation systems,” *IEEE Trans. Energy Convers.*, vol. 21, pp. 586–595, June 2006.

[Wan07a] C. Wang and M. H. Nehrir, “A physically based dynamic model for solid oxide fuel cells,” *IEEE Trans. Energy Convers.*, vol. 22, pp. 887–897, Dec. 2007.

[Wan07b] C. Wang and M. H. Nehrir, “Load transient mitigation for stand-alone fuel cell power generation systems,” *IEEE Trans. Energy Convers.*, vol. 22, pp. 864–872, Dec. 2007.

[Wan07c] J. Wang, B. Taylor, Z. Sun, and D. Howe, ‘‘Experimental characterization of a supercapacitor-based electrical torque-boost system for downsized ICE vehicles,’’ *IEEE Trans. Veh. Technol.*, vol. 56, no. 6, pp. 3674–3681, Nov. 2007.

[Wed11] A. S. Weddell, G. V.Merrett, T. J. Kazmierski, and B. M. Al-Hashimi, “Accurate supercapacitor modeling for energy harvesting wireless sensor nodes,” *IEEE Trans. Circuits Syst. II, Exp. Brief*, vol. 58, no. 12, pp. 911–915, Dec. 2011.

[Xia06] W. Xiao, M. G. J. Lind, W. G. Dunford, and A. Capel, “Real-Time Identification of Optimal Operating Points in Photovoltaic Power Systems,” *IEEE Trans. Ind. Electron.*, vol. 53, no. 4, pp. 1017–1026, Aug. 2006.

[Yan07] Y. P. Yang, J. J. Liu, T. J. Wang, K. C. Kuo, and P. E. Hsu, ‘‘An electric gearshift with ultracapacitors for the power train of an electric vehicle with a directly driven wheel motor,’’ *IEEE Trans. Veh. Technol.*, vol. 56, no. 5, pp. 2421–2431, Sept. 2007.

[Yon07] T. Yoneyama, T. Yamamoto, K. Kondo, T. Furuya, and K. Ogawa, “Fuel cell powered railway vehicle and experimental test results,” in *Proc. EPE’07*, 2–5 Sept. 2007, pp. 1–10.

[You09] N. Yousfi-Steiner, Ph. Moçotéguy, D. Candusso, and D. Hissel, “A review on polymer electrolyte membrane fuel cell catalyst degradation and starvation issues: Causes, consequences and diagnostic for mitigation,” *J. Power Sources*, no. 194, no. 1, pp. 130–145, Oct. 2009.

[Zan11] M. Zandi, A. Payman, J.-Ph. Martin, S. Pierfederici, B. Davat, and F. Meibody-Tabar, ‘‘Energy Management of a Fuel cell / SuperCapacitor / Battery Power Source for Electric Vehicular applications,’’ *IEEE Trans. Veh. Technol.*, vol. 20, no. 2, pp. 433–443, 2011.

[Zhu06] T. Zhu, S. R. Shaw, and S. B. Leeb, “Transient recognition control for hybrid fuel cell systems,” *IEEE Trans. Energy Convers.*, vol. 21, pp. 195–201, Mar. 2006

@@@ END @@@

In the early 90s, the flatness theory was introduced by Fliess *et al*. [Fli95] in a differential algebraic framework. A nonlinear system is flat if there exists a set of differentially independent variables (equal in number to the number of inputs) such that all state variables **x** and (control) input variables **u** can be expressed in terms of those output variables **y** and a finite number of their time derivatives without integrating differential equations. More specifically, consider the nonlinear dynamic system of the general form

$$\left.\begin{aligned}\dot{\mathbf{x}}(t) &= f\left(\mathbf{x}(t),\mathbf{u}(t)\right)\\ \mathbf{y}(t) &= h\left(\mathbf{x}(t),\mathbf{u}(t)\right)\end{aligned}\right\} \tag{A.1}$$

where

$$\mathbf{x} = \left[x_1, x_2, \ldots x_n\right]^T; \quad \mathbf{x} \in \Re^n \tag{A.2}$$

$$\mathbf{u} = \left[u_1, u_2, \ldots u_m\right]^T; \quad \mathbf{u} \in \Re^m \tag{A.3}$$

$$\mathbf{y} = \left[y_1, y_2, \ldots, y_m\right]^T; \quad \mathbf{y} \in \Re^m \tag{A.4}$$

$f(\cdot)$ and $h(\cdot)$ are smooth nonlinear functions, and $(n, m) \in \mathbb{N}$. Moreover, it is assumed that $m \le n$.

As depicted in Fig. A1, nonlinear flat systems are equivalent, in a more general way, to linear controllable systems. A system is denoted flat if an output vector **y** exists that fulfills the following conditions:

(i) The output variables y_i can be stated as functions of the state variables x_i, the input variables u_i and a finite number α of their time derivatives

$$\mathbf{y} = \phi\left(\mathbf{x}, u, \dot{u}, \ldots, u^{(\alpha)}\right) \tag{A.5}$$

(ii) All state variables x_i and all control inputs u_i can be stated as functions of the output variables y_i and a finite number β of their time derivatives

$$\mathbf{x} = \varphi\left(y, \dot{y}, \ldots, y^{(\beta)}\right) \tag{A.6}$$

$$\mathbf{u} = \psi\left(y, \dot{y}, \ldots, y^{(\beta+1)}\right) \tag{A.7}$$

where $\phi(\cdot)$, $\varphi(\cdot)$, and $\psi(\cdot)$ are smooth mapping functions.

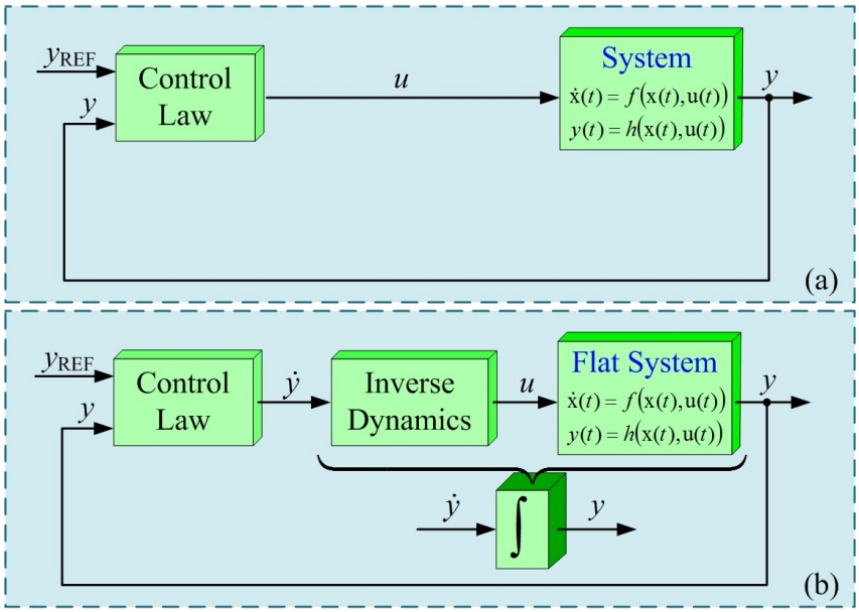

Fig. A1. Concept of control system, (a) linear control, (b) differential flatness-based control, where y is the output variable, y_{REF} is the output set-point, and u is the control input variable.

If the output variables of interest can be proven to be flat outputs **y**, reference control design y_{REF} becomes straightforward. The dynamics of the resulting linear error dynamics can be specified by introducing a new stabilizing input v_i (control law, refer to Fig. A1).

$$0 = \left(y_i^{(\beta+1)} - y_{i,REF}^{(\beta+1)}\right) + K_\beta\left(y_i^{\beta} - y_{i,REF}^{\beta}\right) + \cdots + K_0\left(y_i - y_{i,REF}\right) \tag{A.8}$$

Then,

$$\begin{aligned} v_i &= y_{i,REF}^{(\beta+1)} + K_\beta\left(y_{i,REF}^{\beta} - y_i^{\beta}\right) + \cdots + K_0\left(y_{i,REF} - y_i\right) \\ &= y_i^{(\beta+1)} \end{aligned} \tag{A.9}$$

where $K_\beta,\ldots,K_0$ are the set of controller parameters and replace the highest derivative of y_i in the expression of the control input with v_i according to (A.7). This results in the following inverse dynamics

$$\mathbf{u} = \psi\left(y, \dot{y}, \ldots, y^{\beta}, \mathbf{v}\right) \tag{A.10}$$

where the control inputs are calculated depending on the measured outputs **y** and desired outputs y_{REF}. The set of controller parameters $K_\beta,\ldots,K_0$ are chosen such that the roots of the closed loop characteristic polynomial, in the complex variable *s*,

$$p(s) = s^{\beta+1} + \lambda_\beta s^\beta \cdots + \lambda_2 s^2 + \lambda_1 s^1 + \lambda_0 \tag{A.11}$$

is a Hurwitz polynomial.

Obviously, the tracking error, $e_i = y_i - y_{i,REF}$, satisfies

$$e_i^{(\beta+1)} + K_\beta e_i^{(\beta)} + \cdots + K_0 e_1 = 0 \tag{A.12}$$

An optimum choice of the design controller parameters is obtained by matching the characteristic polynomial, $p(s)$, to a desired characteristic polynomial, with pre-specified root locations.

Currently, these ideas have lately been used in a variety of nonlinear systems across various engineering disciplines, including the following:

1) process of stirred tank chemical reactor [Gua02];
2) vehicle steering control [Vil07];
3) control of a high-speed linear axis driven by pneumatic muscle actuators [Asc08];
4) control of cathode pressure and oxygen excess ratio of a PEMFC system [Dan08];
5) steering control of a two-level quantum system [Sil08];
6) reactive power and dc voltage tracking control of a three phase voltage source converter, refer to Fig. A2 [Son09];
7) control of open-channel flow in an irrigation canal [Rab09];
8) current control for three-phase three-wire boost converters [Gen09];
9) design of a guidance algorithm for the hypersonic phase of a lifting-body vehicle [Mor09];

10) control of space robot with arbitrarily oriented joint axes and two momentum wheels at the base [Agr09].

At least, Fig. A3 shows a comparison of the flatness-based and traditional linear proportional-integral (PI) control methods (vector control), which uses a dc bus voltage regulation in a three phase voltage source converter (AC-to-DC converter, Fig. A2) to step a dc bus voltage reference v_{BusREF}, as demonstrated by Song *et al*. [Son09]. The parameters of the linear controller were tuned to obtain the best possible performance. Fig. A3 shows the real experimental results obtained for both controllers during a set-point step. The flatness-based control shows good stability and an optimum response during dc bus voltage regulation. Using this data, one can conclude that the flatness-based control method provides better performance as compared to the classic PI controller.

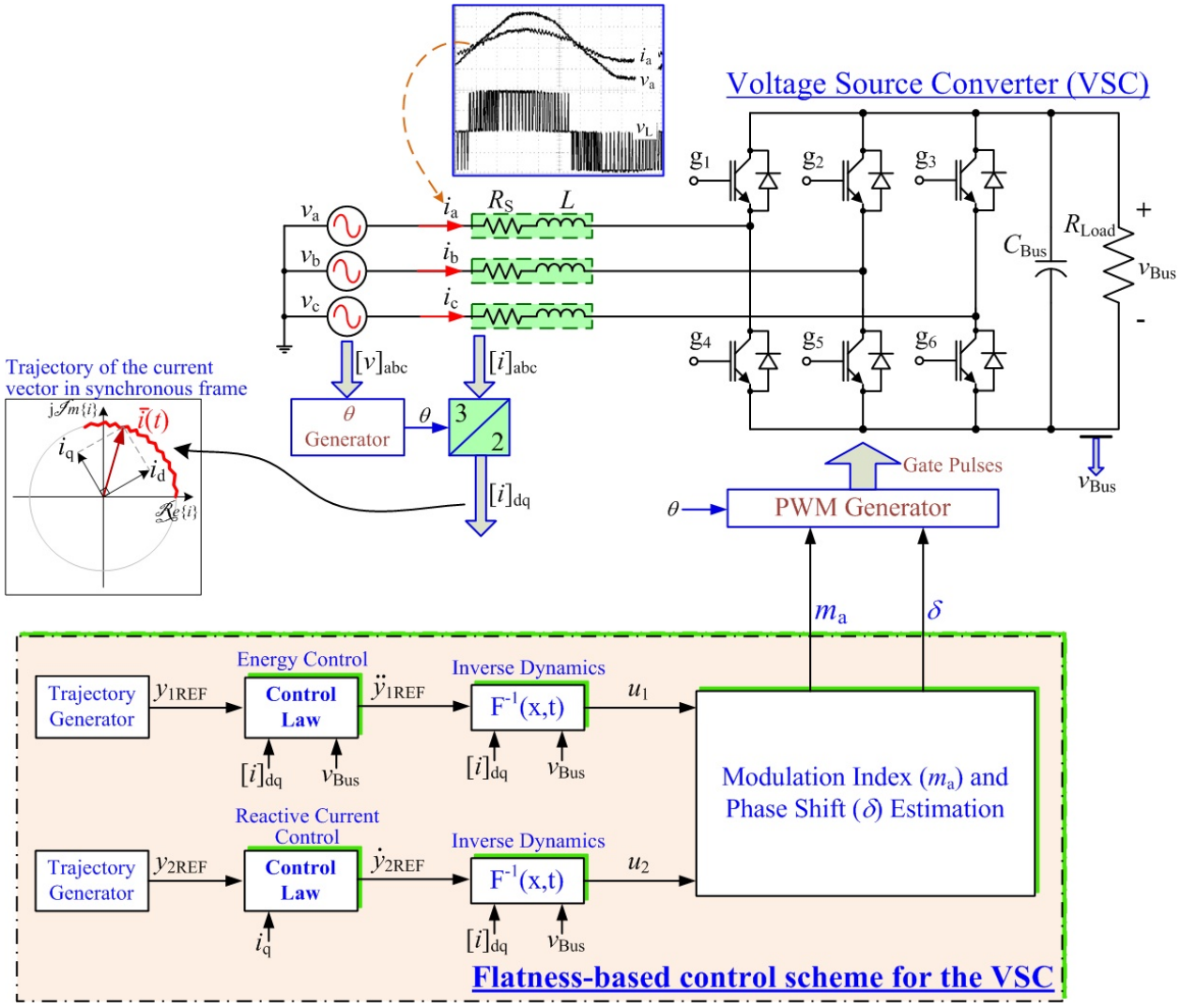

Fig. A2. Flatness-based control scheme for the VSC-based STATCOM system [Son09].

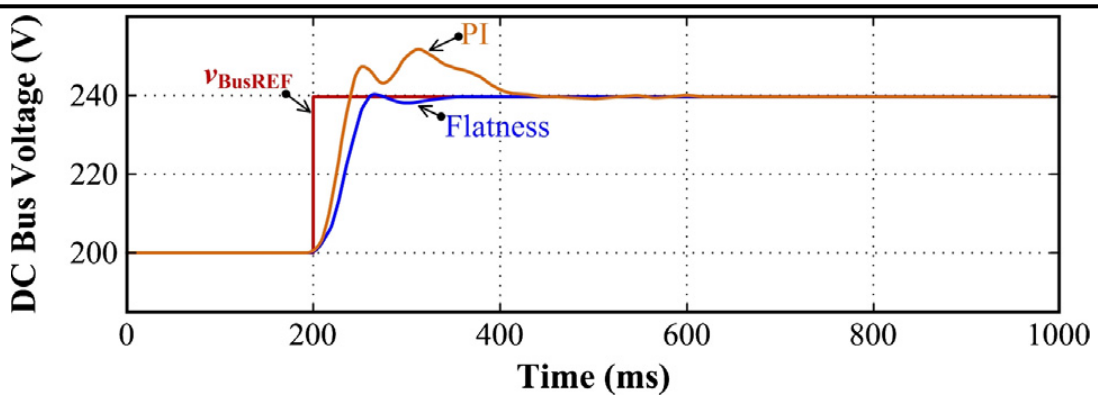

Fig. A3. Experimental result: Comparison of the flatness-based control law with a linear PI control law for a dc bus voltage regulation during a step of dc bus voltage set-point v_{BusREF} at t = 200 ms from 200 V to 240 V.

@@@ END @@@